M -P -I ¨ A

Multi-dimensional simulations of core collapse supernovae with different equations of state for hot proto-neutron stars

Andreas Marek

Vollständiger Abdruck der von der Fakultät für Physik der Technischen Universität München zur Erlangung des akademischen Grades eines

Doktors der Naturwissenschaften (Dr. rer. nat.)

genehmigten Dissertation.

Vorsitzender:	Univ.-Prof. Dr. F. v. Feilitzsch
Prüfer der Dissertation:	1. Priv.-Doz. Dr. H.-Th. Janka
	2. Univ.-Prof. Dr. W. Weise

Die Dissertation wurde am 8.2.2007 bei der Technischen Universität München eingereicht und durch die Fakultät für Physik am 16.4.2007 angenommen.

Mehrdimensionale Simulationen von Kernkollaps-Supernovae mit unterschiedlichen Zustandsgleichungen für heiße Proto-Neutronensterne

Kernkollaps-Supernovae gehören mit zu den energiereichsten Explosionen, die man in unserem Universum beobachten kann. Nur mittels numerischer Simulationen ist es möglich, die komplexen Vorgänge, die zu diesen Explosionen führen, zu verstehen. Der genaue Mechanismus für diese Explosionen ist bis heute noch nicht verstanden, was unter anderem daran liegt, dass die Zustandsgleichung für die Beschreibung der Materie im Sterninneren nur unzureichend bekannt ist. Die vorliegende Arbeit präsentiert die weltweit ersten Supernovasimulationen in denen mittels mehrdimensionaler Rechnungen der Einfluss der Zustandsgleichung auf den Explosionsmechanismus untersucht werden konnnte. Es konnte gezeigt werden, dass die Zustandsgleichung einen erheblichen Einfluss auf die Vorgänge innerhalb der Supernova hat, und dass deshalb eine bessere Kenntnis der Zustandsgleichung zum Verständnis von Kernkollaps-Supernovae unerlässlich ist.

Contents

Most of what follows is true.

Butch Cassidy and the Sundance Kid, 1969

1 Introduction

Observations of rare, but very luminous events, when suddenly and temporarily an extremely bright "new" star appears on the sky, led to the term "supernova". As the term indicates, originally these events were believed to be the birth cries of new stars. However, today it is known that quite the opposite is true — a supernova event tells us about the final stages of a star's life, when the star is disrupted in a powerful explosion. Furthermore, it is nowadays known that two distinct classes of supernovae exist which are called "thermonuclear supernovae" or "core collapse supernovae". The former, which are thermonuclear explosions of accreting or merging white dwarfs, will not be discussed in this thesis. The latter mark the end stage of stars whose mass exceeds eight times the mass of our Sun.

The term "core collapse supernova" describes the fact that these explosive events are triggered by the collapse of the central core of a massive star. During their life all stars create energy by the fusion of lighter elements to heavier ones. However, the stars that are to undergo a supernova explosion reach the endpoint of this possible energy source and evolve a core which consists of iron–group nuclei and which is stabilised against its own gravitational pull mainly by the pressure of the degenerate electron gas inside this "iron core"[1]. Without the possibility to create energy by the fusion of elements heavier than the iron group elements, and with the acceleration of electron captures on protons that decrease the stabilising pressure of degenerate electrons, the iron core slowly contracts and heats up. Once the photons contained in the core become energetic enough to photo–dissociate the nuclei, the contraction speeds up and the core is driven to a runaway collapse. Neutrinos, which are continuously created by electron captures in the collapsing core, leave the core unhindered until a density of about 10^{12} g/cm^3 is reached. Around this density, coherent scattering of neutrinos becomes so rapid that the neutrinos get effectively trapped in the core, since the diffusion timescale begins to exceed the dynamical timescale of the collapse. As a consequence of the electron captures on free and bound protons,

[1] Stars below $\approx 10\,M_\odot$ develop cores with dominant mass fractions of O, Ne, and Mg until these cores become gravitationally unstable mainly by the onset of very rapid electron captures.

matter in the stellar core becomes more and more neutron rich. Now, within a few milliseconds only, the density in the collapsing core reaches that of nuclear matter ($\approx 2 \times 10^{14} \mathrm{g/cm^3}$), where the nuclei dissolve into a homogenous phase of non–relativistic nucleons. At this time the repulsive terms of the nucleon–nucleon potential become important and the pressure in the central part of the core increases strongly due to the "stiffening" of the equation of state. The increase of the pressure counteracts the gravitational force, the collapse is suddenly halted, and the inner core rebounds. The outer parts of the core, however, falling towards the centre of the star with supersonic velocities, collide with the rebounding inner core and a strong shock forms. This so–called "prompt shock" rapidly travels outward through the iron core. Although, for a long time it was believed that this shock triggers a supernova explosion immediately (i.e. the formed shock would continue travelling through the whole star), it is nowadays clear that the prompt shock loses too much energy and stalls (see, e.g. Bethe 1990). These energy losses occur mainly by two processes: On the one hand, iron–like nuclei that are falling through the shock front are dissociated into free nucleons, which consumes roughly 8.8 MeV per nucleon. On the other hand, when the shock front reaches densities of around 10^{11} g/cm^3, the matter behind the shock is not any longer opaque to neutrinos, and the neutrinos diffusing behind the shock front can suddenly stream off freely. As a consequence, huge amounts of energy and lepton number are suddenly released in the so–called "neutrino burst". Both processes deprive the moving shock front of energy so strongly that it stagnates after a few milliseconds.

From the time of the neutrino burst on, the dense nascent neutron star at the centre (the so–called "proto–neutron star") continuously emits neutrinos that are created at high rates in its interior and which slowly diffuse out. Almost all of the gravitational binding energy that was set free during the collapse is stored in degeneracy energy of electrons and later on is slowly released by neutrinos. On their way out of the iron core and through the rest of the collapsing star, these neutrinos can be absorbed and can transfer energy to the matter. In the current paradigm for the core–collapse supernova explosion mechanism, the neutrinos are the agent that transfers energy from the dense forming neutron star to the matter behind the shock front, thereby reviving the shock and ultimately causing the explosion.

Although this basic picture of neutrino driven–explosions is commonly accepted, theorists have struggled already for more than 40 years to answer the following question: How is it possible, in order to power the explosion, to tap the pool of gravitational binding energy that is released during the collapse of the stellar core ? In order to comprehend why the supernova explosion mechanism is so complicated to be understood, one has to remind oneself of the complexity of the problem to be solved: In a core collapse supernova all interactions (i.e gravity, electro–weak interaction, and strong interactions) are important and govern collectively the explosive event. Gravity causes the collapse and provides the (released gravitational binding) energy necessary for the explosion. The strong interaction is responsible for the incompressibility of nuclear matter that halts the collapse of the inner core, and determines the equation of state of the proto–neutron star. Weak interactions create the neutrinos (depending on the matter composition) that transfer energy from the dense core to the stalled shock front. The details of the propagation of the neutrinos through the supernova core as well as their reactions with matter (i.e energy deposition or emission) also depend strongly on the equation of state and the composition of supernova matter, which in turn depend on electromagnetic, weak, and

strong interactions. Due to the complexity of the problem supernova research relies heavily on numerical modelling and supernova theory is driven by the increase of computer power and the availability of better numerical tools.

After Colgate & White (1966) proposed that neutrinos can power the explosion of core collapse supernovae, simulations of Wilson (1982) showed that this might indeed be the case. Wilson et. al followed the supernova calculations to unexplored evolution times of several hundred milliseconds after the shock formation, and indeed observed an explosion, thus discovering the "delayed neutrino–driven" supernova explosion mechanism. However, subsequent research turned out that the details of the neutrino energy transfer to stellar matter and the revival of the supernova shock front depend sensitively on the details of the neutrino propagation out of the proto–neutron star and through the rest of the stellar core.

Epstein (1979) proposed that convective motions inside the proto–neutron star could drag neutrinos with the matter flow from the optically thick region towards the region of free streaming thereby enhancing — by effectively reducing the diffusion timescale — the neutrino emission of the dense core. Indeed, Mayle et al. (1993) obtained explosions in one–dimensional simulations by assuming a special mode of convection inside the proto–neutron star. With their assumptions, so–called "neutron finger convection" established, where — similar to the salt–finger convection in fluids with a unstable stratification of water with a large salt–content on top of layer of water with less salt–content — an unstable matter stratification of specific heavier neutrons on top of specific lighter material was found which causes the heavier part of the fluid to sink and causes the convective motion. In these models this type of convection increased the neutrino flux of the dense core such that more neutrinos were absorbed in the layer behind the shock front, thus the neutrino heating was increased and explosions could be launched.

However, the assumptions of Mayle et al. (1993) on the nuclear equation of state, the onset of proto–neutron star convection, and their treatment of neutrinos are controversially debated among supernova physicists. Nevertheless, the results of Mayle et. al showed that proto–neutron star convection, which is a purely multi–dimensional effect, may influence the supernova evolution strongly and much work was put forward in studying this phenomenon (see, e.g. Keil et al. 1996, Mezzacappa et al. 1998b, only to name a few).

In 1987, another major breakthrough in supernova theory came with the observations of Supernova SN1987A that showed that the ejected mass distribution was highly anisotropic (see, e.g. Hillebrandt et al. 1989, Arnett et al. 1989, McCray 1993, Nomoto et al. 1994, Wooden 1997, Müller 1998, and references therein). Subsequent simulations (see, e.g. Kifonidis et al. 2003, 2006, and references therein) showed that these observations can only be explained if hydrodynamic instabilities set in at early times after the shock formation, since the observed mixing of heavy elements from deep inside of the supernova core far out to the envelop of the star can only be explained with the presence of "mixing instabilities" from early times on. One type of instability is convection in the heating region behind the shock front, where strong turbulent flows can develop which transport neutrino heated matter from the region of strongest heating towards the shock front and, simultaneously, cooler matter flows from the shock front

down to the heating region (Herant et al. 1992, Burrows et al. 1995, Fryer 1999, Fryer & Heger 2000, Fryer & Warren 2002, 2004).

Another type of hydrodynamic instability is the only recently discovered so–called "standing accretion shock instability", where pressure fluctuations in the matter behind the shock front can lead to the development of large non–radial modes of shock deformation and anisotropic explosions (see, e.g. Blondin et al. 2003, Scheck 2006).

Thus, nowadays it is commonly accepted that the supernova explosion mechanism is based on multi–dimensional effects and that spherically–symmetric models (such as the ones of Mezzacappa & Bruenn 1993a, Burrows et al. 2000, Rampp & Janka 2002, Mezzacappa et al. 2001, Liebendörfer et al. 2001, only to mention a few) are — even if explosions would be obtained — not appropriate to explain the observed explosion characteristics. Although, the importance of multi–dimensional effects has been recognised it is, however, not understood in satisfactory detail what governs the growth of hydrodynamic instabilities in the supernova core.

However, at least for convection in the heating region below the shock front one may intuitively assume that different heating of the matter may influence the strength of convection: Like a soup boiling differently strong on an oven, dependent on the amount of heating from the plate, different neutrino fluxes from the dense core and different neutrino heating might lead to a stronger or weaker development of convective flows. One possibly candidate for changing the neutrino emission from the dense core is the nuclear equation of state of hot proto–neutron stars. On the one hand, from theoretical as well as experimental point of view the equation of state for hot and dense supernova cores is highly uncertain (see, e.g. Lattimer 2005, 2006, Lattimer & Prakash 2006), which implies that the whole evolution of the dense core and its neutrino emission are also uncertain. It is thus unclear how the nuclear equation of state influences convective instabilities inside the proto–neutron star and thus either boosts or damps the neutrino emission of the dense core. On the other hand, investigations of different descriptions of the dense neutron star matter showed in spherically symmetric simulations (i.e. proto–neutron star convection or other multi–dimensional effects have not been taken into account in these studies) that the neutrino fluxes and the neutrino energy deposition in the heating region depend on the equation of state (see, e.g. Marek 2003, Sumiyoshi et al. 2005). Thus there are strong indications that the nuclear equation of state can influence the development of convection inside the supernova core. However, up to now the influence of the nuclear equation of state of proto–neutron stars on the growth of hydrodynamic instabilities in the supernova core has not been investigated in multi–dimensional simulations.

In this thesis I aim at clarifying in general the role of the nuclear equation of state during the supernova evolution, but the focus is on the influence of the equation of state on the development of instabilities inside the supernova core. For this purpose, multi–dimensional as well as spherically symmetric simulations are applied and compared. That this is possible is due to the numerical tool used in this thesis which allows to calculate both one–dimensional and two–dimensional simulations with the same treatment of physics and numerics. Thus a direct comparison of multi–dimensional and spherically symmetric calculations, which is impossible for other supernova modellers, are feasible. Due to the reduced complexity, the latter simula-

tions are used to analyse different aspects of the interplay between the equation of state and the supernova evolution. Furthermore, since these simulations are much faster than the multi–dimensional ones, several different calculations are used in parameter–like studies, in order to understand the importance of the nuclear equation of state. The implications of these calculations are manifold. They show that the whole proto–neutron star evolution and its neutrino emission depend sensitively on the description of the strong interaction between baryons, and that the supra–nuclear phase can influence the supernova evolution strongly. Also the observed neutrino signal from supernova explosions shows a dependence of the equation of state, which might be used in the future to constrain the nuclear equation of state.

The main focus of this work is, however, on multi–dimensional effects during the supernova evolution. For the first time the influence of the equation of state on convection and on other multi–dimensional effects is investigated together with calculations of spectral Boltzmann neutrino transport. The step from spherically symmetric studies to multi–dimensional ones is a major one: As I will show, the equation of state influences strongly the appearance of convective instabilities and thus the neutrino emission of the dense core. This leads to interesting implications for the evolution of core collapse supernovae.

Conceptually, this thesis is divided in two major parts. In Chapter 2 the code used throughout this thesis is shortly introduced. The subsequent Part I is dedicated to the investigation of the equation of state effects in one–dimensional calculations. As a specific example, with simulations of a $15M_{\odot}$ progenitor star, I discuss in Section 3.2 the major influences of the equation of state on the supernova evolution. Then, in the Sections 3.3 through 3.4, I try to disentangle what properties of the equations of state influence the various phases of the supernova evolution, before I conclude Part I with a study of the influence of the equations of state on the neutrino emission of exploding models.

The second Part of this thesis is dedicated to the discussion of multi–dimensional simulations. With simulations of $11.2M_{\odot}$ progenitor star, I discuss in Chapter 4 why multi–dimensional effects can lead to explosions which otherwise are not observed in spherically symmetric calculations. The influence of the equation of state on these multi–dimensional effects is then investigated in Chapter 5. I conclude this Part II in Chapter 6 with a discussion of the effects of rotation or the progenitor structure. Finally, in Chapter 7, I will present my conclusions from the studies presented in this thesis.

A tool is usually more simple than a machine; it is generally used with the hand, whilst a machine is frequently moved by animal or steam power

C. Babbage, "The Father of Computing"

2

The VERTEX/MUDBATH tool: a radiation hydrodynamics code for core collapse supernovae

The numerical tool which is used in this thesis was specifically written to the application to the simulations of core collapse supernovae. V [1], the spherically symmetric (i.e. 1D) version of this code, was developed by Rampp & Janka (2002) and is described in detail in their publication. The two–dimensional version of this code, called M DB TH[2], is described in great detail in Buras et al. (2006a,b).

Since both version of the code are already documented very precisely, this Chapter does not intend to give such a detailed description, but it rather explains the numerical approach to simulate core collapse supernovae. However, before the underlying physics of the V - /M DB TH tool is described, it shall be stressed here that this tools are unique since it is possible to calculate one–dimensional and two–dimensional simulations with exactly the same micro–physics and the same numerical treatment. This allows to directly compare results of one–dimensional and multi–dimensional simulations, which can not be done by other supernova modellers.

Considering the physical treatment of a core collapse supernova one has to realise that the key assumption to do the simulations is that one can treat the stellar plasma and the interior of the nascent neutron star as fluids with different chemical composition. One has thus to solve the equations of hydrodynamics together with evolution equations of the composition. The neutrinos on the other hand, which are created by nuclear reactions and propagate through the stellar fluid and can interact with this fluid, can be treated as radiation whose properties can be described by a distribution function. The time evolution of this distribution function is then

[1] An abbreviation of **V**ariable **E**ddington factor **R**adiative **T**ransfer for supernova E**x**plosions.
[2] An abbreviation of **V**ariable **M**ulti–**D**imensional **B**oltzm**a**nn **T**ransport and **H**dro.

expressed by the Boltzmann equation. Thus, in addition to the hydrodynamics one has to solve the neutrino transport problem by finding a solution to the Boltzmann equation (neutrinos are created by nuclear reactions out of the stellar plasma, and they can transfer or absorb energy from the stellar plasma). The V /M DB TH code uses the operator splitting method to solve this coupled system of evolution equations: for each cycle of the code the hydrodynamics part and the transport/interactions part are computed in two independent, subsequent steps. In the following Sections these subsequent steps will be described sepeately.

2.1. Hydrodynamics part

The hydrodynamics part solves the Eulerian, non relativistic equations of hydrodynamics together with the evolution equations of the chemical composition. These equations can be written in spherical symmetry, with the additional assumption of azimuthal symmetry as follows:

$$\frac{\partial}{\partial t}\rho + \frac{1}{r^2}(r^2\rho v_r) + \frac{1}{r\sin\theta}\frac{\partial}{\partial\theta}(\rho\sin\theta\, v_\theta) = 0. \tag{2.1}$$

$$\frac{\partial}{\partial t}(\rho\, v_r) + \frac{1}{r^2}\frac{\partial}{\partial r}(r^2\rho\, v_r\, v_r) + \frac{1}{r\sin\theta}\frac{\partial}{\partial\theta}(\rho\sin\theta\, v_\theta\, v_r) - \rho\frac{{v_\theta}^2 + {v_\phi}^2}{r} + \frac{\partial p}{\partial r} = -\rho\frac{\partial\Phi}{\partial r} + Q_{M_r} \tag{2.2}$$

$$\frac{\partial}{\partial t}(\rho v_\theta) + \frac{1}{r^2}(\rho\, v_r\, v_\theta) + \frac{1}{r\sin\theta}\frac{\partial}{\partial\theta}(\rho\sin\theta\, v_\theta\, v_\theta) + \rho\frac{v_r\, v_\theta - {v_\phi}^2\cot\theta}{r} + \frac{1}{r}\frac{\partial p}{\partial\theta} = -\frac{\rho}{r}\frac{\partial\Phi}{\partial\theta} + Q_{m_\theta} \tag{2.3}$$

$$\frac{\partial}{\partial t}(\rho v_\phi) + \frac{1}{r^2}\frac{\partial}{\partial r}(r^2\rho\, v_r\, v_\phi) + \frac{1}{r\sin\theta}\frac{\partial}{\partial\theta}(\rho\sin\theta\, v_\theta\, v_\phi) + \rho\frac{v_r\, v_\phi + v_\theta\, v_\phi\,\cot\theta}{r} = 0 \tag{2.4}$$

$$\frac{\partial}{\partial t}(\rho\epsilon + \frac{1}{r^2}\frac{\partial}{\partial r}\left(r^2(\rho\epsilon + p)v_r\right) + \frac{1}{r\sin\theta}\frac{\partial}{\partial\theta}\left((\rho\epsilon + p)\sin\theta\, v_\theta\right) = -\rho\left(v_r\,\frac{\partial\Phi}{\partial r} + \frac{v_\theta}{r}\frac{\partial\Phi}{\partial\theta}\right) + Q_E + v_r\, Q_{M_r} + v_\theta\, Q_{M_\theta} \tag{2.5}$$

$$\frac{\partial}{\partial t}(\rho Y_e) + \frac{1}{r^2}\frac{\partial}{\partial r}(r^2\rho Y_e\, v_r) + \frac{1}{r\sin\theta}\frac{\partial}{\partial\theta}(\sin\theta\,\rho Y_e\, v_\theta) = Q_N \tag{2.6}$$

$$\frac{\partial}{\partial t}(\rho Y_k) + \frac{1}{r^2}\frac{\partial}{\partial r}(r^2\rho Y_k\, v_r) + \frac{1}{r\sin\theta}\frac{\partial}{\partial\theta}(\sin\theta\,\rho Y_k\, v_\theta) = R_k \tag{2.7}$$

Here ρ denotes the mass density, v_r, v_θ, and v_ϕ denote the radial, lateral, and azimuthal components of the velocity, and $\epsilon = e + 1/2({v_r}^2 + {v_\theta}^2 + {v_\phi}^2)$ the specific energy, with e being the specific internal energy. Furthermore, p denotes the gas pressure, Φ the gravitational potential

of the fluid, and Q_{M_r}, Q_{M_θ}, and Q_{M_E} denote the neutrino source terms of momentum and energy transfer. Note that the equations of hydrodynamics (Eqs. (2.1)–(2.5)) are closed by the EoS[3] that relates the gas pressure p to the density ρ, the internal energy e, and the composition.

The time evolution of the composition, on the other hand is given by Eqs. (2.6)–(2.7): if nuclear statistical equilibrium can be assumed the chemical evolution is determined by the evolution of the electron fraction Y_e (Eqn. (2.6)), otherwise for each nucleus k an equation of form (2.7) must be solved, where $Y_k = n_k/n_\mathrm{b}$ with n_k being the number density of the respective nucleus and n_b being the baryon number density.

Numerically in our code, the Eqs. (2.1)–(2.7) are integrated with the Newtonian finite–volume code P (Fryxell et al. 1989, 2000), which was improved to be applicable to core collapse supernova simulations by Keil (1997) and Kifonidis et al. (2003). P is a direct Eulerian implementation of the Piecewise Parabolic Method (PPM) of Colella & Woodward (1984), which is a time–explicit, third–order in space, second–order in time Godunov scheme with a Riemann solver and is very well suited for following discontinuities in the fluid flow such as shocks, contact discontinuities, or boundaries between layers of different chemical composition. It is capable to solve multi–dimensional problems with both high computational efficiency and numerical accuracy.

Though our hydrodynamic part is Newtonian, effects of general relativity are included in an approximative way: the gravitational potential Φ can be written as $\Phi_{2\mathrm{D}} = {\Phi_{2\mathrm{D}}}^{\mathrm{Newt}} + \left({\Phi_{1\mathrm{D}}}^{\mathrm{GR}} - {\Phi_{1\mathrm{D}}}^{\mathrm{Newt}}\right)$, where $\Phi_{2\mathrm{D}}^{\mathrm{Newt}}$ is calculated for the two–dimensional axis–symmetric mass distribution by expanding the integral solution of the Poisson equation into a Legendre series, see Müller & Steinmetz (1995). The spherically symmetric "correction term" $\left({\Phi_{1\mathrm{D}}}^{\mathrm{GR}} - {\Phi_{1\mathrm{D}}}^{\mathrm{Newt}}\right)$ includes general relativistic effects, such as contributions of the pressure and the energy to the gravitational potential. This "relativistic gravitational potential" is discussed in Appendix B. The other source terms on the right hand sides of Eqs. (2.1)–(2.7) are computed from the solutions of the neutrino transport equations.

2.2. Transport part

The solution of the neutrino–transport equations in the V /M DB TH code relies on the so called "Variable Eddington factor" approach, which is shortly described in the following.

As already mentioned the source terms for the energy, momentum, and electron fraction of the fluid owing to its interaction with neutrinos can be calculated from the neutrino distribution function $f(r, \vartheta, \phi, \epsilon, \Theta, \Phi, t)$ in phase space. In the full problem, this is a seven–dimensional function, as it describes at every point in space (r, ϑ, ϕ), the distribution of neutrinos propagating with energy ϵ into the direction (Θ, Φ) at time t, see Fig. 2.1. Instead of f mostly the neutrino intensity $I = c/(2\pi\hbar c)^3 \epsilon^3 f$ is used. However, since the source terms in the Eqs. (2.1)–(2.6) are integrals over I over momentum space and thus only a fraction of the information contained in I is required to compute the dynamics of the flow. Thus, in the V /M DB T code angular moments of I are considered, instead of using the Boltzmann equation directly, which reduces

[3] Note that in modern supernova simulations quite complicated EoS are used which can not be calculated during the simulation. Thus, normally supernova modelers use EoS–tables and obtain the desired quantities by looking them up in the tables.

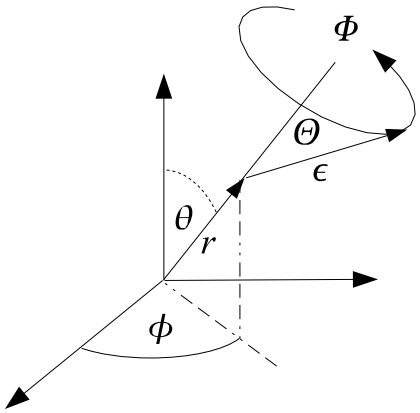

Figure 2.1.: A sketch of the coordinates used in the V /M DB TH code. Note that each coordinate point (r, θ, ϕ) a neutrino with energy ϵ can propagate in direction (Θ, Φ).

the problem to a four dimensional one. The first three moments of I are defined as

$$J, \boldsymbol{H}, \mathbf{K}, \mathbf{L}, \ldots (r, \theta, \phi, \epsilon, t) = \frac{1}{4\pi} \int I(r, \theta, \phi, \epsilon, \Theta, \Phi, t)\, \boldsymbol{n}^{0,1,2,3,\ldots}\, \mathrm{d}\Omega \tag{2.8}$$

where $\mathrm{d}\Omega = \sin\Theta\, \mathrm{d}\Theta\, \mathrm{d}\Phi$, $\boldsymbol{n} = (\cos\Theta, \sin\Theta\cos\Phi, \sin\Theta\sin\Phi)$, and exponentiation represents repeated application of the dyadic product. In order to reduce the size of the problem even further, one needs to resort to assumptions on its symmetry. At this point, one usually employs azimuthal symmetry for the stellar matter distribution, i.e. any dependence on the azimuth angle ϕ is ignored, which implies that the hydrodynamics of the problem can be treated in two dimensions. It also implies $I(r, \theta, \epsilon, \Theta, \Phi) = I(r, \theta, \epsilon, \Theta, -\Phi)$. If, in addition, it is assumed that I is even independent of Φ, then each of the angular moments of I becomes a *scalar*, which depends on two spatial dimensions, and one dimension in momentum space: $J, H, K, L = J, H, K, L(r, \theta, \epsilon, t)$. Thus the problem is reduced to three dimensions in total.

With the aforementioned assumptions it can be shown (see Buras et al. 2006b), that in order to compute the source terms for the energy and electron fraction of the fluid, the following two transport equations need to be solved:

$$\begin{aligned}
&\left(\frac{1}{c}\frac{\partial}{\partial t} + \beta_r \frac{\partial}{\partial r} + \frac{\boldsymbol{\beta_\vartheta}}{\boldsymbol{r}}\frac{\boldsymbol{\partial}}{\boldsymbol{\partial\vartheta}}\right) J + J\left(\frac{1}{r^2}\frac{\partial(r^2\beta_r)}{\partial r} + \frac{\mathbf{1}}{\boldsymbol{r}\sin\boldsymbol{\vartheta}}\frac{\boldsymbol{\partial}(\sin\boldsymbol{\vartheta}\boldsymbol{\beta_\vartheta})}{\boldsymbol{\partial\vartheta}}\right) \\
&\quad + \frac{1}{r^2}\frac{\partial(r^2 H)}{\partial r} + \frac{\beta_r}{c}\frac{\partial H}{\partial t} - \frac{\partial}{\partial\epsilon}\left\{\frac{\epsilon}{c}\frac{\partial\beta_r}{\partial t}H\right\} - \frac{\partial}{\partial\epsilon}\left\{\epsilon J\left(\frac{\beta_r}{r} + \frac{\mathbf{1}}{\mathbf{2}\boldsymbol{r}\sin\boldsymbol{\vartheta}}\frac{\boldsymbol{\partial}(\sin\boldsymbol{\vartheta}\boldsymbol{\beta_\vartheta})}{\boldsymbol{\partial\vartheta}}\right)\right\} \\
&\quad - \frac{\partial}{\partial\epsilon}\left\{\epsilon K\left(\frac{\partial\beta_r}{\partial r} - \frac{\beta_r}{r} - \frac{\mathbf{1}}{\mathbf{2}\boldsymbol{r}\sin\boldsymbol{\vartheta}}\frac{\boldsymbol{\partial}(\sin\boldsymbol{\vartheta}\boldsymbol{\beta_\vartheta})}{\boldsymbol{\partial\vartheta}}\right)\right\} + J\left(\frac{\beta_r}{r} + \frac{\mathbf{1}}{\mathbf{2}\boldsymbol{r}\sin\boldsymbol{\vartheta}}\frac{\boldsymbol{\partial}(\sin\boldsymbol{\vartheta}\boldsymbol{\beta_\vartheta})}{\boldsymbol{\partial\vartheta}}\right) \\
&\quad + K\left(\frac{\partial\beta_r}{\partial r} - \frac{\beta_r}{r} - \frac{\mathbf{1}}{\mathbf{2}\boldsymbol{r}\sin\boldsymbol{\vartheta}}\frac{\boldsymbol{\partial}(\sin\boldsymbol{\vartheta}\boldsymbol{\beta_\vartheta})}{\boldsymbol{\partial\vartheta}}\right) + \frac{2}{c}\frac{\partial\beta_r}{\partial t}H = C^{(0)},
\end{aligned} \tag{2.9}$$

$$\left(\frac{1}{c}\frac{\partial}{\partial t}+\beta_r\frac{\partial}{\partial r}+\frac{\boldsymbol{\beta_\vartheta}}{\boldsymbol{r}}\frac{\boldsymbol{\partial}}{\boldsymbol{\partial\vartheta}}\right)H+H\left(\frac{1}{r^2}\frac{\partial(r^2\beta_r)}{\partial r}+\frac{\mathbf{1}}{\boldsymbol{r\sin\vartheta}}\frac{\boldsymbol{\partial(\sin\vartheta\beta_\vartheta)}}{\boldsymbol{\partial\vartheta}}\right)$$
$$+\frac{\partial K}{\partial r}+\frac{3K-J}{r}+H\left(\frac{\partial\beta_r}{\partial r}\right)+\frac{\beta_r}{c}\frac{\partial K}{\partial t}-\frac{\partial}{\partial\epsilon}\left\{\frac{\epsilon}{c}\frac{\partial\beta_r}{\partial t}K\right\}$$
$$-\frac{\partial}{\partial\epsilon}\left\{\epsilon L\left(\frac{\partial\beta_r}{\partial r}-\frac{\beta_r}{r}-\frac{\mathbf{1}}{\boldsymbol{2r\sin\vartheta}}\frac{\boldsymbol{\partial(\sin\vartheta\beta_\vartheta)}}{\boldsymbol{\partial\vartheta}}\right)\right\}$$
$$-\frac{\partial}{\partial\epsilon}\left\{\epsilon H\left(\frac{\beta_r}{r}+\frac{\mathbf{1}}{\boldsymbol{2r\sin\vartheta}}\frac{\boldsymbol{\partial(\sin\vartheta\beta_\vartheta)}}{\boldsymbol{\partial\vartheta}}\right)\right\}+\frac{1}{c}\frac{\partial\beta_r}{\partial t}(J+K)=C^{(1)}. \quad (2.10)$$

These are evolution equations for the neutrino energy density, J, and the neutrino flux, H, and follow from the zeroth and first moment equations of the comoving frame (Boltzmann) transport equation in the Newtonian, $O(v/c)$ approximation. The quantities $C^{(0)}$ and $C^{(1)}$ are source terms that result from the collision term of the Boltzmann equation, while $\beta_r = v_r/c$ and $\beta_\vartheta = v_\vartheta/c$, where v_r and v_ϑ are the components of the hydrodynamic velocity, and c is the speed of light. The functional dependences $\beta_r = \beta_r(r,\vartheta,t)$, $J = J(r,\vartheta,\epsilon,t)$, etc. are suppressed in the notation. This system includes four unknown moments (J, H, K, L) but only two equations, and thus needs to be supplemented by two more relations. This is done by substituting $K = f_K \cdot J$ and $L = f_L \cdot J$, where f_K and f_L are the variable Eddington factors, which for the moment may be regarded as being known, but in our case is indeed determined from a separate simplified ("model") Boltzmann equation. A finite volume discretisation of Eqs. (2.9–2.10) is sufficient to guarantee exact conservation of the total neutrino energy. However, and as described in detail in Rampp & Janka (2002), this is not sufficient to guarantee also exact conservation of the neutrino number. To achieve this, we discretise and solve a set of two additional equations. With $\mathcal{J} = J/\epsilon$, $\mathcal{H} = H/\epsilon$, $\mathcal{K} = K/\epsilon$, and $\mathcal{L} = L/\epsilon$, this set of equations reads

$$\left(\frac{1}{c}\frac{\partial}{\partial t}+\beta_r\frac{\partial}{\partial r}+\frac{\boldsymbol{\beta_\vartheta}}{\boldsymbol{r}}\frac{\boldsymbol{\partial}}{\boldsymbol{\partial\vartheta}}\right)\mathcal{J}+\mathcal{J}\left(\frac{1}{r^2}\frac{\partial(r^2\beta_r)}{\partial r}+\frac{\mathbf{1}}{\boldsymbol{r\sin\vartheta}}\frac{\boldsymbol{\partial(\sin\vartheta\beta_\vartheta)}}{\boldsymbol{\partial\vartheta}}\right)$$
$$+\frac{1}{r^2}\frac{\partial(r^2\mathcal{H})}{\partial r}+\frac{\beta_r}{c}\frac{\partial\mathcal{H}}{\partial t}-\frac{\partial}{\partial\epsilon}\left\{\frac{\epsilon}{c}\frac{\partial\beta_r}{\partial t}\mathcal{H}\right\}-\frac{\partial}{\partial\epsilon}\left\{\epsilon\mathcal{J}\left(\frac{\beta_r}{r}+\frac{\mathbf{1}}{\boldsymbol{2r\sin\vartheta}}\frac{\boldsymbol{\partial(\sin\vartheta\beta_\vartheta)}}{\boldsymbol{\partial\vartheta}}\right)\right\}$$
$$-\frac{\partial}{\partial\epsilon}\left\{\epsilon\mathcal{K}\left(\frac{\partial\beta_r}{\partial r}-\frac{\beta_r}{r}-\frac{\mathbf{1}}{\boldsymbol{2r\sin\vartheta}}\frac{\boldsymbol{\partial(\sin\vartheta\beta_\vartheta)}}{\boldsymbol{\partial\vartheta}}\right)\right\}+\frac{1}{c}\frac{\partial\beta_r}{\partial t}\mathcal{H}=C^{(0)}, \quad (2.11)$$

Reaction			References
$\nu\, e^{\pm}$	$\rightleftharpoons$	$\nu\, e^{\pm}$	Mezzacappa & Bruenn (1993b)
			Cernohorsky & Bludman (1994)
$\nu\, A$	$\rightleftharpoons$	$\nu\, A$	Horowitz (1997)
			Bruenn & Mezzacappa (1997)
$\nu\, N$	$\rightleftharpoons$	$\nu\, N$	Burrows & Sawyer (1998)
$\nu_e\, n$	$\rightleftharpoons$	$e^-\, p$	Burrows & Sawyer (1999)
$\bar{\nu}_e\, p$	$\rightleftharpoons$	$e^+\, n$	Burrows & Sawyer (1999)
$\nu_e\, A'$	$\rightleftharpoons$	$e^-\, A$	Bruenn (1985), Langanke et al. (2003)
			Mezzacappa & Bruenn (1993a)
$\nu\, \bar{\nu}$	$\rightleftharpoons$	$e^-\, e^+$	Bruenn (1985), Pons et al. (1998)
$\nu\bar{\nu} NN$	$\rightleftharpoons$	NN	Hannestad & Raffelt (1998)
$\nu_{\mu,\tau}\bar{\nu}_{\mu,\tau}$	$\rightleftharpoons$	$\nu_e\bar{\nu}_e$	Buras et al. (2003)
$\overset{(-)}{\nu}_{\mu,\tau}\overset{(-)}{\nu}_e$	$\rightleftharpoons$	$\overset{(-)}{\nu}_{\mu,\tau}\overset{(-)}{\nu}_e$	Buras et al. (2003)

Table 2.1.: Overview of neutrino-matter and neutrino-neutrino interactions included in our simulations. For each process we provide reference(s) where more information can be found about physics and approximations employed in the rate calculations. The numerical implementation is described in detail in Rampp & Janka (2002) and Buras et al. (2003). The symbol ν represents any of the neutrinos $\nu_e, \bar{\nu}_e, \nu_\mu, \bar{\nu}_\mu, \nu_\tau, \bar{\nu}_\tau$, the symbols e^-, e^+, n, p and A denote electrons, positrons, free neutrons and protons, and heavy nuclei, respectively. The symbol N means neutrons or protons.

$$\left(\frac{1}{c}\frac{\partial}{\partial t}+\beta_r\frac{\partial}{\partial r}+\boldsymbol{\frac{\beta_\vartheta}{r}\frac{\partial}{\partial\vartheta}}\right)\mathcal{H}+\mathcal{H}\left(\frac{1}{r^2}\frac{\partial(r^2\beta_r)}{\partial r}+\boldsymbol{\frac{1}{r\sin\vartheta}\frac{\partial(\sin\vartheta\beta_\vartheta)}{\partial\vartheta}}\right)$$
$$+\frac{\partial\mathcal{K}}{\partial r}+\frac{3\mathcal{K}-\mathcal{J}}{r}+\mathcal{H}\left(\frac{\partial\beta_r}{\partial r}\right)+\frac{\beta_r}{c}\frac{\partial\mathcal{K}}{\partial t}-\frac{\partial}{\partial\epsilon}\left\{\frac{\epsilon}{c}\frac{\partial\beta_r}{\partial t}\mathcal{K}\right\}$$
$$-\frac{\partial}{\partial\epsilon}\left\{\epsilon\mathcal{L}\left(\frac{\partial\beta_r}{\partial r}-\frac{\beta_r}{r}-\boldsymbol{\frac{1}{2r\sin\vartheta}\frac{\partial(\sin\vartheta\beta_\vartheta)}{\partial\vartheta}}\right)\right\}$$
$$-\frac{\partial}{\partial\epsilon}\left\{\epsilon\mathcal{H}\left(\frac{\beta_r}{r}+\boldsymbol{\frac{1}{2r\sin\vartheta}\frac{\partial(\sin\vartheta\beta_\vartheta)}{\partial\vartheta}}\right)\right\}-\mathcal{L}\left(\frac{\partial\beta_r}{\partial r}-\frac{\beta_r}{r}-\boldsymbol{\frac{1}{2r\sin\vartheta}\frac{\partial(\sin\vartheta\beta_\vartheta)}{\partial\vartheta}}\right)$$
$$-\mathcal{H}\left(\frac{\beta_r}{r}+\boldsymbol{\frac{1}{2r\sin\vartheta}\frac{\partial(\sin\vartheta\beta_\vartheta)}{\partial\vartheta}}\right)+\frac{1}{c}\frac{\partial\beta_r}{\partial t}\mathcal{J}=C^{(1)}. \quad (2.12)$$

The moment equations (2.9–2.12) are very similar to the $O(v/c)$ equations in spherical symmetry which were solved in the 1D simulations of Rampp & Janka (2002) (see Eqs. 7, 8, 30, and 31 of the latter work). This similarity has allowed us to reuse a good fraction of the one-dimensional version of V , for coding the multi-dimensional algorithm. The additional terms necessary for this purpose have been set in boldface above.

Finally, the changes of the energy, e, and electron fraction, Y_e, required for the hydrodynamics

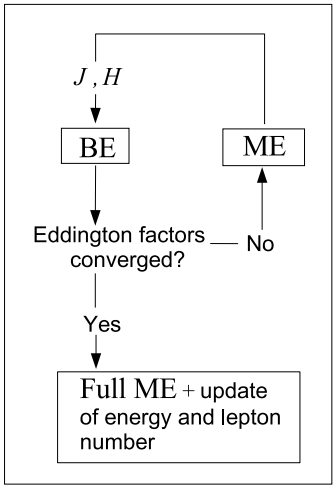

Figure 2.2.: A sketch of the iterative procedure between the moments equations (ME) and the "model" Boltzmann equation (BE) in the algorithm for obtaining the Variable Eddington factors.

are given by the following two equations

$$\frac{\mathrm{d}e}{\mathrm{d}t} = -\frac{4\pi}{\rho}\int_0^\infty \mathrm{d}\epsilon \sum_{\nu\in(\nu_\mathrm{e},\bar{\nu}_\mathrm{e},\dots)} C_\nu^{(0)}(\epsilon), \tag{2.13}$$

$$\frac{\mathrm{d}Y_e}{\mathrm{d}t} = -\frac{4\pi\, m_\mathrm{B}}{\rho}\int_0^\infty \mathrm{d}\epsilon \left(C_{\nu_\mathrm{e}}^{(0)}(\epsilon) - C_{\bar{\nu}_\mathrm{e}}^{(0)}(\epsilon)\right) \tag{2.14}$$

(for the momentum source terms due to neutrinos see Buras et al. (2006b)). Here m_B is the baryon mass, and the sum in Eqn. (2.13) runs over all neutrino types. The full system consisting of Eqs. (2.9–2.14) is stiff, and thus requires an appropriate discretisation scheme for its stable solution. In order to discretise Eqs. (2.9–2.14), the spatial domain $[0, r_\mathrm{max}] \times [\vartheta_\mathrm{min}, \vartheta_\mathrm{max}]$ is covered by N_r radial, and N_ϑ angular zones, where $\vartheta_\mathrm{min} = 0$ and $\vartheta_\mathrm{max} = \pi$ correspond to the north and south poles, respectively, of the spherical grid. (In general, we allow for grids with different radial resolutions in the neutrino transport and hydrodynamic parts of the code. The number of radial zones for the hydrodynamics will be denoted by N_r^hyd.) The number of bins used in energy space is N_ϵ and the number of neutrino types taken into account is N_ν.

The equations are solved in two operator-split steps corresponding to a lateral and a radial sweep.

In the first step, we treat the boldface terms in the respectively first lines of Eqs. (2.9–2.12), which describe the lateral advection of the neutrinos with the stellar fluid, and thus couple the angular moments of the neutrino distribution of neighbouring angular zones. For this purpose we consider the equation

$$\frac{1}{c}\frac{\partial \Xi}{\partial t} + \frac{1}{r\sin\vartheta}\frac{\partial(\sin\vartheta\,\beta_\vartheta\,\Xi)}{\partial\vartheta} = 0\,, \tag{2.15}$$

where Ξ represents one of the moments J, H, $\mathcal{J}$, or $\mathcal{H}$. Although it has been suppressed in the above notation, an equation of this form has to be solved for each radius, for each energy bin, and for each type of neutrino. An explicit upwind scheme is used for this purpose.

In the second step, the radial sweep is performed. Several points need to be noted here:

- terms in boldface not yet taken into account in the lateral sweep, need to be included into the discretisation scheme of the radial sweep. This can be done in a straightforward way since these remaining terms do not include derivatives of the transport variables (J, H) or $(\mathcal{J}, \mathcal{H})$. They only depend on the hydrodynamic velocity v_ϑ, which is a *constant* scalar field for the transport problem.

- the right hand sides (source terms) of the equations and the coupling in energy space have to be accounted for. The coupling in energy is non-local, since the source terms of Eqs. (2.9–2.12) stem from the Boltzmann equation, which is an integro-differential equation and couples all the energy bins

- the discretisation scheme for the radial sweep is *implicit* in time. Explicit schemes would require very small time steps to cope with the stiffness of the source terms in the optically thick regime, and the small CFL[4] time step dictated by neutrino propagation with the speed of light in the optically thin regime. Still, even with an implicit scheme $\gtrsim 10^5$ time steps are required per simulation. This makes the calculations expensive.

Once the equations for the radial sweep have been discretised in radius and energy, the resulting solver is applied ray-by-ray for each angle ϑ and for each type of neutrino, i.e. for constant ϑ, N_ν two-dimensional problems need to be solved. The discretisation itself is done using a second order accurate scheme with backward differencing in time according to Rampp & Janka (2002). This leads to a non-linear system of algebraic equations, which is solved by Newton-Raphson iteration with explicit construction and inversion of the corresponding Jacobian matrix.

To solve Eqs. (2.9–2.14), we need the variable Eddington factors $f_K = K/J$ and $f_L = L/J$. These closure relations are obtained from the solution of a simplified ("model") Boltzmann equation. The integro-differential character of this equation is tackled by expressing the angular integrals in the interaction kernels of its right-hand side, with the moments J and H, for which estimates are obtained from a solution of the system of moment equations (2.9–2.10), (2.13) and (2.14). With the right-hand side known, the model Boltzmann equation is solved by means of the so-called tangent ray method (see Mihalas & Mihalas (1984), and Rampp & Janka (2002) for details), and the entire procedure is iterated until convergence of the Eddington factors is achieved (cf. Fig. 2.2). Note that this apparently involved procedure is computationally efficient, since the Eddington factors are geometrical quantities, which vary only slowly, and thus can be computed relatively cheaply using only a "model" transport equation. Note also that only the system of equations (2.9–2.10), (2.13) and (2.14), and not the full system Eqs. (2.9–2.14), is used in the iteration. This allows us to save computer time. Once the Eddington factors are known, the complete system Eqs. (2.9–2.14), enforcing conservation of energy and neutrino number, is solved once, in order to update the energy and electron fraction (lepton number) of the fluid.

An important part of the code are the various neutrino–matter and neutrino–neutrino interaction rates that produce the opacities for the neutrino radiation field. Note here that in the code the electron neutrinos and anti–electron neutrinos are treated separately, all other "heavy lepton neutrinos", however, are treated as as one species. The justification here for is that during

[4]The **C**ourant–**F**riedrichs–**L**ewy condition states that in oder to be numerically stable a timestep of the algorithm has to be so small that information does not travel more than one zone within a single timestep.

a core collapse supernova the medium does not initially contain any muons and temperatures and densities are always too low to produce tauons, which implies small or vanishing chemical potentials for the μ and τ (anti)–neutrinos. Furthermore, the opacities are nearly equal for all "heavy lepton neutrinos."

The neutrino interactions are summarised in Table 2.1. Note that neutral–current scatterings of neutrinos off nucleons and charged–current β–processes include the effects of nucleon recoil, thermal motions, and phase space blocking, nucleon correlations in dense media (Burrows & Sawyer 1998, 1999), corrections due to the weak magnetism of nucleons (Horowitz 2002), the possible quenching of the axial–vector coupling in nuclear matter (Carter & Prakash 2002), and the reduction of the effective nucleon mass at high densities (Reddy et al. 1999). Electron captures on nuclei are implemented according to the improved treatment of Langanke et al. (2003) in regions where NSE holds, taking into account the collective *e*–captures of a large sample of nuclei in NSE with rates determined from shell model Monte Carlo calculations; the prescription of Bruenn (1985) is used in regions which are out of NSE. With this input, the production of ν_e's by nuclei dominates the one by protons during core collapse (Langanke et al. 2003). For details the reader is referred to Appendix A.3.1, where these electron capture rates are discussed in detail.

If not stated otherwise, all simulations discussed in this work use this set of micro–physics and gravity is treated as described in Appendix B. The used progenitor models and the EoSs will be introduced later and for each model specifically.

Part I: 1D–simulations

Everything should be made as simple as possible, but not simpler

A. Einstein

The ability to simplify means to eliminate the unnecessary so that the necessary may speak

H. Hofmann, Introduction to the Bootstrap, 1993

3

The role of the nuclear EoS in spherically symmetric simulations of core collapse supernovae

The following first Part of this thesis is dedicated to spherically symmetric calculations of core collapse supernovae with different nuclear equations of state (EoSs). These strongly simplified simulations, which reduce the complexity by assuming radial symmetry, allows me to study with a large number of models the role of the nuclear equation of state (EoS) during the collapse of a star, the formation of the shock wave, the subsequent supernova evolution, and the differences of the explosion characteristics arising from different equations of state. With several spherically symmetric (i.e. 1D) models an attempt is made to understand the "action" of different EoSs on these phases of a core collapse supernova. Furthermore, the influence of different regimes of a EoS (i.e. the supra–nuclear phase, the sub–nuclear phase, and the "low"–density phase) on the evolution of the final stages of a massive stars life will be investigated.

This Part I of this thesis is organised as follows: after a short preface in Section 3.1 I will introduce in Section 3.2 the different EoSs which are used throughout this thesis. As a specific example I will then discuss the supernova evolution of a $15\,M_\odot$ progenitor star when three different equations of state are employed in the simulations. In this section, along the line of discussion, I will introduce technical terms and physical concepts that will be used throughout this thesis. In Section 3.3 I will focus on the supra–nuclear phase of the EoS. Simulations with progenitor models of different masses will be discussed, and I will find a dependence of the sensitivity of my calculations on the supra–nuclear EoS that varies with these progenitor masses. In Section 3.4 I will discuss the influence of the "low"–density EoS (i.e. densities below 10^{11} g/cm^3) on the supernova evolution.

Since none of the models we discuss in this chapter does explode, I will then investigate the EoS dependence on the supernova explosion "characteristics" with models that were artifically

made to explode. Here, of course, I can not investigated the explosion mechanism but rather I will investigate if different equations of state for hot proto neutron stars cause different neutrino emission (i.e. luminosities, energies, and spectra) of the dense core.

Finally, this chapter will be concluded by a short summary of my findings.

3.1. Preface

Core collapse supernova are known to be objects with extreme physical conditions. From the intermediate conditions of the pre-collapse core at nuclear statistical equilibrium with a central density of roughly 10^{10} g/cm^3, a core temperature of about 1 MeV, and nearly symmetric matter (electron fraction close to 0.5) the properties of the stellar plasma change drastically after the onset of gravitational instability: the density in the inner core rises to supra-nuclear values ($\rho > 2.7\times10^{14}$ g/cm^3) and the temperature can become as high as several 10 MeV. Furthermore, since a neutron star forms, matter becomes neutron rich and the proton-to-neutron ratio changes from close to unity to much smaller values than unity in neutron star matter at beta equilibrium. In order to describe the stellar plasma thermodynamically an EoS is needed that relates the pressure of the plasma to its density, temperature, and chemical composition. However, little is known about an EoS that describes this kind of stellar plasma. On the one hand, experimental information for matter at these extreme conditions is limited, and on the other hand the uncertainties in theoretical models are considerable. In particular in the sub-nuclear regime, where nucleons co-exist in equilibrium with large, neutron-rich nuclei, and in the supra-nuclear regime, where new hadronic degrees of freedom (kaons, hyperons, pion condensates, ...) or a quark phase might occur the knowledge is incomplete. These problems make calculations of nuclear equations of state difficult and thus there exist only a few finite-temperature equations of state which span the whole parameter range required for a supernova simulation. Since our knowledge of matter in the supernova core is incomplete it has been suggested that the EoS of hot, dense matter may be crucial for the simulations of core collapse supernovae.

Indeed, the EoS influences considerably the stellar core collapse, the shock formation and the propagation of the prompt shock (see, e.g. Baron et al. 1985, 1987a, Myra & Bludman 1989, Hillebrandt & Wolff 1985, Swesty et al. 1994), however, for reasonable assumptions about the EoS prompt explosions cannot be obtained for massive stars.

The influence of the EoS on the long-time supernova evolution has hardly been investigated. Only few equations of state were applied for this purpose so far. Wilson and collaborators (see Wilson & Mayle 1988, Totani et al. 1998) routinely get supernova explosions with their EoS in spherically symmetric calculations. This equation of state, however, is based on controversial physical assumptions, e.g. it involves the formation of pion condensates at moderate densities due to a special dispersion relation for the pions, see Mayle et al. (1993). Similar to Wilson's results Hillebrandt & Wolff (1985) obtained an explosion with the their EoS (from hereon Wolff-EoS) for a star in the lower mass range for core collapse supernovae. However as a newer study of Kitaura et al. (2006) showed, due to special properties of this particular low-mass star, this explosion does not depend on the nuclear EoS.

Also the use of the equation of state of Lattimer & Swesty (1991) (from hereon L&S-EoS) does not lead to explosions (see e.g. Thompson et al. 2003).

Subsequently, Sumiyoshi et al. (2005) compared the L&S-EoS and the EoS of Shen et al. (1998a,b) (from hereon Shen-EoS) and found quantitative but not qualitative differences in the long-time supernova evolution.

In the following Section I will discuss the role the nuclear EoS plays in spherically symmetric core collapse supernova simulations. In particular, it is the aim of this Part I to discuss to what the extend supernova simulations are sensitive to the applied EoS by addressing the following

questions:

- How does the EoS influence the collapse dynamics?
- Do different realistic equations of state lead to significantly changed results concerning the shock formation and the propagation of the prompt shock?
- Does the poorly known supra-nuclear density phase of an EoS play an important role? How does the produced dense core influence the shock propagation ?
- How do different EoSs influence the neutrino emission and neutrino heating of stellar matter? How important are differences in the matter composition?
- Do some EoSs favour the growth of convective flows?

Of course, many of these questions are connected and disentangling them is not an easy task, but they can be regarded as "guideline" for understanding the importance of the EoS in supernova calculations, before in the subsequent sections an attempt is made to disentangle the various influences of the nuclear equation of state.

3.2. EoS comparison with a 15 $M_\odot$ star

Throughout the discussion of this thesis we employ different nuclear equations of state for our simulations. Before we start our discussion of the role of the nuclear equation of state during the evolution of core collapse supernovae we will in the following introduce the EoSs used for these simulations.

3.2.1. Equations of state

Since the nuclear equations of state which are available for core collapse supernova simulations do not cover the whole density range necessary for the calculations (i.e. from supra-nuclear densities in the dense core down to a few 100 g/cm^3 in the outer regions of the stellar envelope) different EoSs have to be used simultaneously in the simulations. It this thus naturally to divide the whole density range into a "high-density" part and a "low density" part. In the following the EoSs used in these parts are shortly introduced.

High density equation of state

In this study we use three different nuclear equations of state for the description of nuclear matter at high densities. All three equations of state assume nuclear statistical equilibrium and describe the baryonic part of inhomogeneous matter as a mixture of free protons and neutrons, alpha particles, and one representative species of a heavy nucleus with atomic number A and charge Z. The homogeneous part consists of free protons and neutrons, i.e. no heavy nuclei are present there. It shall be stressed that all three equations of state describe matter above nuclear density to be homogeneous, without the existence of possible hadronic degrees of freedom (like kaons, hyperons, pion condensates, ...). Both in the inhomogeneous phase and in the

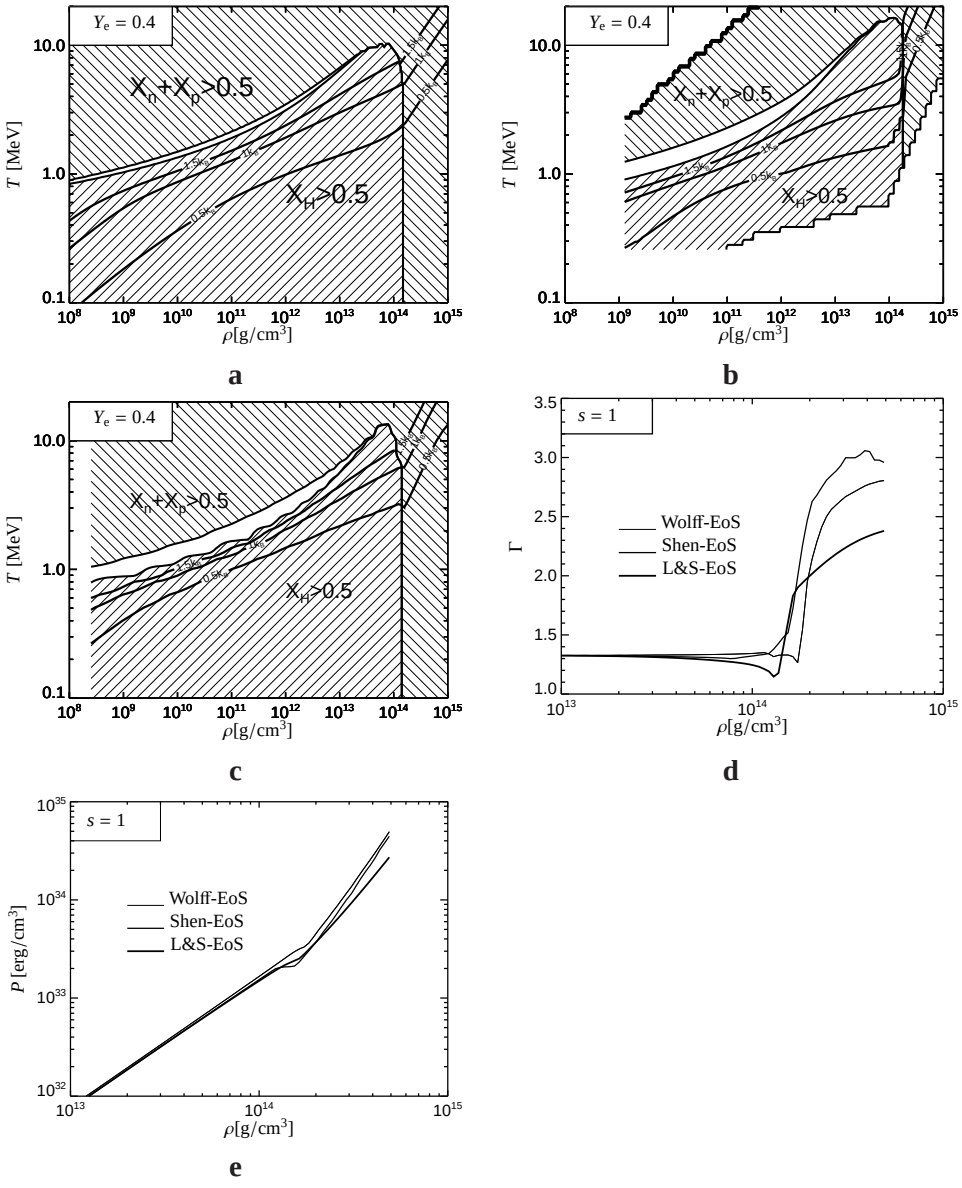

Figure 3.1.: a: Dominant composition in the ρ-T-plane for the L&S-EoS. Shaded are regions where free nucleons ($X_n + X_p > 0.5$) or heavy nuclei ($X_H > 0.5$) contribute the majority of the mass. Note the narrow white stripe of conditions where alpha particles dominate the composition. The labelled lines indicate isentropes for different values of the entropy. **b**: The same dominant composition of the Wolff-EoS. **c**: The same dominant composition of the Shen-EoS. **d**: The adiabatic index for all three equations of state over density for constant entropy-density of $1k_B$ per nucleon and a electron fraction $Y_e = 0.4$. **e**: The pressure of all three equations of state for the same conditions as in panel d.

homogeneous phase the baryons are immersed in an electron and positron gas that equilibrates with a photon gas by the pair creation process. We use the EoS for hot and dense nuclear matter by Lattimer & Swesty (1991), which is based on the compressible liquid drop model by Lattimer et al. (1985). In this EoS the transition from inhomogeneous to homogenous matter is established by a Maxwell construction. The nucleon-nucleon interactions are expressed by a Skyrme-force. In our version of this EoS the incompressibility modulus of bulk nuclear matter is taken to be 180 MeV and the symmetry energy parameter has a value of 29.3 MeV. Studies with different values for these parameters have been conducted and showed little differences (see Thompson et al. 2003, Swesty et al. 1994). This equation of state is most widely used by supernova modellers (see, e.g. Thompson et al. 2003, Swesty et al. 1994, Rampp 2000, Liebendörfer et al. 2005, Buras et al. 2006b,a) and can thus be regarded as the "standard" EoS for supernova simulations. The second equation of state we use in our studies has been developed by Shen, Toki, Oyamatsu, and Sumiyoshi and is described in detail in Shen et al. (1998b,a). It is based on a relativistic mean field model and is extended with the Thomas-Fermi approximation to describe the homogeneous phase of matter as well as the inhomogeneous matter composition. The parameter for the incompressibility of nuclear matter is 281 MeV and the symmetry energy has a value of 36.9 MeV. Except for our studies, this equation of state was to used in simulations of r-processes in neutrino driven winds (see Sumiyoshi et al. 2000), proto-neutron star cooling (see Sumiyoshi et al. 1995), and in supernova simulations (see Terasawa et al. 2001, Sumiyoshi et al. 2005, Burrows et al. 2006a,c,b). As a third alternative description for dense and hot nuclear matter we make use of the EoS by Wolff and Hillebrandt. It is based on a full Hartree-Fock calculation, assuming a Skyrme force for nucleon-nucleon interactions with parameters given by Köhler (1975). The incompressibility has a value of 263 MeV and the parameter of the symmetry energy was chosen to be 32.9 MeV. Details of the calculation can be found in Hillebrandt et al. (1984) and Hillebrandt & Wolff (1985). In the past this equation of state was used in several supernova simulations (see Hillebrandt et al. 1984, Hillebrandt & Wolff 1985, Kitaura et al. 2006). For comparison of the three equations of state, we show the composition of the three EoS in the density-temperature-plane, see Fig. 3.1a – 3.1c. Note that the region where alpha particles contribute more than 50% is different in all three equations of state. In Fig. 3.1d we depict the adiabatic index, $\Gamma = (\partial \ln P / \partial \ln \rho)_s$, as a function of density for an adiabatic collapse, i.e. the entropy s is kept constant for a value of 1 k_B per baryon. Figure 3.1e shows the pressure corresponding to the adiabatic index of Fig. 3.1d. Below densities of 10^{13} g/cm^3 the pressure of the different equations of state becomes identical whereas at a density above 10^{14} g/cm^3, where nuclear forces become important, the stiffer equations of state of Shen and Wolff show a steeper pressure gradient.

Low density equation of state

For low densities we extend the above described equations of state with our low-density equation of state. This EoS considers electrons and positrons, photons, free protons and neutrons, alpha particles, and up to 14 species of nuclei in thermodynamic equilibrium. Electrons and positrons are treated as Fermi gases of arbitrary degeneracy and arbitrary degree of relativity. The baryonic components are treated as classical non-relativistic Boltzmann gases. Coulomb lattice corrections for the pressure, energy density, entropy and adiabatic index are taken into ac-

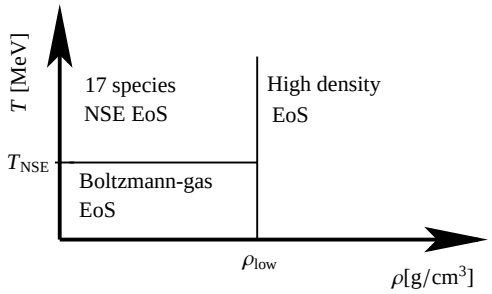

Figure 3.2.: The setup for the EoSs in the density-temperature plane. Below a value $\rho_{\rm low}$ we make use of our low density EoS. This EoS is divided into two parts: above a temperature of 0.5 MeV we assume NSE, and below this temperature we take into account nuclear burning.

count. For temperatures above $T_{\rm NSE}$=0.5 MeV we assume nuclear statistical equilibrium in this EoS (see Fig. 3.2). For temperatures below 0.5 MeV we take nuclear burning into account (see Rampp & Janka 2002). The transition between the high-density EoS and the low-density EoS takes place at a specific value for the density $\rho_{\rm low}$, which was chosen to guarantee a sufficiently smooth transition as far as e.g. the pressure, internal energy density, and chemical potentials as function of density are concerned. During the collapse phase these specific values for the transition density $\rho_{\rm low}$ were chosen to be 6×10^7 g/cm^3, 3×10^8 g/cm^3, and 1.5×10^9 g/cm^3 in case of the L&S, Shen, and Wolff-EoS, respectively. In the postbounce phase this value was changed to 10^{11} g/cm^3 for the L&S-EoS in order to bypass an error in this EoS for low densities and temperatures typically for the postbounce phase (see Buras et al. 2006b,, see also Section 3.4). The three different equations of state were used in spherically symmetric core collapse simulations of a 15 $M_\odot$ stellar model (model s15a28) provided by Heger et al. (2001). In the following we will denote the different models by L&S(io)slms, Shen(io)slms, and Wolff(io)slms. These names indicate the used equation of state, the full set of improved (io) neutrino opacities, and the use of the electron capture rates on nuclei calculated by Langanke et. al (see Hix et al. 2003, Langanke et al. 2003), including electron screening effects, see Appendix A.3.1.

3.2.2. Numerical results

Initial models

From the progenitor model “s15a28” we take the density, temperature, electron fraction, and in the regime of the low-density EoS the composition as initial data for our simulations, see Figs. 3.3 and 3.4a. All other quantities (like pressure, see Fig. 3.4b) were obtained by evaluating the respective EoS of the simulation. Starting from the same progenitor model we nevertheless find the following differences in the initial models that are due to the equations of state:

- The pressure profile and value of the adiabatic index that are obtained from the EoS with the stellar progenitor conditions are EoS dependent (see Fig. 3.4b). This influences the collapse dynamics.

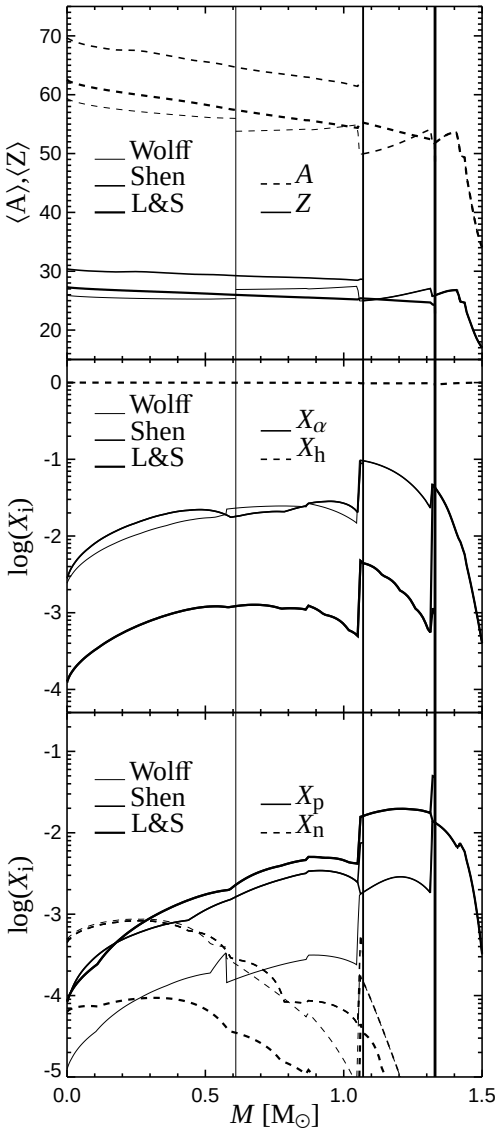

Figure 3.3.: The initial composition (centre and bottom panel) in the inner core of the stellar model "s15a28" and the charge and mass number of the representative nucleus (top panel). The bold vertical lines indicate the interface between the high density and low density EoS, corresponding to a density of 6×10^7 g/cm^3 for the L&S-EoS, a density of 3×10^8 g/cm^3 for the Shen-EoS, and a density of 1.5×10^9 g/cm^3 for the Wolff-EoS.

- The composition in the NSE-regime strongly depends on the EoS. This may influence the neutrino-matter-interaction rates. Note for example that the mass and charge number of the representative heavy nucleus given by the Shen-EoS is higher than the ones given by the other two equations of state, see Fig. 3.3.

- Up to $1M_\odot$ the initial value of the entropy is lower for the Shen-EoS, see bottom panel of Fig. 3.4a. This implies that the entropy in model Shen(io)slms would have to rise more strongly during the collapse in order to reach the same values of the – also rising – entropies of the models L&S(io)slms and Wolff(io)slms.

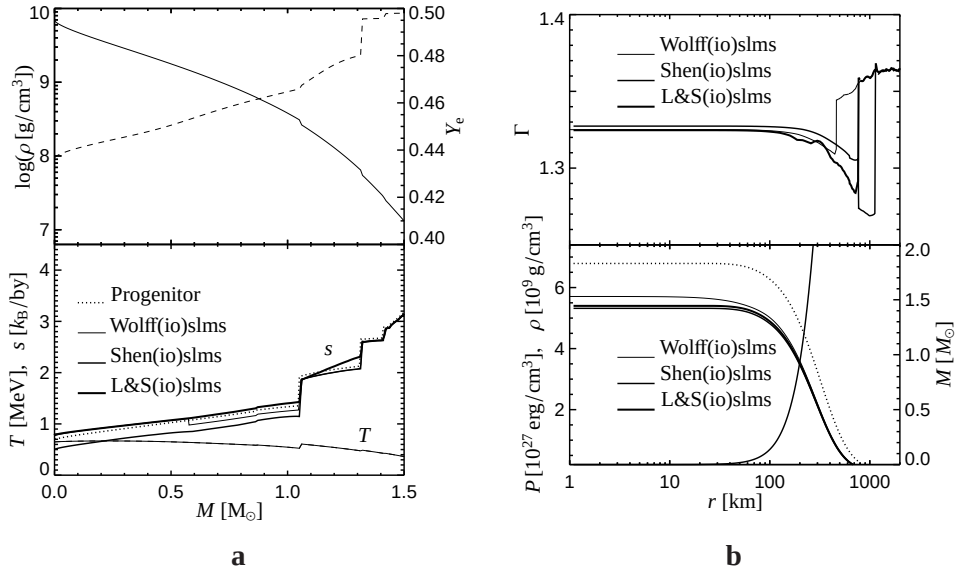

Figure 3.4.: **a**: The initial conditions at the beginning of the simulations. The top panel shows the density profile (solid) and the Y_e profile (dashed) that were given by the progenitor model. The bottom panel shows the temperature profile that was also given by the progenitor model. For comparison the entropy profile of the progenitor is shown and the entropy profiles that were obtained by evaluating the equations of state with the density, temperature, and electron-fraction profile of the progenitor. **b**: Top panel: The adiabatic index of the three equations of state which were evaluated with the progenitor temperature, density, and electron-fraction profile at the beginning of our simulations. Bottom panel: The same for the pressure (solid lines). Furthermore the progenitor density profile (dashed line) is shown. The line going from the lower left to the upper right represents the enclosed mass profile in units of 0.1 $M_\odot$ (left axis).

These differences at the beginning of the simulations have some minor effect on the collapse phase which we will discuss in the following section.

Collapse and prompt shock phase

The simulations show that the collapse times for the models L&S(io)slms and Shen(io)slms are quite similar, while the onset of collapse in the model Wolff(io)slms delayed compared to the other two.

At central densities above 10^{11} g/cm^3 the collapses develop very similar in all models [1], see Figs. 3.6fig:bounce, and 3.5.

However, there still exist some differences in the collapse phase: as the profiles of the electron fraction reveal (see Fig. 3.5) the model Shen(io)slms experiences the lowest deleptonisation

[1] This behaviour was also found by Buras et al. (2006a) with simulations of several different progenitor models and the L&S-EoS

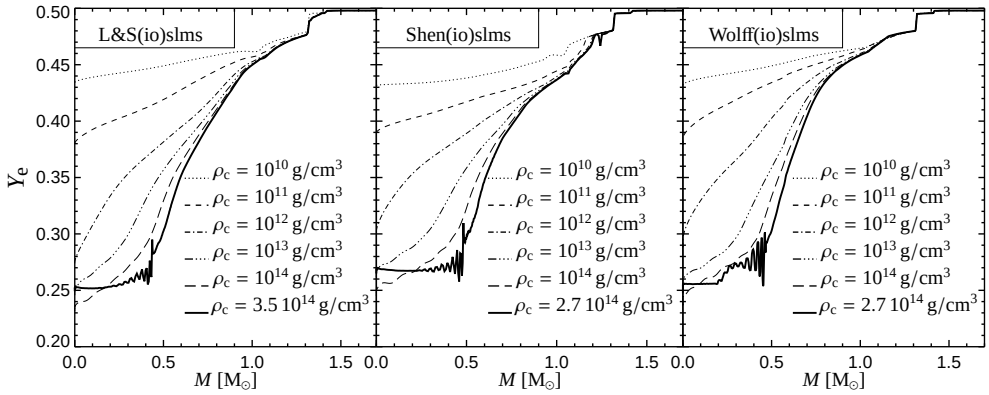

Figure 3.5.: Y_e profiles at specific central densities for the models Wolff(io)slms (left panel), Shen(io)slms (centre panel), and L&S(io)slms (right panel). The bold line indicates the situation at the moment of shock formation.

and thus fewest electron captures of all models. This can be also seen in Fig. 3.7a where the central electron and central lepton fractions are shown as function of central density for all models. As can be deduced from Fig. 3.5 these differences originate from the early stage of collapse when the central density reaches values between 10^{11} and 10^{12} g/cm^3 and neutrinos are not completely trapped. The reason why model Shen(io)slms experiences the lowest deleptonisation, is found in the collapse timescale. Since model Shen(io)slms collapses fastest (see Fig. 3.7b), there is simply less time for electron capture. Another important difference in model Shen(io)slms is that the initial value of the entropy is lower than in the other two models, see again Fig. 3.4a. Since this model does not show an extraordinary strong rise of the central entropy with time a lower entropy can also be seen in Fig. 3.7b.

However, this lower core entropy does *not* imply that the abundance of free protons is also lower in the model with the Shen-EoS compared to the other models. In Figs. 3.6d we depict for all models the evolutionary tracks of the composition.

The development of the four NSE-species is different in all three models. Whereas the general trend is qualitatively the same, the abundance of a species from one EoS to the other can easily differ by a factor of two. More importantly, we find even more extreme variations in the properties (charge and mass number) of the representative heavy nucleus, see Fig. 3.6c: shortly before nuclear density is reached model Shen(io)slms shows the heaviest nuclei whose mass number is up to a factor of six to ten larger compared to the models L&S(io)slms and Wolff(io)slms.

Whereas this clearly stresses the uncertainties in the description of matter at these high densities, the consequences on core collapse supernova simulations are negligible, since neutrinos are trapped in the core and modifications on absorption or scattering rates by these heavy nuclei are almost unimportant.

When the inner cores of the models finally reach nuclear density the in falling material is stopped by nuclear repulsive forces, see Fig. 3.6b. The density overshoots, and the core starts expanding into the still in falling supersonic material, thereby creating a shock. Following

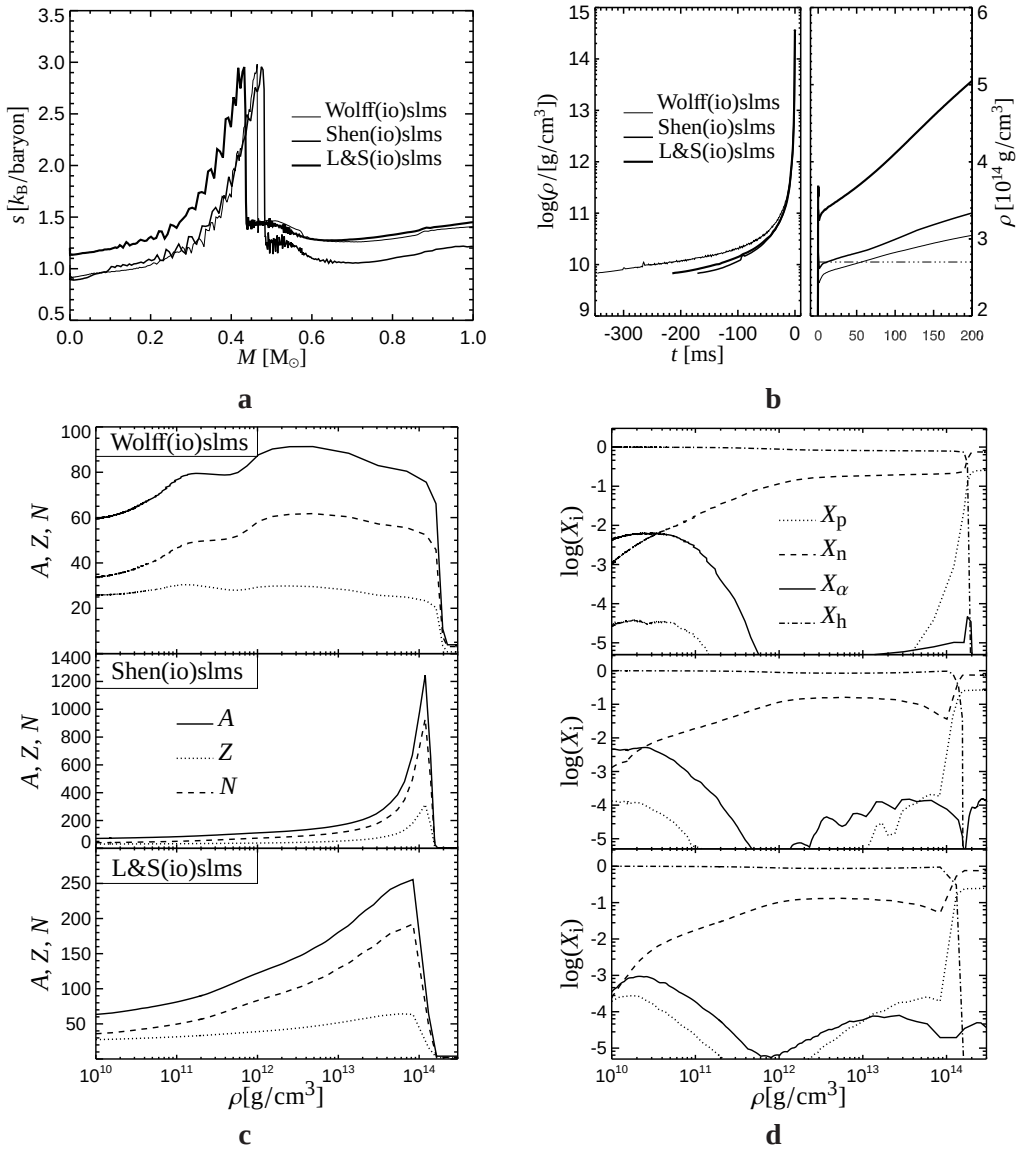

Figure 3.6.: **a**: The moment of shock formation in all three models. **b**: The central density as function of time during collapse (left panel) and in the postbounce phase (right panel). Note that the time is normalised to the point of shock formation in all models. The horizontal dashed-dotted line represents the value of the saturation density at $2.7 \times 10^{14}\,\mathrm{g/cm^3}$. **c**: The properties of the representative heavy nucleus as function of central density in the models Wolff(io)slms (top panel), Shen(io)slms (centre panel), and L&S(io)slms (bottom panel). Shown are the mass number, the charge number, and the number of neutrons. **d**: The composition as a function of central density in the models Wolff(io)slms (top panel), Shen(io)slms (centre panel), and L&S(io)slms (bottom panel).

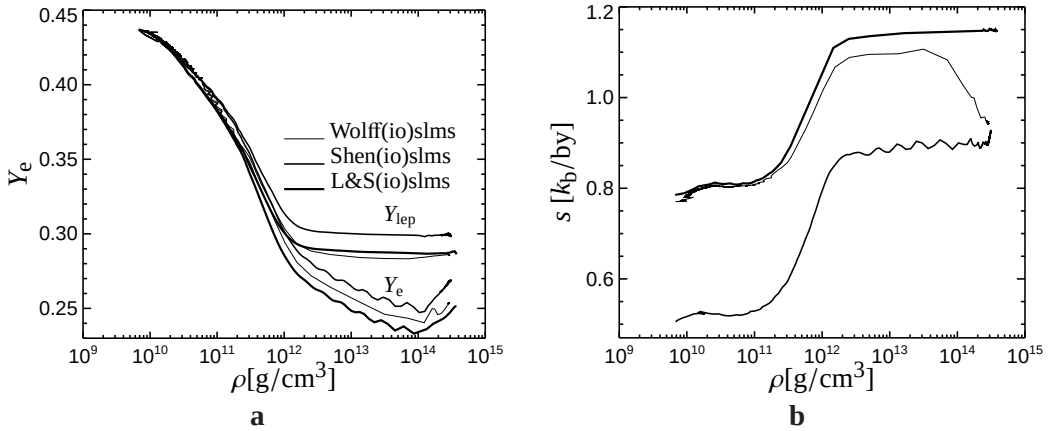

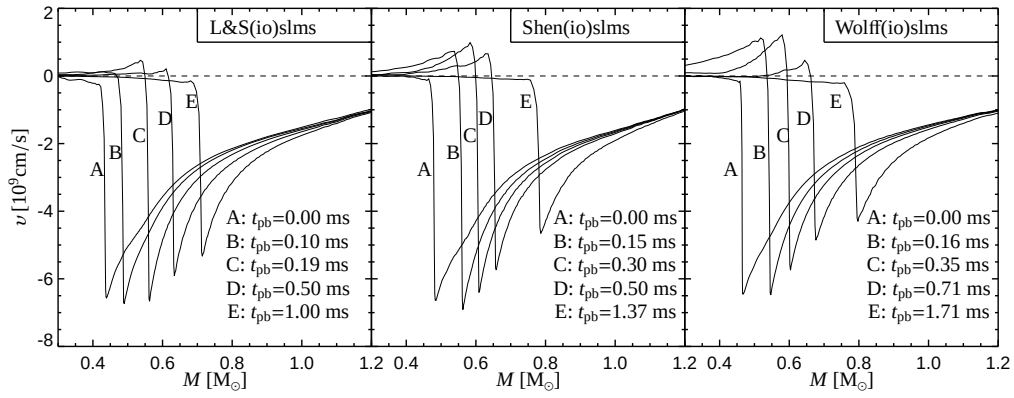

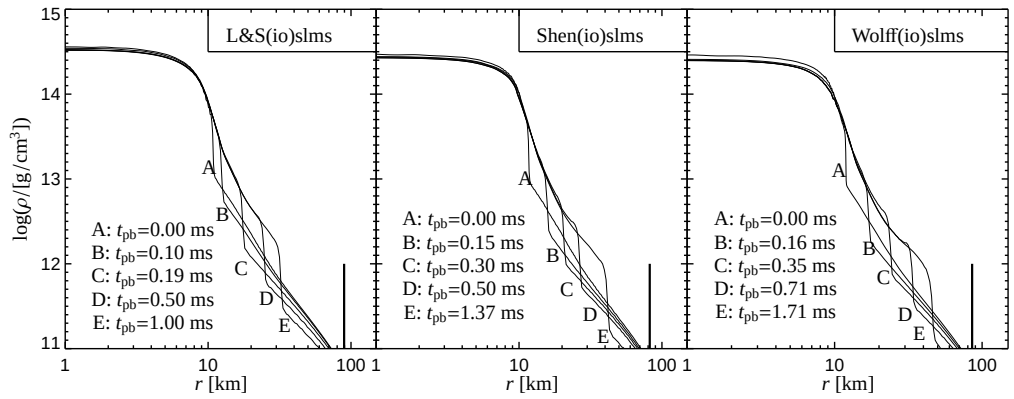

Figure 3.7.: **a**: The central electron fraction and central lepton fraction as function of density during the collapse phase. **b**: The central entropy per baryon. The initially lower entropy in case of model Shen(io)slms is a result of the entropy of the initial model, see Fig. 3.4. The unphysical entropy decline at high densities in model Wolff(io)slms is caused by a too low resolution of the table. **c**: The velocity profiles during the prompt shock phase for models Wolff(io)slms (left panel), Shen(io)slms (centre panel), and L&S(io)slms (right panel). **d**: The corresponding density profiles. The bold vertical line indicates the position of the electron neutrino sphere at the time of the shock stall.

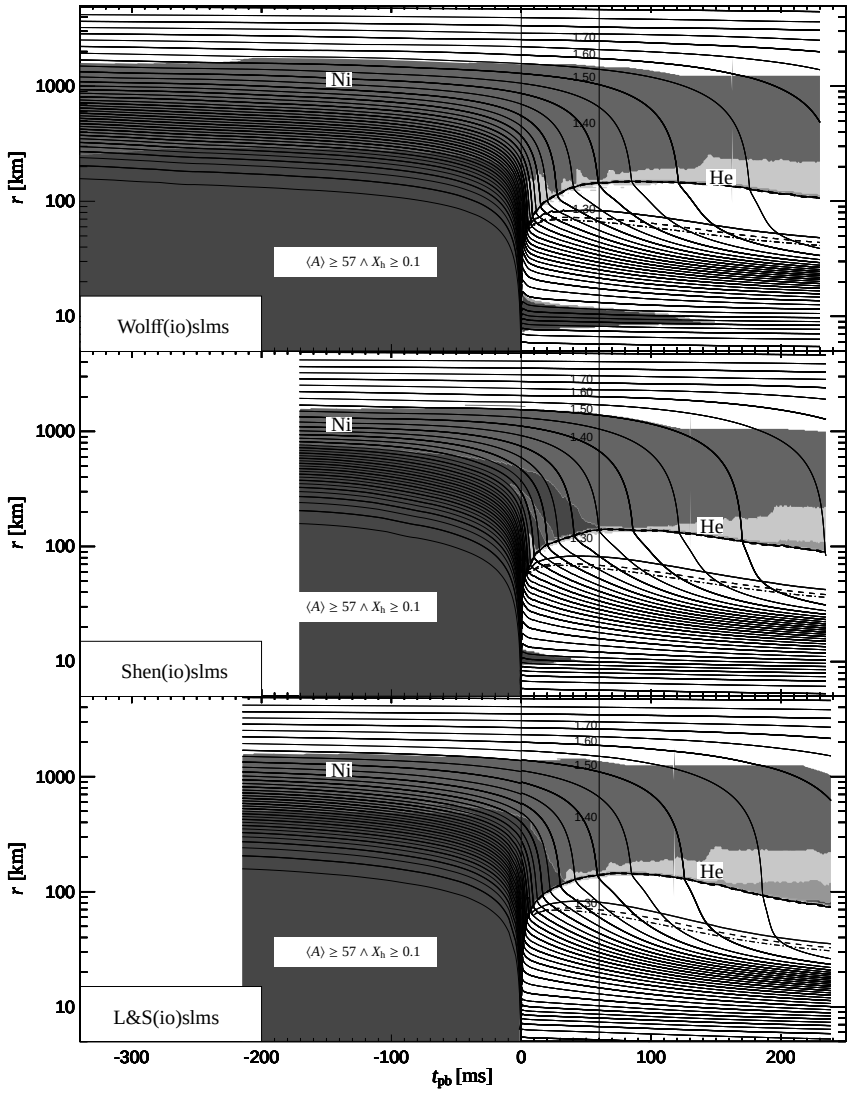

Figure 3.8.: Trajectories of selected mass shells (every 0.05 $M_\odot$) for the model Wolff(io)slms (top panel), Shen(io)slms (centre panel), and L&S(io)slms (bottom panel). The bold trajectories indicate mass shells of multiples of 0.1 $M_\odot$. For reasons of clarity some of them are labelled with the corresponding enclosed mass. Also plotted are the shock position (bold solid line) and the position of the electron neutrinosphere (thin solid), anti-electron neutrinosphere (dashed), and all other flavours (dashed-dotted). The dark grey shaded area marks regions where the representative heavy nucleus contributes more than 10% of the mass and the mass number is larger than 56. The dim gray shaded area marks regions where more than 60% of nickel-like elements are found. The light grey shaded areas mark regions where alpha particles contribute more than 30% (light) and 60%(dark) of the mass, respectively. Note that the models Shen(io)slms and Wolff(io)slms show heavy nuclei below the shock front. Note also that in the region marked by the vertical lines more mass shells pass through the shock in the model L&S(io)slms than in the other models.

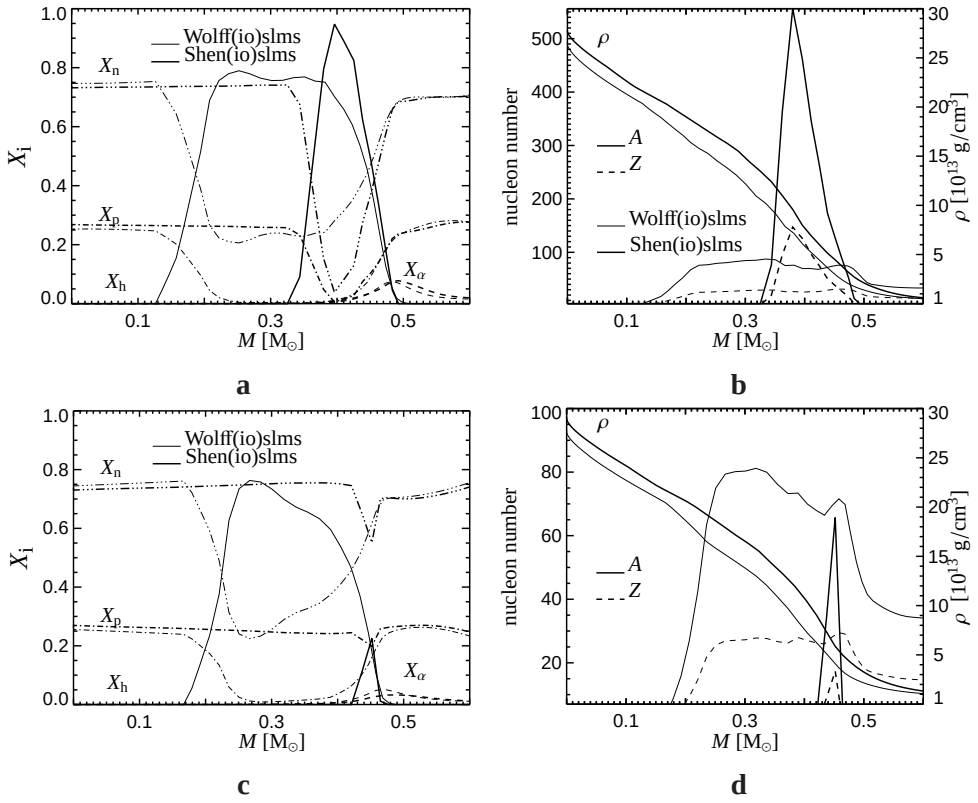

Figure 3.9.: a: The composition versus enclosed mass below the shock front at a time of 10 ms after the shock formation. Note that model L&S(io)slms does not show any representative heavy nucleus anymore, see also Fig. 3.8, whereas in the other models the heavy nucleus still contributes more than 50% of the mass fractions. The barely visible mass fraction of alpha-particles is nearly identical in all three models. **b**: The properties of the representative heavy nucleus in the models Shen(io)slms, and Wolff(io)slms where heavy nuclei can be found below the shock front at a time of 10 ms after shock formation. **c:** The composition versus enclosed mass below the shock front at a time of 50 ms after the shock formation. At this time solely model Wolff(io)slms shows a representative heavy nucleus. **d:** The mass and charge number of the representative heavy nucleus at a time of 50 ms after shock formation.

the definition of Bruenn & Mezzacappa (1997) we define the moment of shock formation as the moment when the core entropy first reaches a value of 3 k_B per nucleon. In Fig. 3.6a we see that the models Shen(io)slms and Wolff(io)slms create their shocks at similar masses, 0.49 M$_\odot$ and 0.47 M$_\odot$, respectively, and roughly at nuclear density (2.7×10^{14} g/cm^3). In model L&S(io)slms, on the other hand, the shock is created at 0.44 M$_\odot$ and at a density of 3.5×10^{14} g/cm^3. The higher central density of this model is caused by the softer L&S-EoS, remember Fig. 3.1d, and the lower enclosed mass at shock formation is consistent with the analysis of Yahil (1983) that the size of the homologous core is proportional to the square of

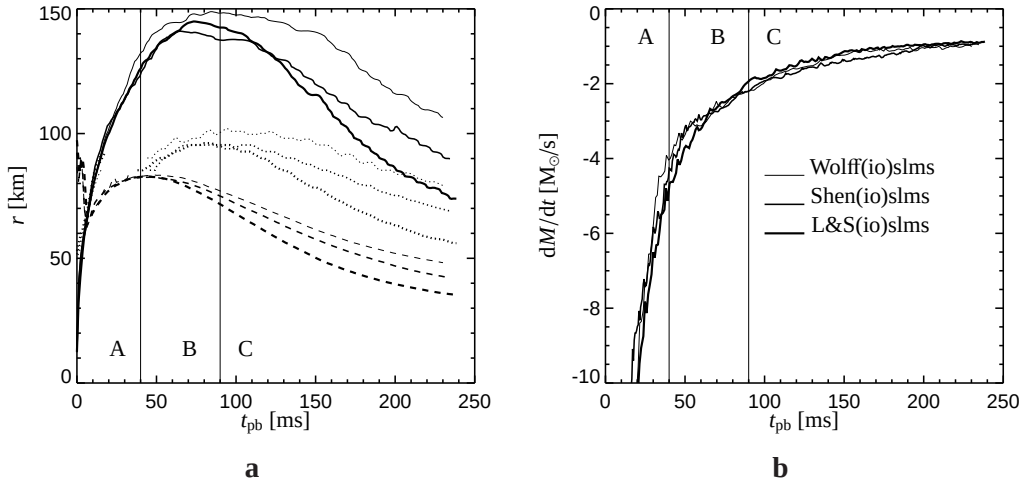

Figure 3.10.: a The positions of the shock (solid), of the electron neutrinosphere (dashed), and of the gain radius (dotted) as a function of time. **b**: The mass accretion rate through the shock as a function of time. The regions labeled "A", "B", and "C" mark different evolutionary phases of the supernova, see the explanation in the main text.

the mean trapped lepton fraction $\langle Y_{lep} \rangle$. We define the mean trapped lepton fraction within the enclosed mass at the shock formation point as

$$\langle Y_{lep} \rangle = \frac{n_{lep}(r < r_{sf})}{n_B(r < r_{sf})} = \frac{\sum_i Y_{lep,i}\, n_{B,i}}{\sum_i n_{B,i}}, \tag{3.1}$$

where n_B, n_{lep} are the baryon number density and lepton number density, respectively, r_{sf} is the shock formation radius, and the sum over i extends over all zones below the shock formation point. We then find values of the mean lepton fraction of 0.29, 0.31, and 0.30 in the models L&S(io)slms, Shen(io)slms, and Wolff(io)slms, respectively.

Prompt shock

After the shock formation the newly created shock travels outward and loses energy by photo-disintegrating the bound iron group nuclei in its path. With all three equations of state the prompt shock turns into an accretion shock during roughly the first millisecond and at this time the shock is well inside of the electron neutrino-sphere, see Fig. 3.7c,d. This implies that the shock dampening due to energy losses is caused in our models solely by the photo-disintegration of the nuclei and not by the neutrino burst at the shock-breakout. Therefore we can approximately calculate the prompt-shock energy by the assumption that the binding energy per nucleon is 8.8 MeV which means that the energy for dissociating 0.1 $M_\odot$ (roughly 10^{56} nucleons) amounts to roughly 1.6×10^{51} erg. In our calculations the shocks pass through 0.240 $M_\odot$, 0.257 $M_\odot$, and 0.254 $M_\odot$ of material and stall at radii of 29.6 km, 37.2 km, and 36.4 km in the models L&S(io)slms, Shen(io)slms, and Wolff(io)slms, respectively. Thus the

energies of the prompt shocks are roughly 3.84×10^{51} erg, 4.11×10^{51} erg, and 4.06×10^{51} erg for the models L&S(io)slms, Shen(io)slms, and Wolff(io)slms, respectively. In agreement with Bruenn & Mezzacappa (1997) we find that a higher enclosed mass at the moment of shock formation leads to a more energetic prompt shock. Although the EoS influences the energetics of the prompt shock these variations are only minor compared to the total amount of energy which is needed to disrupt the star in an explosion.

Cooperstein & Baron (1990) found that the softer the nuclear equation of state is, the more energetic the resulting prompt shock will be (see van Riper 1978, Baron et al. 1985, 1987b,a). However for this study a parameterised EoS was used and these results where contradicted by Swesty et al. (1994) in a study withe the "realistic" L&S-EoS. Using different compressibility modulus of bulk nuclear matter (180 MeV, 220 MeV, 375 MeV) in the L&S-EoS the later authors did not find any strong dependence of the prompt shock energetics on the stiffness of the EoS. Our results completely agree with this study, and show that this is also true for EoSs that are based on different nucleon-nucleon interaction potentials.

Accretion phase and Neutrino emission

After the prompt shock stalls due to energy losses, the accretion phase sets in and the shock gets pushed out by the accreted matter that piles up on the surface of the nascent neutron star. Since the gas falling into the stalled shock is strongly decelerated and the post shock velocities are much smaller than the local sound speed, the structure of the accretion layer between the surface of the proto neutron star and the supernova shock is nearly hydrostatic (see Janka 2001, Janka et al. 2002). Then the change of the shock position is mainly influenced by the conditions at the boundaries of the accretion layer. On the one hand the mass accretion rate through the shock front determines the rate of mass inflow to the accretion layer and the ram pressure at the shock front (ρv^2). On the other hand the mass and radius of the nascent neutron star define the gravitational potential and provide the support of the nearly hydrostatic layer of matter that piles up onto the central core. The compactness of the nascent neutron star is determined by the stiffness of the EoS *and* by the amount of neutrino cooling that allows the cooled matter to settle on the inner core (remember that in simulations without neutrino cooling the shock gets pushed out farther and farther because matter does not cool and settle on the proto-neutron star).

Since our models do not explode, neutrino heating is obviously not strong enough which can be seen in Fig. 3.15, where we show the heating and advection timescales of the stellar plasma. These timescales are calculated by the expression (see Janka et al. 2001)

$$\tau_{\rm adv} \simeq \frac{R_{\rm S} - R_{\rm G}}{\upsilon} \text{ and } \tau_{\rm heat} \simeq \frac{|E_{\rm int} - GM/r|}{\dot{Q}} , \tag{3.2}$$

where $E_{\rm int}$ is the internal energy per nucleon, GM/r is the gravitational energy per nucleon, $\dot{Q}$ is the heating rate per nucleon and all quantities are integrated over the volume enclosed between the shock radius $R_{\rm S}$, and the gain radius $R_{\rm G}$, υ is the postshock velocity.

Alternatively, we adapted the expressions for the advection timescale across a pressure scale height and the timescale for net neutrino heating given by Thompson et al. (2004). The timescales then read

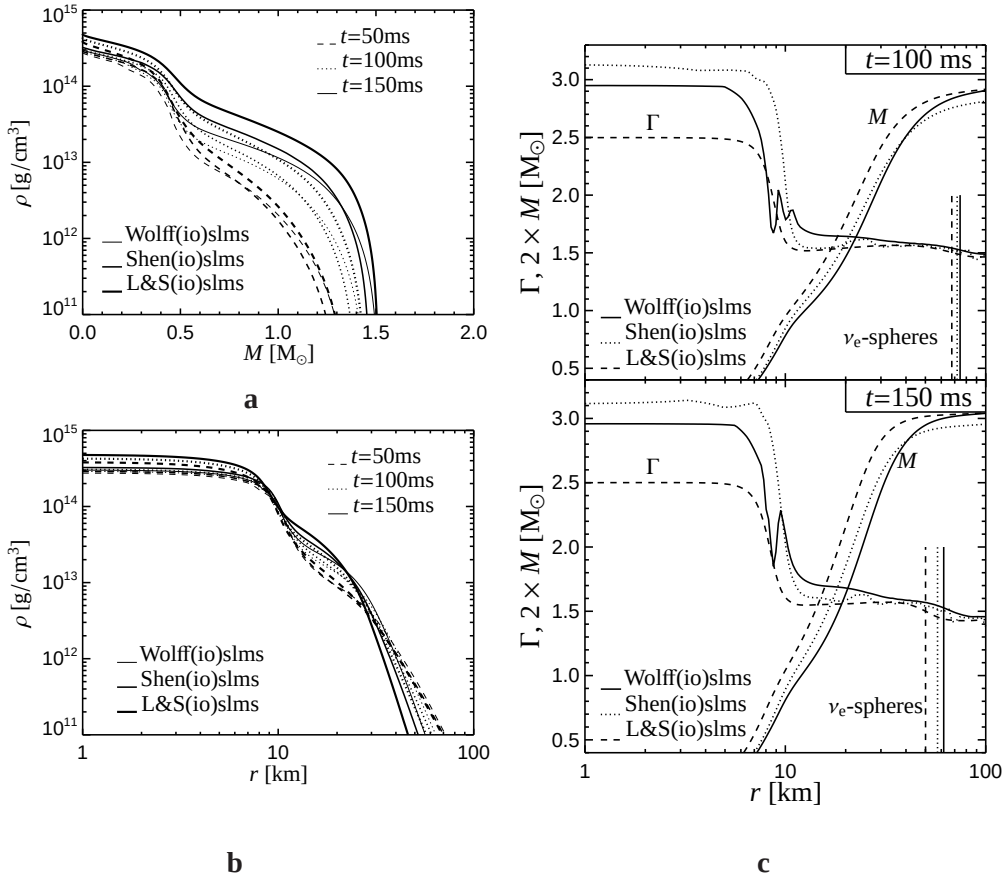

Figure 3.11.: a: The density profile of the models at three different times after the shock formation. **b:** The same density profiles as a function of radius. Note that the models Shen(io)slms and Wolff(io)slms show nearly identical structure in the inner part ($M < 0.3\,M_\odot$, $r < 8$ km). **c**: The adiabatic index and the enclosed mass as function of radius for two different times after the shock formation. The vertical lines represent the position of the electron neutrino sphere.

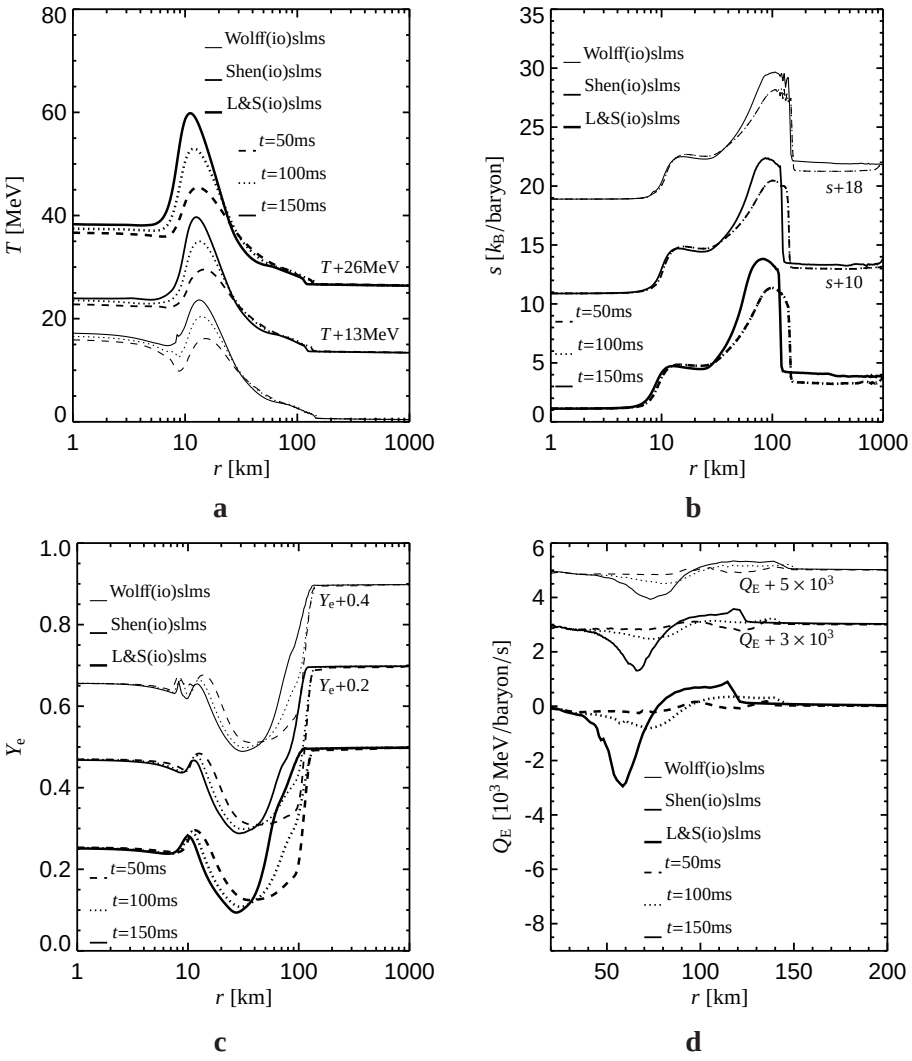

Figure 3.12.: Overview over some quantities during the postbounce phase at times of 50ms, 100ms, and 150ms after the shock formation. For reasons of clarity some curves are shifted upwards by the stated amount. **a**: The temperature for the three models. Whereas the temperature in the proto-neutron star is for all times lowest in model L&S(io)slms, and highest in model Wolff(io)slms, the situation is reversed at the position of the shock (temperature peak). The entropy profiles (**b**) also show that the entropy in the shock is highest for model L&S(io)slms, and lowest in model Wolff(io)slms. **c**: The Y_e-profile shows that the electron-fraction below the shock is for all times slightly lower in model L&S(io)slms, which implies a stronger deleptonisation and cooling (see panel **d**). Note that negative values in (**d**) mean a net neutrino cooling, whereas positive values give a net neutrino heating.

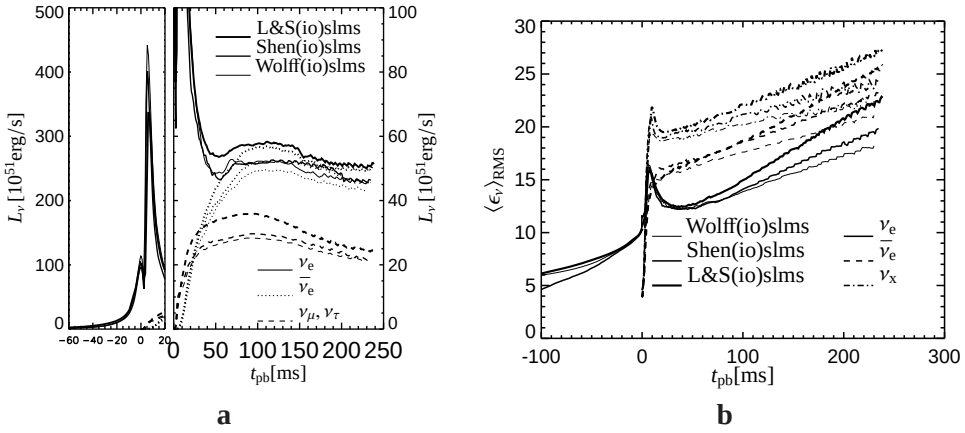

Figure 3.13.: **a**: The luminosity of all neutrinos flavours as seen by an observer at infinity. The numerical evaluation was done at a distance of 500 km from the centre. The left panel shows a time interval around the moment of the prompt ν_e neutrino burst. The right panel shows the neutrino luminosity at later times. Note the different axis scales in both panels. **b**: The corresponding neutrino mean energies to the luminosities in panel a for all neutrino flavours. ν_x denotes muon and tau neutrinos and the corresponding anti-neutrinos.

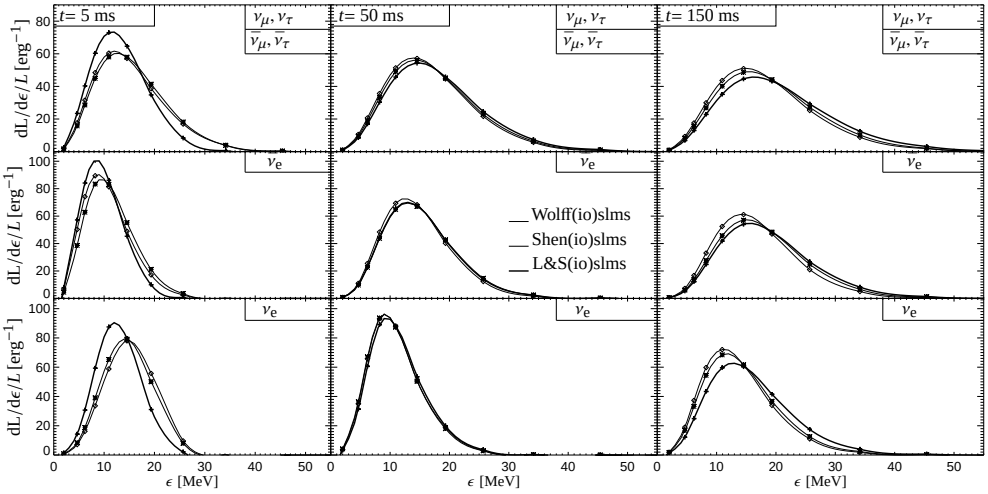

Figure 3.14.: The spectral distribution of the neutrinos at specific times (5 ms panel **a**, 50 ms **b**, and 150 ms **c**) after the shock formation for an observer at infinity evaluated at a radius of 500 km from the centre. The symbols represent our data points, the curves are obtained by a spline interpolation.

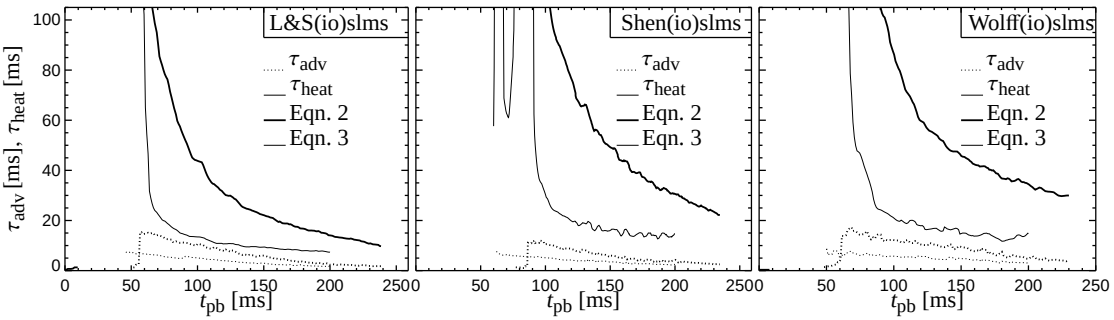

Figure 3.15.: The advection and heating timescale for model Wolff(io)slms (top panel), Shen(io)slms (centre panel), and L&S(io)slms (bottom panel), respectively. Plotted are the timescales according to the definition in Eqn. 3.2 (bold line) and Eqn. 3.3 (thin line).

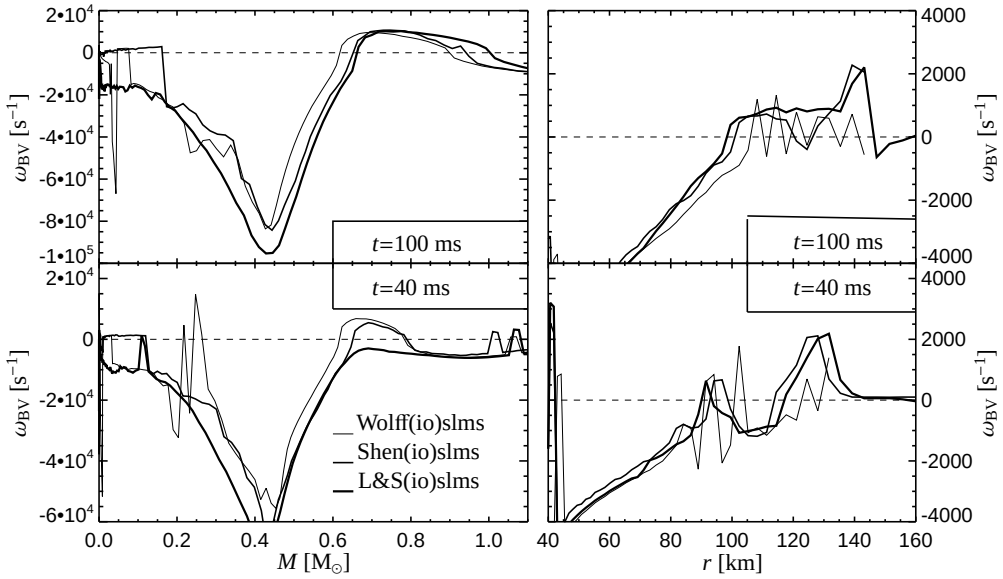

Figure 3.16.: The Brunt-Väisälä frequence, see Eqn. 3.10, as function of mass (left panels) and as function of stellar radius (right panels) for all three models at different points of time.

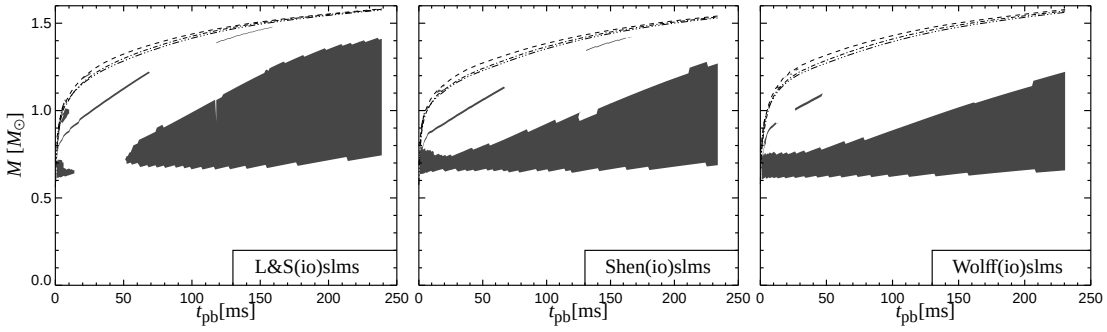

Figure 3.17.: Contour areas of the positive Ledoux criterion (i.e. regions which are unstable to convective flows) inside the nascent neutron star as function of time and the mass coordinate. The lines in the upper part of the plots indicate the positions of the electron neutrinospheres (top), anti–electron neutrinospheres (middle), and heavy lepton (anti) neutrinospheres (bottom).

$$\tau_{\rm adv} \;=\; \frac{H}{\rm v} \;\text{ and }\; \tau_{\rm heat} = \frac{P}{\rho\,\dot{Q}} \;\text{ with }\; \frac{{\rm d}P}{P} = -\frac{{\rm d}r}{H}\;, \tag{3.3}$$

where H is the pressure scale height, P the pressure, ρ the mass density, and $\dot{Q}$ is the heating rate. The timescale for neutrino heating was averaged over all radial zones between the gain radius and the shock position. Since neutrino heating is strongest near the gain radius the pressure scale height was determined at the gain radius. Although the absolute values are different, both definitions of the advection and heating timescales (Eqs. 3.2 and 3.3) show that the respective heating timescale is longer than the respective advection timescale.

For the discussion of the shock expansion we have to introduce some quantities and definitions that will be used. Note that we define the radius of the nascent neutron star at the position of the neutrinosphere for electron neutrinos and we define the neutrinosphere as the radial position where the spectrally averaged transport optical depth

$$\langle\tau^{\rm tr}(r)\rangle = \int_r^\infty \frac{{\rm d}r'}{\langle\lambda^{\rm tr}(r')\rangle} = \int_r^\infty {\rm d}r' \,\frac{\int_0^\infty {\rm d}\epsilon\, H(r',\epsilon)\chi^{\rm tr}(r',\epsilon)}{\int_0^\infty {\rm d}\epsilon\, H(r',\epsilon)} \tag{3.4}$$

equals unity. Here $\chi^{\rm tr}$ is the inverse of the mean free path of neutrinos between two interactions and $H(r,\epsilon)$ is the first angular moment of the specific intensity of radiation. The inverse mean free path $1/\lambda^{\rm tr}$ or the transport opacity $\chi^{\rm tr}$,

$$\frac{1}{\lambda^{\rm tr}} = \chi^{\rm tr} = \kappa_a^* + \kappa_s^{(0)} - \frac{\kappa_s^{(1)}}{3} \tag{3.5}$$

which is relevant for momentum transfer from neutrinos to targets is written as an absorption part κ_a^* (compare with Eqn. 6 of Cernohorsky et al. 1989) which includes phase space blocking

(see, e.g. Eqn. C29 in Bruenn 1985) and an isotropic and an anisotropic scattering part $\kappa_s^{(0)}$ and $\kappa_s^{(1)}$, respectively. Note that the scattering contribution is calculated from the cross section of momentum transfer (cf. Eqn. 12 in Straumann 1989).

Furthermore we define the compactness of the nascent neutron star as ratio of enclosed mass below the neutrinosphere and the position of the electron neutrinosphere. Then we write:

$$\mathrm{C_{NS}} := \frac{M_\nu/[\mathrm{M}_\odot]}{r_\nu/r_\mathrm{S}} \quad \text{with } r_\mathrm{S} = 2GM_\nu c^{-2} \quad , \tag{3.6}$$

where r_S is the Schwarzschild radius of the dense core,

G is the gravitational constant, M_ν is the enclosed mass below the neutrinosphere which has radius r_ν, and c is the speed of light.

In the following we will discuss how the nuclear equation of state influences the shock propagation after the prompt shock stall and how the EoS affects the neutrino emission. We therefore introduce the following sub-phases as indicated by the vertical lines in Fig. (3.10):

- Phase A: from the stall of the prompt shock to the time when the neutrinosphere of electron neutrinos reaches its maximum position. In this phase, which lasts roughly 30 ms, the mass accretion rates through the shock front decreases steadily and quickly; as a consequence the ram pressure on the shock drops and allows a shock expansion. This phase is almost identical for all three EoSs, see Fig. 3.10a, however the model Wolff(io)slms shows the fastest shock expansion because of the fastest drop in the mass accretion rate, see Fig. 3.10b.

- Phase B: from the end of phase A to the time of maximal shock expansion. In this phase, because of neutrino cooling, matter starts to settle, and the nascent neutron star starts to shrink. However, the mass accretion rate still decreases significantly. This results in a still expanding shock despite the fact that the shock is losing its support. Finally, after reaching its maximum position of 149 km, 145 km, and 140 km for the models Wolff(io)slms, Shen(io)slms, and L&S(io)slms respectively, the shock retreats.

- Phase C: From the beginning of the shock decline to the end of our simulation. In this phase the mass accretion rate nearly becomes constant but the compactness of the inner core increases, and the shock recedes further.

Since in this stage neutrino cooling is efficient, the system is nearly hydrostatic (see Fryer et al. 1996, Janka 2001) and one can derive the approximate expression

$$R_\mathrm{s} \propto \left(\frac{(R_\mathrm{NS})^4 (k_\mathrm{B} T_\mathrm{NS})^4}{|\dot{M}| \sqrt{M_\mathrm{NS}}} \right)^{2/3} \quad , \tag{3.7}$$

from the Eqns. (39)-(63) in Janka (2001). Here R_NS is the radius of the neutron star, T its temperature, M its mass, and $\dot{M}$ the mass accretion rate through the shock front. This equation describes the qualitative behaviour of the system as long as heating is not important, the adiabatic index Γ roughly 4/3 and the shock velocity is much smaller than the pre-shock velocity of matter. Thus a slightly more extended neutron star leads to a significant larger shock radius and the shock in the model Wolff(io)slms stays farthest outside.

The link between the compactness of the proto neutron star and the EoS is shown in Figs. 3.11a-c. Our models develop different compact cores in a radial region below the neutrinosphere and above the hardly compressible matter ($\gamma > 2$, $r \approx 10$ km). Below 10 km the density profiles and enclosed masses, and thus compactnesses, of the models Shen(io)slms and Wolff(io)slms are nearly identical, but above 10 km the compactnesses develop differently in time. In this region the Wolff-EoS is the stiffest EoS which results in the most extended core and thus according to Eqn. 3.7 to the largest shock position.

In Fig. 3.12 we show snapshots of profiles of temperature, entropy, electron fraction and heating rates. Interestingly, we find that model L&S(io)slms with the compactest core shows stronger heating and cooling than the other models. Consistency we find that model L&S(io)slms emits more and "hotter" neutrinos than the other models (see Fig. 3.13) and model Wolff(io)slms shows the lowest cooling and emits less energetic neutrinos.

The neutrino processes are influenced by the structure and atmospheric conditions (e.g. density and temperature profiles) of the nascent neutron star and of the accretion layer, which both are influenced by the equation of state. On the other hand, as already discussed, the cooling is responsible for the settling of the accreted matter onto the core and thus the cooling feeds-back at the evolution of the proto–neutron star.

One of the most prominent features that occurs during a core collapse supernova is the so-called shock breakout. It is defined as the moment when the shock front that is born in a neutrino opaque region breaks through the neutrinosphere of the electron neutrinos and thereby produces an luminous burst of electron neutrinos. This happens in our models roughly 4 ms after the shock formation, which is after the prompt shock has stalled. Thompson et al. (2003) already discussed the properties of the neutrino signal for different values of the compressibility modulus of bulk nuclear matter in the Lattimer & Swesty EoS and found only a weak dependence. In our simulations with equations of state that do not only differ in the compressibility but also in the composition we find a larger difference in the neutrino luminosity and energy during the shock breakout as well as in the late time evolution. The electron neutrino luminosity of the breakout peak as seen by a static observer at infinity varies roughly between 15% and 22% [2], see Fig. 3.13, and between 5% and 20% during the later evolution. The energy losses due to neutrino emission during the first 163 ms after the shock formation are 44.6 foe[3] , 39.2 foe, and 38.3 foe in the models L&S(io)slms, Shen(io)slms, and Wolff (io)slms, respectively. The differences in the burst luminosity in our models are a result of the stronger deleptonisation in a more extended spatial region in the models Wolff(io)slms and Shen(io)slms. Furthermore the models behave in such a way that the optical depth in this deleptonisation region is slightly smaller and thus these models are less opaque and allow the electron neutrinos to escape more easily. The average neutrino energies for neutrinos of all flavours also vary between 8% and 20% in our models, see Fig. 3.13. Note that we present here a rms average energy defined by

$$\langle \epsilon_\nu \rangle_{\mathrm{RMS}} := \left(\frac{\int_0^\infty \mathrm{d}\epsilon\, \epsilon^2 J_\nu(\epsilon)}{\int_0^\infty \mathrm{d}\epsilon\, J_\nu(\epsilon)} \right)^{\frac{1}{2}} \quad , \quad \nu \in \{\nu_e, \bar{\nu}_e, \nu_{\mu,\tau}, \bar{\nu}_{\mu,\tau}\} \tag{3.8}$$

[2] However, this variation is not big enough to distinguish different EoSs by the measurement of the burst signal in a neutrino detector (see Kachelrieß et al. 2005).

[3] A "foe" or a "bethe" stand for an energy of 10^{51} erg.

where $J_\nu(\epsilon)$ is the zeroth moment of the specific intensity. The spectral information of the various neutrino flavours is shown in Figs. 3.14a – 3.14c at a time of 5ms, 50 ms, and 150 ms after the shock formation, respectively. We find only little variation of the spectra with the EoS. However, at early times the model with the L&S-EoS shows a slightly softer spectrum than the models with the stiffer EoSs.

During the accretion phase another interesting difference in the models becomes visible: Whereas model L&S(io)slms shows no mass fraction of a representative heavy nucleus below the shock front ($X_h < 0.1\%$), we find sometimes significant amounts of heavy nuclei in the other two models, see Fig. 3.9a – Fig. 3.9d , where a snapshot of the composition 10 ms and 50 ms after shock formation is shown. The corresponding density profile can be found in Fig. 3.9e. Again the representative nucleus in model Shen(io)slms is heavier than the one in model Wolff(io)slms. At later times after shock formation the representative nucleus contributes less and less of the mass fractions but in case of model Wolff(io)slms nuclei can be found up to 120 ms after the shock formation, see Fig. 3.8. This mass shell of heavy nuclei between fluid layers of free protons and neutrons in the nascent neutron star may be very interesting in multi-dimensional simulations of these models, since this matter stratification may influence instabilities in the nascent neutron star.

Analysis of hydrodynamic instabilities

Convection is known to be of great importance for the shock evolution, since it influences the heating of matter behind the shock front and can influence the neutrino luminosity at the neutrino spheres (see e.g. Herant et al. 1994, Guillot et al. 1995, Keil et al. 1996, Mezzacappa et al. 1998a, Fryer 1999, Fryer & Warren 2002, Buras et al. 2003, 2006b,a). However, spherically symmetric models do of course not show any convective flows *but* they do show the gradients of entropy and total lepton number which are mainly responsible for convective instabilities.

In our spherical symmetric simulations, we discovered conditions that should lead to convectivly unstable regions in multi-dimensional simulations. However, one has to be careful with this analysis since in a multi-dimensional simulation the back reaction of convection onto the structure of the atmosphere can change the conditions that lead to convection in the first place.

We identified the regions of potential convection with the Ledoux-criterion, which can be written in the form Buras et al. (2006b)

$$C_{\mathrm{led}} = \left(\frac{\partial\rho}{\partial s}\right)_{Y,P} \frac{\mathrm{d}s}{\mathrm{d}r} + \left(\frac{\partial\rho}{\partial Y}\right)_{s,P} \frac{\mathrm{d}Y}{\mathrm{d}r} \geq 0, \tag{3.9}$$

where $s = s + s_\nu$ is the entropy per baryon *including* the neutrino entropy, ρ the density, $Y = Y_e + Y_\nu$ is the total lepton number per baryon. In a multi-dimensional simulation we expect that convection would develop in regions where Eqn. 3.9 gives positive values. Regions with $C_{\mathrm{led}} < 0$ are otherwise stable against convective instability. From Eqn. 3.9 one can calculate the Brunt-Väisälä frequency

$$\omega_{\mathrm{BV}} := \mathrm{sign}(C_{\mathrm{led}}) \sqrt{-\frac{g}{\rho}\,|C_{\mathrm{led}}|}, \text{ with} \tag{3.10}$$

$g = -\mathrm{d}\Phi/\mathrm{d}r$ being the gravitational acceleration.

The Brunt-Väisälä frequency denotes the growth rate of fluctuations if it is positive (instability), and the negative of the oscillation frequency of stable modes, if it is negative. In Fig. 3.17 we show for the proto-neutron star contours of the evaluated Ledoux-criterion as a function of time and radius. Whereas we expect the development of convective growths at all times in the models Shen(io)slms and Wolff(io)slms, the model L&S(io)slms does not show a continuous positive Ledoux-criterion. This might imply that proto-neutron star convection would develop faster in 2D-models which would apply the Shen and Wolff EoSs. However, for all models our analysis reveals that the unstable region is expected to be deep inside the PNS, which may prevent a modification of the neutrino emission by convective flows. This question can only be answered in 2D-models where the strength of convective growths and the over- and undershooting of fluid flows is taken into account.

3.2.3. Summary

We have simulated the collapse of a $15\,M_\odot$ star and the subsequent shock propagation with three different nuclear equations of state with a Boltzmann neutrino transport code in spherical symmetry. We have considered the three equations of state available to us, namely the L&S-EoS which is based on a finite temperature liquid drop model, the Wolff-Eos which is calculated with a Hartree-Fock method, and the Shen-EoS which adopts a relativistic mean field treatment for dense baryonic matter. All three nuclear equations of state use different values for the nuclear parameters and show e.g. different softness.

We find that the properties of the representative nucleus, i.e. charge number and mass number, are different in the three equations of state as well as the density when the transition to homogeneous matter proceeds.

These differences in the EoSs effect the deleptonisation during the collapse phase and thus the collapse timescale and the shock formation point. The launched shock is more energetic for stiffer EoSs, but this energy gain is by far lower than the energy needed for a prompt explosion. In our models we find a much stronger variation of the burst signal with different EoSs than it was found by Thompson et al. (2003). However, we point out that these variations are nevertheless to small to allow for the differentiation of different EoSs by the measurement of the neutrino burst signal (see Kachelrieß et al. 2005).

The EoS is more relevant for the subsequent accretion phase. Here, we find that a stiffer EoS shows lower and “cooler” neutrino emission. Thus matter does not cool very efficiently and a less compact core forms that pushes the shock farther outwards compared to simulations with softer EoSs. On the other hand, a softer EoS shows stronger cooling and heating and it is thus not clear from first principle which kind of EoS is more favourable for creating a supernova explosion. This answer can probably only be given in multi-dimensional simulations that are more sensitive to the changes in neutrino heating and cooling since the growth of convection strongly depends on these two values. However, a stability analysis of conditions that may lead to convection in the proto-neutron star reveals that details of the EoS may be important for convective instabilities. Especially the Shen-EoS and Wolff-EoS show a matter stratification in the nascent neutron star that seems promising for the development of Rayleigh-Taylor instabilities. We thus conclude that the detailed knowledge of the EoS for hot and dense matter is indispensable for a correct treatment of the supernova problem.

3.3. EoS changes: Mimicking a high density phase transition

In the previous section it was shown — by using three different EoSs — that the supernova evolution depends in a complex manner on the EoS. This is a somewhat unsatisfactory situation, since the nuclear equation of state is still poorly known — if not to say unknown — at high baryon densities (see, e.g. Lattimer & Prakash 2004, Lattimer 2005, Horowitz et al. 2004b,a, Tartamella et al. 2005, Lattimer 2006, Lattimer & Prakash 2006). On the one hand, the nucleon–nucleon interaction potential is not known at high densities and on the other hand, it is also unclear what matter looks like if it is compressed to supra–nuclear densities. Does a high–density fluid of unbound protons and neutrons form? Or, does at some phase space points a phase transition occur, and other hadronic particles such as pions or kaons appear? Of course, there exist plenty different theoretical models, and they predict different states of matter such as quark or strange matter, pion and kaon condensates, only to mention a few.

Thus the question arrises whether such possibly states of matter are relevant for supernova explosions ? From the point of view of a supernova modeller it is interesting to know to what extend present simulations are sensitive to changes of the EoS at high densities.

C. J. Horowitz provided a clever idea to test these questions in our simulations. The trick is to artificially — but in a physical parameter range— modify the supra–nuclear phase of an EoS in order to mimic a high density phase transition from a nucleon gas to e.g. a pion condensate. In this approach it is assumed that the EoS below nuclear densities is not affected by the above mentioned possible phase transitions and thus the EoS is modified only above a threshold baryon density ρ_t. Furthermore the amount of softening in the EoS from a possible exotic phase is limited because the EoS must still support cold neutron stars up to some maximum mass $M_{\max}$. Adopting relatively aggressive choices (i.e. low values) for ρ_t and $M_{\max}$ in order to maximise the effects of this EoS softening, we chose the threshold density of

$$\rho_t = 1.25 \times \rho_{nuc} = 1.25 \times 2.7\,10^{14}\,\frac{\mathrm{g}}{\mathrm{cm}^3}\,, \tag{3.11}$$

where ρ_{nuc} is normal nuclear density. This implies that the changes in the EoS do not impact normal nuclei or the value of the incompressibility at densities below ρ_{nuc} and the changes will only become active as soon as the density in our simulation exceeds ρ_t.

Above the threshold density ρ_t we then apply the following changes to the EoS: We add an additional component to the EoS that is assumed to reduce or increase the energy density ϵ. We then calculate consistently the change in pressure, adiabatic index, and baryon chemical potentials which are caused by the change in the energy density[4]:

- By adding a term $\Delta\epsilon$ to the energy density ϵ for a system at baryon density $\rho_{\mathrm{B}} > \rho_t$ we obtain the new energy density ϵ'

$$\epsilon' = \epsilon + \Delta\epsilon = \epsilon - a(\rho_{\mathrm{B}} - \rho_t)^2\Theta(\rho_{\mathrm{B}} - \rho_t)\ . \tag{3.12}$$

[4]With this ansatz we are not able to take into account that the state of matter changes, and e.g. neutrino interactions for pion condensates may change the opacities. However, since the "model" phase transition takes place deep inside of the dense core the supernova does not realize possible different opacities on the timescale we do consider here.

Here a is a constant that can be chosen to vary the maximum mass that the EoS will support (a larger value of a implies a smaller maximum mass). Note that this modification of the EoS in assumed to be independent of the temperature T and the electron fraction Y_e.

- The change in pressure associated with $\Delta\epsilon$ can than be calculated from the derivative of $\Delta\epsilon$ with respect to the density $\rho_{\rm B}$ and we obtain

$$\Delta P = -a(\rho_{\rm B}^2 - \rho_t^2)\Theta(\rho_{\rm B} - \rho_t) \ . \tag{3.13}$$

- The changes of the proton chemical potential $\mu_{\rm P}$ or neutron chemical potential $\mu_{\rm N}$ can than be expressed as

$$\Delta\mu_{\rm P} = \Delta\mu_{\rm N} = -2a(\rho_{\rm B} - \rho_t)\Theta(\rho_{\rm B} - \rho_t) \ . \tag{3.14}$$

  Note that $\mu_{\rm N}$ - $\mu_{\rm P}$ is unchanged because our correction is independent of Y_e.

- The adiabatic index Γ is then calculated according to

$$\Gamma = \left(\frac{\partial \ln P}{\partial \ln \rho}\right)_s = \frac{\rho}{P}\left[\left(\frac{\partial P}{\partial \rho}\right)_{T,Y_e} + \frac{T}{\rho}\frac{\left[\left(\frac{\partial P}{\partial T}\right)_{\rho,Y_e}\right]^2}{\left(\frac{\partial E}{\partial T}\right)_{\rho,Y_e}}\right] \ , \tag{3.15}$$

  where s is the entropy per baryon.

Note that by construction, these changes to the high density phase of the EoS are thermodynamically consistent and obey the Maxwell relations of thermodynamics.

These modifications allow us to soften or stiffen the EoS above the threshold density ρ_t and to investigate in parameter studies to what extend this high density regime (and some possible phase transitions in this regime) influence the time evolution of supernova simulations. Furthermore, these parameter studies are complementary to our overall goal to understand the importance of the EoS during a core collapse supernova explosion.

In Figs. 3.18 and 3.19 we show for some representative values of a the changes of the energy density and the pressure for the L&S and Wolff EoS.

Parameter study with a 15 $\rm M_\odot$ progenitor model

With this ansatz for a parameter study we have calculated a series of collapse and postbounce models with the same $15\,\rm M_\odot$ progenitor star of Heger et al. (2001) which was already used in Section 3.2. In these calculations different values of a and the L&S–EoS or the Wolff–EoS were used. The models and the values of a are summarised in Table 3.1.

Surprisingly, we find that in our calculations the changes of the EoS in the high density phase above $\rho > 10^{14}\rm g/cm^3$ have no influence on the simulations neither with the intrinsically soft L&S–EoS nor with the stiffer Wolff–EoS. The reason for this is simply found in the evolution

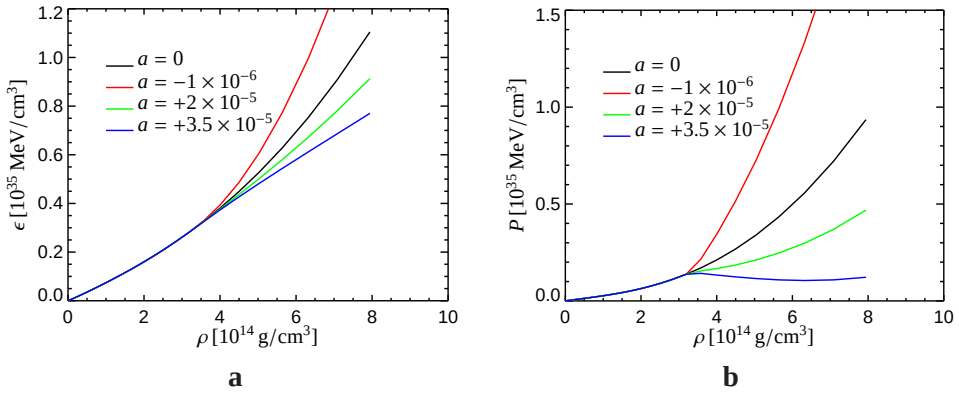

Figure 3.18.: The modifications of the L&S–EoS: (**a)** The energy density as function of density and (**b)** The pressure as function of density.

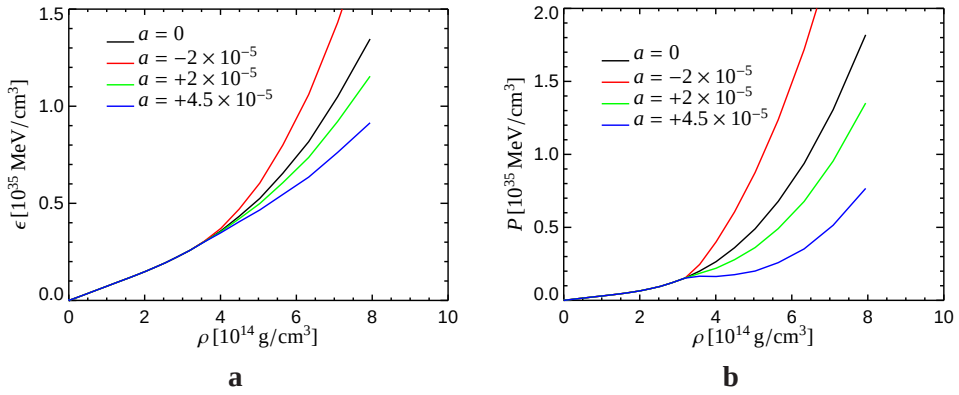

Figure 3.19.: The modifications of the Wolff–EoS: (**a)** The energy density as function of density and (**b)** The pressure as function of density.

of the density in our simulations. During the collapse the density never exceeds the threshold density ρ_t and hence the modifications of the EoS never come into being.

During the postbounce evolution only at very late times the density exceeds the threshold density ρ_t and the EoS modifications start to play a role. However, this only happens in a spatially very narrow region in the centre of the proto neutron star which does not effect the supernova evolution until we have stopped these simulations. In this narrow region, depending on the choice of the parameter a, the EoS becomes softer or stiffer. This can be seen in Fig. 3.20 where we show the shock trajectories, the radius of the electron neutrinosphere (which we define as the radius of the neutron star), and the value of the adiabatic index in the nascent neutron star at a time of 250 ms after the shock evolution.

However, it is possible that the changes in the EoS become important at very late times when the ongoing mass accretion increases the density of the neutron star such that the density of

Model name	progenitor	a [MeV^{-2}]	$M_{\max}$ [M$_\odot$]	r [km]	EoS
W0	s15a28	0	2.21	13.5	Wolff
W−2e−5	s15a28	-2×10^{-5}	2.45	13.8	Wolff
W+2e−5	s15a28	$+2 \times 10^{-5}$	1.91	13.0	Wolff
W+4.5e−5	s15a28	$+4.5 \times 10^{-5}$	1.41	12.1	Wolff
W0−20	s20	7	2.21	13.5	Wolff
W+2e−5	s20	$+2 \times 10^{-5}$	1.91	13.0	Wolff
LS0	s15a28	0	1.84	10.0	L&S
LS−1e−6	s15a28	-1×10^{-6}	2.57	12.8	L&S
LS+2e−5	s15s28	$+2 \times 10^{-5}$	1.51	8.65	L&S
LS0−20	s20	0	1.84	10.0	L&S
LS+2e−5−20	s20	$+2 \times 10^{-5}$	1.51	8.65	L&S
LS−1e−6−20	s20	-1×10^{-6}	2.57	12.8	L&S
LS0−25	s20	0	1.84	10.0	L&S
LS+2e−5−25	s20	$+2 \times 10^{-5}$	1.51	8.65	L&S
LS−1e−6−25	s20	-1×10^{-6}	2.57	12.8	L&S

Table 3.1.: Overview over the models calculated with different progenitor stars and the Wolff–EoS or L&S–EoS, respectively. Stated are the progenitor models the values of a, the maximum supported mass of this (modified) EoS and the radius of a neutron star with maximum mass.

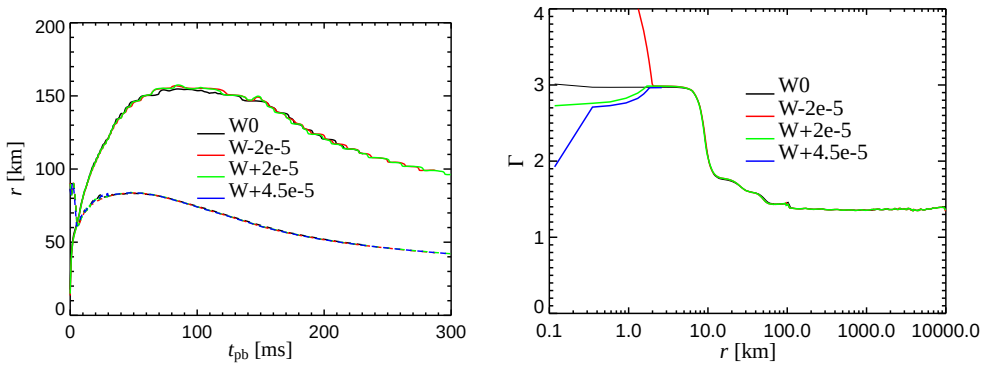

Figure 3.20.: **a**: The shock position as function of time in the (modified) models with the Wolff–EoS for the 15 M$_\odot$ progenitor star. **b**: The adiabatic index as function of stellar radius at a time of 250 ms after the shock formation. It is clearly visible that the modifications of the EoS only affect the inner 10 km of the dense core.

a larger spatially extended region exceeds the threshold density ρ_t.[5] Instead of running this model to very late times, the same effect can be obtained faster by simulating the evolution of

[5]We will discuss this point in the following section.

more massive progenitor models. We have thus additionally simulated the supernova evolution of progenitor models whose masses exceed $15\,M_\odot$, which we will discuss in the following section.

More massive progenitors

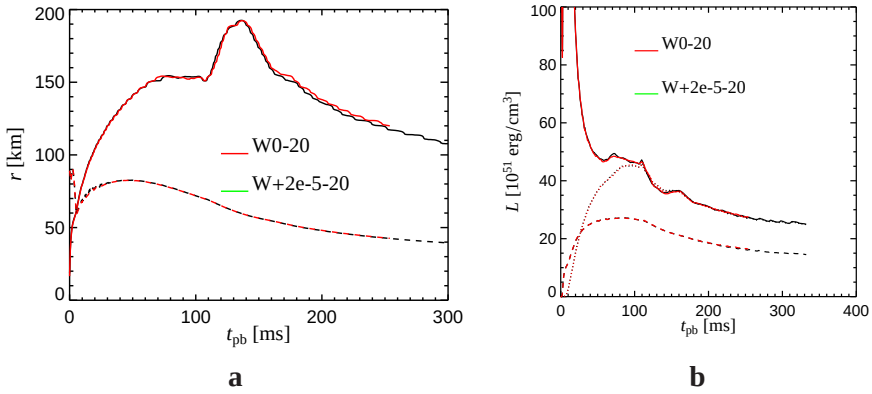

Figure 3.21.: **a**: The shock position (upper solid lines) as function of time for the models W0–20 and W+2e−5−20. Also shown are the electron neutrino spheres (dashed lines). **b**: The luminosity for both models as seen by an static observer at rest at infinity. The evaluation was done at a radius of 500 km. Shown are the luminosities of electron neutrinos (solid), anti–electron neutrinos (dotted), and heavy lepton (anti) neutrinos (dashed).

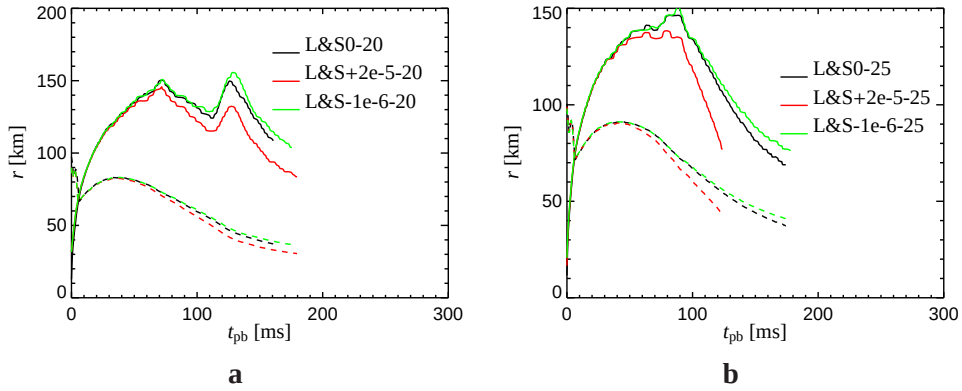

Figure 3.22.: **a**: The shock position (solid lines) of models L&S0 – 20, L&S+2e−5 – 20, and L&S−1e−6 – 20. The position of the electron neutrino spheres are indicated by the dashed lines. **b**: The shock position (solid lines) of models L&S0 – 25, L&S+2e−5 – 25, and L&S−1e−6 – 25. The position of the electron neutrino spheres are indicated by the dashed lines.

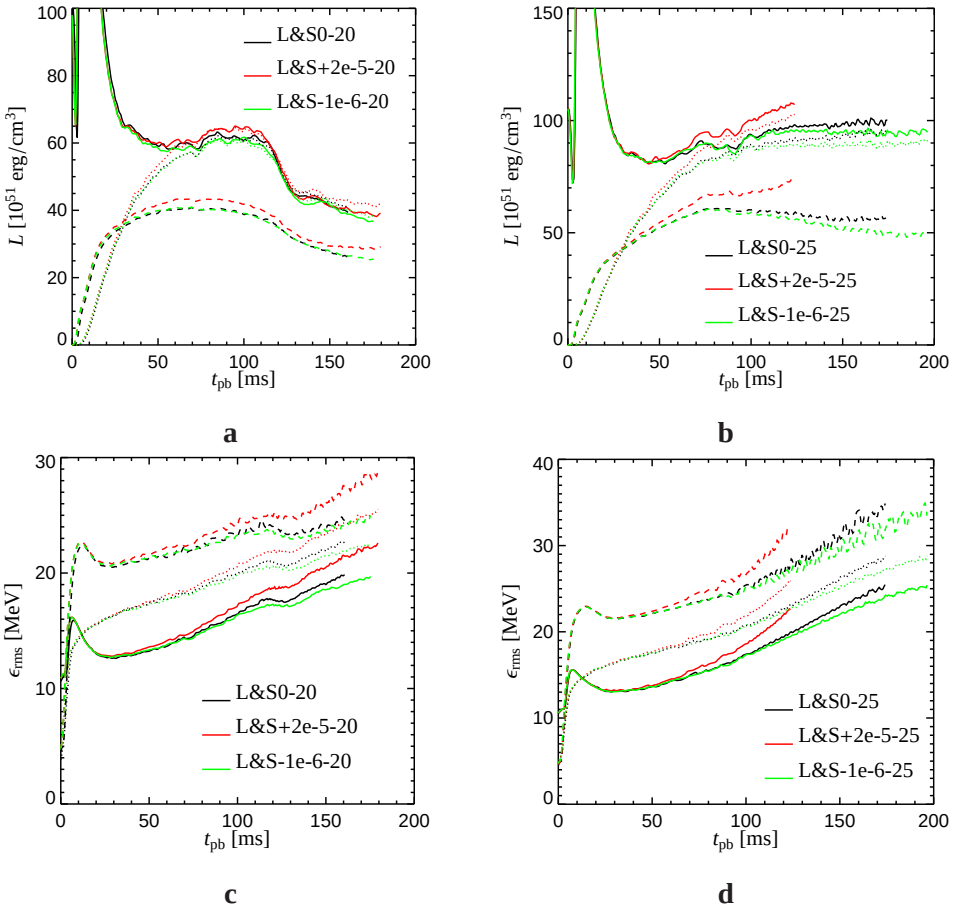

Figure 3.23.: The neutrino luminosities (upper panels) and rms neutrino energies (lower panels) for the same models as in Fig. 3.22: **a**,**c** for the $20M_\odot$ progenitor model, and **b**,**d** for the $25M_\odot$ progenitor model. Both the luminosity and the rms energy were evaluated at a radius of 500 km and they were transformed to the values as seen by an static observer resting at infinity.

During a supernova evolution the central density reaches higher values for more massive stellar progenitors. Thus the above mentioned modifications of the supra–nuclear phase of the EoS should become more important when the mass of the stellar progenitor is larger. Although this statement is true in general, it strongly depends on the stiffness of the EoS for which masses of progenitor models and at which time (i.e. how much mass was accreted on the nascent neutron star) the supra–nuclear modifications of the EoS become important. As already discussed above, a supra–nuclear phase can only become important if a large fraction of the neutron star exists in this supra–nuclear density range. This should be demonstrated with a softer version ($a = +2 \times 10^{-5}\,\mathrm{MeV}^{-2}$) of the Wolff–EoS and a $20\,M_\odot$ progenitor model of Woosley et al. (2002). As Fig. 3.21 shows, this combination of the progenitor mass and the rather stiff Wolff–EoS at densities below saturation density does not change the supernova evo-

lution during the first 300 ms after the shock formation, as was already seen in the calculations with the $15\,M_\odot$ progenitor model. Quite contrary, in case of the L&S–EoS the corresponding model L&S+2e−5−20 clearly shows a changed supernova evolution and a faster shrinking dense core, see Fig. 3.22a. Vice versa a stiffer version of the L&S–EoS (model L&S−1e−6−20) clearly shows a more extended neutron star and a trend towards the results with the Wolff–EoS. Inspired by this result we have also calculated a supernova model with a $25\,M_\odot$ progenitor star, where the effects should even be stronger. Indeed, in these models (L&S+2e−5−25 and L&S−1e−6−25) we find a (strong) sensitivity to the EoS physics of the supra–nuclear phase.

This can be seen in Fig. 3.22b where we depict the shock positions and the radii of the nascent neutron stars for the simulation with the unmodified and the softened/stiffened EoS for the $25\,M_\odot$ progenitor model. As one can clearly deduce from Figs. 3.22a–b, the choice of the progenitor model has such an tremendous effect on the importance of the supra–nuclear density phase of neutron star matter that in the softened run with the $25\,M_\odot$ progenitor the whole inner core collapses to densities above 10^{15} g/cm^3. Physically this probably means that at this stage a black hole forms, however, V is numerically not suitable to follow the evolution of the dense core to such high densities and the run was stopped at this moment. Stiffening of the EoS leads — as expected — to a more extended neutron star for this progenitor model. In Fig. 3.23 we depict the neutrino luminosities and rms energies for the models with the $20\,M_\odot$ and the $25\,M_\odot$ progenitor star, respectively. A faster shrinking neutron star implies, by conversion of potential energy, higher neutrino luminosities and energies, which then also increases the neutrino heating. Vice versa a model with a more extended neutron star shows lower luminosities, neutrino energies, and thus less neutrino heating. Figure 3.23 shows exactly this effect.

As we showed in Table 3.1 a different supra–nuclear phase has influence of the maximum mass of the neutron star that can be supported by the EoS. However in our models, we do not see different masses for the *same* progenitor model with modified EoSs. The reason for this is the following: first, the mass accumulated in the nascent neutron star is determined by the accretion history of the model. However, this accretion history is the same since the (high–density) EoS modifications do not influence the mass accretion rate which is determined by low density matter falling towards the neutron star. For the reason of mass conservation all of our models have the same mass[6] at the same time, which e.g. is $1.46\,M_\odot$ for the $20\,M_\odot$ model 150 ms after the shock launch. Second, all of our models do not explode and thus no explosion related *mass–cutoff* can be found. The question if the supra–density phase has influence on the mass of an isolated neutron star (i.e. after the explosion happened) can thus not be answered with these models.

3.3.1. Summary

From the simulations presented in this Section we conclude that the — unknown — supra–nuclear density phase (strongly) influences the supernova evolution in spherically symmetric models. A supra–nuclear phase that softens the EoS will lead to a denser and smaller proto neutron star and higher neutrino luminosities, energies, and thus more neutrino heating of matter.

[6]Here, to be precise, the term “mass” means baryonic mass. Differences in the neutrino luminosities can lead to different gravitational masses.

However, the supra–nuclear phase will be only important if the a sizeable fraction of the dense core enters this regime. This depends both on the mass of the progenitor and on the stiffness of the EoS below saturation density. For example in case of stiff Wolff–EoS almost no matter was compressed to supra–nuclear densities but instead almost all of the neutron star matter was not able to overcome the "incompressible wall" at densities below saturation density. In case of the softer L&S–EoS this was not the case; the simulations showed a strong dependence on the supra–nuclear phase of matter *and* the mass of the progenitor model. Our results imply that in an extreme case for a certain progenitor mass range the supra–nuclear phase either triggers or prevents the collapse to black hole which might be of strong influence for the collapsar model of gamma ray bursts (see, e.g. MacFadyen & Woosley 1998). A more detailed study, which could not be conducted in this thesis, with a larger sequence of progenitor models and different values of a would thus be very helpful in order to understand the importance of the supra–nuclear phase of the EoS in more detail.

Although our less extreme models did not form a black hole and the changes of the supra–nuclear phase did not cause qualitative different results in 1D–models, these changes might be of great importance in multi–dimensional simulations. Depending on the progenitors mass the supra–nuclear EoS produces either faster or slower contracting cores if the EoS becomes softer or stiffer. This might be of large importance for multi–dimensional supernova calculations: as Scheck (2006) found the development of a $l = 1$ shock instability and the thereby caused explosion is favoured by a faster shrinking neutron star. The reason for this is that a faster contracting neutron star produces, by conversion of potential energy, higher neutrino luminosities and energies , which then also increases the neutrino heating. In the models by Scheck (2006) this contraction of the dense core was given by a chosen boundary condition *but* it could as well be explained by a softening of the EoS at high densities. It is thus important to also examine the consequences of a phase transition in the EoS in multi–dimensional simulations that allow convection and low modes shock instabilities to occur. However, due to lack of computer time, this ansatz could not be followed in this thesis.

3.4. Expansion of the Wolff-EoS to low densities: the importance of the density regime below 10^{10} g/cm^3

A considerable shortcoming of the runs with the Wolff–EoS which were discussed in the previous sections is that the Wolff–EoS is not tabulated for densities below 10^9 g/cm^3. Therefore, we switched to our low–density EoS at already this high density compared to the switch at a density of 6×10^7 g/cm^3 in case of the L&S–EoS. On the other hand, it is reported (Lattimer, Fryer, personal communication) that the L&S–EoS does produce a wrong number of alpha particles for some thermodynamical combinations of the temperature T and the electron fraction Y_e for densities lower than 10^{11} g/cm^3, and that this may cause a qualitative difference of the simulations[7]. Therefore, in this Section we will discuss whether the above mentioned shortcomings of the Wolff and the L&S–EoS do influence the results of our simulations. For this purpose

[7]Therefore, as already mentioned in Section 3.2, we normally do not apply the L&S–EoS for densities below 10^{11} g/cm^3.

we apply an extension of the Wolff–EoS table (from hereon called Wolff–lowden–EoS) which is tabulated for densities between 10^{10} g/cm^3 and 10^7 g/cm^3. In case of calculations with the Wolff–EoS, we apply this low–density EoS for the density range below 10^9 g/cm^3 and are thus able to determine whether relative high density value of the lower boundary in the Wolff–EoS causes any problems in our simulations.

For the runs with the L&S–EoS, we apply this Wolff–lowden–EoS for densities below 10^{11} g/cm^{3}and are thus able to exclude a large fraction of the L&S–EoS where the number fractions of alpha particles are wrong. Additionally, to model L&S(io)slms, which was introduced in Section 3.2, where we switched in the postbounce evolution from the L&S–EoS to our 17–species "low–density" EoS for densities lower than 10^{11} g/cm^3 (see Section 3.2). We have calculated the postbounce evolution of two more models: On the one hand model L&S(io)slms–pur, where the collapse phase was computed purely with the L&S–EoS for densities larger than 6×10^7 g/cm^3. On the other hand we also computed a model L&S(io)slms–4, where we replaced our 17 species "low–density" EoS with a four species "low–density" EoS.

Altogether, these runs allow us to judge the importance of the wrong alpha–particle mass fractions in the L&S–EoS for our numerical results.

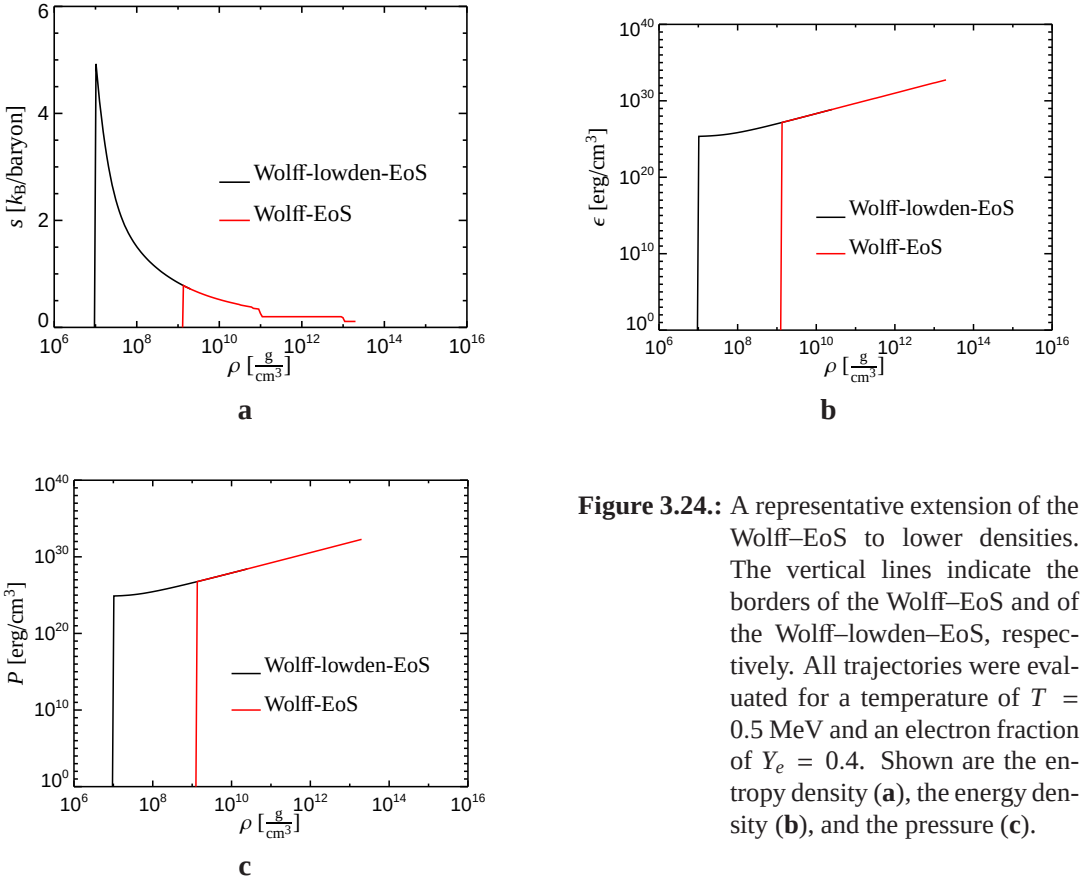

Figure 3.24.: A representative extension of the Wolff–EoS to lower densities. The vertical lines indicate the borders of the Wolff–EoS and of the Wolff–lowden–EoS, respectively. All trajectories were evaluated for a temperature of T = 0.5 MeV and an electron fraction of Y_e = 0.4. Shown are the entropy density (**a**), the energy density (**b**), and the pressure (**c**).

In Fig. 3.24 we show representative examples for the extension of the Wolff–EoS to lower densities for the energy density, pressure, and entropy for a constant value of the electron frac-

tion and temperature.

3.4.1. The density regime below 10^9 g/cm^3 in the Wolff–EoS runs

We have simulated the collapse and postbounce phase of a model (model Wolff(io)slms–low) that uses the Wolff–lowden–EoS for densities between 10^9 g/cm^3 and 10^7 g/cm^3 but has otherwise the same micro–physics and numerical treatment as the model Wolff(io)slms, which is discussed in Section 3.2.

During the collapse phase only minor quantitative differences occur: since model Wolff(io)slms–low collapses faster ($\approx$ 250ms) than model Wolff(io)slms ($\approx$ 350ms), see Fig. 3.25a, but while the same implementation of electron capture rates is used, less time for electron capture is available and thus the central electron and lepton fraction stays slightly higher in the model Wolff(io)slms–low, see Fig. 3.25b. Though this difference is small it is of the same order than the observed differences between the different EoS–runs, which are discussed in Section 3.2 (cf. Fig. 3.7). Consequently, the shocks form at slightly different mass-coordinates ($\Delta M \approx 0.02\,\mathrm{M}_\odot$).

These difference obviously originate in the density regime between 10^9 g/cm^3 and 10^7 g/cm^3, since nothing else is different in the models and the reason is a technically one: the new electron capture rates of Langanke et al. (2003) are only tabulated for densities above 10^8g/cm^3. Furthermore, for technical reasons (cf. Appendix A.3.1), these rates are only evaluated for the "high–density" NSE–EoS. Thus in model Wolff(io)slms in a small density window (10^8g/cm^3 < ρ < 10^9g/cm^3) instead of the new rates of Langanke et al. (2003) the description of Bruenn (1985) was used, whereas in model Wolff(io)slms–low the new rates were used also in this density window. This resulted in more electron captures in this density range and thus reduced the collapse timescale.

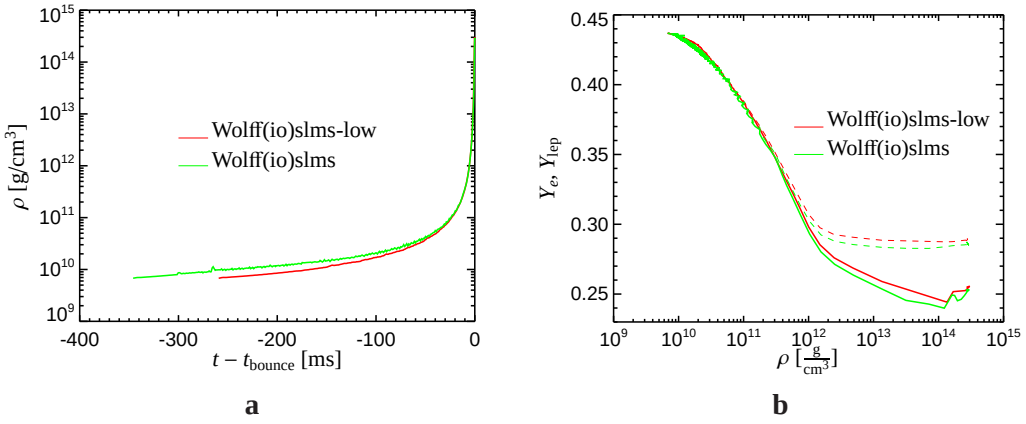

Figure 3.25.: a: The central density during the collapse as function of time. Note that the time is normalised to the moment of shock formation. **b**: The central electron fraction (solid) and lepton fraction (dashed) as function of central density.

The postbounce evolution is qualitative the same, except for small, transient differences are visible, see Fig. 3.26. As was already discussed in Section 3.2, the shock radius in the ac-

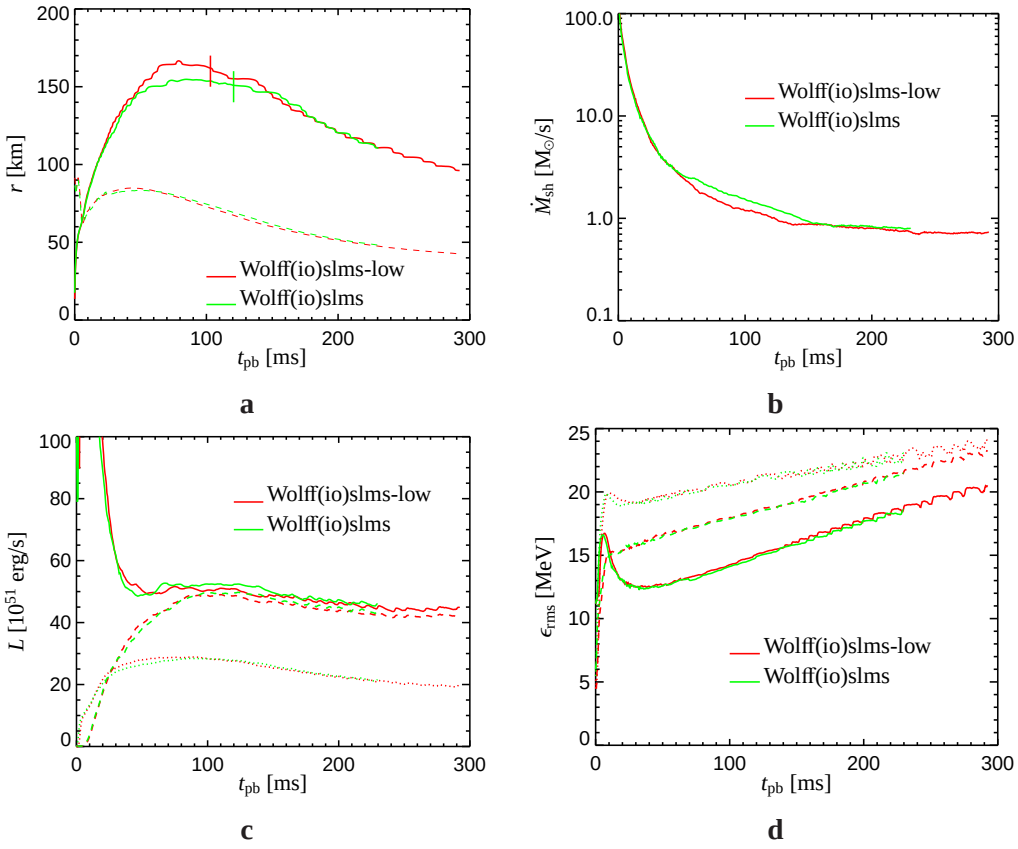

Figure 3.26.: A comparison between models Wolff(io)slms and Wolff(io)slms–low. **a**: the positions of the shock front (solid) and of the electron neutrinosphere (dashed) as function of time. The vertical lines indicate the time when the mass shell corresponding to 1.5 $M_\odot$ reaches the shock front. **b**: The mass accretion rate through the shock front as function of time. **c**: The luminosity of electron neutrinos (solid), of anti–electron neutrinos (dashed) and heavy lepton (anti) neutrinos (dotted). **d**: The rms neutrino energy. The linestyles are chosen identical to the ones used in panel c.

cretion phase is a function of the proto–neutron star mass and radius, and of the mass accretion rate through the shock front (cf. Eqn. 3.7). As one can see in Fig. 3.26b for a time interval of roughly 100 ms model Wolff(io)slms–low shows a smaller mass accretion rate than model Wolff(io)slms. This leads immediately to a faster shock expansion, which is seen in Fig. 3.26a. The mass accretion rate becomes lower, since model Wolff(io)slms–low collapses faster ($\Delta t \approx 100$ ms) and therefore mass shells with lower density reach the shock front earlier. This is depicted by the vertical lines in Fig. 3.26a that indicated the time when the mass shell corresponding to 1.5 $M_\odot$ reaches the shock front. When the mass accretion rates become again nearly equal the shock fronts adjust to the same positions. The transient nature of the drop in the mass accretion rate is caused during the collapse phase, where the mass shells that resided

at the start of the simulation in the regime of the Wolff–lowden–EoS (i.e. at densities between 10^9 g/cm^3 and 10^7 g/cm^3) collapsed faster. As one can see in Fig. 3.26c the different mass accretion rates also cause slightly different neutrino luminosities, since as already explained in Section 3.2, stronger mass accretion leads to more release of gravitational binding energy that can be radiated away in neutrinos. Together with the other differences this transient disappears when the mass accretion rates become identical.

We thus conclude this discussion by stating that the EoS in the density range between 10^9 g/cm^3 and 10^7 g/cm^3 can influence the collapse of a stellar model. Furthermore, the details of the collapse history determine at which time which mass shell passes through the shock front, which can have some effect on the shock expansion. However, these effects are small and therefore do not make a qualitative differences in our simulations. Thus the central question if an early transition at density of 10^9 g/cm^3 between the Wolff–EoS and a low–density EoS did strongly influence our numerical results has to be answered for two different regimes:

We find that the collapse phase (regime I) is indeed influenced by the choice of the EoS in the density regime below 10^9 g/cm^3, and the differences are comparable to the differences we found in Section 3.2 where we used in collapse simulations three different EoSs for the densities larger 6×10^7 g/cm^3 . It is highly probable that all results of the collapse phase which are linked to the collapse timescale are indeed set by the EoS differences in the density regime below 10^{11} g/cm^3 and it is thus not astonishing that the differences we find here are comparable to the differences that were discussed in Section 3.2.

The postbounce phase (regime II), however, shows only small, transient differences for the extension of the Wolff–EoS to low densities, which dissappear when the different "collapse histories" are advected through the shock front. Thus, these transient features can be linked back to the collapse phase of the simulations. Furthermore, these differences are small compared to the ones we found in Sections 3.2 and 3.3 where we showed that the high density ($\rho > 10^{11}$ g/cm^3 or supra nuclear EoS ($\rho > 10^{14}$ g/cm^3) has a large effect on the postbounce evolution. Thus in the postbounce phase the low–density EoS plays a minor role.

3.4.2. The L&S–EoS below 10^{10} g/cm^3

In the previous subsection we showed that the choice of the EoS at densities below 10^9 g/cm^3 has only minor influence on the supernova evolution for runs with the Wolff–EoS. In this paragraph we will address the wrong number fractions of alpha particles in the L&S–EoS (see also Section 3.2). In a first step we will discuss model L&S(io)slms–low–pb, which was started at the moment of shock launch from the *same* collapse model as model L&S(io)slms, which was already discussed in Section 3.2. The difference between the models L&S(io)slms and L&S(io)slms–low–pb is that for densities between 10^{10} g/cm^3 and 10^7 g/cm^3 the Wolff–lowden–EoS table was used. This approach allows us to investigate this density regime in the postbounce phase without comparing models that have a different collapse history which "contaminates" the postbounce phase, as was shown in the previous paragraph. Afterwards, in a second step, we will re-investigate this issue with a "consistent" model where even in the collapse phase the low–density version of the Wolff–EoS was used.

Figure 3.27a shows the shock trajectories and the radii of the nascent neutron stars for models L&S(io)slms and L&S(io)slms–low–pb. The latter model shows a slightly larger shock radius,

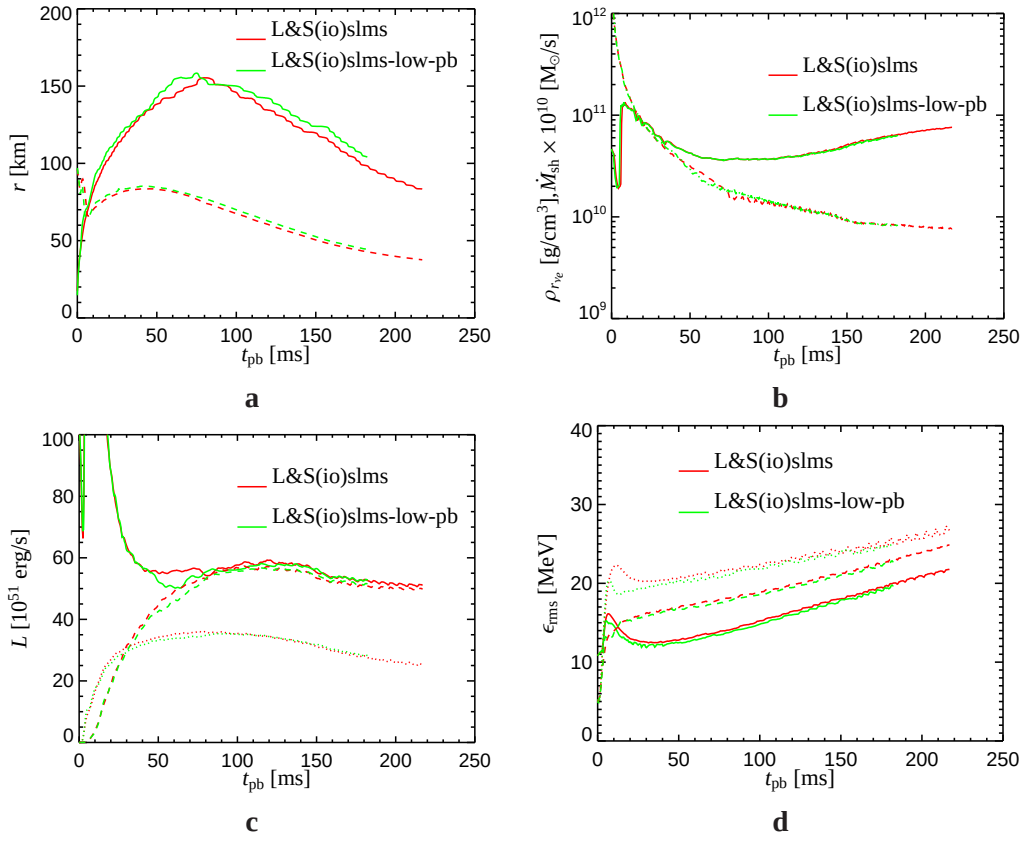

Figure 3.27.: A comparison between models L&S(io)slms and L&S(io)slms–low–pb. **a**: the positions of the shock front (solid) and of the electron neutrinosphere (dashed) as function of time.**b**: the density at which the neutrinosphere resides (solid) and the mass accretion rate through the shock front (dashed). Note that the accretion rate was multiplied by 10^{10} in order to be on the same scale. **c**: the luminosity of electron neutrinos (solid), of anti–electron neutrinos (dashed) and heavy lepton (anti) neutrinos (dotted). **d**: the rms neutrino energy. The linestyles are chosen identical to the ones used in panel c.

which is due to a combination of two facts: Firstly, the mass accretion rate in this model is slightly lower for a time between 50 ms and 70 ms after the shock launch[8], see Fig. 3.27b. As it was already discussed several times, this causes the rapid shock expansion in the same time interval. Secondly, at later times the shock radius stays larger, since the neutron star radius is slightly larger (see the discussion in Section 3.2, Eqn. 3.7). It is important to realise that the larger neutron star radius is not a direct effect of the EoS below densities of 10^{10} g/cm^3, since the neutrinosphere resides for all times at density around $2 - 3 \times 10^{10}$ g/cm^3 . This can also be seen in Fig. 3.27b. The larger neutrino sphere radius, however, is an hydrostatic adjustment to

[8]This change in the mass accretion rate is a result from the "inconsistent" treatment that we interchanged a part of the L&S–EoS to the Wolff–lowden–EoS

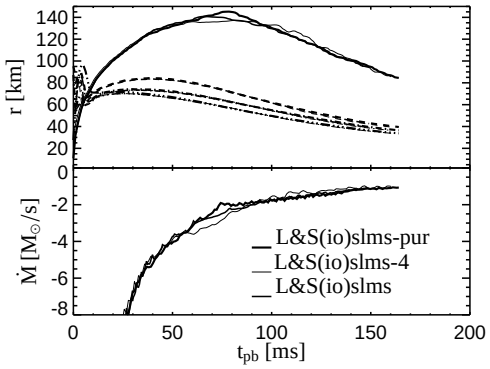

Figure 3.28.: Upper panel: The shock trajectories (solid lines) as function of time for models where different EoS were used for densities below 10^{11} g/cm^3. Also shown are the electron neutrinospheres (dashed), the anti–electron neutrinospheres are (dashed–dotted), and the heavy (anti) lepton neutrinospheres (dashed-several-dots). Lower panel: The mass accretion rate through the shock front for the models.

the changed conditions in the accretion atmosphere between the shock front and the neutron star which are influenced by the EoS. This adjustment takes place immediately after we switched to the Wolff–lowden–EoS which gives a strong hint that this switch was too abrupt. However, this even enhances the predictability of this test model, since even this sudden and extreme change in the conditions did not lead to very different results compared to model L&S(io)slms.

Smaller changes are also visible in the neutrino luminosities and rms energies, see Fig. 3.27c–d. These changes, however, are only shown for completeness since they are so small.

Finally, we want to discuss model L&S(io)slms–low which was calculated with the use of the Wolff–lowden–EoS even in the collapse phase. Except for this change in the collapse simulation, the same micro–physics was used as in model L&S(io)slms–low–pb. This model is thought to complete the discussion of the importance of the density range below 10^{10} g/cm^3 in the L&S–EoS. Using the Wolff–lowden–EoS in a collapse simulation together with the L&S–EoS leads to a slightly prolonged collapse (250 ms instead of 208 ms). This delay happens, as we have already discussed in Section 3.2, until a central density of 10^{11} g/cm^3 is reached (this takes 190 ms and 232 ms, respectively) and the core collapses very fast to nuclear saturation density. In this early phase, model L&S(io)slms–low experiences stronger deleptonisation, as is visible in Fig. 3.29a, which results in a stronger deleptonisation (by two percent) at the end of the collapse. This change is again comparable with the values found in Section 3.2 for simulations with three different EoSs. Thus, again, we find that the collapse time and the deleptonisation are sensitive functions of the EoS–physics for densities below 10^{11} g/cm^3.

The postbounce evolution in models L&S(io)slms and L&S(io)slms–low is again very similar: the maximum shock positions are the same and the rate of shock decline is practical identical, see Fig. 3.29b. Only for a short time interval the shock trajectories move asynchronously, which is again caused by different mass accretion rates through the shock front at these times, see Fig. 3.29c. This transient different mass accretion rate is again a result of the different collapse history. However, a comparison between models L&S(io)slms–low and L&S(io)slms–low–pb reveals an interesting fact: the "inconsistent" model L&S(io)slms–low–pb shows a larger nascent neutron star than model L&S(io)slms–low (or model L&S(io)slms), see Figs. 3.29b and 3.27a. As already mentioned this expanding neutron star is caused by the sudden switch to

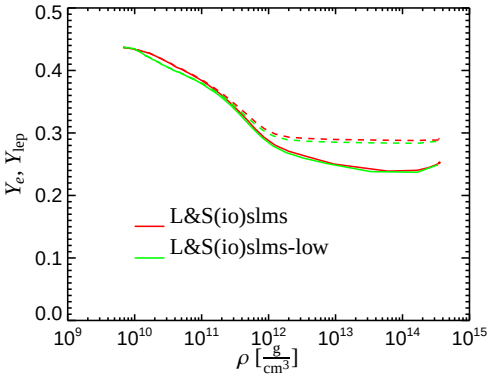

a

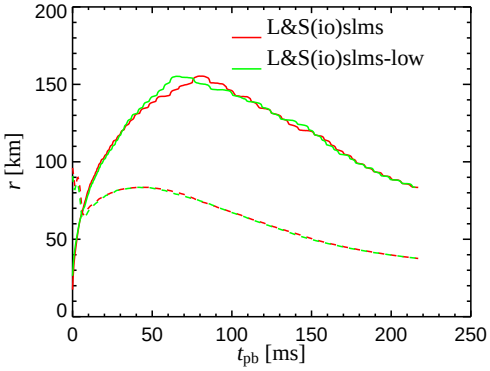

b

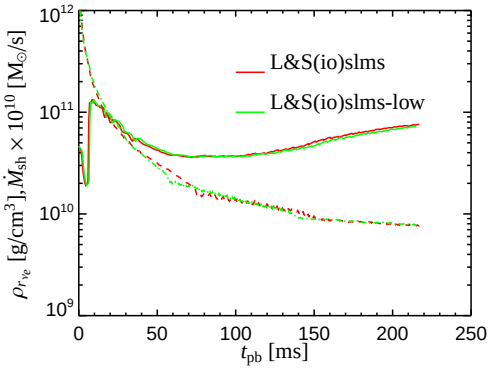

c

Figure 3.29.: The central electron fraction (solid) and lepton fraction (dashed) as function of central density during the collapse for the models L&S(io)slms and L&S(io)slms–low.

another EoS, and is obviously not visible if the EoS setup is not changed during the simulation.

Last, we show in Fig. 3.28, for models L&S(io)slms–pur, L&S(io)slms–4, and L&S(io)slms, the shock trajectories as function of time and the mass accretion rate through the shock front. Clearly, in our calculation of a $15\,M_\odot$ star the "bug" in the L&S–EoS does not influence the supernova evolution: The shock trajectories are qualitatively and quantitatively very similar, except for some transient features where the mass accretion rates are different, which was already seen in the simulations discussed in the previous paragraph.

To summarise this discussion, we conclude that in our calculations the wrong number fraction of alpha particles in the L&S–EoS does not influence the supernova evolution. We obtain similar results, independent of the details of the EoS used for densities below $10^{11}\,\mathrm{g/cm^3}$. Thus, we have learned from the simulations with the L&S–EoS *and* the Wolff–EoS that the details of the EoS for densities below $10^{11}\,\mathrm{g/cm^3}$ only slightly influences the postbounce evolution by changing the mass accretion flow through the shock front. However, the collapse phase is more strongly dependent on the EoS in this regime. The collapse time and the final deleptonisation are strongly determined by the early phase of the collapse until a central density of roughly $10^{11}\,\mathrm{g/cm^3}$ is reached. Of course a different deleptonisation (i.e. different total values of electron captures) may have an influence on the neutrino emission and the structure of the forming neutron star on longer timescales than investigated in this study. Nevertheless, we conclude that — at least for the simulation times regarded here — these different collapse histories hardly influence the postbounce evolution in our models.

3.5. Longtime runs: two parametrised explosion models

In the previous sections the influence of the EoS on the evolution of core collapse supernovae was discussed. Especially the (small) dense core, whose properties are set by the "high–density" EoS ($\rho > 10^{11-12}\,\mathrm{g/cm^3}$), shows a large feedback on the shock propagation at larger radii and densities around $10^8\,\mathrm{g/cm^3}$. Nevertheless, simply because our spherically symmetric calculations do not yield an explosion, the discussions from the previous sections does not allow to investigate the influence of the EoS on the supernova phase when actually the explosion starts. Also it was yet not possible to investigate the influence after the onset of the explosion when a neutrino–driven wind sets in. But, of course, it is interesting to know, how the EoS influences this phase, and how the neutrino emission from the left–behind proto–neutron star looks like.

However, this goal is hampered by the fact that supernova calculations still do not routinely show successful explosions.

On the one hand modern *spherically symmetric* simulations of core collapse supernova agree in two facts:

- the prompt shock mechanism for core collapse supernovae does not work, see Bethe (1990).
- except for very low mass progenitors ($M \approx 9\,M_\odot$, Kitaura et al. 2006) the delayed neutrino heating mechanism does not work [9]

[9] Note that this statement is not (necessarily) true for multi-dimensional simulations, see e.g. the discussion in Section 4.2 and Buras et al. (2006a).

On the other hand, modern *multi–dimensional* simulations of core collapse supernovae do (sometimes) show explosions (see, e.g. Buras et al. 2006b). However, these simulations are computationally so expensive that they cannot be calculated to such late times necessary to investigate the neutrino emission from the "remnant" proto–neutron star.

Therefore, we artificially triggered the explosion in (computationally cheap) spherically symmetric simulations, in order to investigate these longtime EoS effects during a supernova explosion[10].

As was already mentioned in Section 3.2 spherically symmetric simulations do not explode, since matter is not heated strong enough to revive the shock front. This can be explained by the ratio of the advection timescale and the heating timescale (cf. Eqn. 3.2): normally in spherically symmetric simulations fluid elements are accreted too fast through the gain region in order to be heated substantially to trigger a delayed explosion.[11]

The whole idea behind the current supernova explosion paradigm, is that the neutrino heating efficiency must be high enough, in order to trigger a delayed explosion. This explains, why supernova modellers undertake huge efforts to implement as accurate as possible neutrino–matter–interaction rates (which are responsible for the heating, but also cooling) in core collapse supernova codes. However, remembering Fig. 3.15, we find that roughly a 2 times shorter heating timescale (i.e. a 2 times higher heating rate) would be needed for a delayed explosion in spherically symmetric simulations of a $15\,M_\odot$ star. This by itself tells us, that either the current supernova codes calculate the neutrino heating wrong by *factors of 2*, or — which is more likely — other physical processes such as convection, or rotation, or possibly magnetic fields have to be taken into account in multi–dimensional simulations.

Nevertheless, by increasing the heating rate (i.e. reducing the heating timescale) a explosion can be launched in 1D–simulations. We have simulated such artificially explosions for a $20\,M_\odot$ progenitor model with the L&S and Wolff–EoS, respectively, by increasing the neutrino heating rate by an artifically chosen multiplicative heating increase δQ, see Table 3.2. Note, that this approach of course is not conservative, but instead energy is artifically fed into the heating region, however, with this approach we can investigate several issues:

Firstly, these artificially triggered explosions allow us to check by which amount the heating efficiency must rise in order to produce delayed explosions in spherically symmetric simulations. This value of δQ can than be interpreted as upper bound for multi–dimensional simulations, since turbulent flows allow matter to stay longer in the heating region and this by itself increases the heating efficiency compared to 1D–models. Note, that this study is *not* meant (and does not allow) to imply anything on the supernova explosion mechanism itself (i.e. how this increased heating efficiency can be accomplished in a self–consistent manner by the inclusion of different physical aspects).

Secondly, these explosions allow us to study the importance of the EoS on the properties of emitted neutrinos (i.e. luminosities, mean energies and spectra) from the "naked" proto–neutron star. This means that during the explosion a mass cutoff is achieved and an isolated proto–

[10] The role of the EoS in multi–dimensional simulations will be investigated in Part II of this thesis.

[11] Multi–dimensional simulations can circumvent this problem by the additional degrees of freedom, which allow the fluid (e.g. by convective motion) to stay longer in the heating region, but as we will see in Part II this is not necessarily the case.

neutron star forms which cools by neutrino emission. In non–exploding models this neutrino emission is dwarfed by the accretion luminosities (i.e. redistribution of gravitational binding energy into neutrino flux) of the accreted matter and the neutrino emission of the proto–neutron is practically invisible, whereas in an explosion the emission from the neutron star is visible. As was already shown in Section 3.2 the EoS determines the structure and temperature of the nascent neutrons star and thus also influences the properties of the neutrinos radiated from the dense core. As mentioned we have triggered these explosions by artificially increasing the neutrino heating in the heating region by a chosen factor δQ. However, there is also another degree of freedom is the time when this increase becomes effective and the explosion sets in. For two reasons we have chosen a rather late time of roughly 200 ms:

- Firstly, we want the supernova evolution to be well in the accretion phase but we do not want to trigger the explosion at the moment when the Si−O interface passes the shock front and the shock reaches its maximum position (see e.g. Fig. 3.30). This simply represents the careful point of view that though the necessary value of δQ to trigger the explosion might be smaller at the moment of maximum shock expansion, we did not want to constrain the upper bounds of δQ on a case that would require extreme fine tuning.[12]

- Secondly, since we want to look at the neutrino emission of the "naked" nascent neutron star we want the neutron star to be in agreement with observed neutron stars. This implies that after the mass cut the proto–neutron star should have a mass around $1.4\,M_\odot$, see Lattimer & Prakash (2004) , which implies that the explosion must set in late enough for such a dense core to form.

In Table 3.2 we summarise for our models the value of the increased heating δQ, the time when this modification was applied, and the value of the final mass and radius of the neutron star that we determined at the end of our calculations.

In Figure 3.30 we show the shock trajectories, the radii of the nascent neutron stars (as defined by its neutrinosphere), the neutrino luminosities, and the ratio of the advection and heating time scales for our non–exploding calculations of the $20\,M_\odot$ progenitor with the L&S and the Wolff–EoS. The differences caused by the EoS are clearly visible and are qualitative very similar to the ones that were already discussed in Section 3.2 for a $15\,M_\odot$ progenitor model. It is also apparent that increasing the heating efficiency at the moment of maximum shock expansion would lead to the largest effects since the ratio of the advection and heating timescales becomes largest at this moment. However, as we have discussed above this was not the approach we wanted take in this numerical study.

Figure 3.31 depicts the same quantities for the models calculated with the Wolff–EoS and artifically increased heating rate. It is interesting to note that an increase of the neutrino heating by a factor of $\delta Q = 2$ at a late time does not lead to qualitative changes of the supernova evolution, since the ratio of the characteristic timescales is well below unity. However, a three times stronger neutrino heating does trigger an explosion in these spherically symmetric models, and an even stronger heating ($\delta Q = 5$) does not strongly change the morphology — except for

[12] However, note that this is not correct if the heating efficiency is increased by some (speculative) feedback mechanism when the composition interface reaches the shock front.

Model name	Increase in heating rate	EoS	t_{start} [ms]	M_{NS} [$\mathrm{M}_\odot$]	$r_{\mathrm{NS}}[km]$	t_{stop} [ms]
W20–0	no increase	Wolff	205	1.51	37.8	330
W20–2	2 times	Wolff	205	1.52	36.7	380
W20–3	3 times	Wolff	205	1.56	26.4	890
W20–5	5 times	Wolff	205	1.55	27.9	740
LS20–0	no increase	L&S	214	1.51	28.1	340
LS20–3	3 times	L&S	214	1.54	24.8	470
LS20–4	4 times	L&S	214	1.53	21.2	750

Table 3.2.: Overview over the models calculated with a $20\,\mathrm{M}_\odot$ progenitor star that where artifically exploded by increasing the heating rate by a chosen factor. Shown are the values for this increase, the used EoS, the time when this increase was triggered, and the mass and radius of the neutron star at the time the simulation was stopped. Note that all times are normalised to the moment of shock formation.

Model name	Increase in heating rate	EoS	t_{com} [ms]	M_{NS} [$\mathrm{M}_\odot$]	$r_{\mathrm{NS}}[km]$
W20–3	3 times	Wolff	740	1.56	27.9
W20–5	5 times	Wolff	740	1.55	27.9
LS20–4	4 times	L&S	740	1.53	21.2

Table 3.3.: For the exploding models form Table 3.2 a comparison at a time of 740 ms after the shock formation. Shown are the masses and radii of the neutron stars at this time.

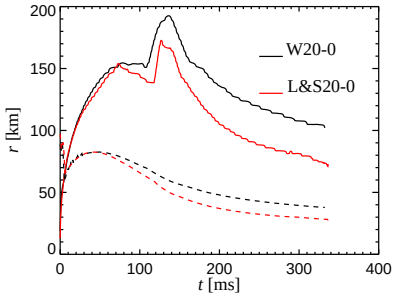

a

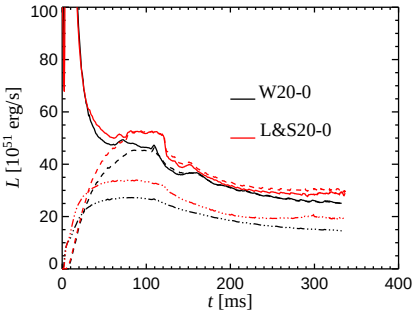

b

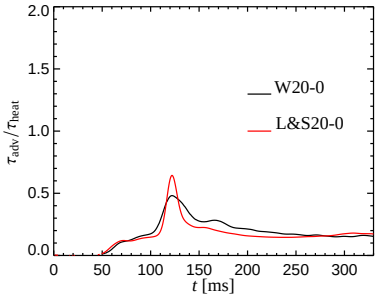

c

Figure 3.30.: **a**: The shock position (solid) as function of time in the for models W20–0 and L&S20–0. The position of the electron neutrinospheres are shown as dashed lines. **b**: The luminosity of electron neutrinos (solid), anti–electron neutrinos (dashed), and heavy (anti) lepton neutrinos (dashed–dotted).**c**: The ratio of the advection timescale and the heating timescale for both models.

a slightly faster onset of the explosion — of the explosion. It is also obvious from Fig. 3.31 that we find some “oscillatory behaviour” in the exploding models: the shock expands and retreats before the final expansion, the ratio of the heating and advection timescale also oscillates, as does the neutrino luminosity. The same behaviour — but in a non–exploding model — was reported by Buras et al. (2006b), where the authors found that a shock expansion reduces the mass accretion and thus the conversion of energy into neutrino luminosity. Thus, in turn, the heating drops, which leads to a shock retreat and, completing the cycle, the mass accretion and neutrino heating rises again. Interestingly, both models W20–3 and W20–5 show this behaviour after a period of constant shock expansion when roughly a radius of 400 km is reached. This implies that at this time the heating is not strong enough to cause a further shock expansion, but this oscillatory behaviour sets in, and after some time the heating becomes strong enough to finally cause the explosion.

An overview over the models which were calculated with the L&S–EoS is given in Fig. 3.32. Here an interesting difference to the models with the Wolff–EoS becomes visible: whereas model W20–3 with an increase of the heating rate by a factor of three already showed a convincing explosion, the corresponding model L&S20–3 did marginally not explode. This can be deduced from the shock position (Fig. 3.32a) and from the value of the timescales which is near

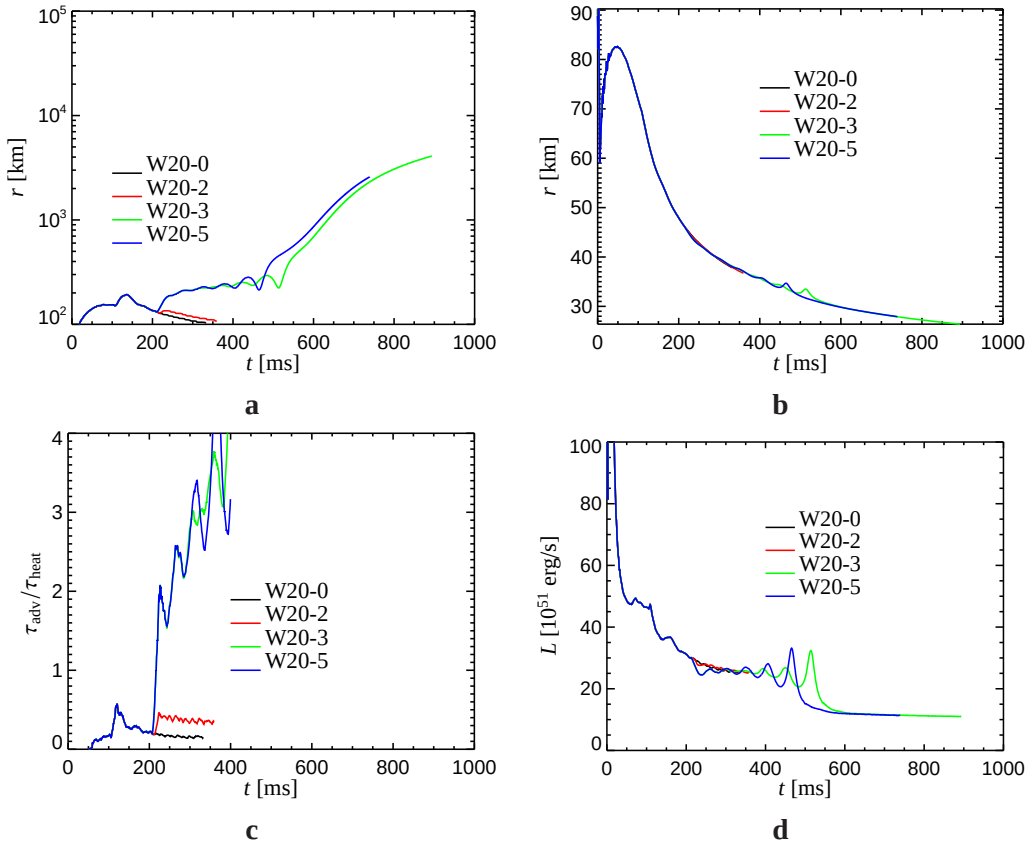

Figure 3.31.: **a**: The shock position as function of time for models that were calculated with the Wolff–EoS and artifically increased neutrino heating. **b**: The radius of the nascent neutron star (defined at the neutrinosphere for electron neutrinos) as function of time. As expected, artificially stronger heating does not influence the neutron star since the heating was increased in outside of the dense core. **c**: The ratio of the advection and heating timescales. **d**: The luminosity for electron neutrinos measured at a radius of 400 km. Note that the oscillations visible in this plot, stem from a feedback cycle between the mass accretion rate and the accretion luminosity (see text).

unity (Fig. 3.32d).[13] This is consistent with the discussion of Section 3.2 where it was already shown that both the heating and advection timescales are quantities that are sensitive to the used EoS. One reasons for this is that the advection timescale naturally depends on the distance between the shock position and the neutron star, which in turn are both strongly influenced by the EoS. Furthermore, this model does not show any oscillatory features, quite in the contrary, the shock is expanding constantly once the heating was increased. This implies that depend-

[13] It is possible that this model would explode at a later time, since a trend that the timescale ratio increases can be extrapolated from Fig. 3.32d.

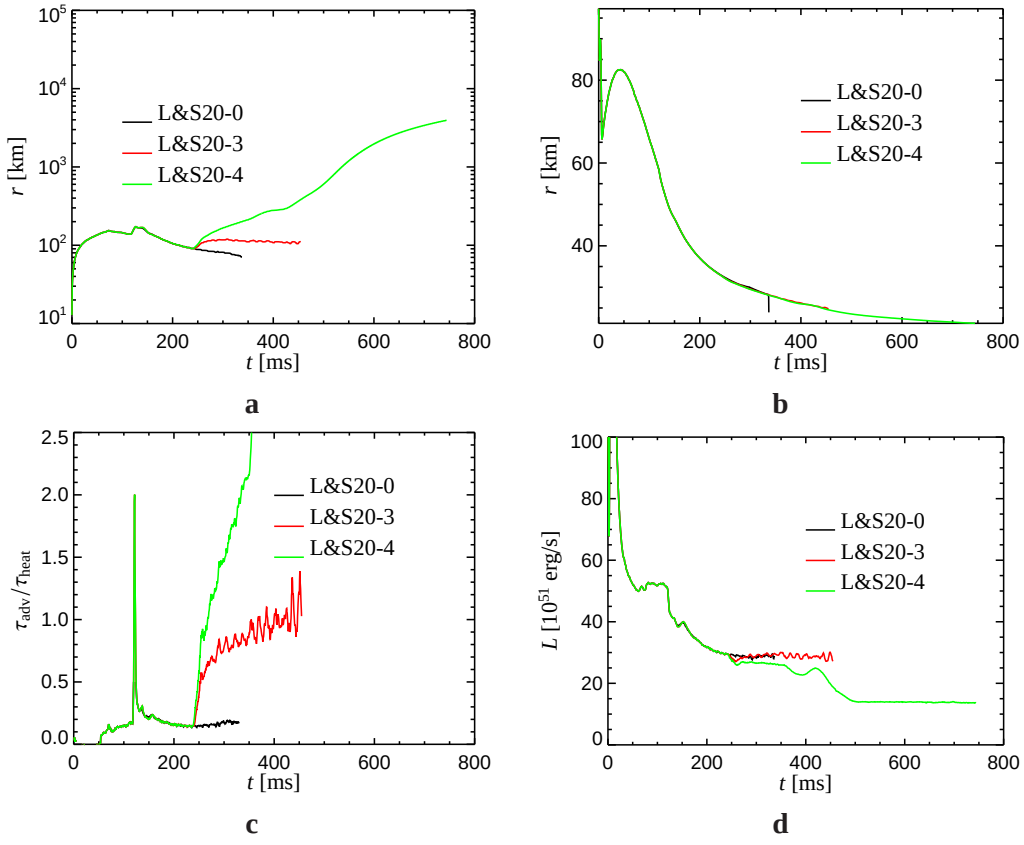

Figure 3.32.: **a**: The shock position as function of time for the L&S–EoS. **b**: The radius of the nascent neutron star (defined at the neutrinosphere for electron neutrinos) as function of time. **c**: The ratio of the advection and heating timescales Note that the jump of this ratio at a time of roughly 100ms is in coincidence with the very fast shock expansion when a composition interface reaches the shock front (see panel a). Note also that model L&S20–3 is marginally not exploding since the ratio is almost above unity. **d**: The luminosity for electron neutrinos measured at a radius of 400 km.

ing on the conditions (EoS, shock position, compactness of the nascent neutron star) and the value of the heating efficiency a "direct" explosion (i.e. immediate shock expansion) or some "lingering phase" (i.e. the effect of heating has to build up to cause a further shock expansion) can be obtained. We thus deduce from these models that in a multi–dimensional simulation a factor of three or four higher heating efficiency would be sufficient to explode this particular $20\,M_\odot$ progenitor model with the Wolff or the L&S–EoS. Furthermore it is expected that the necessary value strongly depends on both the progenitor model and the used EoS.

Finally, we will discuss the properties of the "naked" nascent neutron star, focusing on the neutrino emission of this hot and dense object. But first a short remark on the properties of the neutron star shall be made. In Table 3.3 the masses and radii of the neutron stars are given at

a time of 740 ms after the shock formation. Here we find, as expected that though the masses are roughly equal, the radius is smaller for the softer L&S–EoS, which leads to a compacter neutron star. The reason why the masses inside the dense core are not equal is that the *total* simulation time is different when time is normalised to the shock formation. Thus the models had different time to accrete matter with different (EoS dependent) mass accretion rates, which leads to different masses of the neutron star.

Considering the (EoS dependent) neutrino emission of two isolated neutron stars we will take models W20–3 and L&S20–4 as examples in the following discussion[14].

As one can see in Figs. 3.31d and 3.32d in the exploding models the luminosities drop compared to the non exploding ones. The reason for this is that the mass accretion onto the core continously decreases and finally completely vanishes when the mass cut is reached, consequently the luminosity reaches a constant level.

Figure 3.33a shows the neutrino luminosity for all neutrino species measured at 50 km as function of time for the models W20–3 and L&S20–4. Obviously the inner core of model with the L&S–EoS always emits higher luminosities than the model with the Wolff–EoS; this amounts to roughly 30% higher luminosities for heavy lepton neutrinos at a time of 700 ms. It is also interesting to note that for some time, as long as the oscillations of the luminosity in model W20–3 are visible, the luminosities for electron and anti–electron neutrinos are equal in this model. The corresponding neutrino energies, are shown in Fig. 3.33b, where again the model with the L&S–EoS emits more energetic neutrinos, however the difference amounts only up to 14%. Consistent with the rms neutrino energies the neutrino spectra for model L&S–4 are broader and show their peak at slightly higher energies, see Fig. 3.34. The results of these simulation clearly show that even after the explosion is happening the equation of state for the dense core still influences the supernova evolution. It is extremely interesting that different EoSs predict different neutrino luminosities and spectra, both in the burst signal (cf. Fig.3.13), and in the neutron star emission during the explosion. Neutrinos are, except for gravitational waves, the only observables that can reveal physical details about the deep interior of the supernova. Naturally, the question arrises whether neutrino signals measured in current or future neutrino detectors allow predictions of the EoS of the dense core. The difference we found in the burst signal in Section 3.2 are too small for such an attempt, see Kachelrieß et al. (2005). However, it will be subject to a future study to answer the question whether or not current neutrino detectors are able to discriminate between our “predictions” of the *late time* neutrino emission during the supernova explosion.

Nevertheless, we conclude that different EoS result in different neutrino properties during the ongoing explosion. Furthermore, different equations of state predict very different contraction laws of the dense core. Though the EoS is poorly known and in this sense this contraction behaviour should be interpreted cautiously, there might be implications on investigations of the neutrino–driven wind and nucleosynthesis, which depend sensitively on the compactness of the neutron star (Arcones et al. 2006).

[14]Of course, for a better comparison it would be useful to recalculate the models with he same amount of artifical heating (e.g. $\delta Q = 4$) and the same explosion time (e.g. $t_{\rm pb} = 214$ ms). However, this will be postponed to a later study.

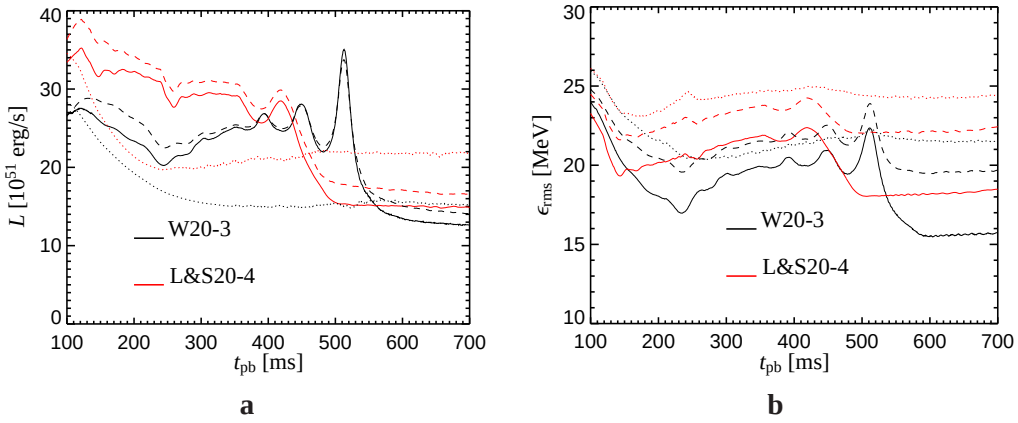

Figure 3.33.: a: The neutrino luminosities measured at 50 km as an static observer would measure them at infinity for the models with the L&S–EoS and Wolff–EoS. Shown are the luminosities of electron neutrinos (solid), anti–electron neutrinos (dashed), and heavy lepton (anti) neutrinos (dotted). **b**: The rms energy for the same models as in panel a. The linestyles are also chosen as in panel a.

3.6. Summary of Part I

In Part I of this thesis we used several spherically symmetric simulations of core collapse supernovae with spectral Boltzmann neutrino transport in order to investigate the importance of the nuclear EoS on the supernova evolution. As explained in the preface to Section 3.2 this study is motivated by the fact that the nuclear EoS is poorly known for the conditions that are encountered during a supernova simulation. Thus the uncertainties of the *structure* of matter (i.e. its constituents and the shape of nuclei) as well as the uncertainties of such fundamental quantities like the pressure are quite large. By investigating how sensitive the evolution of core collapse supernovae really is on different theoretical equations of state, one is able to investigate to what extent the uncertainties of the used EoS change the results of our simulations. Our study of Section 3.2 with three different nuclear equations of state clearly show that the supernova simulations yield quite different results depending on the choice of the EoS; The compactness of the nascent neutron star changes, which directly influences the position of the shock front. Furthermore, also observables as the neutrino luminosities and neutrino energies were found to rely on the applied EoS. These results clearly stress the importance of investigating the physics of core collapse supernova with a focus on the EoS. Since the most difficult and most uncertain part of an EoS is the supra–nuclear regime at densities beyond nuclear saturation (a regime hardly accessible by laboratory measurements) we artifically modified (Section 3.3) existing EoSs in this regime, in order to be able to judge its importance of the already found EoS dependence. The modification that were applied to the EoS were guided by the discussion that matter may undergo a phase transition at these densities at the relation between density and pressure might soften dramatically. We found that this supra–nuclear part of the EoS can become very important for the supernova simulation, if a sizeable fraction of the dense core resides in this high

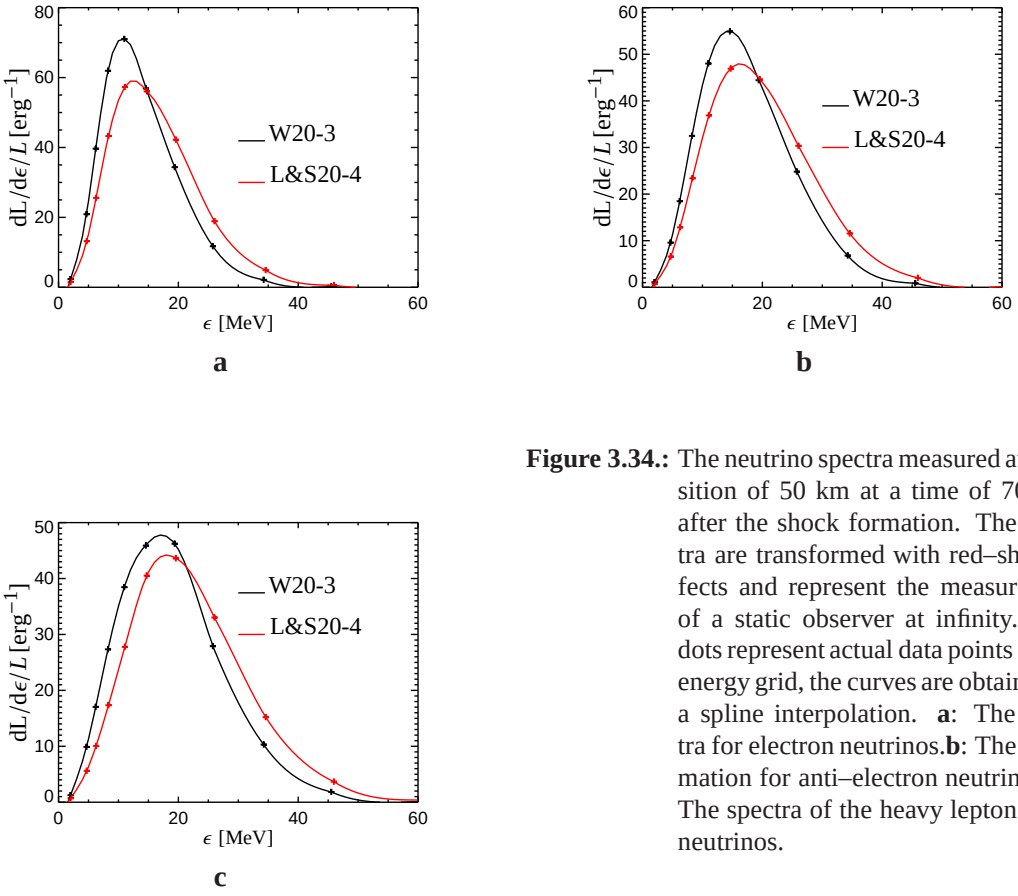

Figure 3.34.: The neutrino spectra measured at a position of 50 km at a time of 700 ms after the shock formation. The spectra are transformed with red–shift effects and represent the measurement of a static observer at infinity. The dots represent actual data points on the energy grid, the curves are obtained by a spline interpolation. **a**: The spectra for electron neutrinos.**b**: The information for anti–electron neutrinos. **c**: The spectra of the heavy lepton (anti) neutrinos.

density regime. We also found a strong progenitor dependence (which reflects the fact that more massive progenitors produce denser cores), where in one case a fast collapse to a very dense core, presumably a black hole, could be observed. Thus, we conclude that the supra–nuclear phase of the EoS is of large importance for the supernova evolution. We furthermore conclude, that observations of core collapse supernovae *and* the masses of their progenitor stars could allow to constrain, by ruling out very soft supra–nuclear phases, the supra–nuclear regime of nuclear EoSs. As Section 3.4 shows, the importance of the "low–density" EoS, turned out to be quite small. We thus conclude, that the differences that were discussed in Section 3.2 where different nuclear EoSs were used are mainly set by the high–density regime of the EoSs.

Since all our implications of the EoS influence on observables like the neutrino luminosities and neutrino energies go back to *non–exploding* models, we artifically triggered the explosion of some models which were calculated with different EoSs, see Section 3.5. Here we found that indeed the dense core that exists in centre of an ongoing explosion emits different neutrinos luminosities, neutrino energies, and spectral distribution of the neutrino flux, if different EoSs are used in the simulations. These results indicate that the observation of the neutrino emission of proto–neutron stars might be useful to infer details of the EoS.

Part II: 2D–simulations

In the following Part II of this study 2D–simulations of core collapse supernovae are addressed. The motivation for doing multi–dimensional (two or three dimensions) simulations of core collapse supernovae is can be summarised : Firstly, there is no reason to believe that stars are perfect spherically symmetric objects neither during the stellar evolution nor in the subsequent supernova phase. For reasons of simplicity spherical symmetry is often assumed, however, even in the pre–collapse phase during stellar evolution local and even global inhomogenities are believed to occur (see, e.g. Bruenn 2005, Young et al. 2005). These inhomegenities during the stellar evolution are caused by convective energy transfer, rotation, magnetic fields, and nucear burning, only to name a few.[15]. Secondly, observations of the non–spherical debris in supernovae remnants as SN 1987a suggest a non–spherical explosion mechanism (see,e.g. Hillebrandt et al. 1989, Arnett et al. 1989, McCray 1993, Nomoto et al. 1994, Wooden 1997, Müller 1998, and references therein). Furthermore, observed fast moving neutron stars that were kicked out of the supernova remnant can be only explained by an anisotropic explosion of the supernova, see e.g. Scheck et al. (2006). Thirdly, it is a long known fact (see,e.g. Herant et al. 1992, 1994, Burrows & Hayes 1995, Janka & Mueller 1994, 1996) that hydrodynamic instabilities such as convective processes have an important influence of the evolution of core collapse supernova simulations. The reason for this is that convection increases the energy transport and supports the heating of matter behind the stalled shock front. Recently, Blondin et al. (2003), Scheck (2006) showed that growing global low mode shock instabilities can trigger supernova explosions.

Hence core collapse supernovae should be treated in multi–dimensional simulations. And of course a 3D–treatment would be favourable. However, at the moment, state of the art simulations which couple hydrodynamics to spectral Boltzmann neutrino transport are restricted to 2D–simulations due to computational costs.[16] Therefore, 2D–simulations are at the moment the only hope to study hydrodynamic instabilities in simulations with Boltzmann neutrino transport. Luckily, there are indications that a 2D–simulation might be quite reliable as (simplified) 3D–simulations of Scheck (2006) show.

In this Part II of the thesis the next natural step is taken and the EoS effects will be discussed for two–dimensional models. It is of special interest whether different EoS trigger different growth of hydrodynamic instabilities in the hot–bubble region and/or inside of the nascent neutron star. As we have seen in Section 3.2 spherically symmetric models give indications that the EoS might influence these instabilities. This Part II is organised as follows: After some introductionary remarks concerning our 2D–simulations in Chapter 4, we will discuss some technical questions regarding these simulations. In Chapter 5 we will then discuss the influence of the EoS on the convection inside the proto–neutron star as well as on the convection in the heating region behind the supernova shock front. Chapter 6 is then dedicated to the influence of rotation on the supernova evolution and the dependence of the supernova explosion mechanism on the mass of the progenitor star.

[15] It should be stressed here that the strength of the deviation from spherical symmetry is still unknown, which introduces another uncertainty in the modelling of core collapse supernovae.

[16] a 3D–simulation of neutrino Boltzmann transport would require roughly 1PFlop of sustained performence on a computer.

Of the Nature of Flatland
I call our world Flatland, not because we call it so, but to make its nature clearer to you, my happy readers, who are privileged to live in Space.

Edwin A. Abbott, Flatland 1884

4
Preface to the 2D–simulations

4.1. Preliminaries

All the 2D–simulations discussed in this work were performed with the M DB TH–code, which is explained in Chapter 2. If not stated otherwise, a 2D–simulation is started from a spherically symmetric (1D) simulation which was mapped to a 2D–run roughly 10ms after the shock formation. During the mapping a random perturbation of the density with an amplitude of one to two percent was applied. As Buras et al. (2006b) showed it makes no difference whether this procedure is applied or whether the model was computed in 2D from the onset of gravitational instability and the perturbations were imposed at that time. We chose the former procedure since a spherically symmetric calculation of the collapse and shock formation phase consumes roughly a factor 100 less computer time than the corresponding 2D run.

By default all 2D–simulations were calculated as an 180° (north to south pole) setup with 192 angular bins which gives an angular resolution of 0.938°. At the pole axis a reflecting boundary condition was applied.

Since we use spherical coordinates in our simulations, angular rays converge towards the centre of our grid and the lateral width of the zone becomes very small, which would reduce the time–step according to the CFL–condition[1]. Thus, in order to save computer time (i.e. use larger timesteps) we calculate the innermost 6 zones (which corresponds to 1.6 km of the whole star) as a 1D spherically symmetric core[2].

If not stated otherwise, the same micro–physical input and relativistic approximations as explained in Section 3.2 were used.

[1] The **C**ourant–**F**riedrichs–**L**ewy condition states that in order to be numerically stable a timestep of the algorithm has to be so small that information does not travel more than one zone within a single timestep.

[2] As we will discuss in Section 5.1.1 this does not destroy any physical process.

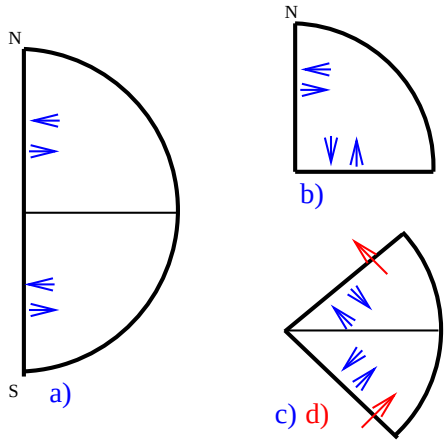

Figure 4.1.: Schematic overview of the setup for the different models. **a:** (model s11.2–180). The blue arrows indicate a reflecting boundary condition at the polar axis. **b:** (model s11.2–90) the upper half was simulated with reflecting boundary conditions at the polar axis and the equator. **c:** (model s11.2-wedge–refl) a 90°-wedge around the equator was simulated. Here also reflecting boundary conditions were applied. **d:** (model s11.2–wedge) a 90°–wedge was calculated. The red arrows indicate the use of periodic boundary conditions.

Our 2D–simulations with spectral Boltzmann neutrino transport are computationally very challenging, and need more that 70000 CPU hours. Needless to say, such a problem has to be solved in parallel on modern supercomputers on a large number of CPUs.

4.2. An exploding model of a 11.2 $M_\odot$ progenitor star: a test case for geometry effects

Buras et al. (2006a) reported two simulations of a 11.2 $M_\odot$ progenitor star of Woosley et al. (2002) in two different geometrically setups: First, a 90° wedge centred around the equatorial plane with periodic boundary conditions was calculated (from hereon model s11.2–wedge). A second full 180° model (north pole to south pole) with reflecting boundary conditions was calculated (from hereon model s11.2–180). In Fig. 4.1 an overview of the setup is given. Except for the volume and the boundary conditions both models have the same angular and radial resolution and the same input physics and the same physical processes were considered (for details see Buras et al. 2006a).

Nevertheless, Buras et al. (2006a) reported a (low–energetic) explosion of model s11.2–180 whereas model s11.2-wedge failed to explode. It was speculated that this difference is caused by a combination of the factor of two larger volume and the reflecting boundary conditions in the 180° model compared to model s11.2–wedge with half the volume and periodic boundary conditions.

To investigate this further we have simulated two additional two–dimensional models: The first one, model s11.2–90, was set up as one quarter of the "2D–star", or upper hemisphere[3] , (90° from pole to equator) with reflecting boundary conditions. Additionally this model was calculated with slightly changed input physics[4] to investigate these influences in a two–dimensional simulation.[5] The second model, model s11.2–wedge–refl, was calculated in a 90° wedge around the equator but in difference to model s11.2–wedge reflecting boundary conditions were applied, otherwise this model is identical to model s11.2–90.

In particular these new models allows us to investigate whether the smaller volume in model s11.2–wedge, or the periodic boundary condition, or the existence of the singular polar axis was responsible for the failed explosion of the model s11.2–wedge. This comparison is possible for the following reasons:

- model s11.2–wedge–refl is comparable to model s11.2–wedge except for the boundary conditions. This is a test for the boundary conditions.
- model s11.2–90 is identical to model s11.2–180 except for the smaller volume (factor 0.5). This tests the volume effect.
- model s11.2–90 is identical to model s11.2–wedge–refl, if one rotates the model by 45°. By "leaving" the polar axis, one is able to test the axis effect.

Furthermore this comparison also allows us to investigate whether the time evolution in the model s11.2–90 is different compared to the model s11–2–180. This might tell us whether or not it is important to calculate a "full" 2D–model (i.e. 180°) or a smaller volume is sufficient. Last but not least, from this calculations we can learn the influence of the newly implemented electron capture rates on heavy nuclei, see Appendix A.3.1, which is expected to be very small, and we can judge the influence of the existence of small amplitude entropy oscillations (see Buras et al. 2006b) on a two–dimensional simulation.

First, we show in Fig. 4.5 the averaged neutrino luminosities and rms energies for the different models. Here a two groups are visible: the models s11.2–180 and s11.2–wedge show almost similar neutrino luminosities and energies in all neutrino flavours, and the models s11.2–90 and s11.2–wedge–refl do show almost identical behaviour. Both groups are separated from the early beginning (i.e. from roughly 40 ms after the shock lunch) and the differences become larger at a time of about 70 ms after the shock formation. All the time the latter group (models s11.2–90 and s11.2–wedge–refl), which were calculated with the description of electron capture on heavy nuclei according to Langanke et al. (2003) (cf. Appendix A.3.1) shows lower neutrino luminosities and rms energies. The reason for this can be found in the faster collapse of these models which implies that the nuclear O–Si–interface reaches the shock front earlier. This reduces the mass accretion rate through the shock front, and less gravitational binding energy

[3] We define a "hemisphere" of a "2D–star" as the computational domain from the north–pole to the equator...

[4] Instead of the standard Bruenn (1985) description for electron capture on heavy nuclei the newer rates of Langanke et al. (2003), see Appendix A.3.1, were used. Note that in the postbounce phase electron capture on heavy nuclei below the shock front is unimportant, and thus the models do not behaviour differently.

[5] Note that in spherically symmetric models these new electron capture rates have almost no influence on the postbounce phase (cf. A.3.1).

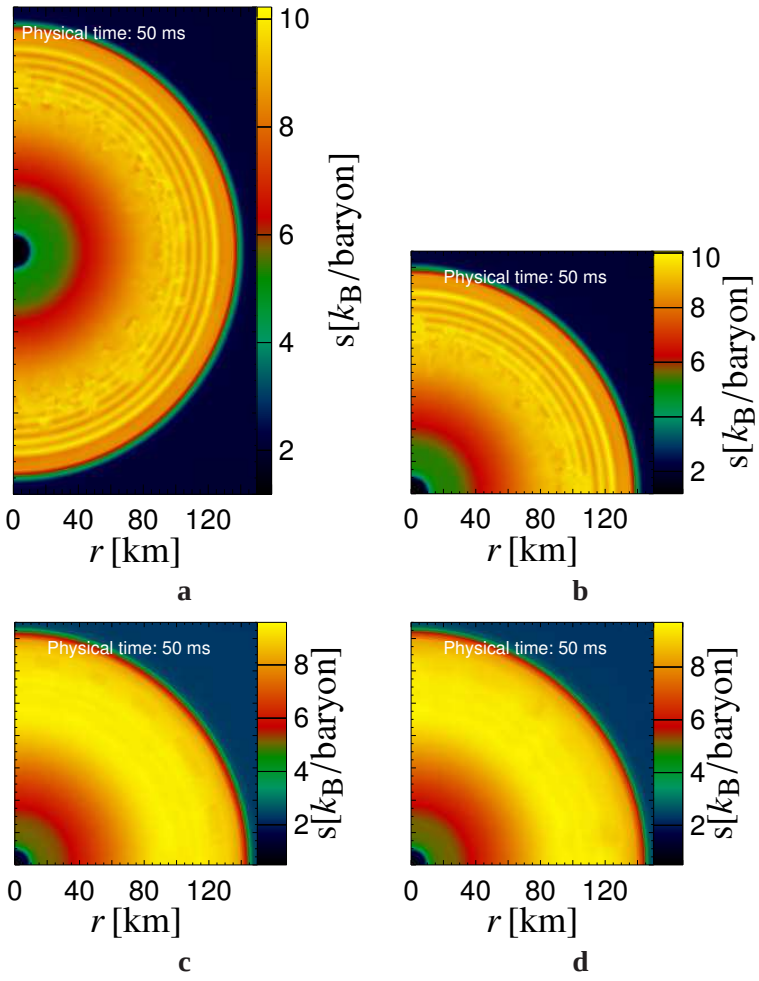

Figure 4.2.: Snapshots of entropy contours for different models at a time of 50 ms after the shock formation. **a**: model s11.2–180, **b**: model s11.2–wedge. **c**: s11.2–90. **d**: s11.2–wedge–refl. Note that model s11.2–180 was calculated in an 180° setup. The snapshots are oriented such that the equator lies horizontally, except in the wedge modes where the equator goes from the lower left to the upper right corner. Different times are shown in Figs. 4.3 and 4.4.

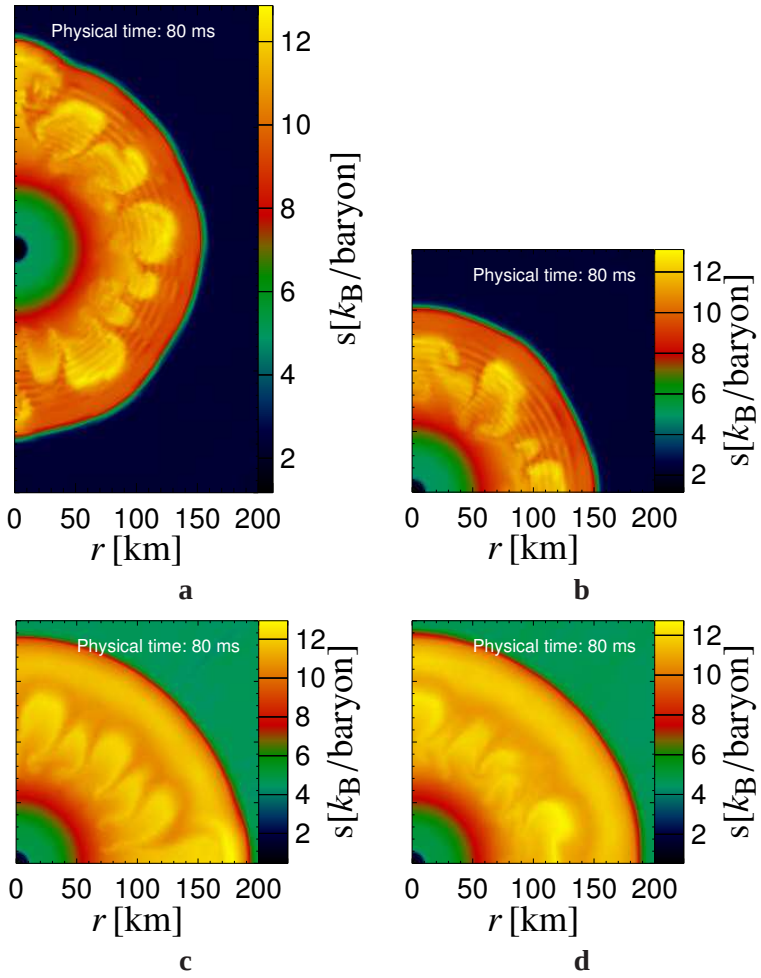

Figure 4.3.: Snapshots of entropy contours for different models at a time of 80 ms after the shock formation. **a**: model s11.2–180. **b**: model s11.2–wedge. **c**: s11.2–90. **d**: s11.2–wedge–refl. The orientation of the snapshots is the same as in Fig. 4.2. Different times are shown in Figs. 4.2 and 4.4.

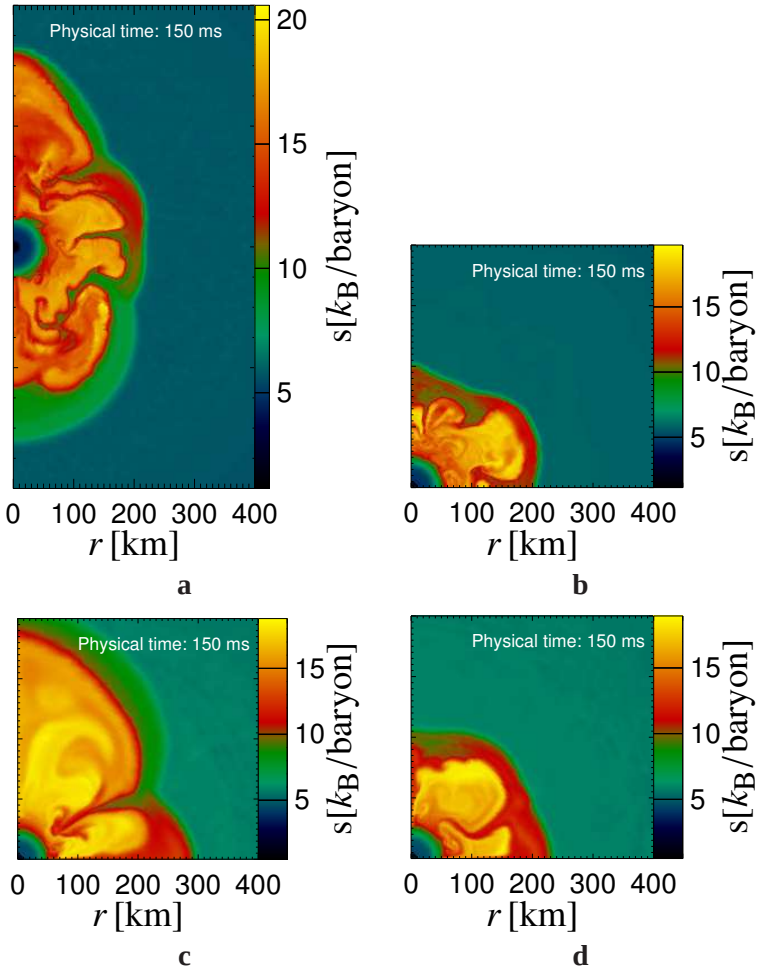

Figure 4.4.: Snapshots of entropy contours for different models at a time of 150 ms after the shock formation. **a**: model s11.2–180. **b**: model s11.2–wedge. **c**: s11.2–90. **d**: s11.2–wedge–refl. The orientation of the snapshots is the same as in Fig. 4.2. Different times are shown in Figs. 4.2 and 4.3.

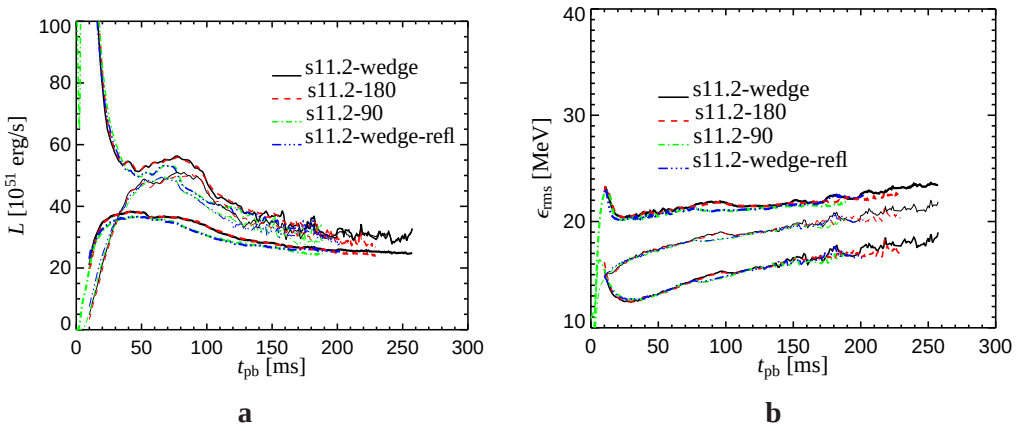

Figure 4.5.: **a**: The laterally averaged neutrino luminosities as function of time for electron neutrinos (upper group of lines), anti-electron neutrinos (group of lines in the middle), and other neutrino flavours (bold, lower group of lines) as function of postbounce time for all models. **b** the rms energy for the electron neutrinos (lowest group), anti–electron neutrinos (group in the middle), and heavy lepton neutrinos (upper group).

is released in less and cooler neutrinos. Figure 4.5 also shows that the (laterally averaged) neutrino luminosities and rms energies did *not* cause the different behaviour of the exploding model s11.2–180 and non–exploding model s11.2–wedge, since both show the same values for the neutrino emission. Furthermore the generic lower values in the models s11.2–90 and s11.2–wedge–refl are also not very important, since model s11.2–90 explodes very similar as model s11.2–180.

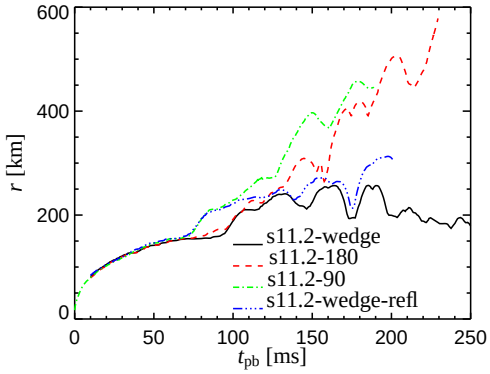

Figure 4.6.: The laterally averaged shock position as function of postbounce time for all models.

This can be seen in Fig. 4.6 where we show the laterally averaged shock position of the models s11.2–180, s11.2–90, s11.2–wedge–refl, and s11.2–wedge. As it is clearly visible both models that include the polar axis (s11.2–180 and s11.2–90) show an explosion, thus simulating only a hemisphere did not suppress physics that was important for the explosion of model s11.2–180. Both exploding models show the beginning of the explosion when the O–Si com-

position interface (see Fig. 4.6) falls through the shock front and the decreasing ram pressure triggers a shock expansion. This happens earlier in the model s11.2–90 which is however not a consequence of the geometry of the model but is instead a consequence of the used electron capture rates of Langanke et al. (2003) that cause a faster collapse of the star. The fact that both models explode also shows that the larger volume in model s11.2–180 was *not* responsible for the explosion. From Fig. 4.6 it is also obvious that both models that were centred around the equator do not explode, independent from the choice of reflecting boundary conditions (model s11.2–wedge–refl) or periodic boundary conditions (model s11.2–wedge). This implies that the periodic boundary conditions in model s11.2–wedge also did *not* suppress the explosion. Quite the opposite seems to be the case: The quite similar shock trajectories in the models s11.2–wedge and s11.2–wedge–refl suggest that the choice of the boundary conditions in a wedge model is not very important, but rather that a wedge–model itself is a bad choice.[6]

In Figures 4.2 – 4.4 we show snapshots of the entropy for all four models at a time of 50ms, 80ms, and 150ms after the shock formation. Clearly, in all models convective instabilities begin to develop at the same time independent of the geometry of the model. On can also clearly see that the entropy fluctuations due to "entropy wiggles" (see Buras et al. 2006b) in models s11.2–wedge and s11.2–180 (visible as circular stripes in these models) cause a faster growth of small scale convective instabilities (see e.g. the snapshots at 50ms), which are visible at later times on top of the larger convective eddies. However, at a time of 150 ms this large scale convective flows show nearly the same pattern (i.e. one big and one smaller bubble) in all models[7]. In this sense the geometry of the calculations shows at early times only little influence on the time evolution of the convective flows. That convection develops in an indeed very similar way can be seen in Fig. 4.7a, where we show the lateral kinetic energy between the shock front and the gain radius:

$$E_\theta{}^{kin}(t) = \int_{r_g}^{r_s} \int \frac{1}{2} m(r,\theta,t) {v_\theta}^2(r,\theta,t)\, \mathrm{d}r\, d\theta, \tag{4.1}$$

where r_h and r_s are the gain radius and the shock radius, and v_θ is the lateral velocity. Obviously, the energy contained in convective flows develops very similar in all models and the exploding models s11.2–180 and s11.2–90 do not contain more energy in convective motion than the other models. Rather we find again two separated groups: model s11.2–180 and model s11.2–wedge contain at the early times more "convective energy" than models s11.2–90 and s11.2–wedge–refl. However, this demonstrates clearly that convective energy contained in the gain layer does not trigger the explosion. This, on the other hand, is also expected from the analysis of Foglizzo et al. (2005) which suggests that convection favours the growth of larger modes than the observed low $l = 1, 2$ modes. The different energies contained in convective motion are probably caused by the perturbations that break the spherical symmetry of our models at the beginning of our simulations: As already explained, models s11.2–180 and s11.2–wedge show larger entropy perturbations (due to the entropy wiggles in these models) which allow a faster grow of convection on smaller scales. Although, as we discussed above, this does not lead to large changes in the development of the convective flows, it seem to produce initially stronger

[6] However, one may of course argue which boundary condition makes physically "more" sense...
[7] Look also at the related discussion in Appendix E.

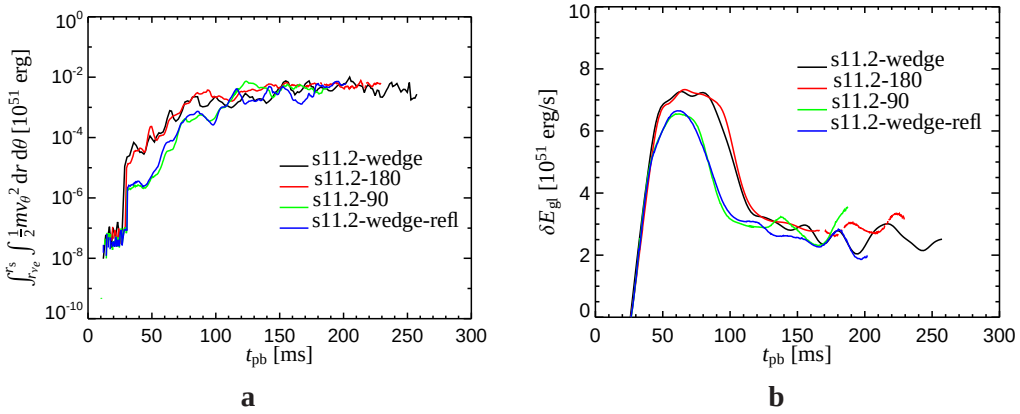

Figure 4.7.: a: The integrated lateral kinetic energy (cf. Eqn. 4.2) in the hot bubble region between the neutron star and the shock. **b**: The "heating" energy deposited by neutrinos in the gain layer between the gain radius and the shock front as function of time.

convection. The fact that two models explode, one with this stronger early convection and one without, clearly shows that this does not influence our explosion mechanism.

Thus, if convection energy is not responsible for the onset of the explosion in models s11.2–180 and s11.2–90 what else may be responsible? Is it possible that neutrino heating deposits more energy in the gain layer in the exploding models ?

The energy deposited by neutrino heating in the gain layer can be calculated by integrating the net neutrino heating term over the volume in the gain layer

$$\delta E_{\rm gl}(t) = \int_{r_{\rm g}}^{r_s} \int Q_{\rm H}(r,\theta,t)\, n_{\rm B}(r,\theta,t)\, {\rm d}r\, {\rm d}\theta\,, \tag{4.2}$$

with $Q_{\rm H}(r,\theta,t)$ being the local net heating rate per baryon and $n_{\rm B}(r,\theta,t)$ being the baryon number density. Again we find two distinct groups for the neutrino heating, see Fig. 4.7b. In the exploding models the energy deposition becomes larger than the one in the non–exploding models at a time of 150 ms after the shock formation. However, this is due to the fact that at this time the exploding models already show a significantly increased shock radius and the contribution to the heating region in the integral of Eqn. 4.2 increases. Obviously, the heating alone is not responsible for the start of the explosion, since at a time of 110 ms model s11.2–90 already shows the shock expansion although the integrated heating rate is equal to the one of the non–exploding model s11.2–wedge–refl. Furthermore, model s11.2–wedge shows almost all the time a similar neutrino heating as model s11.2–180 (and even larger heating than model s11.2–90) but does nevertheless *not* explode.

The angular dependence of the neutrino heating rate, see Fig. 4.9, reveals that at a time of 130 ms after the shock formation it is also not obvious that the exploding models gain more energy by neutrino heating. We find a strong angular dependence in all models and one always finds angles θ where the heating is stronger in the models that do not explode. However, both exploding models have in common that neutrino heating increases in the vicinity of the north–

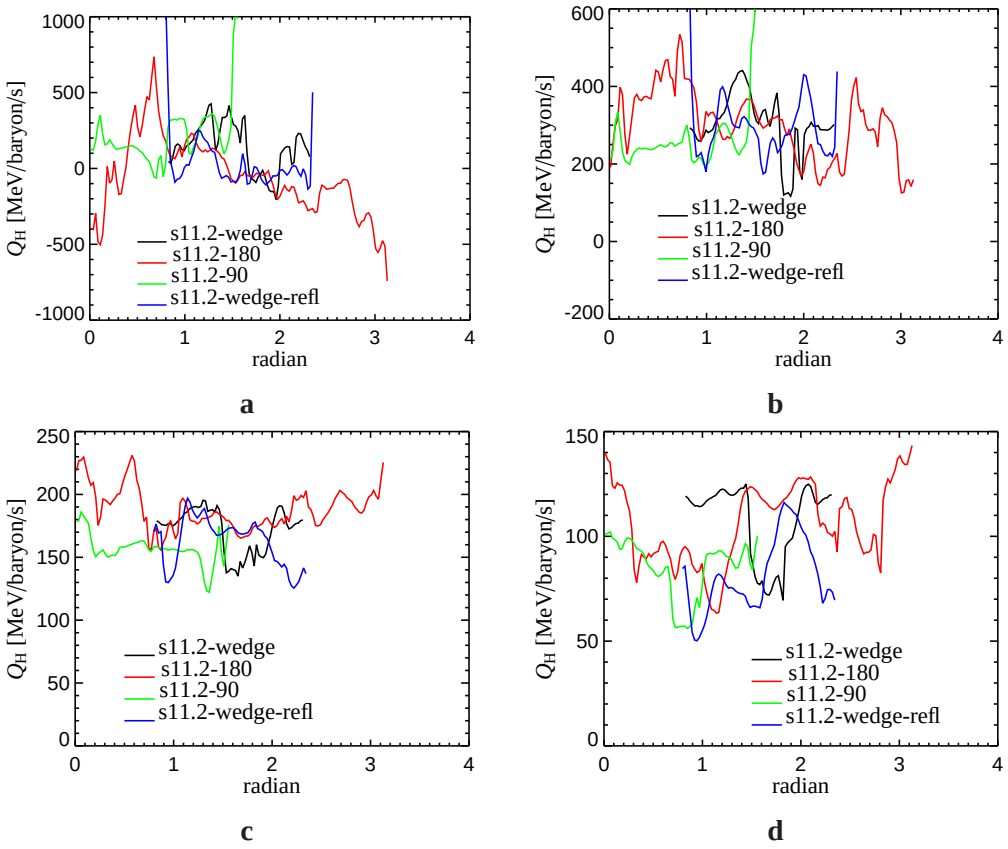

Figure 4.8.: The net heating rate as function of angle θ at a time of 130 ms (where the bifurcation into exploding and non–exploding models already happened) for all models. **a**: at a radius of 80 km **b**: at a radius of 100 km **c**: at a radius of 150 km **d**: at a radius of 180 km

pole ($\theta = 0$) and energy transfer from neutrinos to the stellar plasma is enhanced at this region. Since both models explode with a large oscillatory mode along the polar axis, this implies that neutrino heating certainly helps the shock expansion along the polar axis. But as Fig. 4.9 shows, in the exploding models one does not find a significantly increased neutrino energy or number flux in the region around the polar axis and thus the neutrino emission does not cause the "polar" explosions.

However, obviously, two of our simulations — the ones with reflecting boundary conditions — show an explosion. As Buras et al. (2006a) discuss a sufficient condition for an explosion is that the ratio of the advection timescale and heating timescale is larger than unity for some advection timescales. Note that in 2D–simulations the definition of the advections timescale according to Eqn. 3.2 is not appropriate since this definition does not take into account the convective flows that inevitably prolong the advection. Thus, in 2D–models we adapt the definition

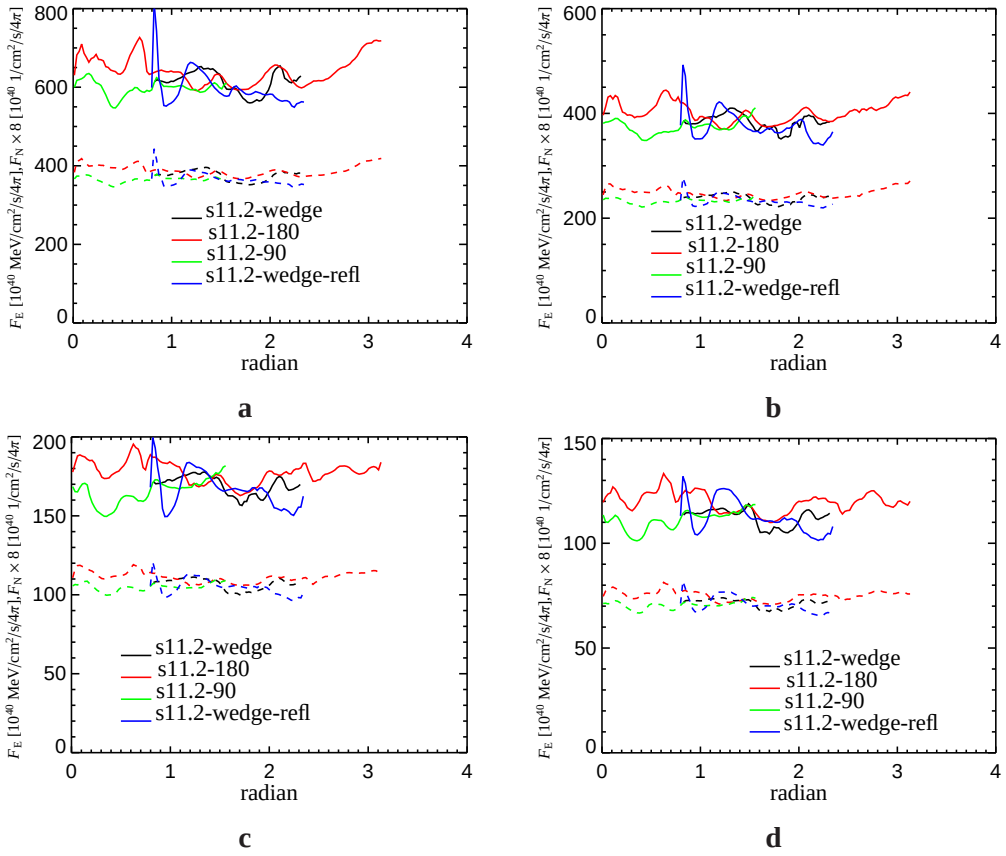

Figure 4.9.: The neutrino energy flux F_E (solid) and the neutrino number flux F_N (dashed) as function of angle θ at a time of 130 ms after the shock formation. Note that both quantities contain the contribution of all neutrino flavours, and that the number flux was multiplied by eight in order to be of the same order of magnitude as the energy flux. Again different radial cuts are shown: **a**: at a radius of 80 km **b**: at a radius of 100 km **c**: at a radius of 150 km **d**: at a radius of 180 km

of an effective advection timescale (see Buras et al. 2006a) which reads:

$$\tau_{\rm adv}(M_i) := \tau_{\rm adv}(t1) = t_2(M_i) - t_1(M_i), \text{ where} \tag{4.3}$$

t_2 is defined by the condition $M(r = r_{\rm gain}, t = t_2) = M_i$ and t_1 by the condition $M(r = r_{\rm shock}, t = t_1) = M_i$. This represents the time difference when the same mass M_i is enclosed by the shock and later by the gain radius. Indeed evaluating this advection timescale reveals a ratio of advection timescale to heating timescale larger unity for the explosion of model s11.2–180, see Fig. 17 in Buras et al. (2006a). We show in Fig. 4.10 the heating timescale and advection timescale for all models with the 11.2 $M_\odot$ progenitor model. For all models the heating timescales are very similar. However, the advection timescale increases for both exploding models at the time the shock starts expanding. From this one can conclude two things:

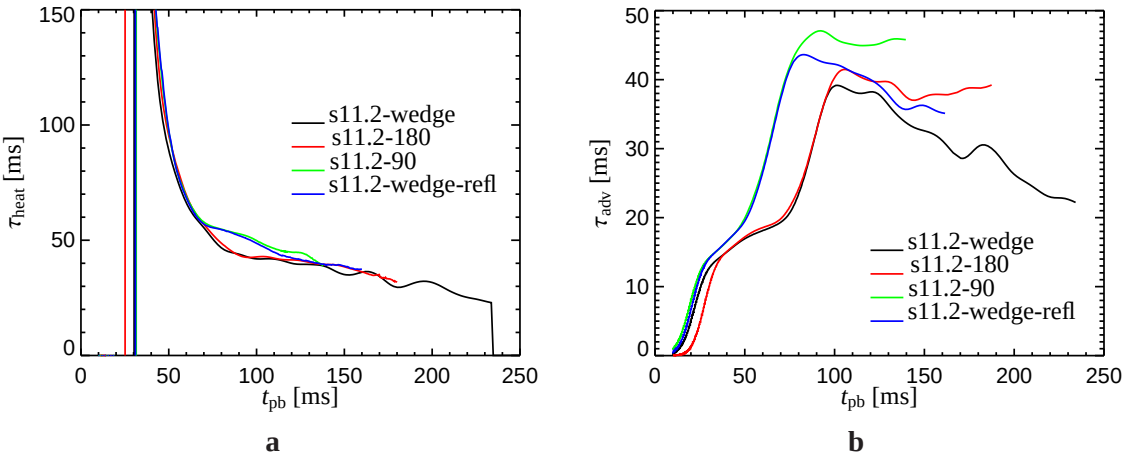

Figure 4.10.: **a**: The heating timescale as defined in Eqn. 3.2 for all models. **b**: The advection timescales as defined in Eqn. 4.3 for the same models.

- Firstly, since the heating timescales develop in the same way in all models it is finally ruled out that neutrino heating causes the onset of the explosion.
- Secondly, same heating timescales but different timescale ratios imply that in the exploding models the *advection timescale* has to grow (as observed in the exploding models) in order the ratio to exceed unity. The advection timescale grows is the shock expands and matter has to be advected over a larger distance to the neutron star surface. Since, neutrino heating does not cause this initial shock expansion another mechanism has to trigger the shock expansion and the increase in the advection timescale.

In recent years it became more and more obvious that additional to neutrino heating the existence of fluid instabilities can be helpful for a successful supernova explosion, since they can lead to a shock expansion. This instability, which is commonly called “a standing accretion shock instability” (or SASI) does lead to a non–radial, low–mode shock instability (see, e.g. Blondin et al. 2003). A promising candidate that causes this for instability is the so called “advective–acoustic cycle” (Foglizzo & Tagger 2000, Foglizzo 2001, 2002), where an acoustic feedback is produced by advection of entropy and vorticity perturbations from the shock front down to the neutron star. These acoustic waves travel back to the shock front and disturb it which again causes entropy and vorticity perturbations. Indeed, as Scheck (2006) convincingly showed the growth of low–mode ($l = 1, 2$ ...) shock instabilities can be linked to the existence of the advective–acoustic cycle.

Following the analysis of Blondin et al. (2003), Scheck (2006) we analyse our models for the presence of the standing accretion shock instability by expanding the pressure $P(r, \theta, t)$ into spherical harmonics

$$P(r,\theta,t) = \sum_{l=0}^{\infty} \sum_{m=-l}^{l} a_{l,m}(r,t) Y_{l,m}(\theta) = \sum_{l=0}^{\infty} a_{l,0}(r,t) Y_{l,0}(\theta) \quad , \tag{4.4}$$

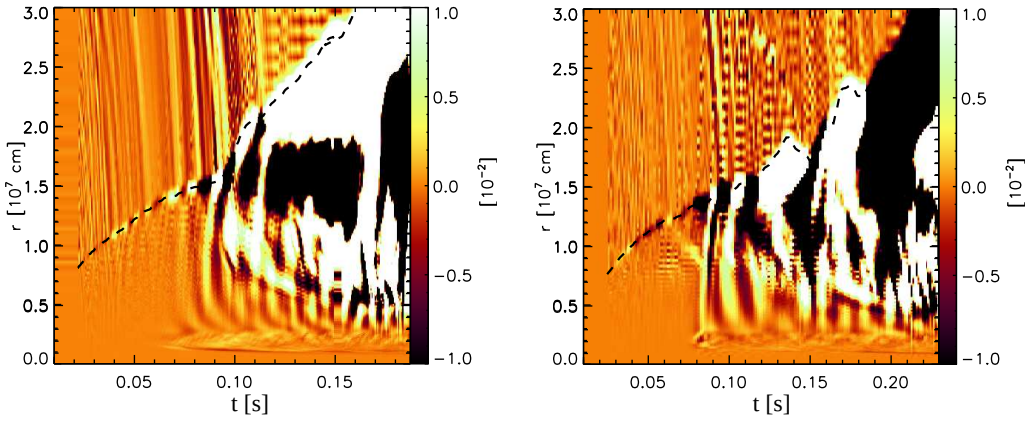

Figure 4.11.: The lowest possible coefficient $a_{l,0}/a_{0,0}$ for the expansion of the pressure into spherical harmonics, as function of time and radius. The maximum shock position is indicated by the dashed line. The "zebra" strip pattern below the shock front (setting in at roughly 70 ms) is a clearly indication for the presence of oscillatory pressure fluctuations, which are possible created by the advective–acoustic cycle. **a**: model s11.2–90. Note that in this model the lowest possible mode which is not zero is the $l = 2$ mode. **b**: model s11.2–180. Here the $l = 1$ mode is shown.

where the last step expresses the rotational symmetry of our models around the polar axis.

Pressure fluctuations caused by the presence of the cycle are than visible as regular pattern with a characteristic frequency, see e.g. Fig. 7 in Blondin et al. (2003).

Indeed our models show the presence of oscillatory pressure fluctuations, which a clear sign for the presence of a standing accretion shock instability, see Fig. 4.11, but only the models containing the polar axis do show an explosion. The reason for this is depicted in Fig. 4.12, where the coefficient of the expansion of the shock radius into spherical harmonics

$$r_{\mathrm{sh}}(\theta, t) = \sum_{l=0}^{\infty} a_{l,0}(t) Y_{l,0}(\theta) \quad , \tag{4.5}$$

(analogous to Eqn. 4.4) are shown.

The important point to note is, that on the one hand, in models s11.2–wedge and s11.2–wedge–refl the low modes do not grow, whereas on the other hand the lowest possible modes do grow in the models s11.2–90 and s11.2–180.

In model s11.2–wedge the modes do not grow because of the applied periodic boundary conditions: the necessary condition that the shock positions are equal at the borders of the wedge forbids the growth of uneven modes, and the constraint that the velocity at the borders of the wedge are equal does not permit the growth of even modes. In model s11.2–wedge–refl the reflecting boundary conditions do not forbid the growth of modes but nevertheless no growing modes are observed.

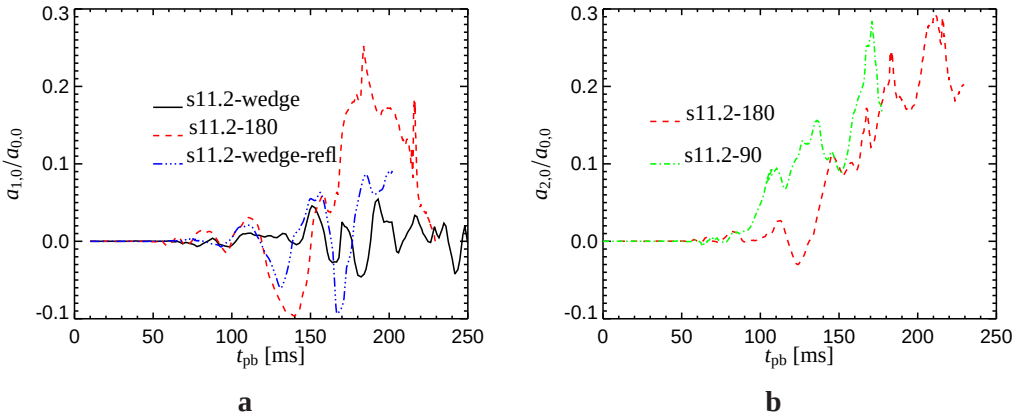

Figure 4.12.: Some time–dependent coefficients obtained by expanding the shock position into spherical harmonics. Note that the coefficients are normalised to the $l = 0$ mode. **a**: The coefficient corresponding to the $l = 1$ mode. Note that a $l = 1$ mode does not exist for the model s11.2–90. **b**: The coefficients for the $l = 2$ mode.

It remains thus to be answered why the standing accretion shock instability leads to a shock expansion — and thus an increase of the advection time scale which is sufficient to cause the explosion — in the models s11.2–90 and s11.2–180, whereas in model s11.2–wedge–refl this is not observed. In the exploding models the cycle leads to a shock expansion along the polar axis which in turn leads to an explosion along the polar axis. This, however, seems logical since along the polar axis an expanding shock has to move less matter than at every other angle θ and thus less pressure has to be applied below the shock front at the polar axis. In model s11.2–wedge–refl the pressure perturbations induced by the cycle can not create a sufficiently shock expansion since in a wedge model of $\pm 45^\circ$ around the equator matter located in a shell has to be moved in order to allow a shock expansion. Thus, though the standing accretion shock instability is allowed in the wedge calculation with reflecting boundary conditions it cannot lead to a shock expansion and can thus not trigger the onset of the explosion.

Of course, one has now to ask oneself whether the explosions in the models s11.2–90 and s11.2–180 are caused by the numerical features of the polar axis in a 2D simulation and these explosions would dissappear in a 3D simulation. While asking that one should bear in mind that in a 3D simulation, however, mass can be easily moved in columns (very similar to the situation at the pole in a 2D simulation) and the shock expansion is not hampered at any angle θ.

Summary

From the analysis of the models presented in this Section we conclude that in two–dimensional models the choice of the simulation setup can artifically suppress an explosion although the physical conditions favour an explosion. In particular, models where the computational domain is centred in a wedge around the equator and the polar axis is excluded can suppress explosions, since rotational symmetry requires that matter has to be moved in shells. Furthermore, we con-

clude that in the particular case of the 11.2 $M_\odot$ progenitor model discussed in this Section the explosion is powered by neutrino heating in favourable conditions that are created by an initial shock expansion which is caused by the presence of the standing accretion shock instability. Only small differences are observed in models where the computational domain covers 180° or 90° (from north pole to the equator), though the lowest possible modes of fluid motion are $l = 1$ or $l = 2$, respectively. From this we conclude that though a calculation with a grid that covers the area between both poles makes physically more sense than a simulation with a grid that covers "only" the area between pole and equator, numerically both setups seem to be almost equivalent. As a remark it should be mentioned that we do also not find an evolutionary difference of a pole–equator or pole–pole setup in models including rotation, see Section 6.1

5

Effects of the nuclear EoS in multi–dimensional simulations

5.1. The growth of neutron star convection and g–mode oscillations

As we have already discussed in Part I of this thesis, the nuclear EoS influences the supernova evolution in various ways. With spherically symmetric models one is able to investigate and understand many aspects of the interplay between the EoS and the supernova evolution. Exemplary we mention here the stiffness of the EoS, which controls the compactness of the neutron star, which in turn directly influences the shock trajectory. However, as we have have already discussed, spherically symmetric models suppress the existence of multi–dimensional phenomena, such as convection, which seem to be crucial ingredients in the supernova explosion mechanism, see e.g. Section 4.2. Furthermore, an analysis for potential convectivly unstable regions in 1D–simulations (cf. Section 3.2) already indicated a (strong) EoS dependence. It is known for a long time that convection inside the proto–neutron star plays a special role and has thus been investigated in numerical studies (see, e.g. Buras et al. 2006b,a, Swesty & Myra 2005, Dessart et al. 2006, only to mention a few). The large interest in proto–neutron star convection can be summarised as follows:

- Proto–neutron star convection happens in the dense core that is optically thick for neutrinos. Thus, by convective flows in the direction of the neutrinospheres, neutrinos are dragged upwards together with the matter flow. This can change the neutrino luminosities and energies compared to non–convective spherically symmetric simulations. These changes in the neutrino flux may be important for the re–pressuring of the stalled supernova shock.

- Convective flows inside the proto–neutron star change the structure of the core. Thus the shrinking of the core can be influenced by the presence of convective instabilities. Since the shock expansion also depends on the compactness of the dense accretor, this effect has to be taken into account.

However, what is still missing is a study which investigates how the EoS of the dense core influences the convection *inside* the dense core. Inevitably, it is expected that the EoS does influence the growth of convective instabilities, see e.g. the discussion in Buras et al. (2006b), but it is totally unclear to what extent this will influence the supernova calculations.

Therefore, the investigation of EoS differences and their coupling to multi–dimensional effects is crucial to understand more deeply the role of the EoS in core collapse supernovae, especially for convection inside the core and its feedback on the whole supernova evolution. For this purpose we have performed two 2D–simulations of a $15M_{\odot}$ star (Woosley & Weaver 1995) with the Wolff and L&S–EoS. In both simulations the same input physics as the one discussed for models Wolff(io)slms and L&S(io)slms from Section 3.2 was used, and the usual mapping procedure (see Section 4.1) onto a 2D–domain was applied. However, the time *when* the mapping was done was different. Since we expect a rapid start of neutron star convection for the model with the Wolff–EoS (remember Fig. 3.17 in Section 3.2), this model was mapped to 2D directly after the shock formation. The first tens ms after the shock formation, however, are computationally very expensive. In order to make this calculation feasible model Wolff–2D was mapped in a first step onto an angular domain that covers the first quadrant[1] (from north pole to the equator) with 96 angular bins which corresponds to a resolution of 0.91°. Subsequently after an evolution time of around 100 ms after the shock formation this model was than mapped onto a full 180° domain.

On the other hand (see Section 3.2) we expect neutron star convection to start more slowly in model L&S–2D. Thus this model was mapped to a 180° domain with a resolution of 0.91° at a time of 10 ms after the shock formation.

We start our discussion by studying (Fig. 5.1) the Brunt–Väisälä frequency (cf. Eqn. 3.10). As described in Section 3.2 the Brunt–Väisälä frequence predicts a growing convective instability for positive values of the Ledoux criterion (cf. Eqn. 3.9) otherwise stable modes are predicted.

It is clearly visible, that at early times a convective instability is found deep inside the dense core of model Wolff–2D , whereas model L&S–2D is stable against convection. A time evolution of the neutron star convection is depicted in Fig. 5.2 where we show the the lateral velocity for the condition $v_\theta > 7 \times 10^7 \mathrm{cm/s}$. Though the behaviour is very similar in the models with both EoSs, one again clearly sees that model Wolff–2D shows convection immediately after the bounce, extending outwards to the neutrinosphere. Then, after a few 10 ms this instability disappears and a convective region similar to model L&S–2D develops, however with the remarkable difference, that in model Wolff–2D a gap of convective stability separates the region of convection around the neutrinosphere from the “deep core” convection. Interestingly, the onset of the early convection in this model can not be directly linked to the presence of heavy

[1] As was shown in Section 4.2, calculating only a 90° domain does not suppress essential physics, since we found explosions for a model that was both calculated with a 180° and a 90° grid. The growth of a $l = 1$ mode, however, is prohibited in such a model — and replaced by the growth of the next lowest $l = 2$ mode — which made the second mapping at later times onto a 180° grid necessary. See also the discussion in Appendix D.

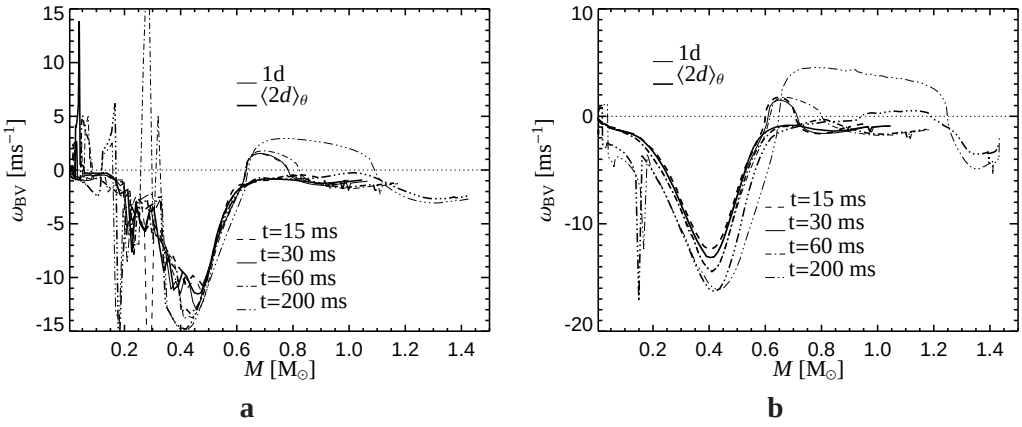

Figure 5.1.: The Brunt–Väisälä frequency as function of the mass coordinate for the laterally averaged 2D–models (thick) and the corresponding 1D–models (thin) at different times and different EoS: **a**: The Wolff–EoS **b**: The L&S–EoS

nuclei in the dense core. Although one would assume that a matter stratification, where heavy nuclei are stacked on a fluid of free nucleons, and free nucleons are again stacked onto the layer of heavy nuclei is convectivly unstable (since the specific weight of nucleons bound in nuclei is smaller than that of free nucleons), however, it is not obvious that convection starts in the vicinity around the region of heavy nuclei (i.e. for mass shells between $0.3\,\mathrm{M}_\odot$ and $0.5\,\mathrm{M}_\odot$), but rather the early convection extends outwards to the neutrinosphere. This implies that the start of early proto–neutron star convection in model Wolff–2D is not only due to the presence of heavy nuclei in the dense core, but also that during the time before shock formation the structure of the dense core develops such that it is unstable against convective flows. It would thus be interesting to calculate also the collapse phase of this model in 2D, in order to investigate whether convection would start even earlier than we observe in model Wolff–2D.

A more detailed impression of the neutron star can be obtained from Figs. 5.3 – 5.5. Clearly, Rayleigh–Taylor instabilities, which cause "Y_e–fingers", develop much earlier in model Wolff–2D, then dissappear around 50 ms, and then reappear at similar times when model L&S–2D shows the first signs of neutron star convection. Overall these "Y_e–fingers" are very similar to the ones found by Swesty & Myra (2005), cf. Figs. 2 and 3 in their paper, but they observe them very early (at roughly 5 ms) after the shock formation even with the L&S–EoS, and they claim that this is due to the fact that they calculated the collapse in 2D. However, as was discussed in Buras et al. (2006a), calculating the collapse in 2D does not lead to this early convection with the L&S–EoS in our simulations[2].

As a measure for the "strength" of the neutron star convection we calculate the lateral kinetic energy inside the electron neutrinosphere

$$E_\theta{}^{\mathrm{kin}}(t) = \frac{1}{2}\int_0^{r_{\nu e}} \int_\theta m(r,\theta,t) v_\theta(r,\theta,t)^2 \,\mathrm{d}r\,\mathrm{d}\theta\,, \tag{5.1}$$

[2] Swesty & Myra (2005) use totally different numerical schemes and physical approximations than we do and these differences may be responsible for the difference in the onset of convection.

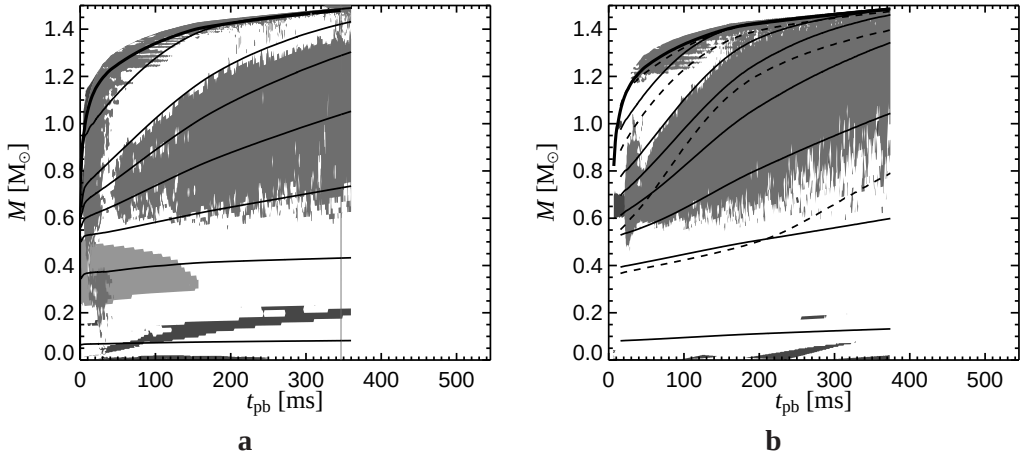

Figure 5.2.: Regions of convective instability inside of the proto–neutron star as function of time for **a**: the Wolff–EoS and **b**: the L&S–EoS. The dashed lines from bottom to top represent density contours of 10^{14}, 10^{13}, 10^{12}, and 10^{11}g/cm^3, respectively. The solid lines indicate the radii of 5 km, 10 km, 15 km, 20 km, 25 km, 30 km, and 50 km (bottom to top). The thick solid line represents the position of the electron neutrinosphere and marks the "border" of the neutron star. The almost black shaded region indicates regions where the evaluation of the Ledoux criterion with the laterally averaged 2D–data indicates instability. The dark grey region indicates where the condition $v_\theta > 7 \times 10^7$ cm/s is fulfilled in a 2D–simulation. Finally, the light grey region indicates where heavy nuclei ($\langle A \rangle \geq 57 \wedge X_{\rm H} \geq 0.1$) are present (compare also to Fig. 3.8). Note that the evaluation of the Ledoux criterion with laterally averaged data predicts convective instability where indeed convective flows are found (compare e.g. to Fig. 3.17), except for the band for $M < 0.2\,{\rm M}_\odot$. **a**: the Wolff–EoS and **b**: the L&S–EoS.

depicted in Fig. 5.6. At early times, model Wolff–2D shows stronger convection, which is expected from the Figs. 5.3, where model Wolff–2D shows vigorous fluid motion, whereas model L&S–2D seems to be in a quiet phase. However, according to Fig. 5.6 at later times model L&S–2D shows about roughly 5 to 6 times stronger convection than model Wolff–2D, which is due to the fact that more mass is in convective motion, remember Fig. 5.2.

This stronger and "continuous" convection (i.e. without the separating stability band) in model L&S–2D leads to a stronger adjustment of the neutron star structure on the convective flows, see Fig. 5.7: As expected, convection tends to "blow up" the neutron star in both models, however the changes are larger in model L&S–2D than in model Wolff–2D. Whereas the average neutron star radius changes only by roughly 5 km in model Wolff–2D, model L&S–2D shows an neutron star which is extended up to 10 km more than the corresponding 1D–model. The results from our 1D studies in Section 3.2 suggest that these different reactions of the proto–neutron stars in 2D–simulations will also influence the evolution of the shock positions, which will be discussed in Section 5.2.

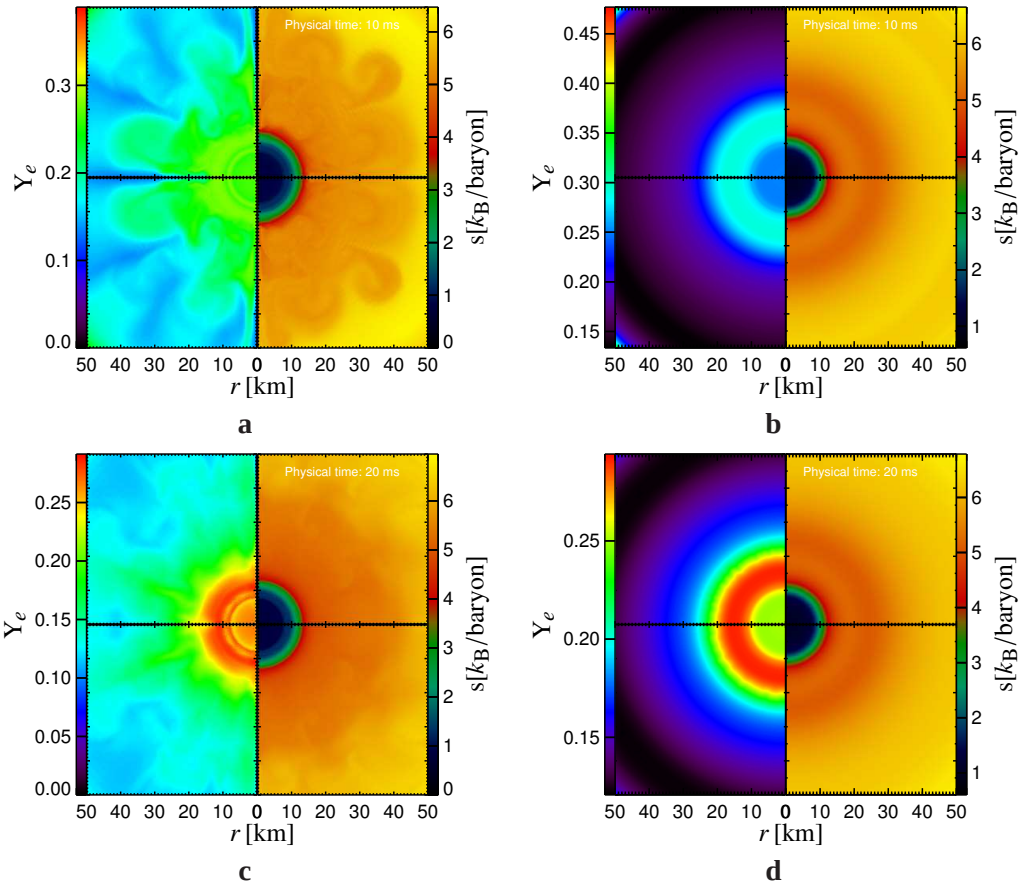

Figure 5.3.: Snapshots of the electron fraction Y_e (left) and the entropy s (right) for the models with the Wolff–EoS (panels a and c) and the L&S–EoS (panels b and d). Shown are the inner 50 km — to give an impression of the neutron star convection and the compactness of the neutron star. The upper row depicts the situation at a time of 10 ms after the shock formation, the lower row at a time of 20 ms after the shock formation. Different times are shown in Figs. 5.4 and 5.5.

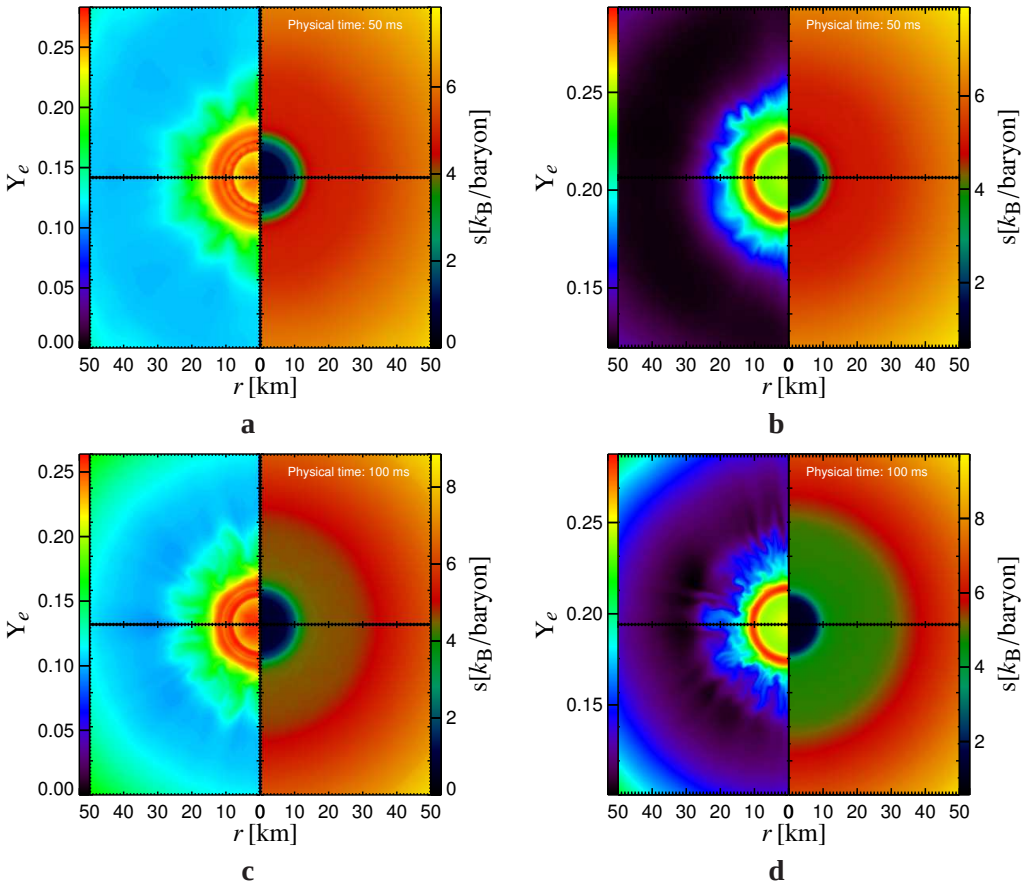

Figure 5.4.: Snapshots of the electron fraction Y_e (left) and the entropy s (right) for the models with the Wolff–EoS (panels a and c) and the L&S–EoS (panels b and d). Shown are the inner 50 km — to give an impression of the neutron star convection and the compactness of the neutron star. The upper row depicts the situation at a time for 50 ms after the shock formation, the lower row at a time of 100 ms after the shock formation. Different times are shown in Figs. 5.3 and 5.5.

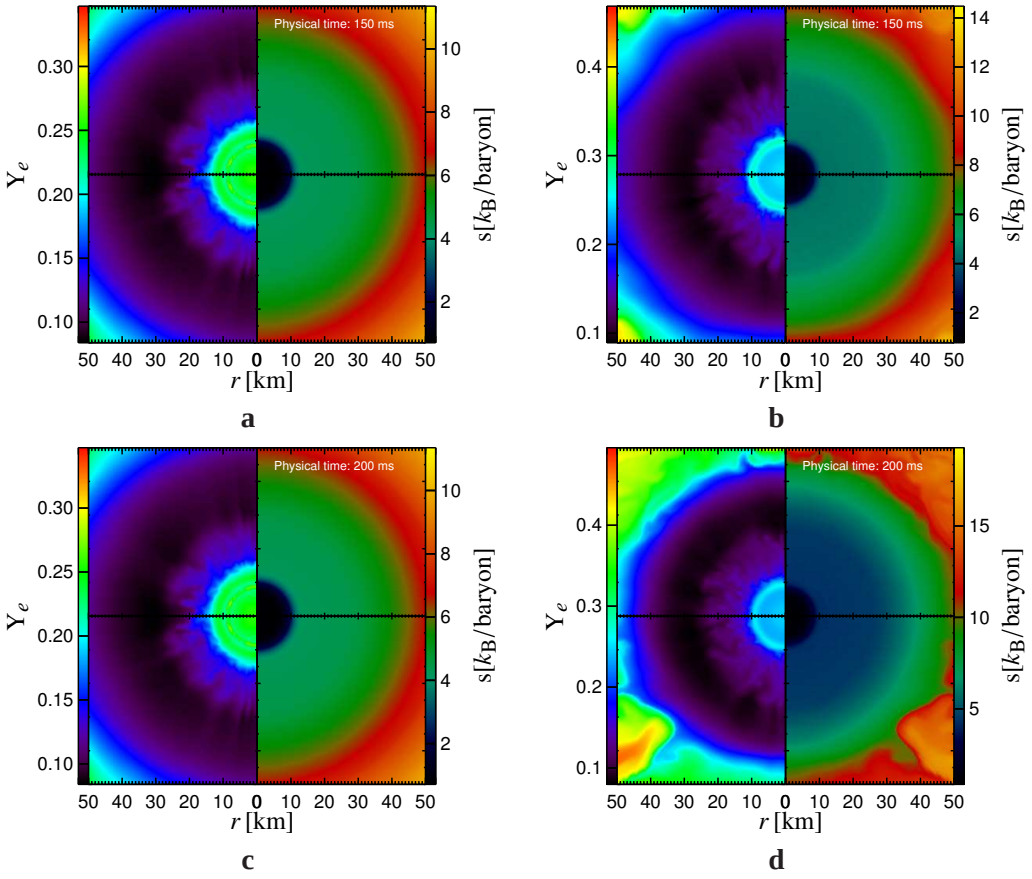

Figure 5.5.: Snapshots of the electron fraction Y_e (left) and the entropy s (right) for the models with the Wolff–EoS (panel a and c) and the L&S–EoS (panel b and d). Shown are the inner 50 km — to give an impression of the neutron star convection and the compactness of the neutron star. The upper row depicts the situation at a time for 150 ms after the shock formation, the lower row at a time of 200 ms after the shock formation. Different times are shown in Figs. 5.3 and 5.4.

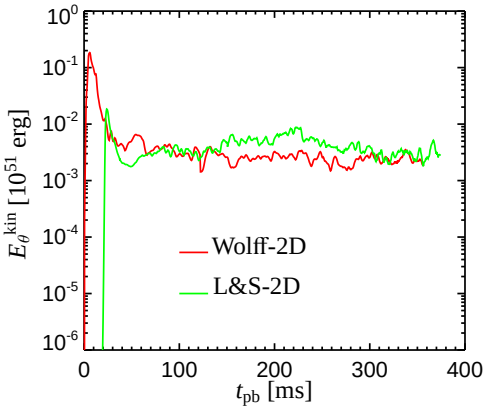

Figure 5.6.: The lateral kinetic energy $E_\theta^{\rm kin}$ inside the electron neutrinosphere for the 2D–models.

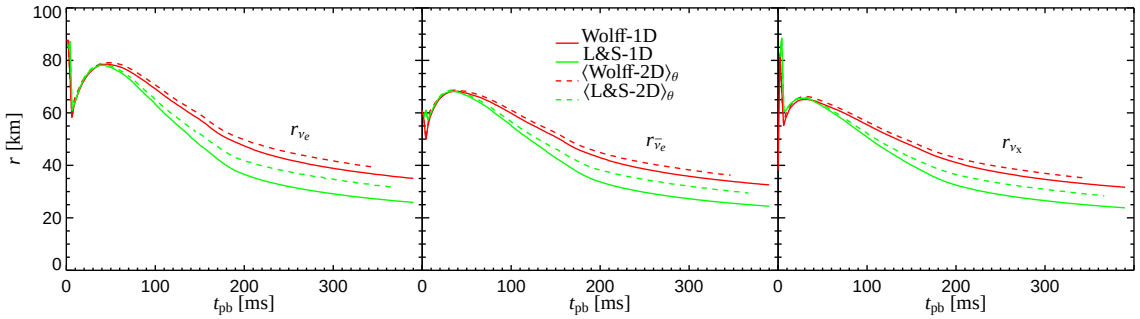

Figure 5.7.: The neutrinospheres of all neutrinos for the 2D–models and the corresponding 1D–models. Note that the radii of the 2D–models were calculated as the lateral average.

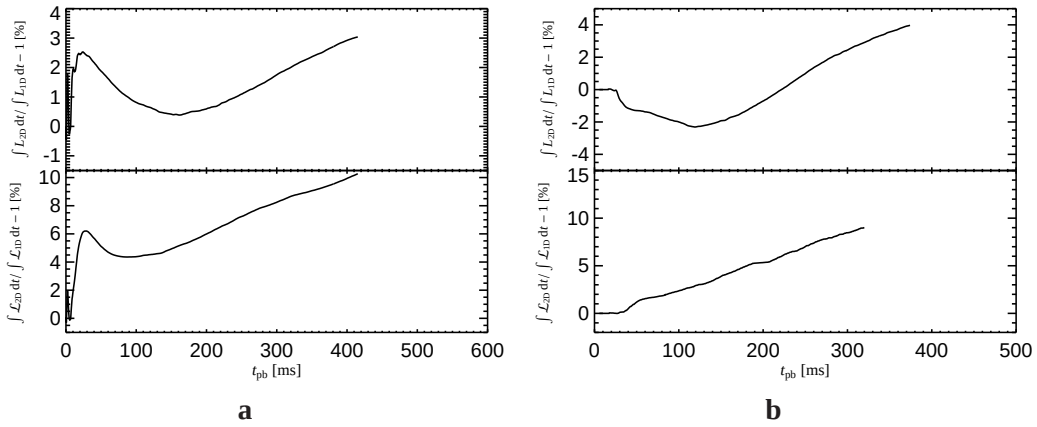

Figure 5.8.: The relative difference between the energy (top) and total lepton number losses (bottom) of the 2D–models and the corresponding 1D–models. Here, $\mathcal{L}$ denotes the total lepton number flux, and L denotes the total neutrino luminosity. **a**: model Wolff–2D **b**: model L&S–2D

As already mentioned, it is expected that convection also increases the neutrino emission of the dense core. However, as one can see in Fig. 5.8 this is not necessarily true. Whereas model Wolff–2D shows an enhancement of the neutrino number and energy fluxes for all times in the 2D model compared to the 1D model, model L&S–2D shows for some time a *reduction* of the neutrino luminosity. Since at the same time the neutrino number flux is *increased* this implies that model L&S–2D emits at this phase more neutrinos with lower mean energy than the corresponding spherically symmetric model[3]. Moreover the vigorous convection in the early phase of model Wolff–2D leads to very strong enhancement of the neutrino (number) emission. As Buras et al. (2006a) showed, an increased loss of lepton number (relatively to an 1D model) leads to a more extended proto–neutron star, while increasing the energy loss leads to a more compact core. This is absolutely consistent with our models, where *both* the neutrino number and energy losses in model L&S–2D tend to produce a more extended core, whereas in model Wolff–2D the effects work against each other, resulting in a smaller expansion of the proto–neutron star.

5.1.1. Excitation of g–mode oscillations

Recently, in a series of papers Burrows et al. (2006a,c,b) claimed to have found a new possible explosion mechanism of core collapse supernovae which is strongly coupled to the dense core. In their scenario *sound waves*, created by low–mode ($l = 1, 2...$) g–mode oscillations[4] of the proto–neutron star (with a typical period of 3 ms), travel outwards and power the explosion. The g–modes are excited by the mass accretion flows onto the dense core, which acts like an excited oscillator and emits the sound waves. Burrows et al. claim that this might be a robust explosion mechanism, since as long as a supernova does not explode, accretion on the neutron star goes on and acoustic flux can be generated. Furthermore the authors claim that supernova modellers will observe this mechanism if they a) calculate the models from north to south–pole, b) calculate the model in 2D without treating any whatsoever small part of the core in 1D (as we do in our 2D–models)[5], and c) calculate to long enough times (i.e. $t_{\rm pb} > 1$ s).

As striking and interesting this new idea is, however, some points need to be mentioned here:

- Firstly, it is *very* likely that proto–neutron stars can be excited to oscillations. However, whether the energetics allow to power a supernova explosion is debatable.

- Secondly, though in principle mass accretion on the core proceeds as long as a supernova does not explode, the mass accretion rate drops dramatically during the first few hundred ms (from several $M_\odot$ /s to a few hundredth $M_\odot$ /s, see e.g. Fig. 2 in Burrows et al. 2006c), whereas the proto–neutron star becomes more massive (typically $1 - 2 M_\odot$). This makes it

[3] The same behaviour was already found in Buras et al. (2006a).
[4] In gravity–modes or g–modes the gravity acts as restoring force (for details, see e.g. Finn 1986, 1987).
[5] We will discuss this in more detail in the next Section.

difficult to continously re–excite the core to oscillations and converse this energy (minus the losses) in acoustic power at times larger than a few hundred ms[6].

- Thirdly, the fact that in Burrows et al. (2006a,c,b) the explosion sets in suddenly without any indication of why at this particular time shows that this mechanism has to be studied in great detail in order to understand and judge it properly.

Nevertheless, given the fact that this energy transfer proposes an interesting alternative to the standard supernova explosion mechanism paradigm, we have searched for the possibility of such a new mechanism to occur in our 2D–simulations. However, simply the long simulation times needed by Burrows et al. in order to see this new phenomena makes it impossible for us to do a comparison calculation. What we *can* do is to analyse our models looking for the excitation of the core oscillations that should be visible after a few hundred ms after the shock formation (see, e.g. Fig. 7 in Burrows et al. 2006a).

In a core collapse supernova an oscillating neutron star embedded in the accretion atmosphere below the shock front inevitably causes pressure fluctuations in the fluid. In order to be consistent with Burrows et al. (2006a) we analyse our models for such pressure fluctuations and expand these into spherical harmonics, in order to see the mode spectrum. Thus one can write

$$P_{\rm fluc}(r,\theta,t) := \frac{P(r,\theta,t) - \langle P(r,t)\rangle_\theta}{\langle P(r,t)\rangle_\theta} \text{ and then} \tag{5.2}$$

$$P_{\rm fluc}(r,\theta,t) = \sum_{l=0}^{\infty} a_{l,0}(r,t) Y_{l,0}(\theta)\,, \tag{5.3}$$

where again rotational symmetry around the polar axis (cf. Eqn. 4.5) was used. Indeed, as Figs. 5.9 – 5.10 confirms, the proto–neutron star shows low g–mode oscillations in our simulations. We observe that all modes are excited with roughly equal strength and no mode seems to be suppressed. Independent of the used EoS, or the radius where the modes are measured, we find that the $l = 1$ mode starts to grow at 150 to 200 ms after the shock formation. However, the amplitudes reached are larger for the L&S–EoS for $r > 25$ km. Nevertheless we find amplitudes roughly two orders of magnitude smaller than the ones reported by Burrows et al. (2006a), see Fig. 7 in their paper. This discrepancy is already present at a time $t_{\rm pb} < 300$ms where we can compare our results to the ones of Burrows et al. (2006a). Since we were not able to calculate our models to longer times, we can not say if the oscillations in our models will grow to their predicted strength at later times. Furthermore the models of Burrows et al. are calculated in Newtonian gravity, whereas we apply general relativistic corrections. Thus it might be possible that this also causes a different growth of modes[7]. Looking more carefully at model Wolff–2D, one finds that the $l = 1$ mode shows a higher frequency (period of 3–4 ms) for $r < 25$ km and

[6] A way around this problem would be that the excitation of the oscillations stem from the early phase when the mass accretion rate is still high. However, then the damping and conversion of kinetic energy in sound waves must be small so that the oscillation is still present at later times. Which of course leads to the following question: Why will then — *suddenly* — the conversion of energy become more efficient and trigger the explosion?

[7] If, however, the growth of the modes and thus this new explosion mechanism depends on the formulation of gravity then fully general relativistic models are necessary to give a final answer.

a smaller one (period of 9–10 ms at $r = 35$km) for $r > 30$ km, see Figs. 5.11 – 5.13. Since in this region convection appears and than disappears, remember Fig. 5.2, this shows that the modes are influenced by the convective regions. A frequency change of $l = 1$ mode across the convective region is also observed in model L&S–2D.

5.1.2. Testing the code ability to follow neutron star g–modes: artifically triggered neutron star oscillations

As we have seen in the previous Section we find the existence of low frequency g–modes in the dense supernova core in our 2D–simulations. However, from the point of view of Burrows et al. (2006b) our numerical treatment in M DB TH to calculate the innermost 1.6 km of the star in spherical symmetry does not allow to excite core oscillations. Indeed, one may believe that a spherically symmetric centre of the core does only allow the excitation of *even* ($l = 2, 4$,...) modes which do not imply fluid flow through the centre, whereas *uneven* modes may be suppressed since they require mass flow through the (1D) centre. However, this is in contradiction to the fact that we find modes — even and uneven ones — with roughly equal strength, which implies that the growth of uneven modes is not suppressed, and the growth of even ones is not favoured. This for itself is already a strong argument for the ability of our numerical scheme to follow such neutron star excitations.

Nevertheless, we came up with a numerical test which proves the ability of our code to follow the lowest possible mode (i.e. $l = 1$): On a existing 2D–simulation we artifically imposed a velocity field in the proto–neutron star which triggers the excitation of a $l = 1$ mode. We then followed the subsequent evolution and checked whether our code does rigorously damp this mode.

For this purpose we have chosen two radii r_2 and r_3 inside the proto–neutron star, but outside of the spherically core with $r_1 = 1.6$ km. Inside the spherical shell with $r_1 < r < r_2$ we added a constant velocity ${v_z}^1$ in z–direction (i.e. along the polar axes) to the already existing velocity field. In the spherical shell with $r_2 < r < r_3$ the same procedure was applied, however, here the velocity ${v_z}^2$ was chosen such that the total momentum of the system is conserved. A sketch of this procedure can be seen in Fig. 5.14.

As we explained in Chapter 2, in a 2D–simulation the gravitational potential *including* general relativistic effects is calculated from a 2D Newtonian potential with 1D corrections for relativistic effects. Thus the general relativistic potential always includes a spherical monopole contribution, which does not follow the neutron star oscillations in our test calculations. One may argue that this leads to unpredictable behaviour of mode excitation. However, normally neutron star oscillations are investigated in the so–called Cowling approximation (Cowling 1941), where the gravitational forces are considered *constant*, which is a stronger restriction than the monopole contribution in our code. But to investigate the influence of this monopole term on the oscillations we have also perturbed a Newtonian model, where the gravitational potential is calculated in its "2D–beauty" without the need of a monopole term[8].

This perturbed Newtonian model is based on model L&S–2D–New, which was calculated with Newtonian gravity, the L&S–EoS, on a full 180° computational domain. As progenitor

[8]Then, of course, the radius $r_1 = 0$, since no spherically symmetric 1D–core is present.

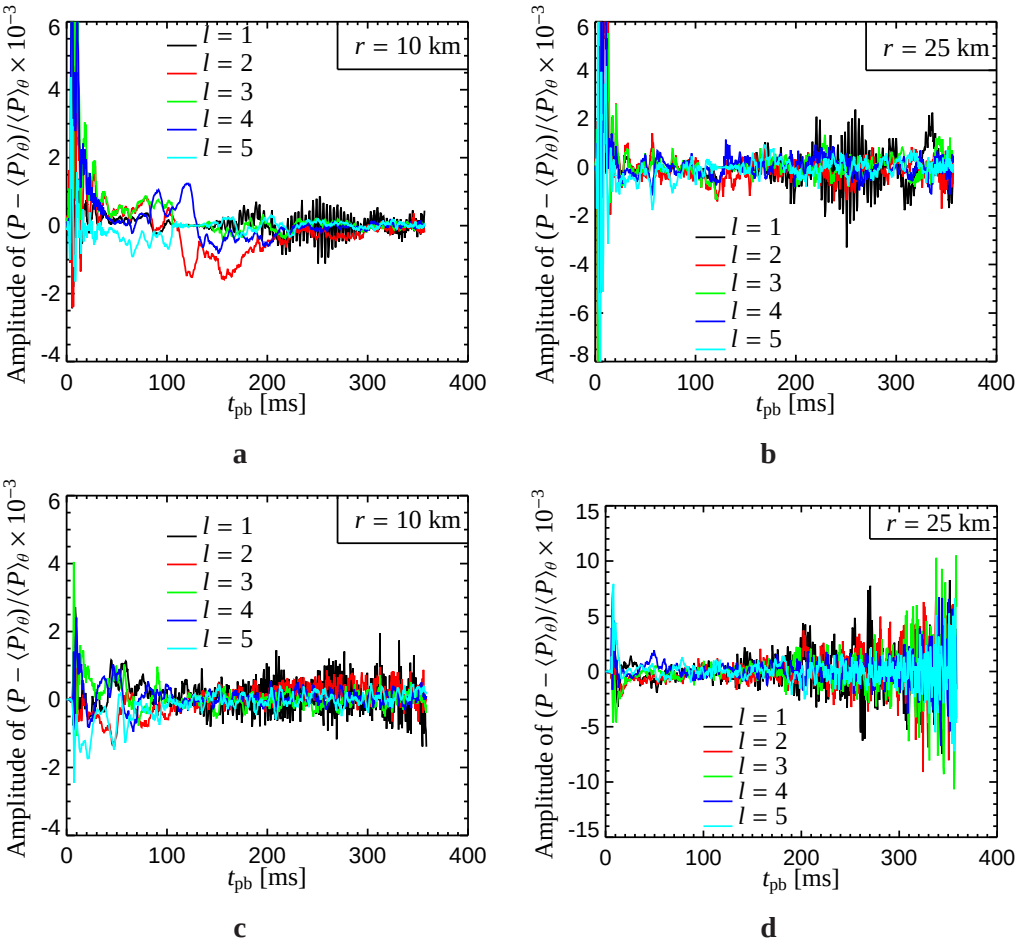

Figure 5.9.: The amplitudes of the expansion into spherical harmonics of the pressure fluctuations $(P - \langle P\rangle_\theta)/\langle P\rangle_\theta$ on spheres with radius r of 10 km and 25 km, respectively **a, b**: model Wolff–2D **c, d**: model L&S–2D. Note that different radii r are shown in Fig. 5.10.

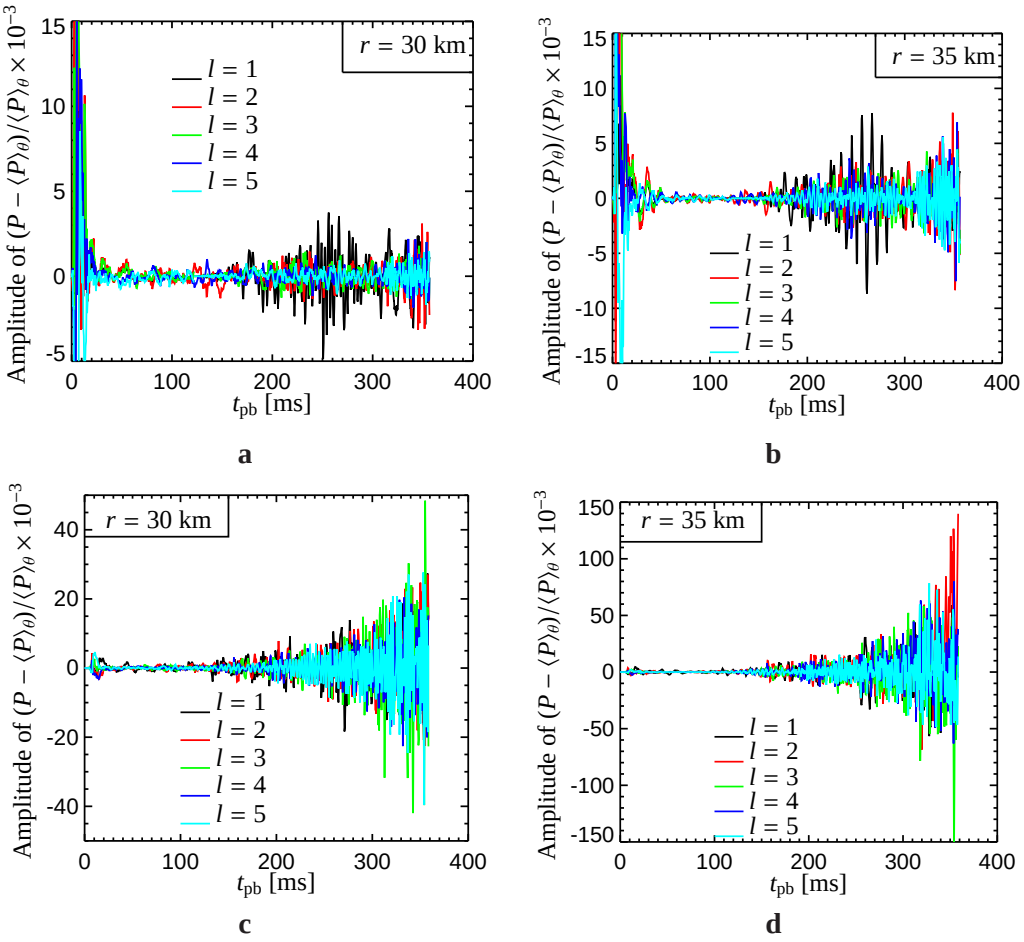

Figure 5.10.: The amplitudes of the expansion into spherical harmonics of the pressure fluctuations $(P-\langle P\rangle_\theta)/\langle P\rangle_\theta$ on spheres with radius r of 30 km and 35 km, respectively **a, b**: model Wolff–2D **c, d**: model L&S–2D. Note that different radii r are shown in Fig. 5.9.

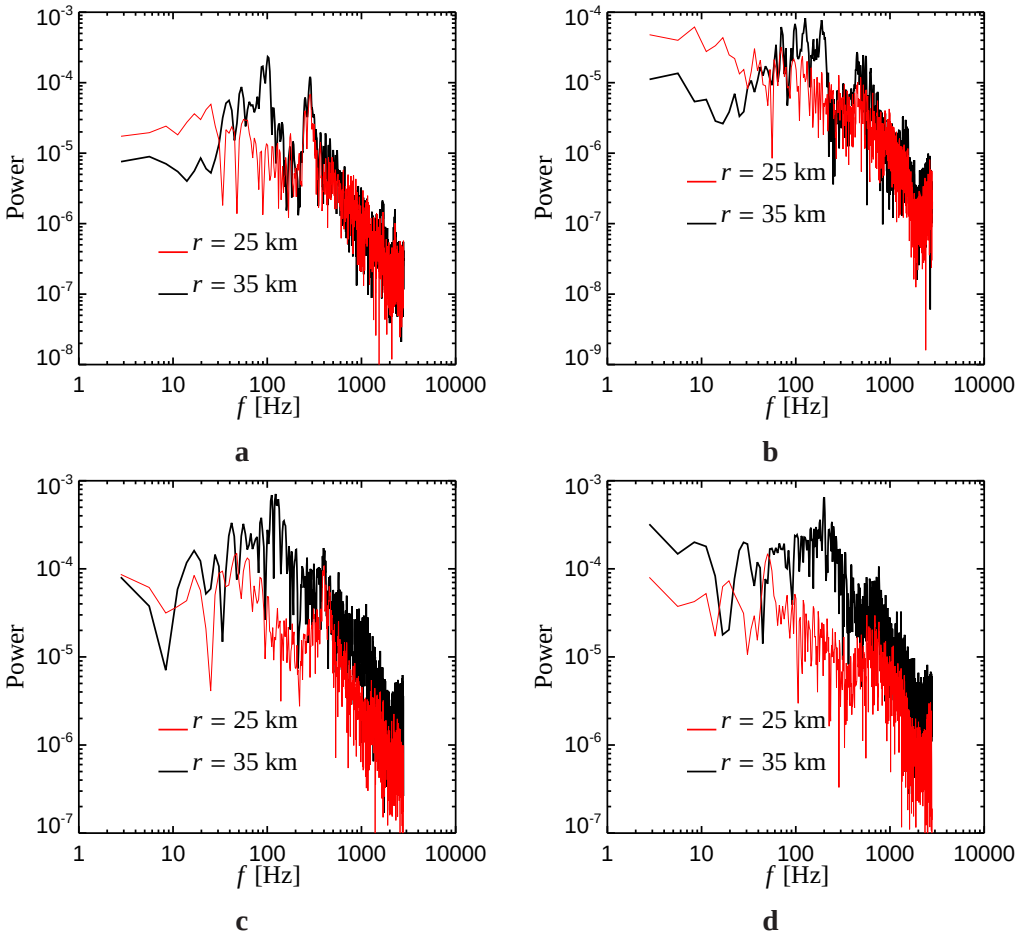

Figure 5.11.: The Fourier decomposition of the different g–mode oscillations at two radii of 25 km and 35 km, respectively. The upper row depicts model Wolff–2D, the lower row model L&S–2D. **a**: $l = 1$ **b**: $l = 2$ **c**: $l = 1$ **d**: $l = 3$ Note that different modes are shown in Figs. 5.12 and 5.13.

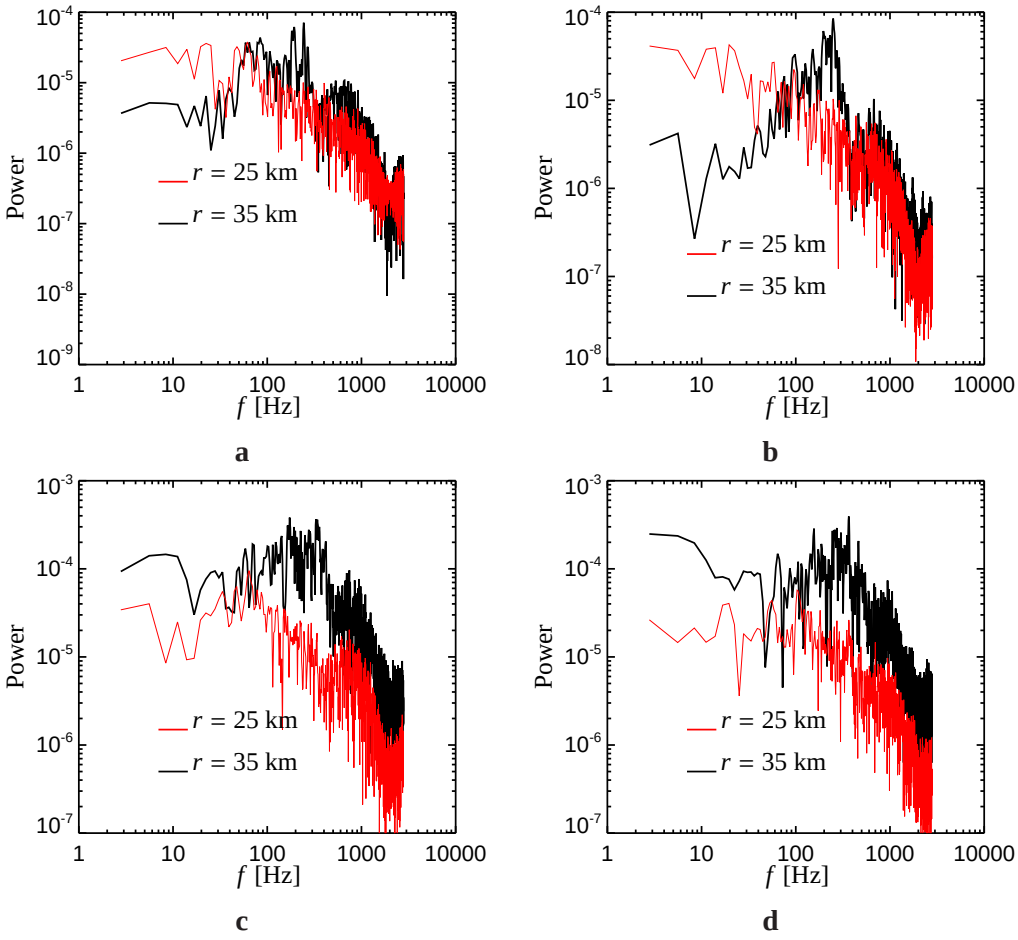

Figure 5.12.: The Fourier decomposition of the different g–mode oscillations at two radii of 25 km and 35 km, respectively. The upper row depicts model Wolff–2D, the lower row model L&S–2D. **a**: $l = 3$ **b**: $l = 4$ **c**: $l = 3$ **d**: $l = 4$ Note that different modes are shown in Figs. 5.11 and 5.13.

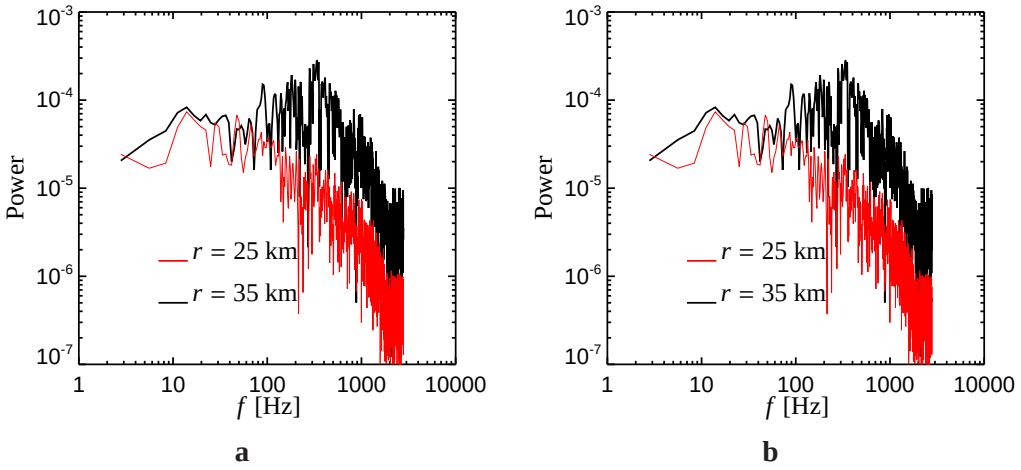

Figure 5.13.: The Fourier decomposition of the different g–mode oscillations at two radii of 25 km and 35 km, respectively. **a**: $l = 5$ in model Wolff–2D. **b**: $l = 5$ L&S–2D. Note that different modes are shown in Figs. 5.11 and 5.12.

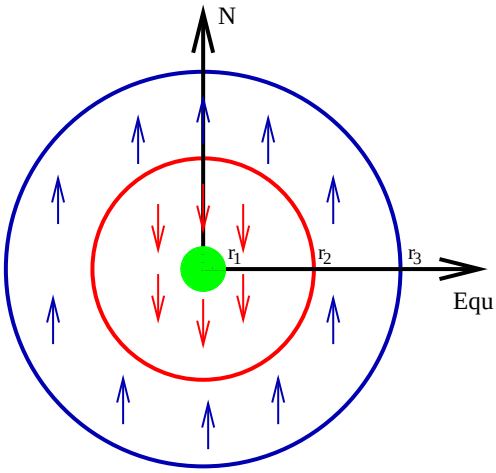

Figure 5.14.: A sketch of the velocity field that is superimposed on the existing velocity field in our test calculations. Note the values of r_2, r_3, v_z^1 (red arrows), and v_z^2 (blue arrows) are chosen such that the perturbation resides well inside the electron neutrinosphere, momentum is conserved, and that the masses inside the shells are roughly equal, The green region denotes the innermost 1.6 km of our models were we use a 1D calculation.

Model	r_1 [km]	r_2 [km]	r_3 [km]	${v_z}^1$ [cm/s]	${v_z}^2$ [cm/s]	$E_{\rm kin}$ [erg]	Φ
GR–5e7	1.6	15	50	5×10^7	-5×10^7	3.66×10^{48}	GR
GR–2e8	1.6	15	50	2×10^8	-2×10^8	5.86×10^{49}	GR
NEW–5e7	0.	14	49	5×10^7	-5×10^7	3.66×10^{48}	Newt.

Table 5.1.: Overview over all test models. Stated are the radii of the shells were the velocities ${v_z}^1$ or ${v_z}^2$ were superimposed. Also stated are whether a general relativistic correction to the gravitational potential was applied.

model the same $15\,M_\odot$ progenitor model of Woosley & Weaver (1995) was used which also the models Wolff–2D and L&S–2D are based on.

An overview over all test models that were perturbed artificially is given in Table 5.1, where we state the size of the perturbations and the radial shells within which we applied the perturbations. Furthermore we give the value for the kinetic energy that we artifically fed into the neutron star movement when we added the velocity field.

Figures 5.15 and 5.16 show convincingly that the M DB T code is numerically able to follow an $l = 1$ mode inside the neutron star once it is excited. More importantly, our method only excites the $l = 1$ mode and no rapid damping of this mode or a growth of higher order modes is observed. Again we observe a frequency change in the region where neutron star convection begins, see Fig. 5.17. Thus, the code is able to follow an $l = 1$ mode very accurately as well in amplitude as in frequency, although we replace the inner 1.6 km of the 2D–core by a spherically symmetric core. Thus the fact that we do not observe as large g–mode amplitudes as Burrows et al. in our models Wolff–2D and L&S–2D *cannot* be justified by the argument that our code is not able to *follow* these modes[9]. Furthermore a comparison of models GR–5e7 and GR–4e8, where in the later model the artifically input of kinetic energy is 16 times larger than in model GR–5e7, shows that the amplitudes grow almost exactly by a factor of four, which corresponds to the factor of four higher values of the perturbation velocity. Thus, though the energy input in model GR–4e8 was about 0.6×10^{50} erg, the growth of the g–mode oscillations is still in the *linear regime* and the amplitudes stay at one to two orders of magnitudes below the ones observed by Burrows and collaborators. Though it is impossible to judge — without really doing the simulations — how much energy must be fed into the nascent neutron star in order to achieve a transition from the linear regime into a non–linear growth of the g–mode amplitudes, we conclude that in our model this energy input is larger than 0.6×10^{50} erg. Since it seems logical that in an unperturbed model which should show the same g–mode amplitudes as reported by Burrows et al. a similar kinetic energy transfer to the dense core is required, an efficient mechanism to excite the neutron star oscillations must be proved to exist. This mechanism must transfer enough energy that the amplitudes can grow in a reasonable time to the required values. Yet, the existence of such a mechanism is not proved and in our models the amplitudes do not reach the values which are reported by Burrows and collaborators.

Finally, in Figs. 5.18a and 5.19a we show the conservation of the z–component of the momen-

[9] It may, however, still possible that the M DB TH–code is not able to compute the natural *excitation* of these modes correctly.

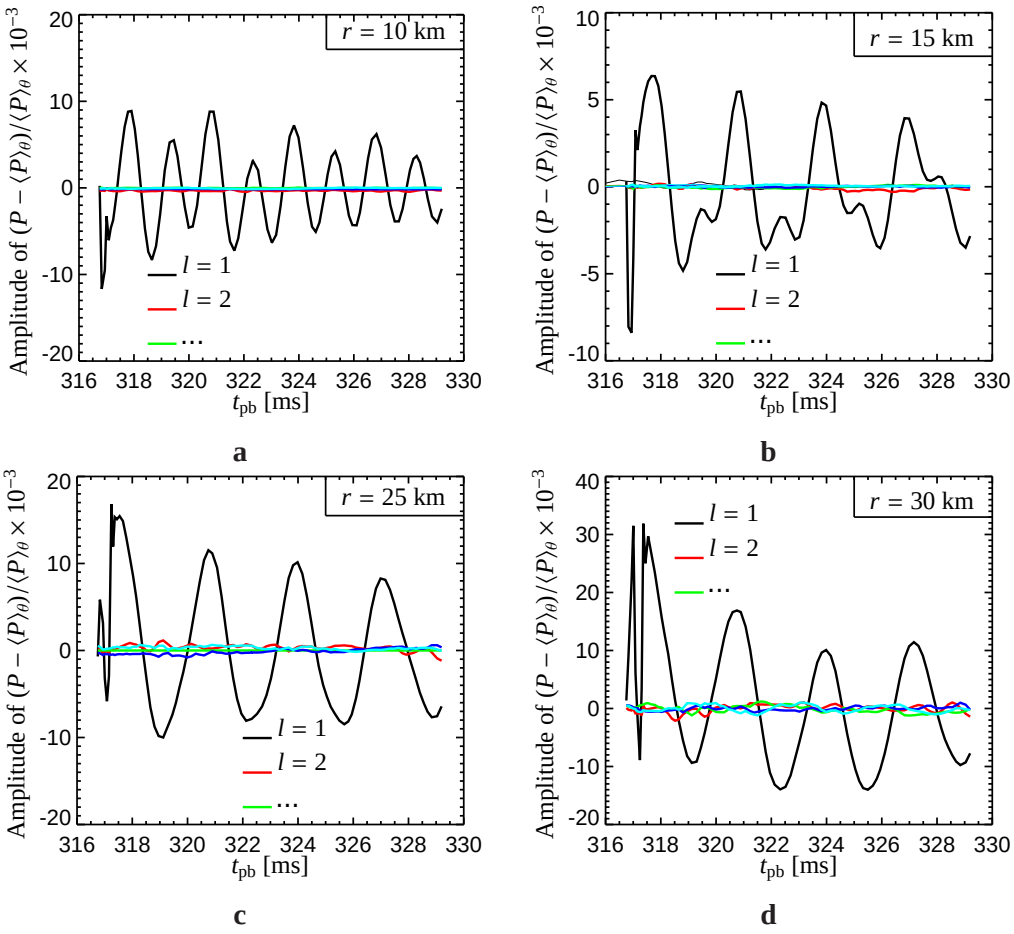

Figure 5.15.: The amplitudes of the expansion into spherical harmonics of the pressure fluctuations $(P-\langle P\rangle_\theta)/\langle P\rangle_\theta$ on spheres with radius r for model GR–5e7. In this model an artificial $l = 1$ mode was excited inside the dense core by adding a velocity field with an amplitude of 5×10^7 cm/s. **a**: at 10 km **b**: at 15 km **c**: at 25 km **d**: at 30 km.

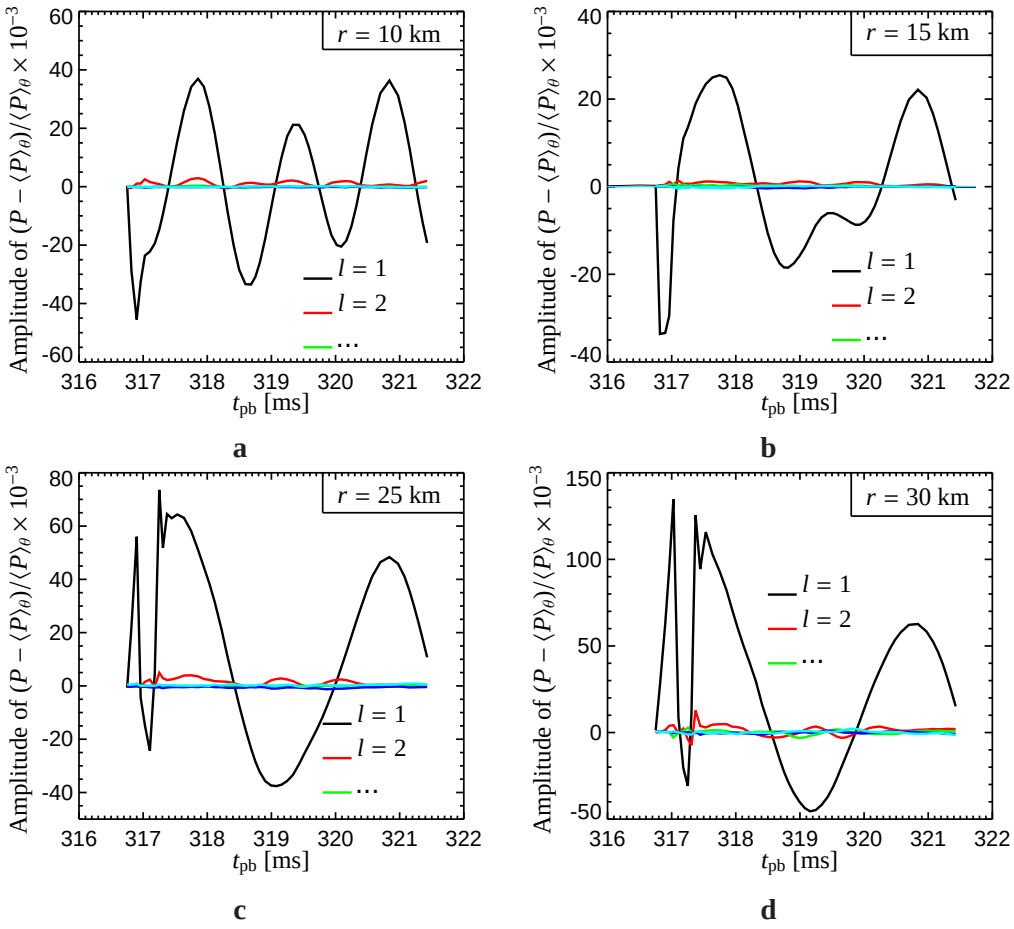

Figure 5.16.: The amplitudes of the expansion into spherical harmonics of the pressure fluctuations $(P-\langle P\rangle_\theta)/\langle P\rangle_\theta$ on spheres with radius r for model GR–2e8. In this model an artificial $l = 1$ mode was excited inside the dense core by adding a velocity field with an amplitude of 2×10^8 cm/s. **a**: at 10 km **b**: at 15 km **c**: at 25 km **d**: at 30 km.

tum for models Wolff–2D, GR–5e7, and GR–2e8. Clearly, momentum is conserved nicely in model Wolff–2D. The artificially perturbed models GR–5e7 and GR–2e8 show a oscillation of the momentum due to the motion of the core. In Figs. 5.18b and 5.19b we depict the amount of displacement of the core from the grid centre one obtains from the evolution of the momentum. Clearly, on average the core does not move. We also show the movement a mass shell located at $r = 10$ km, which is caused by the artificially excitation of the $l = 1$ g–mode.

Figure 5.20 shows the amplitudes of the expansion of the pressure fluctuations for model NEW–5e7. Although the amplitudes are of the same order of magnitude as the ones in the calculations including general relativistic effects, no nice oscillations can be observed in model NEW–5e7. In contrast to the test calculations GR–5e7 and GR–2e8 we also find that in model NEW–5e7 not only the $l = 1$ mode is excited but rather we find non–zero (but roughly con-

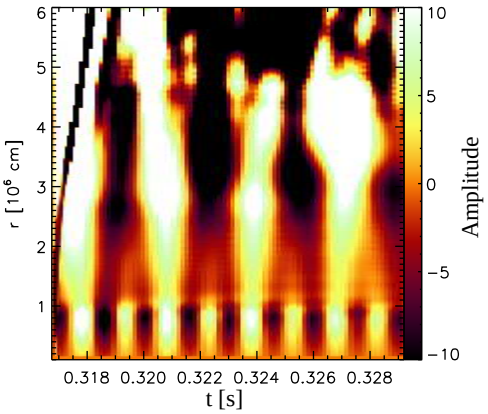

Figure 5.17.: The amplitudes of the $l = 1$ mode of the expansion into spherical harmonics of the pressure fluctuations $(P - \langle P \rangle_\theta)/\langle P \rangle_\theta$.

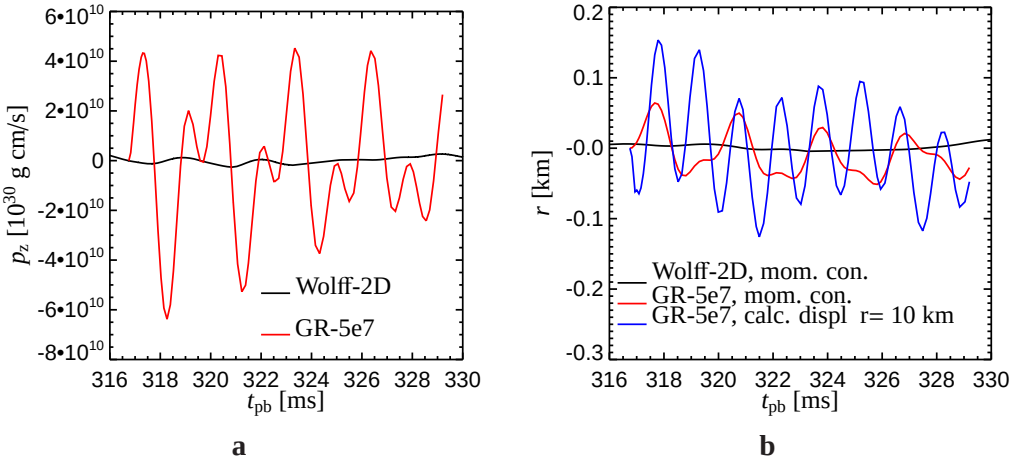

a **b**

Figure 5.18.: **a**: The z–component of the momentum evaluated on the computational domain. **b**: The radial displacement that would result from the momentum evolution in panel a. Also shown is the movement of a mass shell located at $r = 10$ km due to the perturbation that was imposed in the dense core. This movement is calculated from a time integration of the velocity at a radius $r = 10$ km.

stant) contributions of higher order modes, which implies that the dense core in our Newtonian calculation shows some deformation. The reason for this is found studying Fig. 5.21 where the momentum conservation is shown for the Newtonian models. Even in the unperturbed model we find a small violation of momentum conservation (building up around 20 ms after the shock formation). Despite the fact that the net value of this momentum conservation violation is very small it leads to a drift of our core of about 80 m in 40 ms, which corresponds to a velocity of 2 km/s. This leads to the deformed dense core, which explains the contribution of spherical harmonics with $l > 1$ in Fig. 5.20. It also explains why we do not find an oscillation around the centre in our artificially perturbed model. The momentum violation we observe in the Newtonian model is very small and causes only a small drift compared to the oscillation we excited

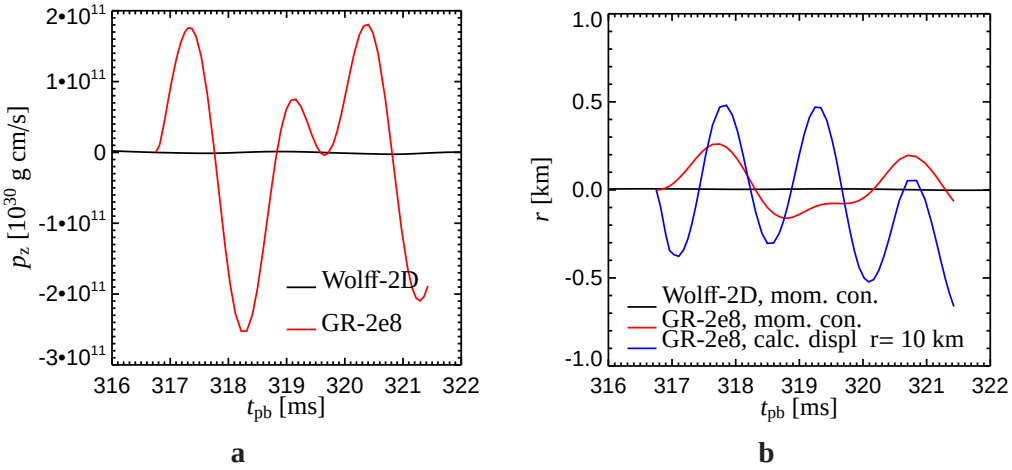

Figure 5.19.: **a**: The z–component of the momentum evaluated on the computational domain. **b**: The radial displacement that would result from the momentum evolution in panel a. Also shown is the movement of a mass shell located at $r = 10$ km shows due to the perturbation that was imposed in the dense core. This movement is calculated from a time integration of the velocity at a radius $r = 10$ km.

in Model NEW–5e7, see Fig. 5.21b. Also in the unperturbed model the drift is so small that it needs 150 ms in order that the centre of the nascent neutron star leaves the first grid zone (width = 300 m). Nevertheless, it is quite unsatisfactory that in a Newtonian model a small momentum violation is found, although physically momentum conservation must be ensured. In Appendix C we will thus discuss this problem in more detail.

Though model NEW–5e7 revealed that in a calculation with Newtonian gravity the M DB TH code produces a small momentum conservation violation, our conclusion from the various test model still holds: treating the inner most 1.6 km of the computational domain as a spherically symmetric core does not hamper the excitation of a $l = 1$ g–mode oscillation. Furthermore, once such a mode is (artificially) excited our numerical scheme is well suited to follow this mode.

Summary

We have found that different nuclear EoS may lead to totally different growth of convective instabilities inside the forming neutron star. On the one hand the time when convection starts can be different but then, of course, also the kinetic energy contained in the convective flow — which is a measure for the strength of convection — can develop differently. The strength of convection is in our results strongly connected to the size of the convectivly unstable regions. Whereas model L&S–2D develops at late times a “fully” convective layer between the neutrinosphere and a mass coordinate of roughly $0.5 M_\odot$ model Wolff–2D shows except for the first few 10 ms, a stability stripe that separates the neutrinosphere from the convective core. The structural changes of the neutron star, due to different convection patterns, lead then to

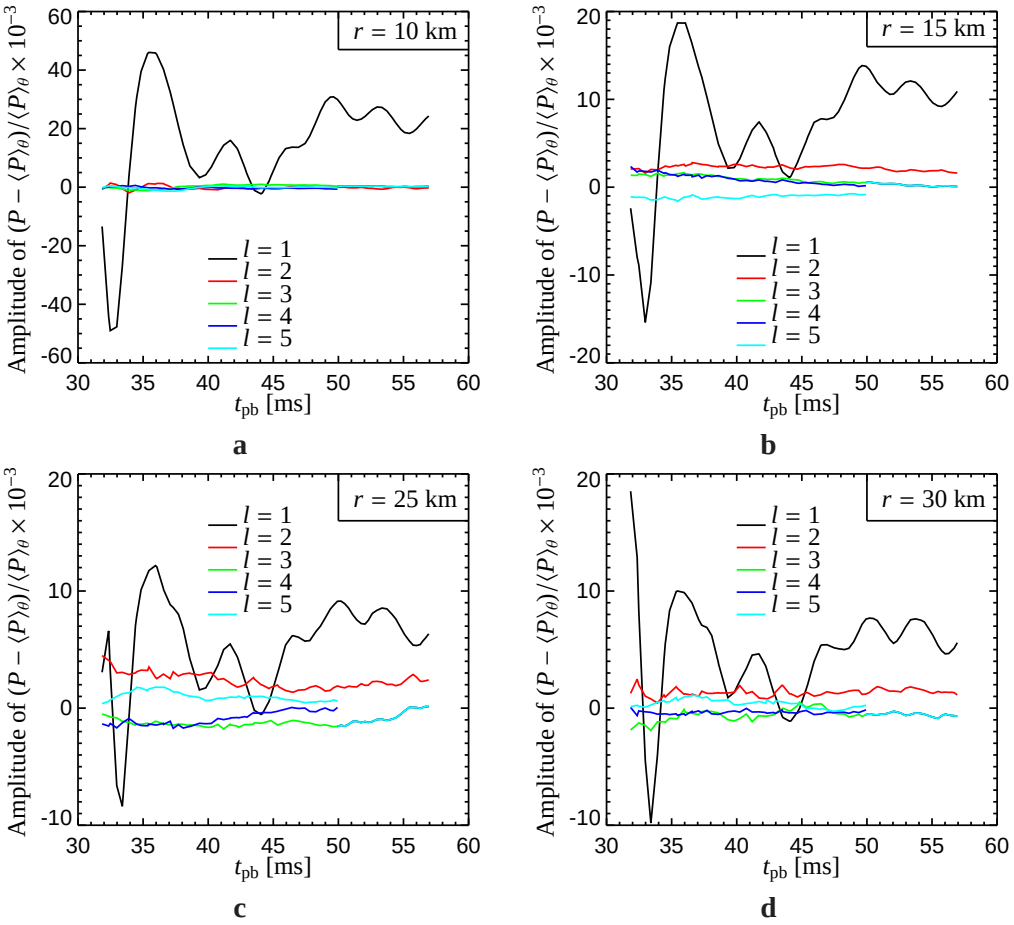

Figure 5.20.: The amplitudes of the expansion into spherical harmonics of the pressure fluctuations $(P - \langle P\rangle_\theta)/\langle P\rangle_\theta$ on spheres with radius r for model NEW–5e7. In this model an artificial $l = 1$ mode was excited inside the dense core by adding a velocity field with an amplitude of 5×10^7 cm/s. **a**: at 10 km **b**: at 15 km **c**: at 25 km **d**: at 30 km.

differently extended cores and neutrino emissions compared to the non–convective spherically symmetric models. These changes definitely feedback on the accretion layer, the neutrino heating, the development of "hot–bubble" convection between the gain radius and the shock front, and thus also on the shock evolution, which will be discussed in Section 5.2.

Concerning the neutron star g–mode oscillations we have found — with several test calculations — that our numerical treatment is well suited to follow these oscillations. Furthermore, we have found that the amplitude of these excitations of the dense core is EoS dependent; in a simulation with a softer EoS and thus compacter dense core we find stronger oscillations (at least a factor of two in amplitude) compared to a simulation with a stiff EoS. This result is clearly interesting with regard of the new explosion mechanism proposed by Burrows et al. (2006a). However, even with the soft EoS, where the amplitudes are largest, we find at least 10

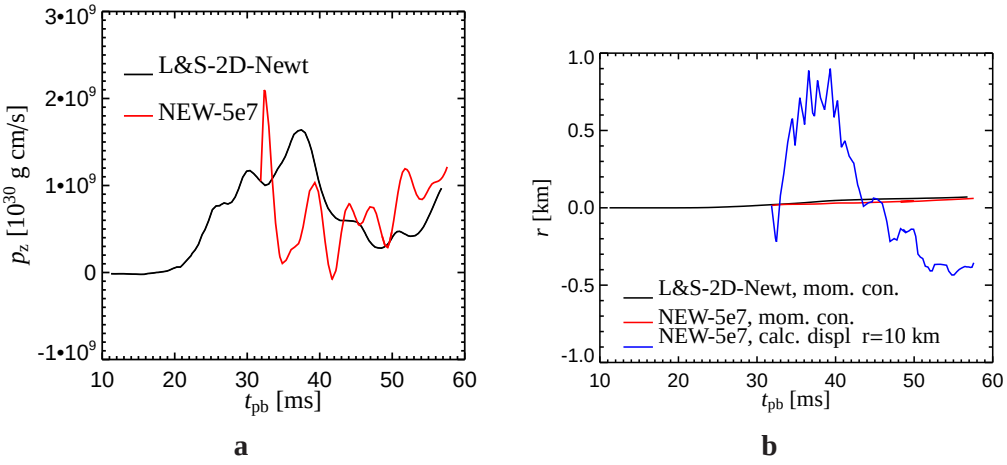

Figure 5.21.: **a**: The z–component of the momentum evaluated on the computational domain for the Newtonian calculations. **b**: The radial displacement that would result from the momentum evolution in panel a. Also shown is the movement a mass shell located at $r = 10$ km shows due to the perturbation that was imposed in the dense core.

times smaller amplitudes then the ones observed by Burrows et al. in their calculations. Thus we conclude that although the excitations of the dense core appear we cannot see any indication of an acoustic–driven explosion.

5.2. The growth of “hot bubble” convection and shock instabilities

In the previous Section 5.1 it was shown that different EoSs influence strongly the growth of convection inside the proto–neutron star, the proto–neutron stars structure, and its neutrino emission. Naturally, it is important to investigate how this couples to the overall supernova evolution. We have already discussed that in *spherically symmetric* models a larger extended neutron star “pushes” the shock position farther outwards. In multi–dimensional models the problem is a more complicated one: Firstly, the assumption of an hydrostatic accretion atmosphere, which was used to link the shock position to the radius of the inner core (cf. 3.7 in Section 3.2), breaks down, as soon as hydrodynamic instabilities (i.e. convection) develops in the accretion layer[10]. Secondly, convection below the shock front itself deforms the shock and leads to an angularly dependent shock expansion or retreat. Thirdly, other shock instabilities such as the advective-acoustic cycle Foglizzo & Tagger (2000), Foglizzo (2001, 2002), Blondin et al. (2003) do develop in multi–dimensional simulations even if hot bubble convection is weak

[10]To separate these convective flows from the convection *inside* the proto–neutron star, this convection is commonly called “hot bubble” convection, due to the fact that one observes the rising and falling of bubbles of hot and cool material.

or not present at all, see Scheck (2006). However, these processes are supposedly all subject to the influences of the equation of state for the following reasons:

- It is natural to assume that the strength and structure of *hot bubble convection* depends on the neutrino heating and on the positions of the neutron star radius, the gain radius, and the shock position, which define the "volume" where hut bubble convection can develop. As we have already discussed the EoS influences all of these conditions.

- The *advective acoustic cycle* depends strongly on the position of the so called "coupling radius" where the advection flow towards the dense core is strongly de-accelerated, see Scheck (2006). First, order this coupling radius is set by the position of the electron neutrinosphere, which again is influenced by the EoS.

We start our discussion of the EoS effects on the overall supernova evolution by showing in Fig. 5.25 some differences between the two–dimensional and corresponding one–dimensional simulations for the neutrino luminosities, rms energies, and heating rates. First, one can see from Figs. 5.25a,b that the time evolution of the neutrino luminosities is very similar in spherically symmetric and 2D–simulations. However, the luminosities decrease slightly in multi–dimensional simulations as was already discussed in Buras et al. (2006a). The reason for this is found in a different structure of the dense core and accretion layer, that leads to lower neutrino temperatures T_ν, and thus less neutrino emission. For the same reason also the rms neutrino energies drop, see Figs. 5.25c,d. Nevertheless, the comparison between the runs with the different nuclear EoS reveals that in 2D–simulations the same effect is observed as in 1D–simulations (see also Section 3.2) : a softer EoS produces higher luminosities and (rms) neutrino energies, because a more compact core — which as we have shown in Part I of this thesis is the consequence of a softer EoS — allows that more gravitational binding energy is converted into neutrino emission. Although the neutrino heating and cooling of matter is reduced in a 2D–simulation compared to a 1D–simulation (since the luminosities and neutrino energies are reduced), this nevertheless results in the fact that even in a 2D–simulation a softer EoS leads to stronger neutrino cooling but also neutrino heating than a stiffer EoS, see Figs. 5.25e,f.

The neutrino energy deposition is almost angle independent, as one can deduce from Fig. 5.22, where we show snapshots of the heating at different times. Of course, the energy deposition shows an angle dependence if the shock does so. However, inside the heating and cooling region the values of the energy deposition do not vary largely as a function of the polar angle, except for the fact that convection distorts the surface of the cooling region. Obviously, model Wolff–2D develops at later times a more extended cooling region, but the absolute values of the cooling stay an order of magnitude below the ones of model L&S–2D. This, however is already observed in spherically symmetric calculations, remember Fig. 5.25e. Nevertheless, this clearly shows how strongly the EoS influences the structure of the accretion layer between the dense core and the shock front. Since Foglizzo has found (private communication) that the details of the advective–acoustic cycle depend strongly on the accretion atmosphere, the cooling region, and the position of strongest de-acceleration of fluid flow (see also Scheck 2006) this is another argument for the influence of the EoS on the standing accretion shock instability.

It is very interesting, that the EoS influence on the neutrino emission as well as the influence on the neutrino energy exchange with the stellar fluid is quite similar (e.g. the stiffness of the

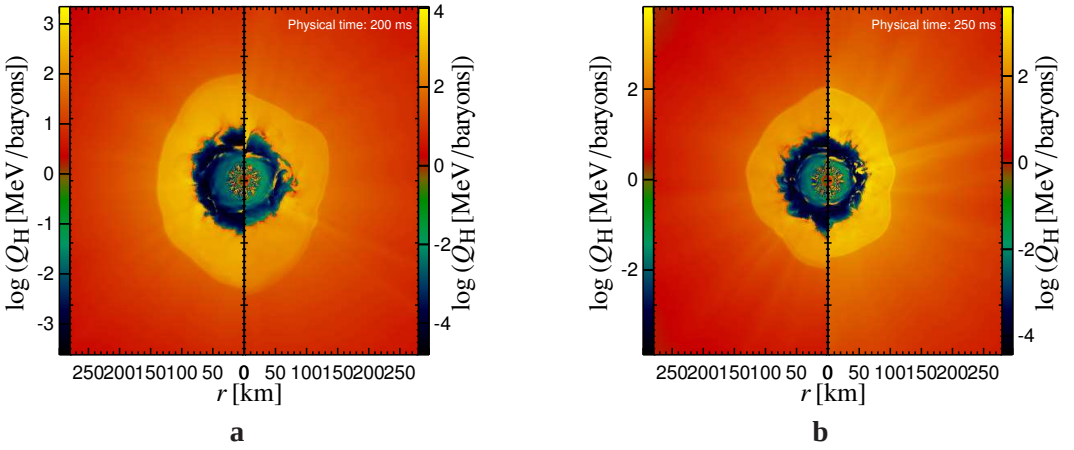

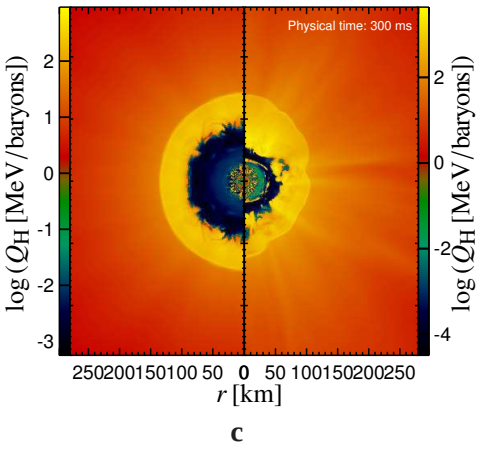

Figure 5.22.: Snapshots of the net neutrino heating source term at different times after the shock formation (**a**: 200 ms, **b**: 250 ms, **c**: 300 ms). The left hand sides of the snapshots depict the situation in model Wolff–2D, whereas the right hand sides depict the situation in model L&S–2D. Note, since the net neutrino heating term is positive in case of neutrino heating and negative if neutrino cooling is dominant, the following procedure was taken: $\log(Q_{\rm H}) := log(Q_{\rm H})$ if $Q_{\rm H} > 1$ MeV/baryon/s, $\log(Q_{\rm H}) := -log(-Q_{\rm H})$ if $Q_{\rm H} < -1$ MeV/baryon/s, and $\log(Q_{\rm H}) := 0$ if $-1 < Q_{\rm H} < 1$ MeV/baryon/s.

EoS controls the heating and cooling in a comparable way) in simulations applying radial or rotational symmetry.

Figure 5.23a depicts the total neutrino energy deposition in the gain layer. Due to the facts that model L&S–2D shows stronger neutrino heating and that the gain layer is more extended in this model, the neutrino energy deposition is at least 50% higher than in model Wolff–2D. As we will discuss in the following the EoS dependent neutrino heating and cooling — which behave very similar in spherically symmetric simulations, and in simulations applying rotational symmetry — leads in multi–dimensional simulations *together* with multi–dimensional effects (such as convection) to a noticeably changed supernova evolution. This can be seen in a compari-

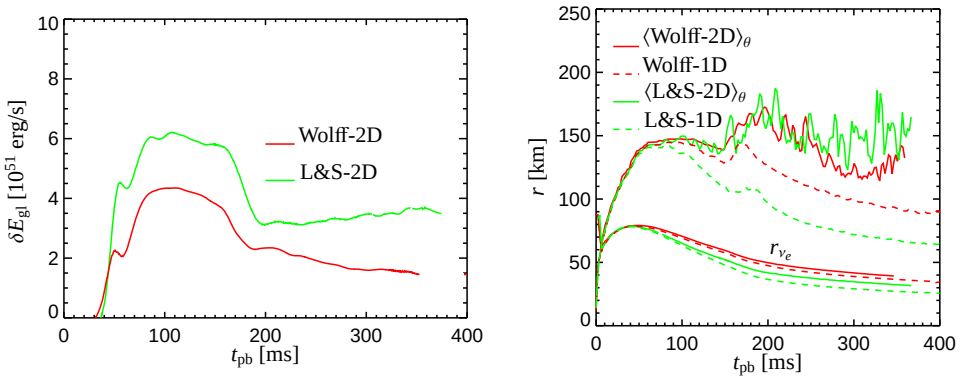

Figure 5.23.: **a**: The total neutrino energy deposition (cf. Eqn. 4.2) as function of time for models Wolff–2D and L&S–2D. **b**: The laterally averaged shock positions (upper solid lines) and the laterally averaged positions of the electron neutrinospheres of models Wolff–2D and L&S–2D. Also shown are the same quantities for the corresponding spherically symmetric models (dashed).

son of the laterally averaged shock position, see Fig. 5.23b, of models Wolff–2D and L&S–2D. Clearly, the model calculated with the L&S–EoS shows stronger 2D–effects than the model with the Wolff–EoS, since the switch from a spherically symmetric model to a 2D–model results in a much stronger expansion of the average shock position than in model Wolff–2D. This Figure impressively demonstrates that in multi–dimensional models an easy correlation between the radii of the neutron star and the shock can not be obtained. Though we only plot the laterally averaged shock positions one can see the already mentioned complex (oscillatory) time dependence of the shock position, which can be caused by (a combination) of convection and/or the advective–acoustic cycle. By expanding the shock radius $r_s(\theta, t)$ into spherical harmonics (cf. Eqn. 4.5) one gets a clearer impression of the shock instabilities in our two–dimensional models, see Fig. 5.26. Due to the early start of convection in model Wolff–2D shock deformations are immediately observed, which, however, are damped when this convection subsides. As convection grows again later, also the shock instabilities grow, but the amplitudes stay roughly a factor of two smaller than in model L&S–2D. A more comprehensive overview of this low–mode shock instability is given in Figs. 5.27 – 5.29, where we depict at different times contours of entropy and of the electron–fraction from the centre to a radius of 300 km. Obviously model Wolff–2D is much more stable against shock formations — and the shock stays more spherically — than model L&S–2D though both models develop volume filling convection in the hot bubble region between the dense core and the shock front. Especially at time between 200 ms and 350 ms after the shock formation an $l = 1$ deformation of the shock front is visible in model L&S–2D.

In Fig. 5.30a we show the lateral kinetic energy contained in convective motion in the gain region between the gain radius and the shock, cf. Eqn. 4.2, for both models. Again in model Wolff–2D we find at early times more energy contained in convective motion than in L&S–2D,

due to the fact that convection develops immediately in the model with the Wolff–EoS. As this convection subsides the lateral kinetic energy develops a local minimum, before it rises steadily during the later evolution. At this time the convective energy grows faster in model L&S–2D and at later times in this models a factor two to three more energy is contained in hot bubble convection. Though it is not possible to find a final reasoning why the model with the L&S–EoS develops a more energetic hot–bubble convection than model Wolff–2D, we suspect that this due to the fact that neutrino heating (the driving force behind the hot–bubble convection) is stronger in this model, since stronger temperature gradients in general supports the development of convection[11]. As we mentioned already in Section 4.2, an analysis of Foglizzo et al. (2005) suggests that the convection in model L&S–2D is probably not the dominant source for the development of the observed low–mode $l = 1, 2$ shock instabilities. Similar as in the explosion models of a $11.2\,M_\odot$ progenitor star, see Section 4.2, we suspect, that the advective-acoustic cycle and not convection is the driving force for the time and angular evolution of the standing accretion shock instability. In deed, an expansion of the local pressure into spherical harmonics, remember Eqn. 4.4 in Section 4.2, of both models reveals the existence of an advective–acoustic cycle, see Fig. 5.31. Thus, why does model Wolff–2D show only a moderate development of a shock asphericity, whereas model L&S–2D shows a strong evolution of a bi–pol mode ? Following in large parts the lead of Blondin & Mezzacappa (2006) we determine the power of the advective–acoustic cycle by

$$\text{Power(t)} = \int_{r_{\rm NS}}^{r_{\rm s}} a_{1,0}(r,t)^2\, r^2\, \mathrm{d}r \text{ , where} \tag{5.4}$$

$r_{\rm NS}$ and $r_{\rm s}$ are the radii of the neutron star and the shock front, respectively, and $a_{1,0}$ is the amplitude of the $l = 1$ contribution to the local pressure deviations from the mean pressure, cf. Eqn. 4.4. This analysis shows that the conditions in the calculation with the L&S–EoS are such that the cycle grows stronger than the one in model Wolff–2D, see Fig. 5.30b, and thus model L&S–2D shows a more dominant $l = 1$ shock deformation, and leads (at sometimes) to stronger shock expansion.

In both models we find rather similar advection timescales, see Fig. 5.24a. At the early times when the average shock radius is slightly larger in model Wolff–2D, see Fig. 5.23b, we also find a larger advection timescale in this model. At later times, when the average shock radius expands more strongly in model L&S–2D and at the same time the heating region becomes smaller (due to the growing of the cooling region) in model Wolff–2D, the advection timescale is slightly larger in model L&S–2D. However, these differences are small (due to the fact that the shock positions are quite similar) compared to the differences we observe in the heating timescales: as we have explained model L&S–2D shows stronger neutrino heating (at least 50%) which leads to a shorter heating timescale, see Fig. 5.24b. Though both models have not reached a condition which favours an explosion at a time of 300 ms after the shock formation, the situation is definitely more advantageous in model L&S–2D, see Fig. 5.24c, since the ratio of the advection timescale and the heating timescale is larger in this model. Furthermore, this ratio increases steadily at later times of the simulation. Continuing this simulation to larger

[11] As an analogy one may thing of a soup boiling on an oven that develops a stronger fluid flow if the heating is stronger.

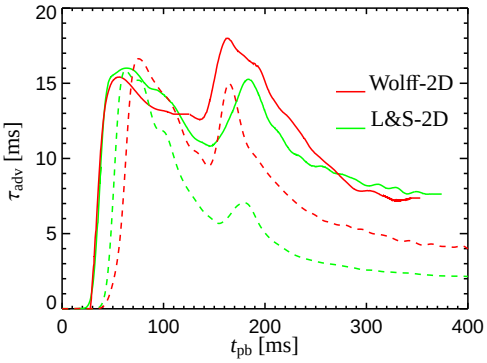

a

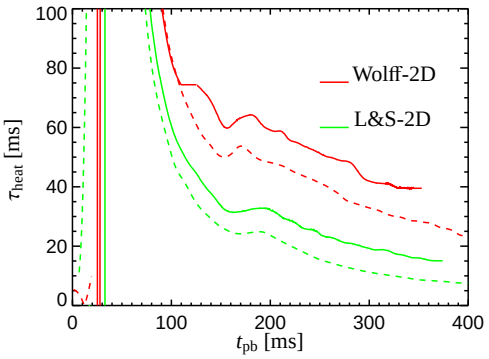

b

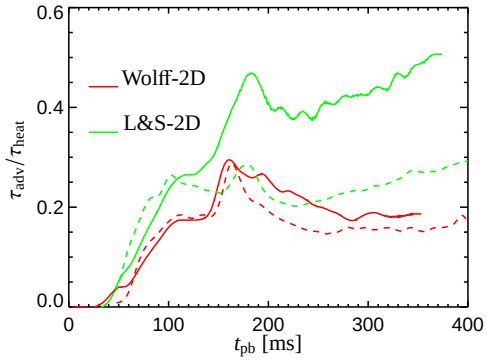

c

Figure 5.24.: **a**: The advection timescale for models Wolff–2D and L&S–2D. **b**: The heating timescale for the same models. **c**: The ratio of both timescales. In all panels the dashed lines represent the corresponding 1D–models.

evolution times is thus necessary in order to see whether this trend increases until an explosion sets in or whether the situation will change such that no explosion will be obtained at later times. Figure 5.24 once more clearly shows that an extrapolation from spherically symmetric simulations to 2D–simulations is not possible in a straightforward way.

Finally, an overview over the whole evolution of the models calculates so far is shown in Fig. 5.32, where we show for the laterally averaged 2D models and the corresponding 1D models trajectories of select mass shells and information of the dominant composition. A striking difference between our spherically symmetric and multi–dimensional models occurs in the region directly ahead of the shock front. Whereas in spherically symmetric models alpha–particles contribute in this region 60% of the mass fraction, this is not found in 2D–simulations. The explanation for this is that in the 2D simulations the shocks reach larger radii and “swallow” this region. More importantly, however, is the fact that we do not find alpha particles behind the shock front in the 2D models. Thus, the shock has not yet expanded to radii where the conditions are such that alpha–particles are formed by recombination of nucleons. This is important, since the shock would gain additional energy by the process, which would support the explosion.

Summary

The stronger convection and a stronger advective–acoustic cycle in mode L&S–2D leads to a conclusion that is not expected from spherically symmetric models: from the models of Section 3.2 one concludes that a stiffer EoS, like the Wolff–EoS, leads to more favourable conditions for an explosion. Though the stiff EoS shows less heating (and cooling) than a soft EoS, the more extended neutron star pushes the shock front to significantly larger radii. From this one may conclude that a stiff EoS is also more favourable than a soft EoS in multi–dimensional simulations. However, coming as a surprise, the conclusion from the 2D models discussed in this Section, is exactly the opposite. As in 1D models, we find in multi–dimensional simulations that a soft EoS produces a compacter core and leads to stronger heating and cooling. *But* this leads now to stronger convection and shock instabilities which seem to be more promising for an explosion. This is consistent with the analysis of Foglizzo et al. where it was found that a smaller cooling region with stronger cooling, leads to a sharper de-acceleration region of the accretion flow, which in turn leads to stronger advective–acoustic cycle. Thus, the EoS effects on the cooling region but also the of the neutrino heating of matter turn out to be far more important, than the different shock positions one obtains from spherically symmetric calculations.

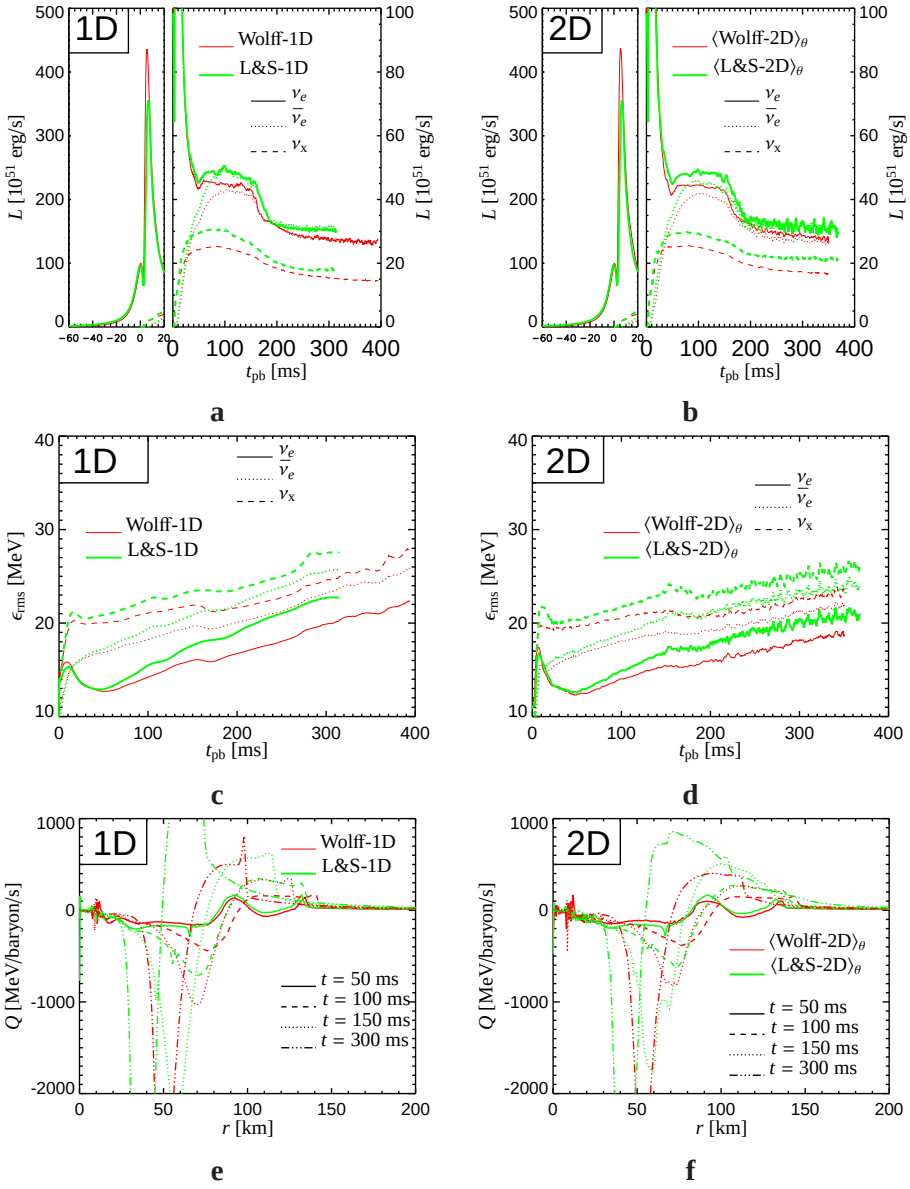

Figure 5.25.: Comparison between the spherically symmetric models (left panels) and the the 2D–models (right panels). The values for the 2D–models were obtained by averaging over the angle θ. **a-b**: The neutrino luminosities as function of time. **c-d**: The neutrino rms energies as function of time. **e-f**: The neutrino heating rates as function of radius at different times after the shock formation.

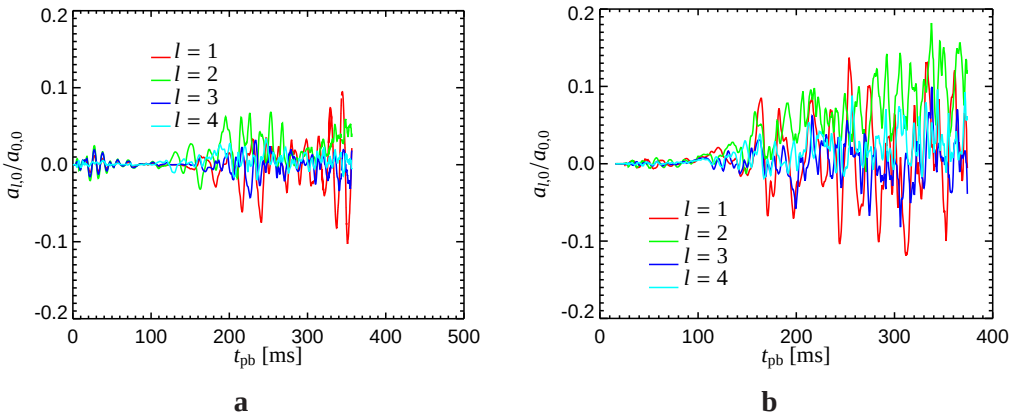

Figure 5.26.: The expansion of the shock position into spherical harmonics as function of time. The amplitudes $a_{i,0}$ are normalised to the monopole contribution $a_{0,0}$. **a**: model Wolff–2D. Note that in this model for the first 130 ms a 90° setup from north pole to equator was calculated, and later a switch to a full 180° model was done. **b**: model L&S–2D.

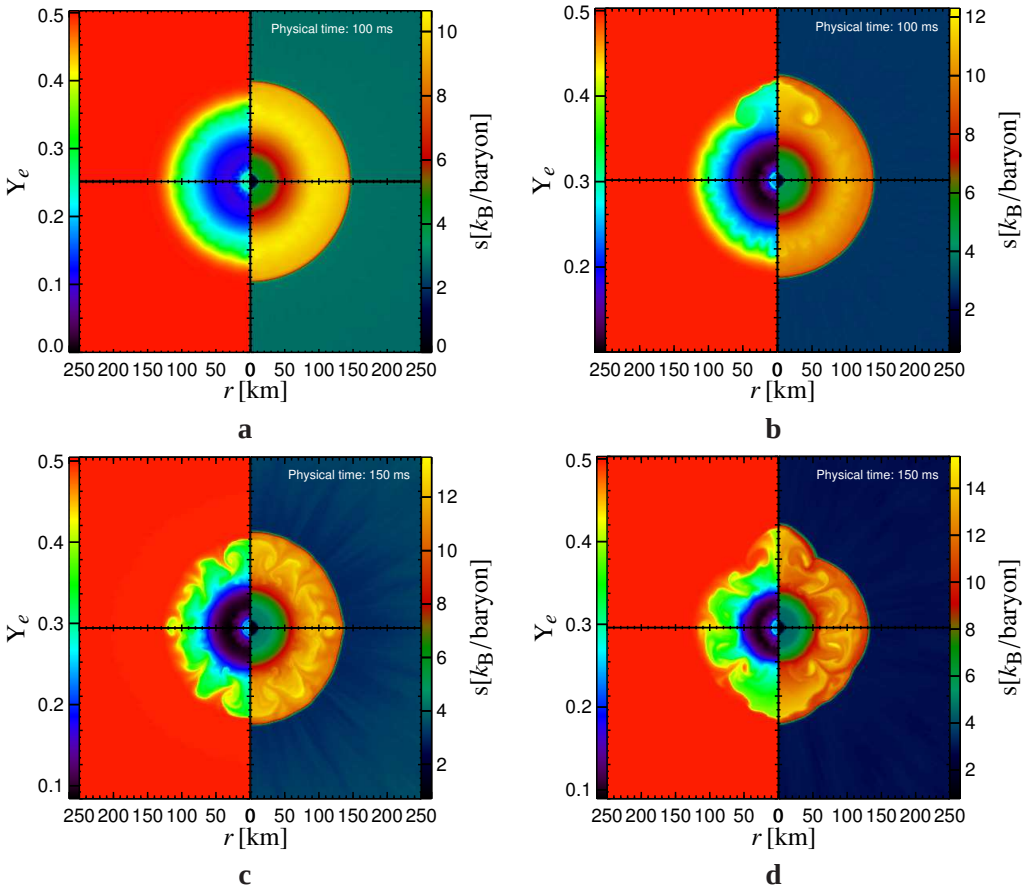

Figure 5.27.: Snapshots of the electron fraction Y_e and the entropy s for the models with the Wolff–EoS and L&S–EoS at 100 ms (upper row) and 150 ms (lower row) after the shock formation. Different times are shown in Figs. 5.28 and 5.29. **a**: model Wolff–2D. **b**: model L&S–2D. **c**: model Wolff–2D. **d**: model L&S–2D.

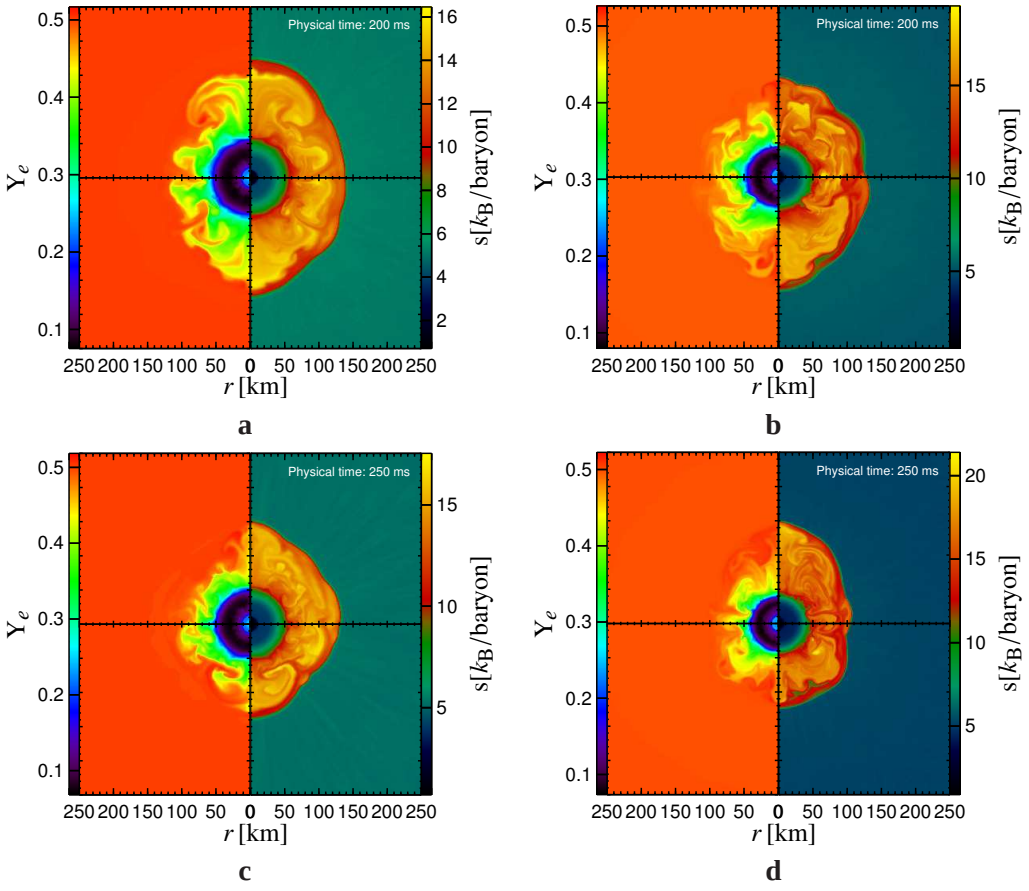

Figure 5.28.: Snapshots of the electron fraction Y_e and the entropy s for the models with the Wolff–EoS and L&S–EoS at 200 ms (upper row) and 250 ms (lower row) after the shock formation. Different times are shown in Figs. 5.27 and 5.29. **a**: model Wolff–2D. **b**: model L&S–2D. **c**: model Wolff–2D. **d**: model L&S–2D.

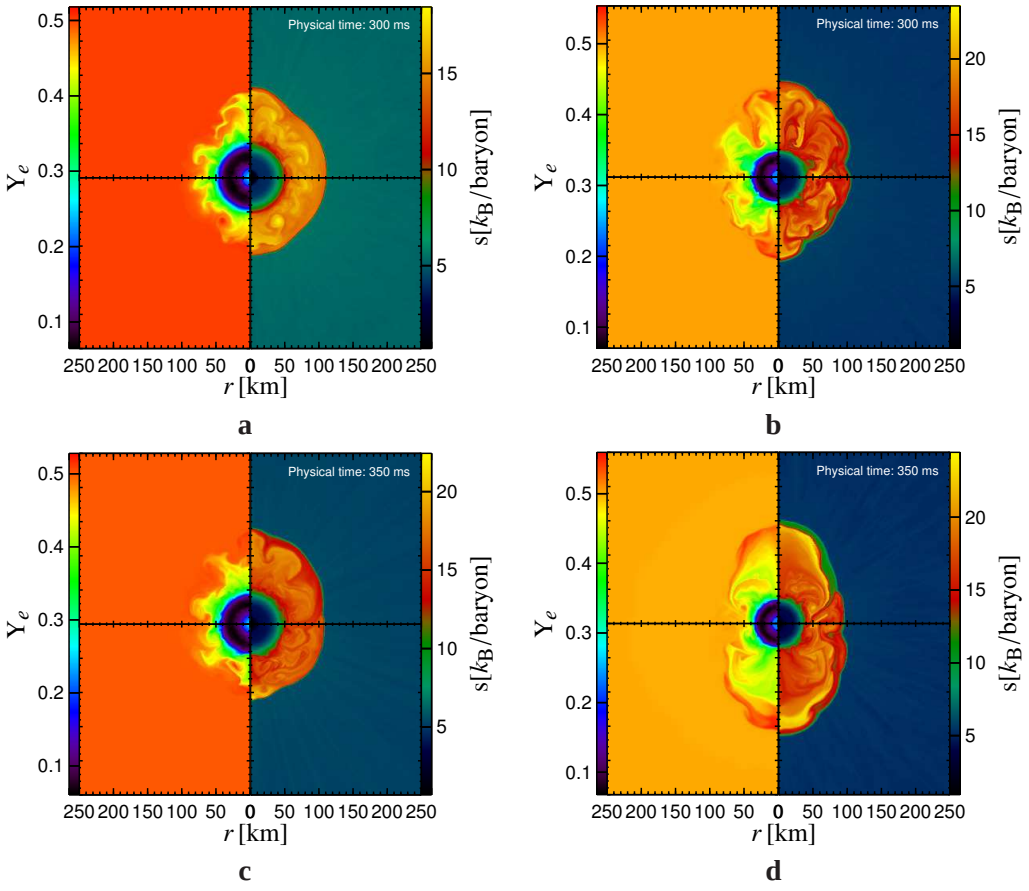

Figure 5.29.: Snapshots of the electron fraction Y_e and the entropy s for the models with the Wolff–EoS and L&S–EoS at 300 ms (upper row) and 350 ms (lower row) after the shock formation. Different times are shown in Figs. 5.27 and 5.28. **a**: model Wolff–2D. **b**: model L&S–2D. **c**: model Wolff–2D. **d**: model L&S–2D.

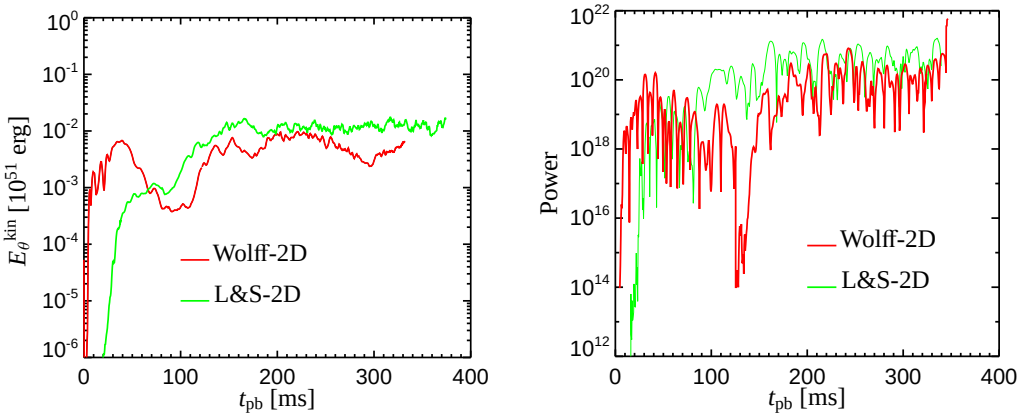

Figure 5.30.: **a**: The lateral kinetic energy contained in the hot bubble region between the gain radius and the shock, for both models with different EoSs. **b**: The power contained in the amplitude of the $l = 1$ contribution of the deviations of the local from the mean pressure for both models.

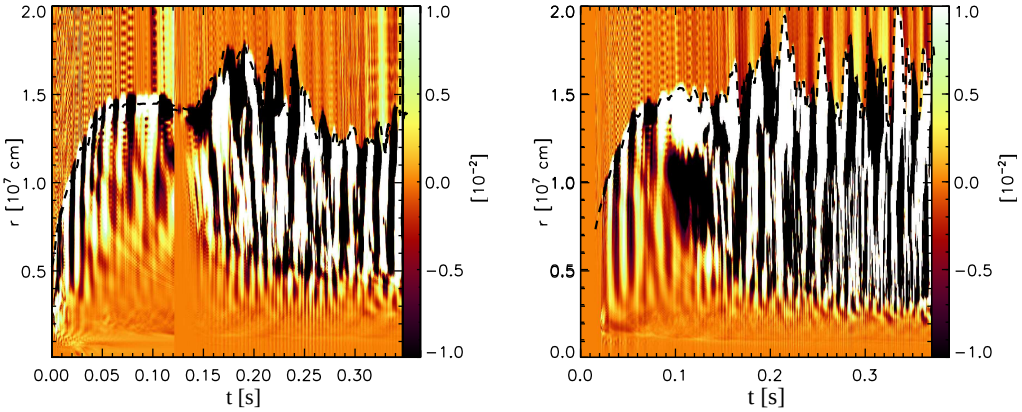

Figure 5.31.: The normalised amplitude $a_{1,0}/a_{0,0}$ of the $l = 1$ contribution to the expansion of the pressure into spherical harmonics.**a**: model Wolff–2D. **b**: model L&S–2D.

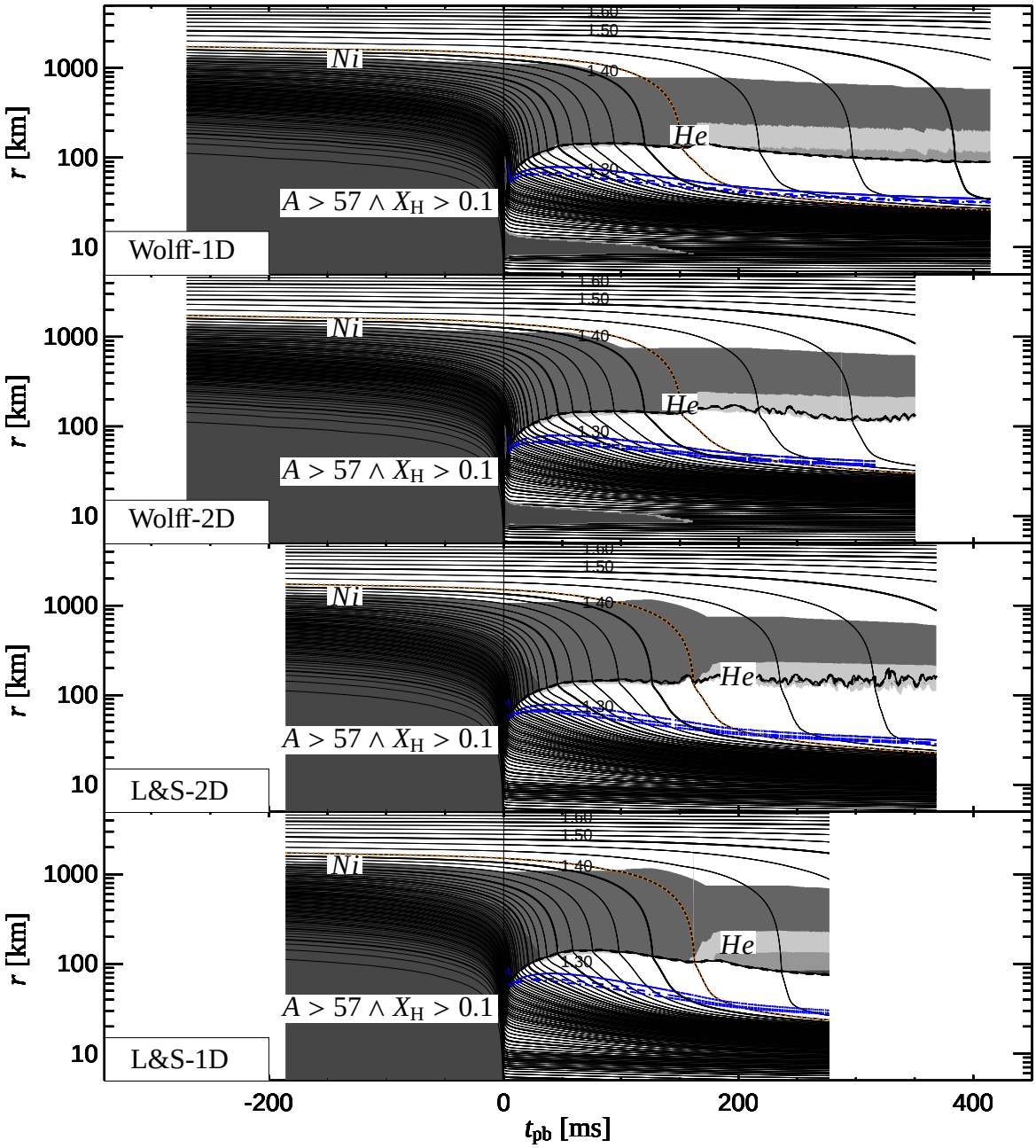

Figure 5.32.: Trajectories of selected mass shells (black lines) for the 2D–models and the corresponding 1D–models. The blue lines indicate (from top to bottom) the positions of the electron, anti electron, and heavy (anti) lepton neutrinospheres. The orange line indicates the time evolution of the O–Si–interface. Dark shaded regions indicate the presence of heavy nuclei, slightly lighter regions indicate the presence of Ni (iron group) nuclei. The light grey shaded region indicates where alpha–particles contribute more than 30% of the mass, and the slightly dimmer grey colour indicates where alpha–particles contribute more than 60% of the mass. Note that the panels for the 2D–simulations where obtained by laterally averaging the data.

6

Exploring other physical parameters in multi–dimensional simulations: rotation and the progenitor star

In the following Chapter the focus of interest will be shifted from the influence of the EoS on the supernova evolution towards other uncertainties, which may influence the supernova evolution. In this sense this Chapter is somewhat special to the rest of this thesis, since the focus does not lie on the nuclear physics part of the simulations but rather on some selected other ingredients of supernova simulations that are unknown and might crucially influence the supernova explosion mechanism. Talking about the ingredients for a supernova simulation, immediately the progenitor star comes to ones mind. Related to the used progenitor model is of course the question to what extend the supernova explosion mechanism might rely on the details and uncertainties of the progenitor stars. The details of the progenitor star models, which are used at the beginning of a core collapse supernova simulation, are uncertain for a few reason: Firstly, though it is a (too?) large simplification, stellar evolution models are spherically symmetric. Thus, the deviations from spherical symmetry are completely unknown and supernova modellers normally impose *random* perturbations of a certain amplitude, see the discussion in Section 4.1. Secondly, spherically symmetric pre–supernova models show sharp composition interface, where different regimes of nuclear burning appear, and which are correlated to sharp density gradients. Fryer & Young (2006) claim that these sharp interfaces would dissappear in multi–dimensional stellar evolution models, which as we will discuss in Section 6.2 might influence the results of supernova simulations noticeably. Thirdly, core collapse supernovae occur on a huge diversity of progenitor stars, whose mass range might easily vary by $20\,M_{\odot}$. This implies that the structure of pre–supernova progenitor cores also largely differs, which might also be influence the supernova explosion. Even without the first two uncertainties, the large variety of different progenitor models has to be studied systematically in simulations of core collapse supernovae.

Since such a parameter study is computationally too demanding with the M DB TH–code, we will discuss in Section 6.2 the supernova evolution for one other progenitor model.

Another physical aspect of multi–dimensional simulations will be discussed in Section 6.1, namely the influence of rotation on the supernova evolution. From observations (e.g. from our Sun) it is clear that stars do rotate, furthermore neutron stars are also known to rotate. Since neutron stars are born during the event of a core collapse supernova, rotation is obviously present at the time of stellar core collapse and the subsequent supernova explosion. However, much more uncertain is the rotation of the iron core shortly before the onset of gravitational instability since the transport of angular momentum cannot be predicted very accurately, see e.g. Woosley et al. (2002) and Heger et al. (2005) for different predictions of stellar evolution modellers.

Thus, though it is commonly accepted that stellar iron cores do rotate, and that this might influence the supernova evolution (see, e.g. Yamasaki & Yamada 2005), it is not clear what kind of rotation rates should be assumed. Thus, rotation is often studied in parameter studies in order to investigate the influence of rotation, however, these studies use mostly simplified calculations of the neutrino–transport problem. As we will discuss in following Section, we have thus calculated with the spectral Boltzmann neutrino transport code M DB TH the evolution of a $15M_{\odot}$ progenitor star including rotation.

6.1. The influence of rotation on the supernova evolution

As already mentioned, the rotation rates of stellar iron cores at the onset of gravitational instability are highly uncertain. Thus an possible approach to investigate the influence of rotation on the supernova evolution is that one calculates several models with different assumed rotation profiles and rotation frequencies. However, due to the challenging computational demands of a multi–dimensional simulation with the M DB TH–code, we refrain from this approach. Instead, it was chosen to calculate a rotating model whose rotation profile maximises the effects of rotation. However, since the model must still be physical plausible, the following constraints were put on the *assumed* rotation profile:

- Since the initial progenitor model is spherically symmetric, the rotation physics is chosen such that the model superimposed with rotation can still be considered spherically symmetric.
- Superimposing a rotation profile must not imply significantly deviations from the hydrostatic equilibrium and from the gravitationally bound state of the (spherically symmetric) progenitor model.

Thus, in order to guarantee both constraints the rotation rate was chosen such that the influence of rotation is small at the onset of gravitational instability and the ratio of the centrifugal force to the gravitational force is smaller 1% everywhere on the computational domain. Keeping these requirements in mind the initial angular frequency at the beginning of the collapse of the stellar core is assumed to be $\Omega_{\mathrm{i}} = 0.5$ rad/s (which corresponds to a rotation period of roughly 12 s). This rotation rate is kept constant throughout the Fe and Si core and decreases beginning at a radius of 1750 km (corresponding to $1.43M_{\odot}$) with $r^{-3/2}$. This choice of the rotation profile was

motivated by results for pre–collapse stellar cores of stars whose evolution is followed including the angular momentum transport by magnetic fields (Heger et al. 2005). However, our choice of the initial angular frequency is about then times lower than predicted by Woosley et al. (2002) for non–magnetic stars, and roughly ten times larger than the rotation rate for magnetised stars predicted by Heger et al. (2005). Nevertheless, for the reasons discussed above, the assumed rotation in model L&S–rot is rather slow compared to the assumptions of other core collapse supernova modellers, see e.g. Kotake et al. (2004) and Ott et al. (2004).

As progenitor model for our study we have chosen the same $15M_{\odot}$ star of Woosley et al. which was already used in the discussion of EoS effects in Chapter 5. Contrary, to our normal approach, this model (denoted L&S–rot) was already calculated from the onset of gravitational instability and through the moment of shock formation in 2D, in order to follow the effects of rotation consistently from the beginning of the collapse through the whole supernova evolution. The model is calculated on a 180° computational domain with an angular resolution of 1.41°. As the model name indicates we used the L&S–EoS and the normal setup of physical input physics (cf. Table 2.1) was chosen. Note, however, that this model was not calculated with the description of electron capture rates on heavy nuclei put forward by Langanke et al. (2003) but instead the description of Bruenn (1985) was used. Furthermore, since we were not able to compare our new approximation of general relativistic effects (see Appendix B) in a rotating model to a rotating fully general relativistic calculation, we have decided to use the original approximation of general relativistic effects of Rampp & Janka (2002). Model L&S–rot, which we will discuss in the following, is identical to model s15_64_r (discussed in Buras et al. 2006a,; which we will denote L&S–rot–90) except that the later was calculated in a 90° (pole–equator) setup and the evolution was only followed to roughly 250 ms after the shock formation[1]. A detailed overview over the models discussed in this Section can be found in Table 6.1. Since the collapse phase, which is identical in models L&S–rot and L&S–rot–90[2], is already discussed in Buras et al. (2006a) the most important fact will only be stated here: Due to angular momentum conservation the angular frequency of the iron Fe–core increases from 0.5 rad/s during collapse to 600–700 rad/s shortly after bounce, see Fig. 25 in Buras et al. (2006a), which implies that the centrifugal forces also grow.

Centrifugal forces directly influence the supernova evolution in two ways. First, the dense core becomes, due to a different hydrostatic equilibrium, oblate and this changes the isotropy of the neutrino emission. Second, centrifugal forces, work again the gravitational force and thus prolongs the advection of matter. While the former effect is trivial to show, see Figs. 6.1, 6.2, and 6.4,and 6.6, the latter one is more complicated to observe, since violent convection tends also to prolong the advection timescale.

We start our discussion of the effects of rotation by comparing the laterally averaged shock positions of the rotating and non–rotating models, see Fig. 6.7. Obviously, all models behave very similar for evolution time up to 300 ms after the shock formation. Note that slightly larger shock radii in model L&S-rot compared to model L&S–2D during this epoch must not necessarily be

[1] A comparison of models L&S–rot–90 and L&S–rot is thus an additional test of the discussion in Section 4.2 that calculating a model in 180° or 90° (pole–equator) does not change the results strongly.

[2] The collapse phase was calculated in 180° and only after the shock formation the a switch to 90° in model s15_64_r was done.

Model	2D	rotation	Setup	GR–potential
L&S–rot	Yes	Yes	180°	Rampp & Janka (2002)
L&S–rot–90	Yes	Yes	90°	Rampp & Janka (2002)
L&S–64	Yes	No	90°	Rampp & Janka (2002)
L&S–2D	Yes	No	180°	Appendix B
L&S–rot–1D	No	No	—	Rampp & Janka (2002)
L&S–1D	No	No	—	Appendix B

Table 6.1.: Overview over all models discussed in this Section. Stated is the model name, whether or not the calculation was done in 2D, and whether rotation was applied. Also stated is the 2D–setup and which approximations of general relativistic effects were used. Note that the potential according to Rampp & Janka (2002) is stronger than the one discussed in Appendix B. Note also that model L&S–rot–1D was calculated with the same micro–physics and gravitational potential as the rotating models (but without rotation), whereas in the models L&S–2D and L&S–1D slightly different micro–physics and a different gravitational potential was used (see text).

due to rotation, but might be caused by the different treatment of GR-approximations. To illustrate this we also show the shock trajectories of models L&S–1D and L&S–rot–1D, which both were calculated — as the models L&S–2D and L&S–rot — with different GR–approximations[3]. Despite these small differences both the rotating and non-rotating calculations evolve very similar at early times. More important, however, is the fact that model L&S-2D-rot shows the onset of an explosion at a time between 500 ms and 600 ms after the shock formation. In the following, we will try to understand whether this onset of the explosion is due to rotation effects or whether it is due to changed conditions in the supernova core which are not necessarily influenced by rotation. Sadly, since our non-rotating two-dimensional model (L&S-2D) is not yet evolved to the time where model L&S-rot shows the explosion, a direct comparison and pinning down the rotational effects is not easily possible.

An overview of the angular dependence and of the evolution of convection can be obtained from Fig. 6.8, where we show snapshots of the entropy and of the electron fraction at different times. Model L&S–rot develops volume filling convection and an $l = 1$ shock instability, which however can be seen much better in Fig. 6.9a where the coefficients of the shock expansion into spherical harmonics (cf. Eqn. 4.5) are shown. The standing accretion shock instability can again be linked to the power of the advective–acoustic cycle, see Fig. 6.9b. Obviously the shock instability shows in the rotating models different evolutionary phases of violent shock deformation and rather quiescent stages (e.g. at a time of 350 ms), however, only after a time of roughly 500 ms (i.e. when the explosive shock expansion already started, Fig. 6.7), the power as well as the shock oscillations grow noticeably. At earlier times the power in the rotating

[3]Note that in spherically symmetric calculations a stronger potential produces a smaller shock radius but also higher neutrino luminosities, see the discussion in Appendix B. These higher luminosities might trigger in multi–dimensional simulations stronger convection and a strong shock expansion, similar to the EoS effects discussed in Section 5.2.

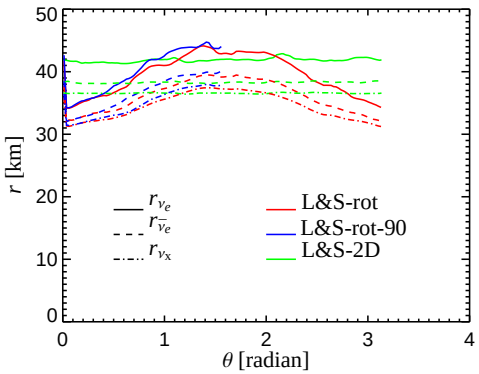

a

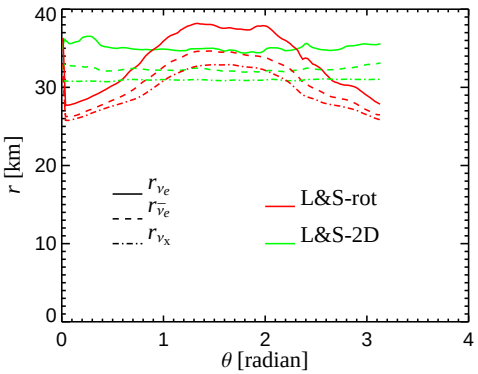

b

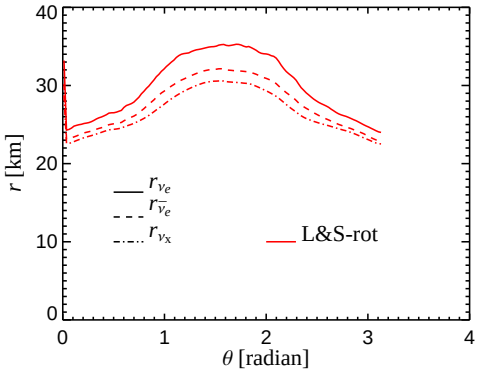

c

Figure 6.1.: The radii of the electron neutrinosphere (solid), anti electron neutrinosphere (dashed), and heavy (anti) lepton neutrinospheres (dashed-dotted) as function of the angle θ at different times. **a**: At a time of 200 ms after the shock formation **b**: At a time of 300 ms after the shock formation. Note that model L&S-rot-90 is not plotted, since it was not calculated this time. **c**: At a time of 400 ms after the shock formation. Only model L&S-rot was calculated to such a long evolution time.

and non–rotating model is comparable, which is consistent with the similar amplitudes of the shock instability. The absence of a clear trend to larger values in both quantities at earlier times makes it very difficult to judge, whether this sudden increase at the explosion stage is due to the expanding shock (which of course influences both the calculation of the shock modes and of the power of pressure fluctuations behind the shock front) or whether small changes in both quantities triggered the explosion. The latter can not be excluded due to the fact that the situation is highly non–linear.

However, looking at the advection and heating timescales, one sees for quite some time a trend towards a condition that favours an explosion, see Fig. 6.10. As is already discussed in Buras et al. (2006a) rotation tends to prolong the heating timescale (since a rotational flattened neutron star, i.e. extended neutron star in the equator region, emits less and cooler neutrinos at the equator, see e.g. Figs. 6.2 and 6.3) but rotation also increases the advection timescale. Both effects are clearly visible in the timescales of our models. Interestingly in the exploding model L&S–rot from a time of roughly 200 ms after the shock formation on, the advection

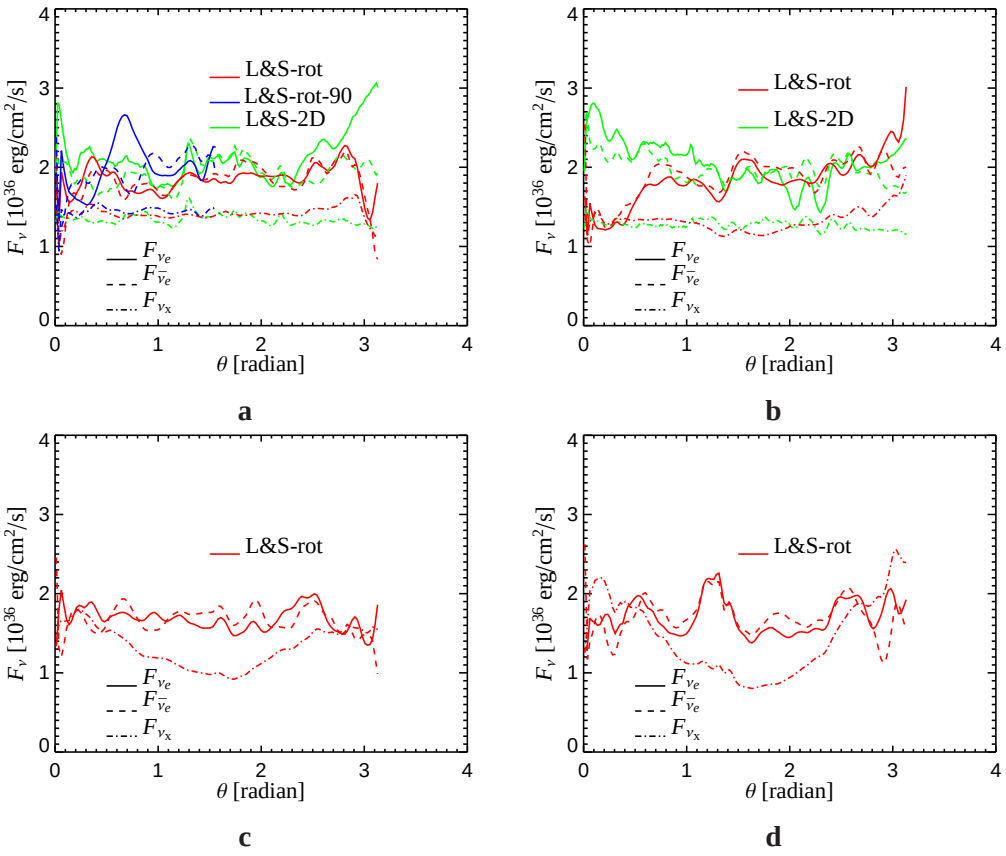

Figure 6.2.: The angular dependence of the neutrino energy fluxes for the rotating and non–rotating models at times of (a) 200 ms, (b) 300 ms, (c) 400 ms, and (d) 500 ms after the shock formation. Note since not all models were evolved to so late times not all panels depict all models. The fluxes were measured at 400 km.

timescale increases more strongly then the neutrino heating is reduced. Thus, though the heating timescale is longer, matter stays sufficiently longer in the heating region that the conditions become favourable for an explosion. However, again, we cannot say that rotation is necessary for the obtained explosion. Looking carefully at the non–rotating model L&S–2D, one observes the same trends, however, starting from "more unfavourable" conditions (i.e. a lower ratio of the advection timescale to the heating timescale). But clearly the rotating and the non–rotating model behave quite similar, which renders it impossible to judge from the timescales the influence of rotation on the onset of the explosion. However, looking at the "energy budget" of the simulations, one can investigate the influence of rotation much better. Figure 6.11 shows for the different models the time evolution of several energies in the heating region between the gain radius and the shock front. Obviously, rotation increases the internal energy in this region, due to the fact that more mass is contained in the gain layer, see Fig. 6.11c. However, the internal energy as well as the kinetic energy contained in rotation $E_\phi^{\rm kin}$ do not vary strongly

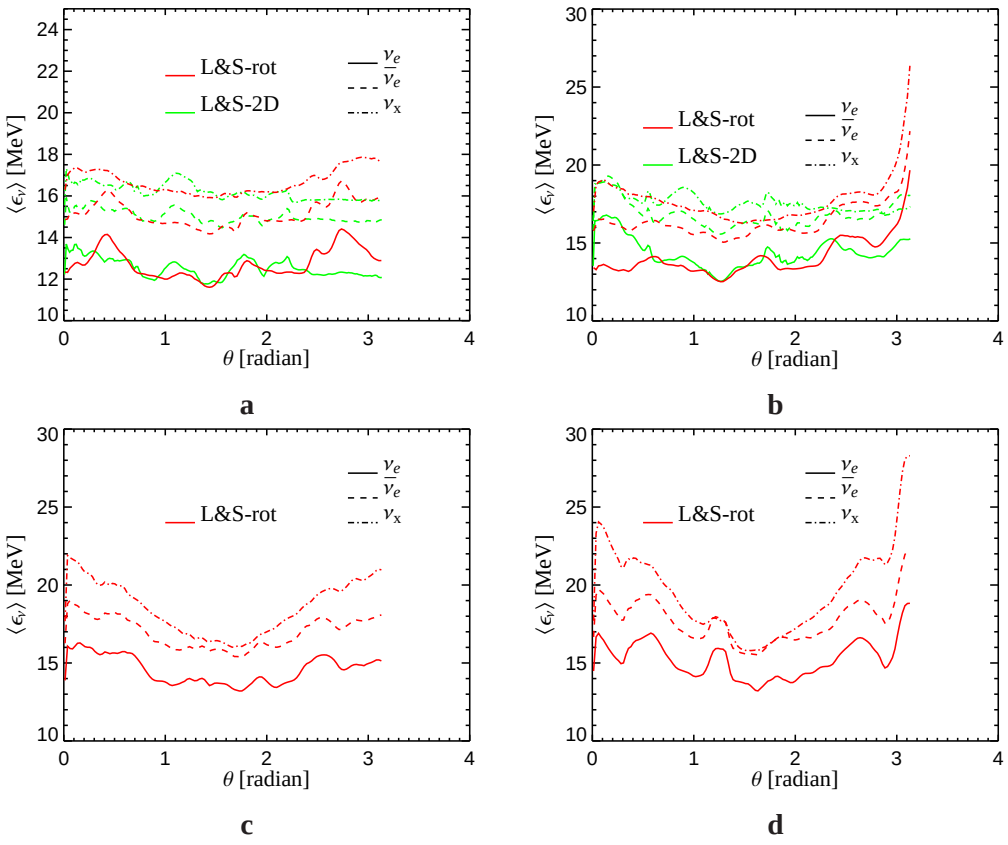

Figure 6.3.: The angular dependence of the mean neutrino energy for the rotating and non–rotating models at times of (a) 200 ms, (b) 300 ms, (c) 400 ms, and (d) 500 ms after the shock formation. Note since not all models were evolved to so late times not all panels depict all models. The energies were measured at 400 km.

at late stages of the evolution. The lateral kinetic energy $E_\theta{}^{\rm kin}$ and the kinetic energy contained in convective flows $E_{\rm conv}{}^{\rm kin} = E_\theta{}^{\rm kin} + E_r{}^{\rm kin}$, on the other hand show a longtime trend to grow, and during the last 250 ms of the calculation this amounts to more than a factor of two.

This suggests that the increase of the turbulent energy $E_{\rm conv}{}^{\rm kin}$ in the gain layer, which on the one hand increases the convection but on the other hand also strengthens the "sloshing" of the shock front, becomes at a time of about 500 ms after the shock formation large enough in order to trigger a strong shock expansion and an increase of the advection timescale. This increase of the advection timescale seems to be sufficiently large in order to produce the conditions for the explosion. As one can see from the rate of energy deposition of neutrinos into the gain layer, see Fig. 6.11d, the increase of convective energy is easily explained by neutrino heating. During the time from 350 ms after the shock formation to 570 ms after the shock formation the energy contained in convection in the gain layer increases by roughly 2×10^{50} erg, whereas the neutrino energy deposition during the same time is roughly 9×10^{50} erg. Thus the increase of the turbulent energy in the gain layer can be easily explained with the amount of neutrino heating

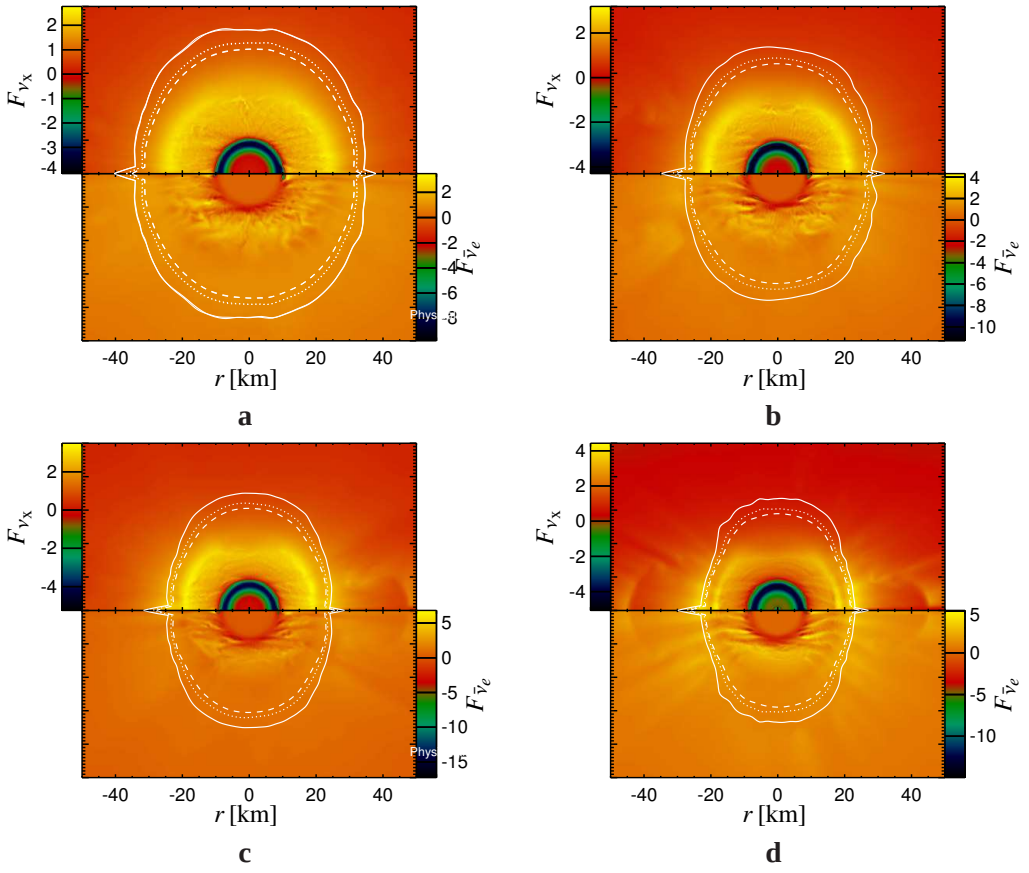

Figure 6.4.: The angular dependence of the neutrino energy flux of anti–electron neutrinos (bottom) and muon and tauon (anti) neutrinos (top) for the rotating model L&S–rot at times of (a) 200 ms, (b) 300 ms, (c) 400 ms, and (d) 500 ms after the shock formation. The positions of the electron neutrinosphere (solid), anti–electron neutrinosphere (dashed), and heavy (anti) lepton neutrinos (dashed–dotted) are also shown. Note that the fluxes are shown in units of 10^{44} MeV/cm^2/s. Also note that the plots are oriented such that the rotation axis lies horizonthally.

and the observed explosion is indeed triggered by delayed neutrino heating. Furthermore, we can exclude that the explosion is acoustically–driven as proposed by Burrows et al. (see the discussion in Section 5.1), since the observed amplitudes of g–mode oscillations, see Fig. 6.12 are again roughly a factor 100 smaller than the ones observed by Burrows et al. (2006a)[4]

Although it is clear that the explosion in model L&S–rot is driven by neutrino heating, or more precisely by neutrino heating together with turbulent flows, the influence of rotation is not very obvious. For the evolution time we are able to compare the non–rotating model L&S–2D with the rotating one L&S–rot both models behave very similar. Especially the shock oscillations and

[4]For a detailed discussion of the g–mode amplitudes see Section 5.1.

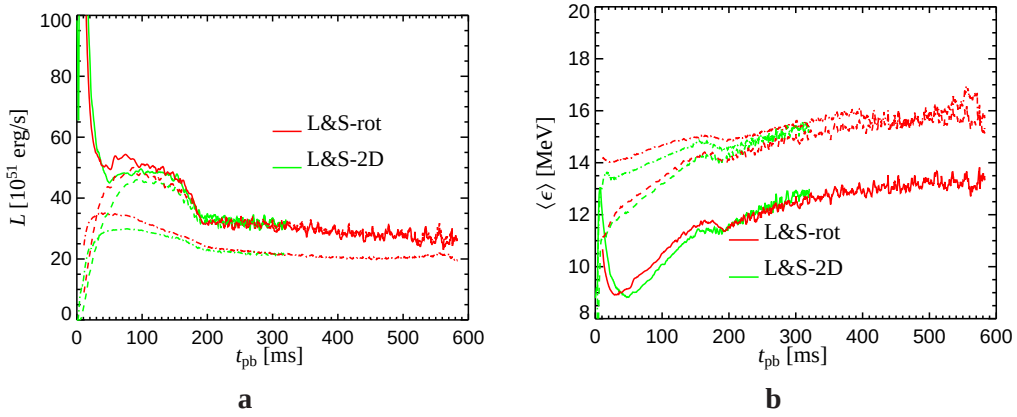

Figure 6.5.: a: A comparison between the laterally averaged luminosities of model L&S–rot and L&S–2D. Electron neutrinos are represented by solid lines, ant–electron neutrinos by dashed lines, all other flavours are represented by dashed–dotted lines. **b**: The laterally averaged rms energies for the same models as in panel a. Note that the same linestyles were used.

the power of the turbulent flows (Fig. 6.9), the ratio of the advection timescale to the heating timescale (Fig. 6.10), and the kinetic energy contained in convective motion (Fig. 6.11a) show the same trends in both models, and effects of rotation are thus not obvious. But rotation clearly increases the mass in the gain layer (Fig. 6.11c) and slightly enhances the neutrino energy deposition rate (Fig. 6.11d). The latter effect, however, seems almost to vanish at a time of about 300 ms after the shock formation, which again makes it difficult to understand the importance of rotation on the found explosion. This implies that only a evolution of the non–rotating model to the time where in the rotating case the explosion starts will give a final answer to this question.

Last but not least, we have to mention that it is possible that model L&S–rot is contaminated by hitherto unknown numerically problems. This might be possible for two reasons: Firstly, model L&S–rot is the longest multi–dimensional simulation ever performed with the M D-B TH–code, which implies that no experience for such simulations exists so far. Secondly, model L&S–rot is a rotating model, which implies that the neutron star becomes strongly deformed, see Fig. 6.1. Since the closure relation for the Boltzmann equation — the variable Eddington factor — is calculated on a spherically averaged model, see Chapter 2, this also might lead to yet un-encountered problems. However, all numerical tests done so far show consistency of model L&S–rot, nevertheless we will further investigate the numerics of this particular model.

6.2. A simulation of a 10.2 $M_\odot$ progenitor star model

In the following Section we will discus the evolution of a supernova simulation of a 10.2 $M_\odot$ progenitor star, without considering any effects of the nuclear equation of state. The focus of this Section lies thus not on the nuclear physics part of the simulations but rather on “special” prop-

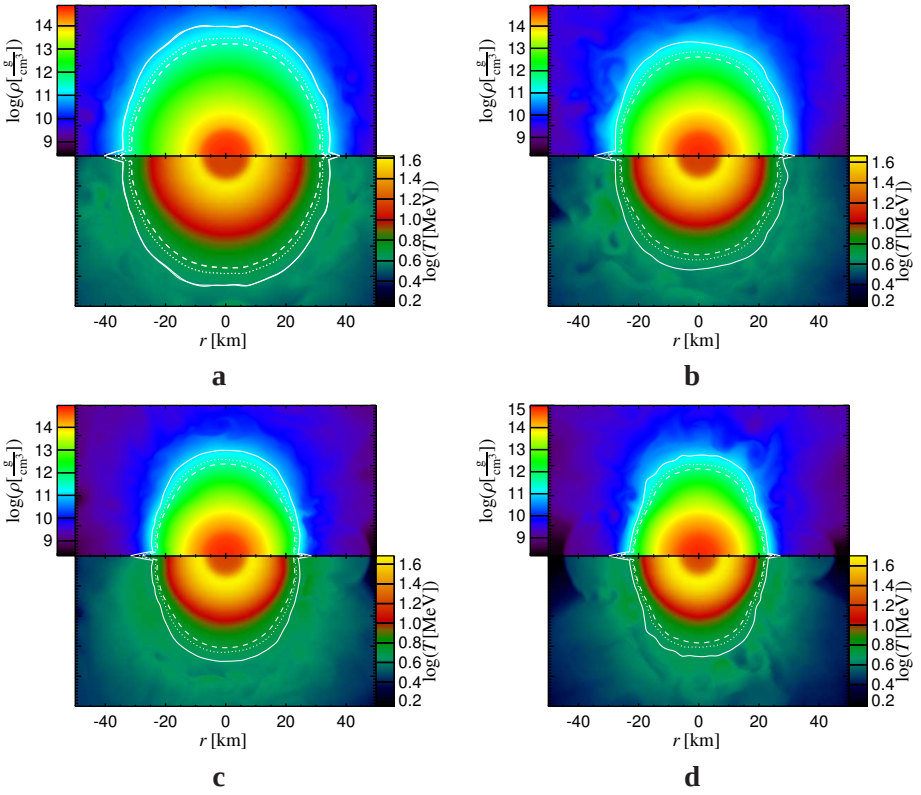

Figure 6.6.: The colour coded density (top) and temperature (bottom) of the rotating model L&S–rot at times of 200 ms (a), 300 ms (b), 400 ms (c), and 500 ms (d) after the shock formation. The lines represent the electron neutrinosphere (solid), anti–electron neutrinosphere (dotted) and heavy (anti) lepton neutrinosphere (dashed). Also note that the plots are oriented such that the rotation axis lies horizonthally.

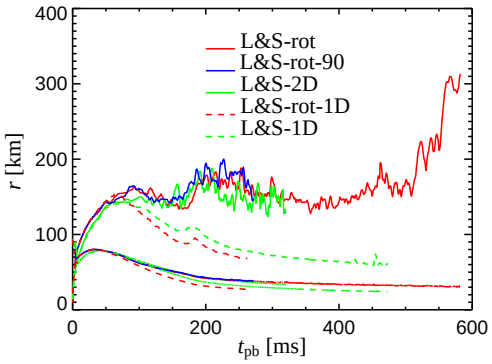

Figure 6.7.: The laterally averaged shock radii (upper lines) and the laterally averaged positions of the electron neutrinospheres (lower lines) for the rotating models L&S-rot, L&S–rot–90, and the the corresponding non-rotating model L&S-2D. Also shown are the corresponding one–dimensional models.

erties of the used progenitor model. The motivation for this study can be summarised by mentioning that sofar in multi–dimensional simulations of core collapse supernovae with spectral

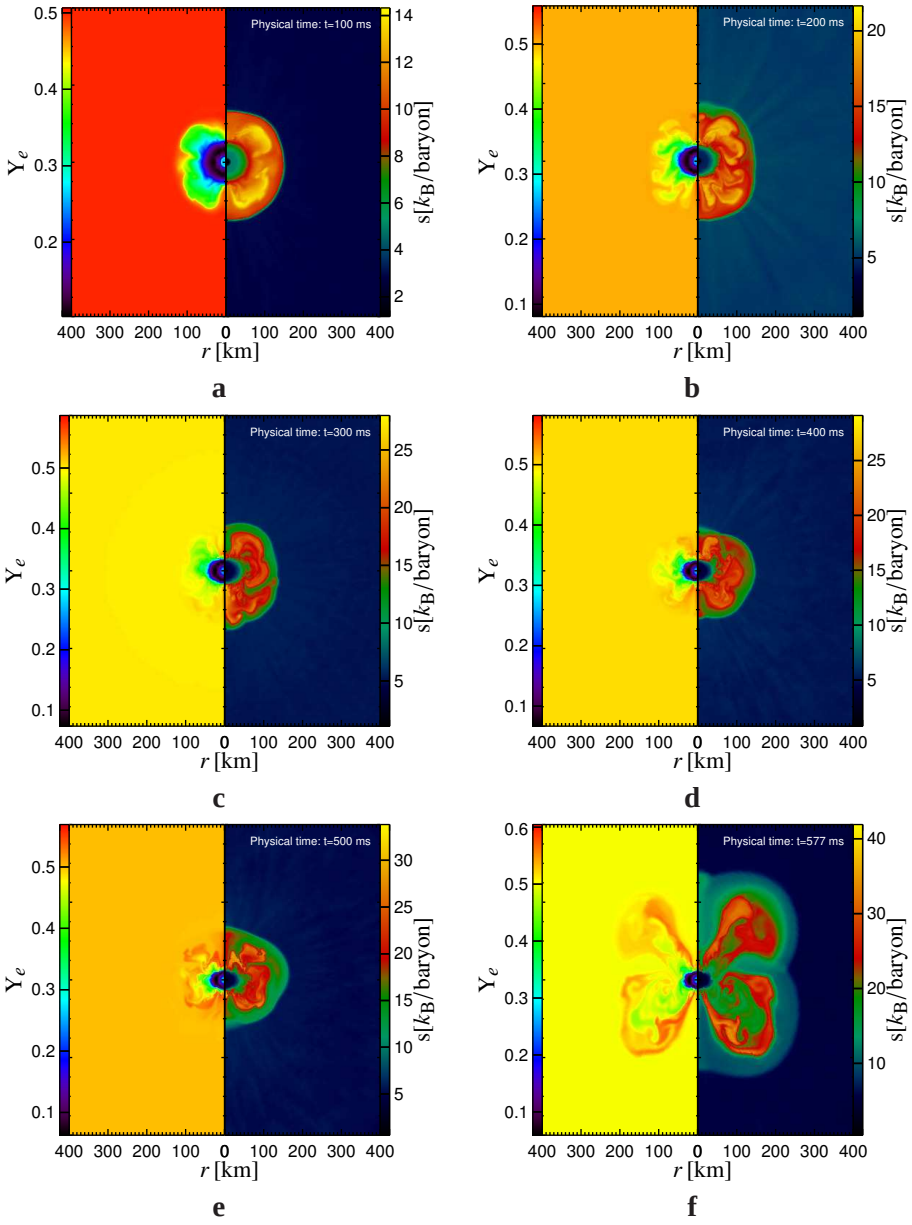

Figure 6.8.: Snapshots of the distribution of the electron fraction (left) and of the entropy (right) distribution at different times after the shock formation for model L&S–rot. Shown are the times of 100 ms (a), 200 ms (b), 300 ms (c), 400 ms (d), 500 ms (e), and 577 ms (f). Note that the scale of the colour bars changes from time to time.

Boltzmann neutrino transport (or approximation to it) neutrino driven explosions were only reported for a few models with peculiar progenitor models whose masses were below 12 $M_\odot$, see

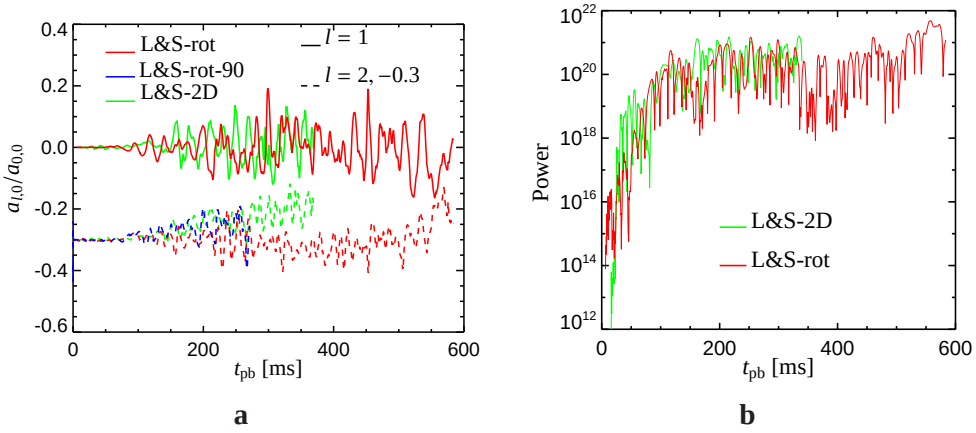

Figure 6.9.: a: The normalised coefficients $a_{l,0}/a_{0,0}$ of the $l = 1$ and $l = 2$ modes of the projection of the shock position onto spherical harmonics. Shown are the two rotating models and the non–rotating model. Note that for reasons of clarity the $l = 2$ modes where shifted down by 0.3. Note furthermore that model L&S–rot–90 can not posses an $l = 1$ mode due to geometry effects. **b**: The power (cf. Eqn. 5.4) contained in the pressure fluctuations.

Kitaura et al. (2006), Buras et al. (2006a). Except for the rotating model of a 15 $M_\odot$ progenitor star discussed in Section 6.1 of this thesis, neutrino–driven explosions of progenitors whose masses exceed 12 $M_\odot$ have not yet been reported[5]. Clearly, a smaller (i.e. less massive) progenitor star favours for several reasons the chance for a supernova explosion:

- Firstly, a smaller progenitor also produces a smaller iron core. This implies that the shock has to travel through less material which contributes to losses in the energy budget of the shock. These energy losses are caused by the fact that at the shock front iron–group nuclei are dissociated into free nucleons, an event which consumes roughly 8.8 MeV per nucleon of binding energy.

- Secondly, smaller progenitor models show a characteristic decline of the density–profile at smaller radii (due to the smaller core) than more massive progenitors. This density decline marks the region of a composition interface, where — due to the onion shell structure of the stellar core — the composition changes from mainly iron–group nuclei to a significant contribution of Si and O. Once this composition interface reaches the shock front it reduces on the one hand the ram pressure ($\propto \rho$) of the matter on the shock front, see the discussion in Section 3.2, and on the other hand can lead to a shock acceleration if the density gradient is large enough. For example, in the model of an O-Mg-Ne–core of a 8–10 $M_\odot$ star (see Kitaura et al. 2006) the explosion sets in when the shock front

[5]Note that the explosions of massive progenitors (up to 20 $M_\odot$) reported by Burrows et al. (2006a,c,b) are thought to be acoustic–driven and are thus not “standard” neutrino–driven explosions.

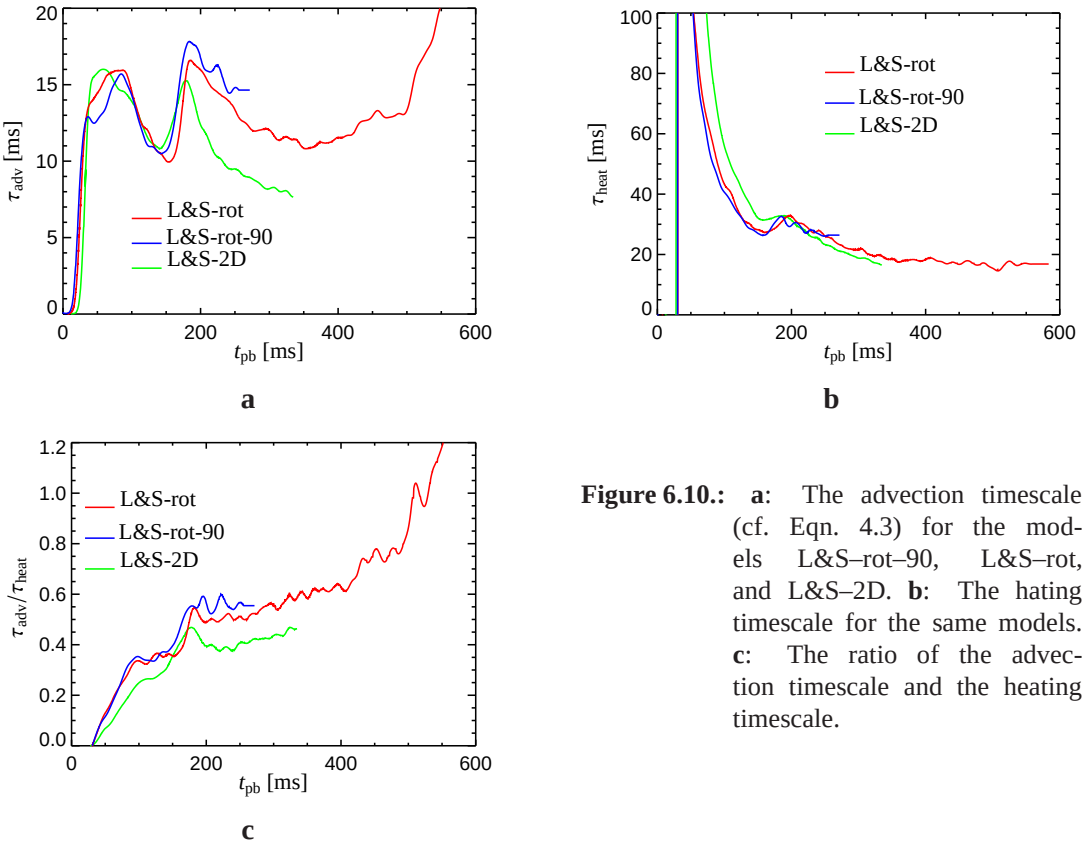

Figure 6.10.: **a**: The advection timescale (cf. Eqn. 4.3) for the models L&S–rot–90, L&S–rot, and L&S–2D. **b**: The hating timescale for the same models. **c**: The ratio of the advection timescale and the heating timescale.

reaches such a density gradient and the shock continously adjusts hydrodynamically to larger radii[6].

Thus the question has to be answered whether the two successful explosions reported by Kitaura et al. (2006) and Buras et al. (2006a) can be traced back to very special conditions of the particular progenitor models (e.g. the density gradient), or whether the neutrino heating mechanism works sufficiently well to produce supernova explosions for a certain (low) mass range of progenitor models[7]. The answer of this question is a very important one, since the following questions are immediately linked to it: Is the neutrino heating mechanism a robust mechanism for a certain class of progenitors? If this is the case, what classifies these progenitor models? Does one have to consider only the progenitor mass for the classification, or is it a multi–parameter space which makes understanding of a successful neutrino heating mechanism more complicated?

Of course it is not feasible to answer or even address all these questions in the following Section. However, we can address the question whether the neutrino heating mechanism works

[6]Though note quite correct one might think of the analogy of a surfer moving down a wave on a step gradient.

[7]The reader may remember from the discussion in Section 4.2 that the explosion of the 11.2 $M_\odot$ progenitor also started when the composition interface reached the shock front...

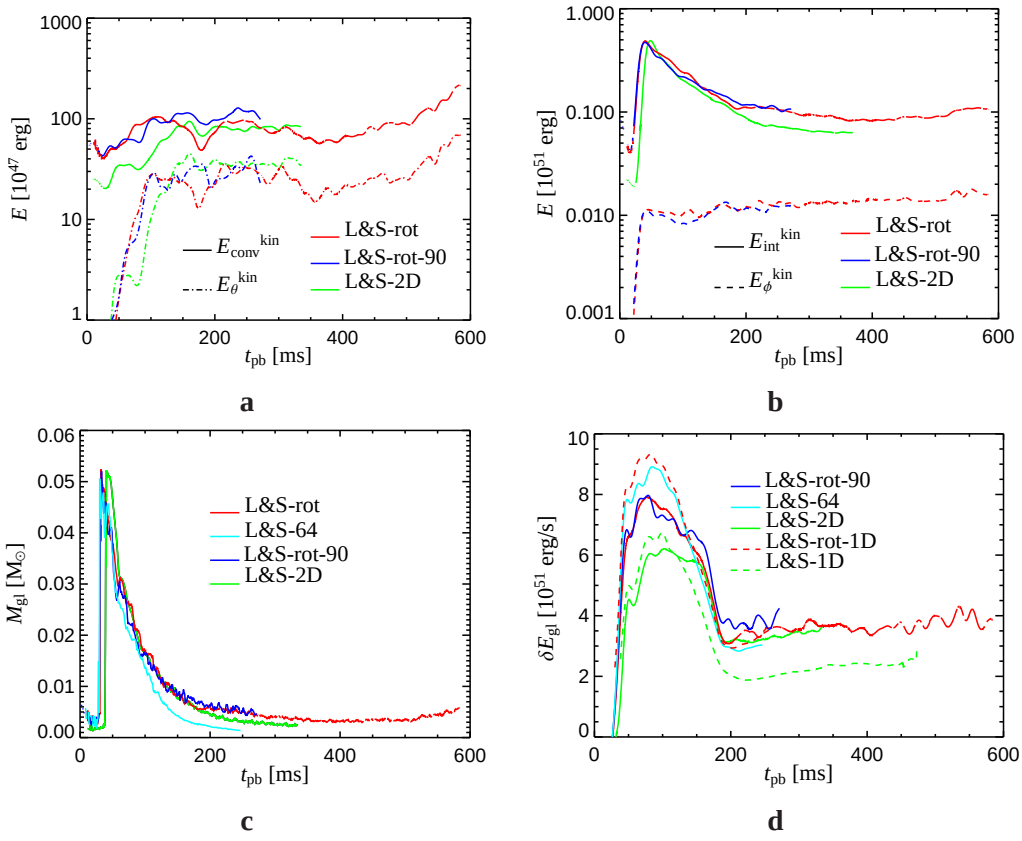

Figure 6.11.: **a**: The kinetic energy in the gain layer contained in lateral direction ($E_\theta{}^{\rm kin}$, dashed–dotted) and in lateral plus radial direction ($E_{\rm conv}{}^{\rm kin}$, solid) for all models. **b**: The internal energy (solid) and kinetic energy contained in rotation (dashed) for all models. Note that model L&S–2D does not rotate. **c**: The mass contained in the gain layer as function of time. **d**: The energy deposited by neutrino in the gain layer as function of time.

for stars with a mass lower than 12 $M_\odot$, by investigating the supernova evolution of a 10.2 $M_\odot$ progenitor[8].

The particular model of this progenitor was provided by Heger et al.[9], and its initial density profile at the moment of the onset of gravitational instability is compared in Fig. 6.13 to the density profiles of the 8.9 $M_\odot$ model of Nomoto (1984, 1987) (denoted model O–Ne–Mg) and the 11.2 $M_\odot$ model of Woosley et al. (2002), which show successful neutrino driven explosions.

Obviously, the progenitor model O–Ne–Mg shows the already mentioned fast drop of the density at radii below 1000 km. Both the progenitors with masses of 10.2 $M_\odot$ and 11.2 $M_\odot$ do not show such a steep density decline. However, both models show the mentioned composition

[8]Of course, a successful explosion of this model will only be another hint and no final answer. However, a failed explosion will rule out an easy correlation between the progenitor mass and the explosion mechanism.

[9]from www.stellarevolution.org

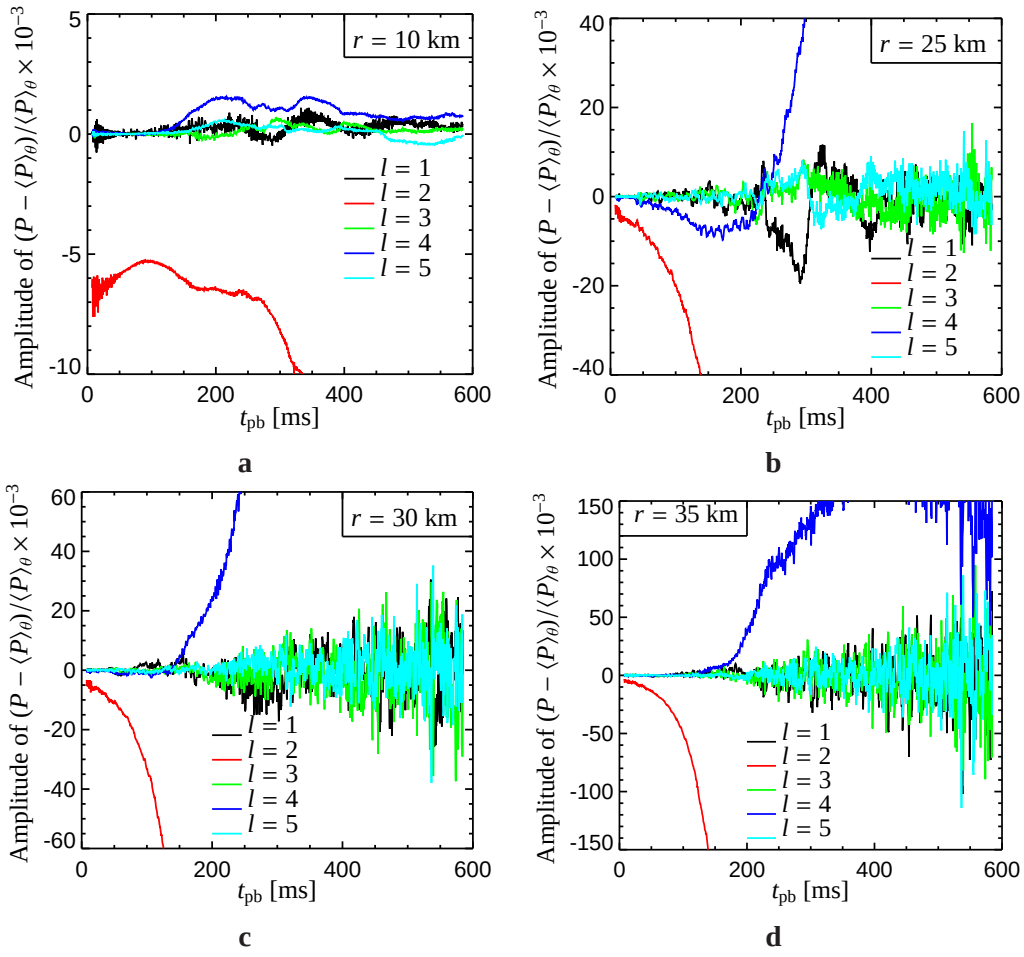

Figure 6.12.: Different coefficients of the expansion of the pressure fluctuations for model L&S–rot into spherical harmonics, cf. Eqn. 5.1.1. Note that the rotational flattening of the dense core leads to strong growth of the $l = 2$ and $l = 4$ contribution. Shown are the amplitudes measured at positions of constant radii of 10 km (panel a), 25 km (panel b), 30 km (panel c), and 35 km (panel d).

interface and a drop of density at radii of roughly 3000 km and 1500 km, respectively and the overall density profiles are very similar. Since the explosion in model s11.2 starts when this density drop reaches the shock front, see the discussion in Section 4.2, it seems promising that the same will happen in model s10.2 when the corresponding mass shells will have collapsed to the shock front. By simulating the supernova evolution with this progenitor model s10.2 we wanted to investigate this hypothesis, and we will discuss in the following our results from this calculation.

The gravitational collapse and the subsequent supernova evolution of this model (denoted s10.2–1D and s10.2–2D, respectively) were calculated with the standard physics used throughout this thesis. Since in a first step we were not interested in equation of state effects for this

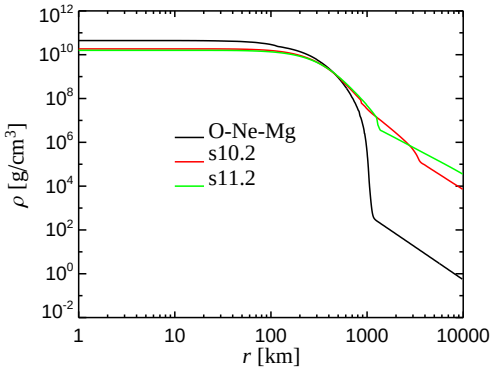

Figure 6.13.: The initial density profile of different low–mass progenitor models at the beginning of the collapse simulations. Model O–Ne–Mg denotes the progenitor model which showed an explosion in the study of Kitaura et al. (2006). Model s10.2 denotes the progenitor used in this study, and s11.2 denotes the progenitor which also showed an explosion in the study of Buras et al. (2006a).

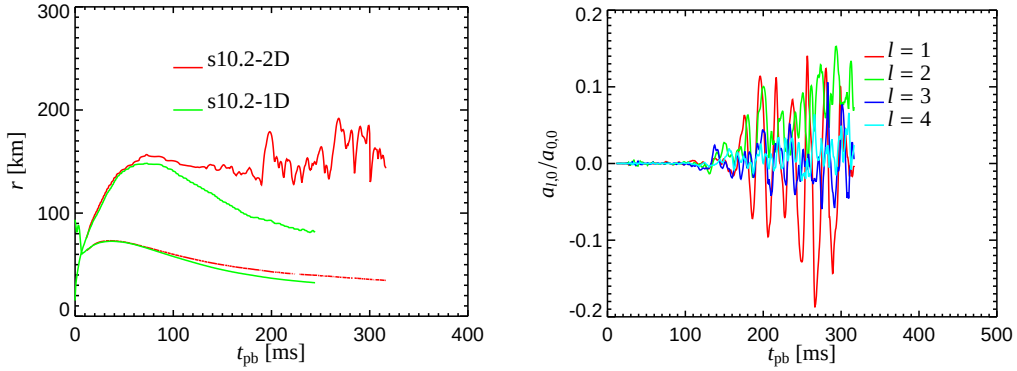

Figure 6.14.: **a**: The (laterally averaged) shock positions (upper lines) of models s10.2–2D and s10.2–1D and the positions of the electron neutrinospheres (lower lines). **b**: The time dependent coefficients $a_{l,0}/a_{0,0}$, which were obtained by expanding the shock position into spherical harmonics, as explained in Section 4.2. Shown are the first five non spherical modes, which are normalised to the spherical contribution $a_{0,0}$.

model, and we wanted to be able to compare the new model to model s11.2 discussed in Buras et al. (2006a) and in Section 4.2, we chose the L&S–EoS as description for the matter in the dense core.

Figure 6.14a shows that model s10.2–2D does not show an explosion during the first 300 ms after the shock formation. However, the model shows a strong shock instability, which if amplified could launch the explosion at later times. A projection of the shock position onto the system of spherical harmonics, analogous to Eqn. 4.4, reveals that in this model the $l = 1$ mode contributes strongest to the shock instability, see Fig. 6.14b. Figure 6.16 gives a more detailed impression of the sloshing of the shock front from one hemisphere to the other, and shows the

growing axis ratio of the shock front, which at a time of 300 ms after the shock formation reaches a value of 1.6 to 1.

Despite the strong shock oscillation and the volume filling convection, model s10.2–2D does not show an explosion, since the shock front is still far a way from roughly 300 km where the shock will gain energy from alpha–particle recombination[10]. However, the question remains to be answered how close this model comes to an explosion. Is it possible that the model will show an explosion at later times ? Of course, a definitive answer can not be given, but several conditions seem to be promising. On the one hand the infalling composition interface which reduces the ram pressure onto the shock front, has not yet reached the shock front during the first 300 ms after the shock formation. Thus, a strong shock expansion is expected when this interface reaches the shock front. Sadly, this will not happen before 600 ms after the shock formation. On the other hand, the shock shows already a strong instability and strong convection. This leads to an increasing ratio of the advection time scale to the heating timescale, see Fig. 6.15. Though this value is far below unity at a time of 300 ms, i.e. the model shows a factor of two too low heating for a successful explosion, this ratio has steadily increased from a time of 200 ms after the shock formation on. Only a continued calculation to longer evolution times will show if this trend will hold on and an explosion will be triggered or if this model will also fail to explode.

Nevertheless we can conclude from this model several things: Though, it is still an unanswered question whether the neutrino heating mechanism generically drives the explosion for progenitors with small iron cores, we can conclude that for such progenitors the explosion must not necessarily set in fast, i.e. for times lower than roughly 200 ms after the shock formation.

[10] A shock radius larger than 300 km is a quite a good first hint for the onset of the explosion, since experience shows that once the shock reaches this “point of no return” and gains extra energy it will not recede anymore, see the discussion in Section 6.1.

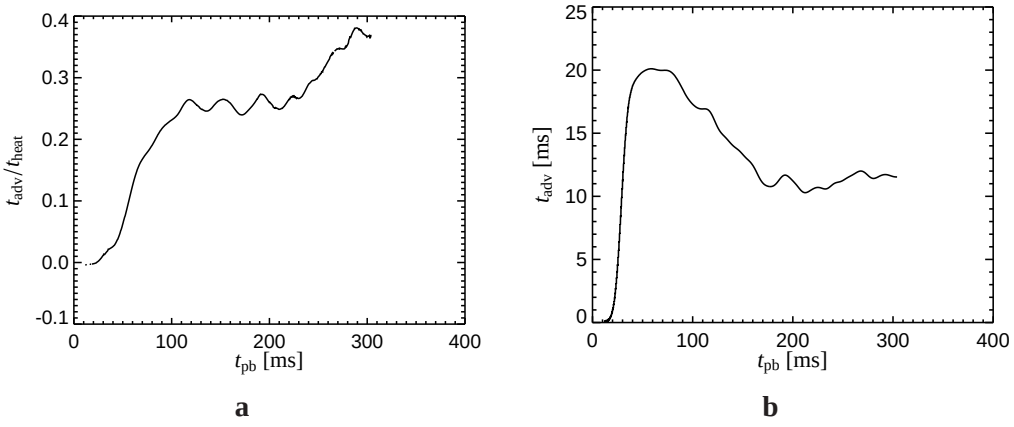

Figure 6.15.: T **a**: The ratio of the advection timescale and the heating timescale in model s10.2–2D. A value above unity indicates a successful explosion, see Buras et al. (2006a). **b**: The advection timescale (cf. Eqn. 4.3).

The successful early explosions reported by Kitaura et al. (2006) and Buras et al. (2006a) are supported by peculiar properties (i.e. density gradients) of the used progenitor models that have rapidly collapsed to the shock fronts. Although it is still possible that model s10.2–2D will show an explosion at later times when its steep density gradient reaches the shock front, the conditions are not favourable for an explosion during the first 300 ms after the shock formation, despite a strong shock instability and convective fluid flows. This fact together with all existing models of successful explosions shows that the neutrino heating needs the support of other processes (such as a drop of the ram pressure onto the shock front or a strong standing accretion shock instability) that cause a shock expansion and an *increase* of the advection time scale. Volume filling convection alone, driven by neutrino heating , seems to be insufficient in a at least some models, such as model s10.2–2D. Thus we conclude that the neutrino heating mechanism for shock revival in core collapse supernovae is not robust in the sense that the final explosion depends — even for low mass stars — strongly on the details of the progenitor structure.

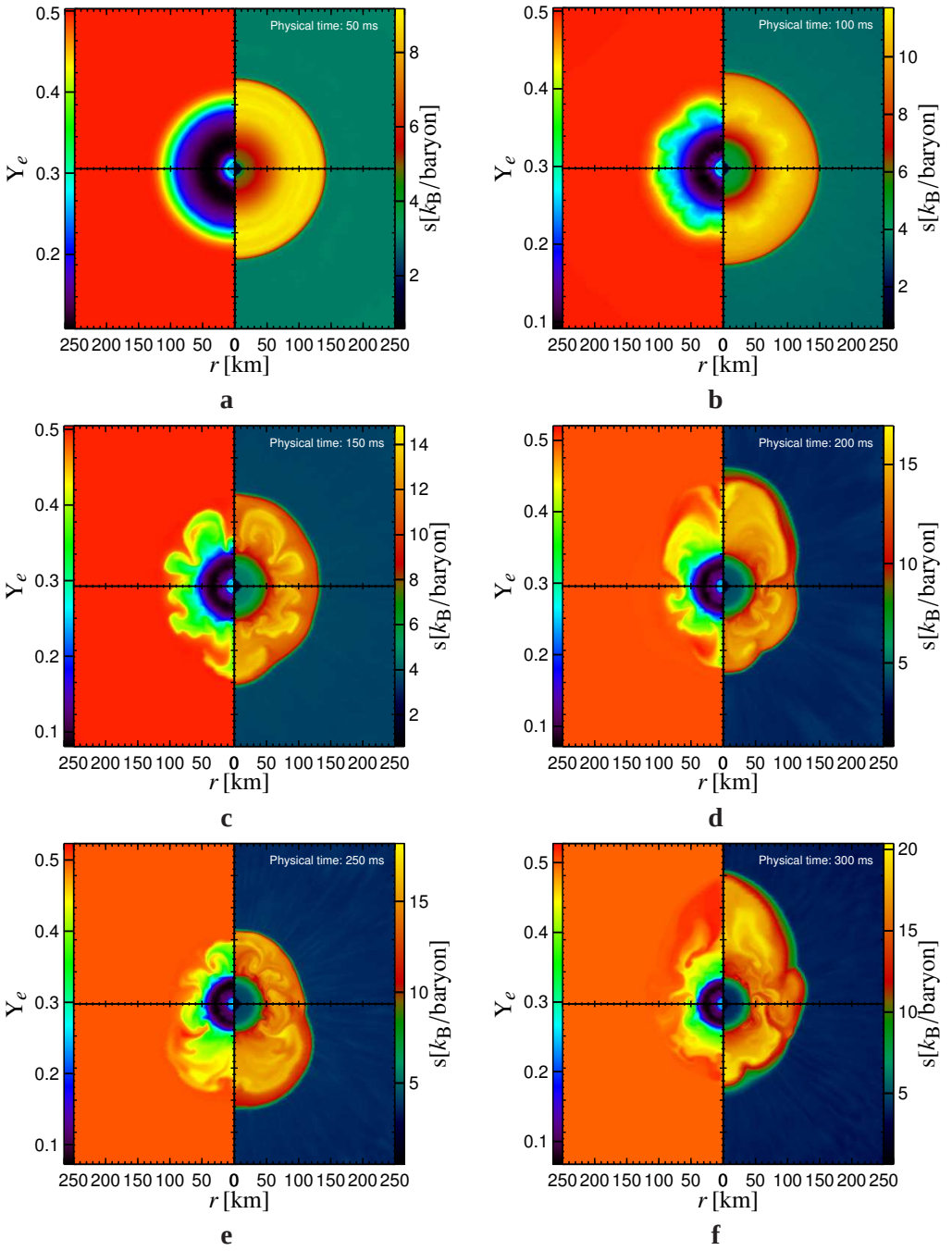

Figure 6.16.: Snapshots at different time after the shock formation of the electron fraction Y_e and the entropy s for model s10.2–2D. The development of an $l = 1$ shock instability is clearly visible. The snapshots are taken at **a**: 50 ms, **b**: 100 ms, **c**: 150 ms, **d**: 200 ms, **e**: 250 ms, and **f**: 300 ms after the shock formation, respectively.

7
Summary and Conclusions

In the main part of this thesis I have investigated the influence of the nuclear equation of state on the evolution of simulations of core collapse supernovae. The motivation for this study can be summarised by mentioning that the equation of state of supernova matter is neither from experiments nor from theory well constrained and the uncertainties are thus high. Different theoretical models of the nuclear equation of state of supernova matter reflect these uncertainties in their different predictions of such quantities as, e.g. , the nuclear composition or the stiffness around nuclear matter density.

In a first step, in Part I of this thesis, one–dimensional simulations have been used in order to clarify how the nuclear equation of state governs the supernova evolution and to clarify to what extent uncertainties of the description of dense matter influence the results obtained from supernova simulations. Although one–dimensional simulations neglect multi–dimensional effects, which are important for the supernova explosion mechanism, these simplified models are helpful for understanding these questions because the reduced complexity allows one to concentrate on the equation of state effects without having to deal with complicated multi–dimensional effects.

These studies, which are discussed in Part I of this thesis, are comparable to the earlier ones of (e.g. Thompson et al. 2003, Marek 2003, Sumiyoshi et al. 2005,only to mention a few), however, for the first time the influence of different regimes of the nuclear equation of state (i.e. the supra–nuclear regime, the intermediate density regime, . . .) has been investigated in self–consistent simulations.

In my studies I have used mainly the description of hot and dense matter according to Lattimer & Swesty (1991), which is based on the compressible liquid drop model by Lattimer et al. (1985), or I have applied the equation of state of Hillebrandt and Wolff, which is based on a full Hartree-Fock calculation and a Skyrme force for the nucleon–nucleon interaction is assumed, see Hillebrandt et al. (1984). In some studies as a third alternative, the relativistic mean field equation of state of Shen et al. (1998b,a) has been used.

With these equations of state it has been found that the nuclear equation of state influences sizeably the supernova evolution: Firstly, the collapse timescale and the deleptonisation of the core are different for simulations with different equations of state. This results in different neutrino luminosities of the burst signal, when the neutrinos that were trapped in the dense core are suddenly released in large numbers. Secondly, during the late-time evolution (i.e. starting at several 10 ms after the shock formation) the equation of state controls the compactness (i.e. the mass to radius ratio) of the dense core and the characteristics of the emitted neutrinos, in particular the neutrino luminosities and the mean neutrino energies, change strongly when different descriptions of dense matter are applied in the simulations. As the results from both non–exploding models and (artificially) exploding ones have shown, this is true for the "accretion neutrinos" (i.e. neutrinos that are produced from the release of gravitational binding energy as accreted matter settles on the proto–neutron star) and it is also true for neutrinos diffusing out of the dense core. It was found that in models with soft equations of state, i.e. equations of state that produce compact cores, the neutrino luminosity and mean neutrino energy are higher than in models that were calculated with stiff equations of state. The importance of this result cannot be stressed enough: On the one hand these equation–of–state–induced differences have to be taken into account when one calculates the detector response to a supernova neutrino signal of modern or future neutrino detectors, see e.g. Kachelrieß et al. (2005). On the other hand measurements of neutrino signals might be used to constrain some properties of the nuclear equation of state of supernova cores, since they leave a fingerprint in the supernova neutrino signal.

In particular, it has been shown in this thesis that the supra–nuclear regime of the equation of state — which is also the most unknown regime —, influences the supernova evolution strongly. By stiffening or softening of the nuclear equation of state in this regime one can reproduce the differences found in the simulations with the L&S and the Wolff–EoS. This leads to the conclusion that the differences in runs with alternative equations of state stem mainly from the supra–nuclear phase. Furthermore it has been shown that theoretically possible and experimentally not excluded phase transitions from normal nuclear matter (i.e. a homogeneous phase of protons and neutrons) to an exotic phase (such as pion or hyperon condensates), which can soften the equation of state considerably, lead e.g. to significantly changes of the neutrino signals. However, it has been found that this depends strongly on the amount of softening of the supra–nuclear phase and the mass of the progenitor star. For either low–mass progenitors or only minor softening of the equation of state the influence on the supernova evolution is small and in the range of the variations observed in simulations with the Wolff and the L&S–EoS. More massive progenitors with a considerable amount of softening of the equation of state lead to significantly increased neutrino luminosities and to a collapse of the proto–neutron star to a black hole. The implications of these results are twofold. On the one hand, they clearly demonstrate the influence of the supra–nuclear phase of the equation of state on the proto–neutron star evolution. Dependent on the combination of the supra–nuclear phase and the mass of the progenitor star a collapse of the dense core to a black hole can occur and simultaneously the neutrino emission rises strongly. This might be of large importance for the so–called collapsar model of gamma ray bursts (MacFadyen & Woosley 1998), in which a delayed collapse of the dense core to a black hole is necessary to power the central engine of the gamma ray burst. If the supra–nuclear phases influences either for which progenitor masses

or at which time such a black hole collapse can occur, then the supra–nuclear phase also sets constraints on the possible progenitors for gamma ray bursts. On the other hand, the (strong) sensitivity of the supernova evolution (i.e. the neutrino emission as well as the possible collapse to a black hole) on the supra–nuclear regime of the equation of state might be — together with observations of core collapse supernovae *and* with the knowledge about the mass of the progenitor star — used to constrain the supra–nuclear equation of state.

Altogether, the one–dimensional simulations of Part I have shown that the influence of the equation of state is of significant importance for the supernova evolution. Consequently, in Part II of this thesis I have investigated the influence of the nuclear equation of state in multi–dimensional simulations, that take multi–dimensional effects such as convection into account, which — as supernova modellers do agree — are necessary for the supernova explosion mechanism. It shall be stressed here that a clean comparison of the one–dimensional and two–dimensional simulations, and thus a direct comparison of equation of state effects in simulations where spherical or axial symmetry was applied, is only possible due to the advantage that both types of simulations could be performed with the same code and thus the same numerical treatment.

For the first time, it has thus been possible to study equation of state effects in two–dimensional simulations with spectral Boltzmann neutrino transport *and* to compare these simulations with the corresponding spherically symmetric calculations. The two–dimensional models discussed in Part II of this thesis have shown that the conclusions from spherically symmetric simulations still hold, but convection inside the proto–neutron star significantly changes the structure of the dense core. The region where convection develops as well as the strength of convection depends on the choice of the equation of state. This influences noticeably the neutrino emission of the dense core, but the general trend of one–dimensional simulations that models with softer equations of state emit more and more energetic neutrinos has been found to hold in multi–dimensional simulations as well.

Furthermore, it has been observed that the proto–neutron star is excited to perform g–mode oscillations. The amplitudes of these oscillations are — due to the different compactnesses and structures of the dense cores — also influenced by the nuclear equation of state. With regard on the possible explosion mechanism of core collapse supernovae, where the explosions are powered by acoustically damping of these g–mode oscillations (see, e.g. Burrows et al. 2006a), these results require further investigation.

It has also been found that different equations of state change the strength of the non–radial shock instability, where the shock front oscillates in low–modes ($l = 1, 2...$), and the equations of state influence the growth of convection in the region between the proto–neutron star and the standing supernova shock front. These purely multi–dimensional effects are mainly influenced by the equation of state through the structural changes of the dense core and the different neutrino luminosities and neutrino energies emitted from the core, and show that the neutrino heating of matter is strongly equation of state dependent. Thus, at a time of 250 ms after the shock formation, the conditions for shock revival differ drastically for the models with different equations of state. The conditions in the model, which was calculated with a soft equation of state seem more favourable for an explosion than in the simulation with a stiff equation of state. From this the conclusion arises that the neutrino heating explosion mechanism may crucially dependent on the nuclear equation of state.

However, all multi–dimensional models which were presented in this thesis also show clearly that modern supernova simulations are not far from successful explosions: all models, except for the model calculated with a stiff equation of state, show a clear trend to favourable conditions for an explosion. These conditions stem from continuous neutrino heating of matter on the one hand, and on the other hand from the presence of the standing accretion shock instability, which increases the advection timescale of matter through the heating region (i.e. the time that it takes matter to be accreted from the shock front down to the lower border of the heating region). The latter increases the time in which matter is heated, whereas the former supplies the energy input. In late-time calculations, in all models both quantities produce a trend towards conditions that are necessary for an explosion. This is independent of the used progenitor model, or whether or not the model includes rotation. However, as the models also show, these favourable conditions need a long evolution time to develop, and the model of a rotating $15\,M_\odot$ progenitor star shows an explosion at roughly 600 ms after the shock formation. This explosion is not directly caused by the rotation but by a combination of the standing accretion shock instability and the neutrino heating. A comparison of the rotating model with a non–rotating one has shown that until a time of 350 ms after the shock formation the evolution in both models is very similar and no large influence of rotation could be observed. It is thus necessary to continue all models discussed in this thesis to longer evolution times, in order to decide whether this promising trend will really continue and will lead to an explosion.

Despite the long evolution times no indication of an acoustic–driven explosion as proposed by Burrows et al. (2006a) has been found in the multi–dimensional models. Although the — for this explosion mechanism necessary — g–mode oscillations of the proto–neutron have been observed, the amplitudes are at least two orders of magnitude below the ones observed by Burrows et al. (2006a). Although the models discussed in this thesis do not rule out the possibility of acoustically–driven explosions as proposed by Burrows et al., they rather indicate that the delayed neutrino-driven mechanism might actually power the explosion at late evolution times, which had not been investigated in multi–dimensional simulations before. The explosion obtained for a rotating $15\,M_\odot$ progenitor star, together with the promising conditions in simulations of non–rotating stars of different stellar progenitors do actually inspire the hope that the neutrino heating supernova explosion mechanism might work at later evolution times.

Only evolving all these promising models to later evolution times will show if this hope is justified. Furthermore these long evolution times of the models will be necessary to investigate in more detail the acoustic damping of proto–neutron star g–mode oscillations. Finally, if the finding of this thesis we be confirmed that for a soft equation of state an explosion is obtained and not for a stiff one, this will stress the importance of the nuclear equation of state for core collapse supernovae even more. Thus I want to conclude with the (brave) statement that it is still possible that the “correct” nuclear equation of state is the missing ingredient to understand the explosion mechanism of core collapse supernovae.

Appendices

A

Neutrino opacities

A.1. Ion-ion correlation effects in stellar core collapse

Heavy (iron-group or more massive) nuclei dominate the composition in stellar iron cores until nuclear densities are reached in the inner core and the bounce shock raises the entropies in the outer core to values where free nucleons are favoured in nuclear statistical equilibrium (NSE). During the infall phase therefore coherent, isoenergetic scattering off nuclei is the main source of opacity for the electron neutrinos produced by electron captures (cf., e.g., Bruenn 1985, 1989a,b). Neutrino-nucleus scattering thus hampers the free escape of neutrinos, is responsible for neutrino trapping around a density of $10^{12}\,\mathrm{g\,cm^{-3}}$, and regulates the deleptonization and increase of entropy during core collapse.

In the medium of the supernova core nuclei are coupled strongly with each other by Coulomb forces. They thus form a highly correlated plasma, in which the interactions of neutrinos with wavelengths larger than the average ion-ion separation a_{ion} (corresponding to neutrino energies $\epsilon_\nu \lesssim 2\hbar c/a_{\mathrm{ion}} \sim 20\,\mathrm{MeV}$) are reduced by phase interference effects (Itoh 1975). The corresponding ion screening was more recently calculated by Horowitz (1997) and Itoh et al. (2004), and investigated in its effects on stellar core collapse by Bruenn & Mezzacappa (1997). The latter authors employed the correction factor for neutrino-nucleus scattering cross sections as given by Horowitz (1997).

Itoh et al. (2004), however, pointed out that the Monte Carlo calculations, which Horowitz's fit was based on, did not allow him to accurately represent the cross section reduction for low neutrino energies, i.e., for energies $\epsilon_\nu \lesssim \hbar c/a_{\mathrm{ion}} \sim 10\,\mathrm{MeV}$, thus underestimating the importance of ion-ion correlation effects. Itoh et al. (2004) provided a more accurate analytic fitting formula by using the correct behaviour of the liquid structure factor for small momentum transfer in neutrino-nucleus scattering.

The investigations presented in this Section have two goals. On the one hand we aim at studying the differences for stellar core collapse and the formation of the supernova shock which

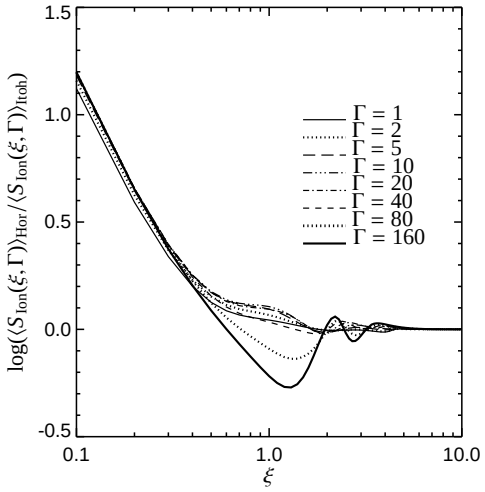

Figure A.1.: The ratio of the angle-averaged ion-ion correlation factor as calculated with the fitting formula of Horowitz (1997) (see Fig. 9 in Bruenn & Mezzacappa 1997) relative to the one obtained from the prescription provided by Itoh et al. (2004) (see their Fig. 2) as a function of the variable ξ for different values of the dimensionless parameter Γ.

arise from the improved description of ion screening as suggested by Itoh et al. (2004), compared to a treatment using the formulae of Horowitz (1997). On the other hand we intend to explore the sensitivity of the evolution to ion screening effects associated with the ionic mixture of nuclei and nucleons that are present during core collapse. In accordance with the treatment of NSE in current equations of state (EoSs) for supernova simulations, we consider the nuclear components to be free neutrons, free protons, α particles, and one kind of heavy nucleus which is considered as representative of the NSE distribution of nuclei beyond ^{4}He. Two different nuclear EoSs with largely different α mass fractions during core collapse are employed. The first EoS ("L&S"), provided by Lattimer & Swesty (1991), is based on a compressible liquid drop model and uses a Skyrme force for the nucleon interaction (Lattimer et al. 1985). Our choice of the compressibility modulus of bulk nuclear matter is 180 MeV, and the symmetry energy parameter 29.3 MeV, but the differences in the supernova evolution caused by other values of the compressibility were shown to be minor (Thompson et al. 2003, Swesty et al. 1994). The second EoS used here ("Shen") is the new relativistic mean field EoS of Shen et al. (1998a,b) with a compressibility of nuclear matter of 281 MeV and a symmetry energy of 36.9 MeV.

A.1.1. Ion-ion correlation factor

In this study we make use of two different fitting formulae for the angle-averaged correlation factor $\langle S_{\rm ion}\rangle$, which describes the reduction of the neutral-current scattering of neutrinos off nuclei by ion-ion correlation effects. It is used as a multiplicative correction to the neutrino-nucleus isoenergetic scattering opacity (cf. Horowitz 1997, Bruenn & Mezzacappa 1997, Rampp & Janka 2002). The first formula is provided by Horowitz (1997) and is based on Monte Carlo results. The second one is given by Itoh et al. (2004) and was obtained from data calculated with the improved hypernetted-chain method (see Itoh et al. 1983, and references therein) for a classical one-component plasma. In all simulations with ion screening we also take into account (the rather small) electron screening effects according to Horowitz (1997) by applying the additional correction factor of his Eqn. (19) to the rates of coherent neutrino-nucleus scattering.

One-component plasma

If the stellar plasma consists of only one nuclear species of ions ($Z_{\rm ion}, A_{\rm ion}$), the ion sphere radius which gives the mean inter-ion distance is defined as

$$a_{\rm ion} = \left(\frac{3}{4\pi n_{\rm ion}}\right)^{1/3} , \tag{A.1}$$

where $n_{\rm ion} = n_{\rm b} X_{\rm ion}/A_{\rm ion}$ is the number density of the ions with mass number $A_{\rm ion}$, charge $Z_{\rm ion}e$, and mass fraction $X_{\rm ion}$ ($n_{\rm b}$ is the number density of baryons). The strength of the ion-ion correlations is characterised by the dimensionless parameter

$$\Gamma = \frac{Z_{\rm ion}^2 e^2}{a_{\rm ion} k_{\rm B} T} = 0.2275\, \frac{Z_{\rm ion}^2}{T_{10}} \left(\rho_{12}\, \frac{X_{\rm ion}}{A_{\rm ion}}\right)^{1/3} , \tag{A.2}$$

which is the ratio of the unshielded electrostatic potential energy between the neighbouring ions to the thermal energy. Here T_{10} denotes the temperature in units of 10^{10} K and ρ_{12} the mass density in $10^{12}\,{\rm g\,cm^{-3}}$. Note that the definition of Γ in Horowitz (1997) differs from the ones used here and in Bruenn & Mezzacappa (1997) and Itoh et al. (2004) by a factor (4π) in the denominator of Eqn. (A.2). In Horowitz's notation this factor is absorbed in the employed value of e^2.

Horowitz (1997) provided the following fitting formula for the angle-averaged suppression factor $\langle S_{\rm ion}(\xi,\Gamma)\rangle_{\rm Hor}$:

$$\langle S_{\rm ion}(\xi,\Gamma)\rangle_{\rm Hor} = \frac{1}{1+\exp\left(-\sum_{i=0}^{6}\beta_i(\Gamma)\xi\right)} , \quad \text{for} \quad \xi < 3 + \frac{4}{\Gamma^{1/2}} , \tag{A.3}$$

and

$$\langle S_{\rm ion}(\xi,\Gamma)\rangle_{\rm Hor} = 1 , \quad \text{otherwise} , \tag{A.4}$$

to be applied for $1 \le \Gamma \le 150$; for values of $\Gamma < 1$ or $\Gamma > 150$, Horowitz (1997) recommends to simply set Γ to 1 or 150, respectively. The β_i are coefficient functions of Γ determined from fits to Monte Carlo data. In Eqn. (A.3) the variable ξ is the ratio of the mean ion-ion separation $a_{\rm ion}$ to the wavelength for neutrinos (during core collapse primarily electron neutrinos with energy ϵ_ν), i.e.,

$$\xi = a_{\rm ion}\frac{\epsilon_\nu}{\hbar c} . \tag{A.5}$$

Itoh et al. (2004) provide a different fitting formula, see Eqs. (23)–(26) in their paper, which is restricted to the case of a strongly degenerate electron gas, a usually well fulfilled condition during stellar core collapse. Their treatment gives different results for the ion-ion correlation factor, $\langle S_{\rm ion}(\xi,\Gamma)\rangle$, in the limit of low neutrino energies ($\xi \lesssim 1$). This can be seen in Fig. A.1. Itoh et al. (2004) argue that the reason for this difference compared to the description by Horowitz (1997) is their correct calculation of the liquid structure factor $S(k)$ for small momentum transfer k. This makes the suppression of neutrino-nucleus scattering by ion-ion correlations more important than estimated by Horowitz (1997) and Bruenn & Mezzacappa (1997).

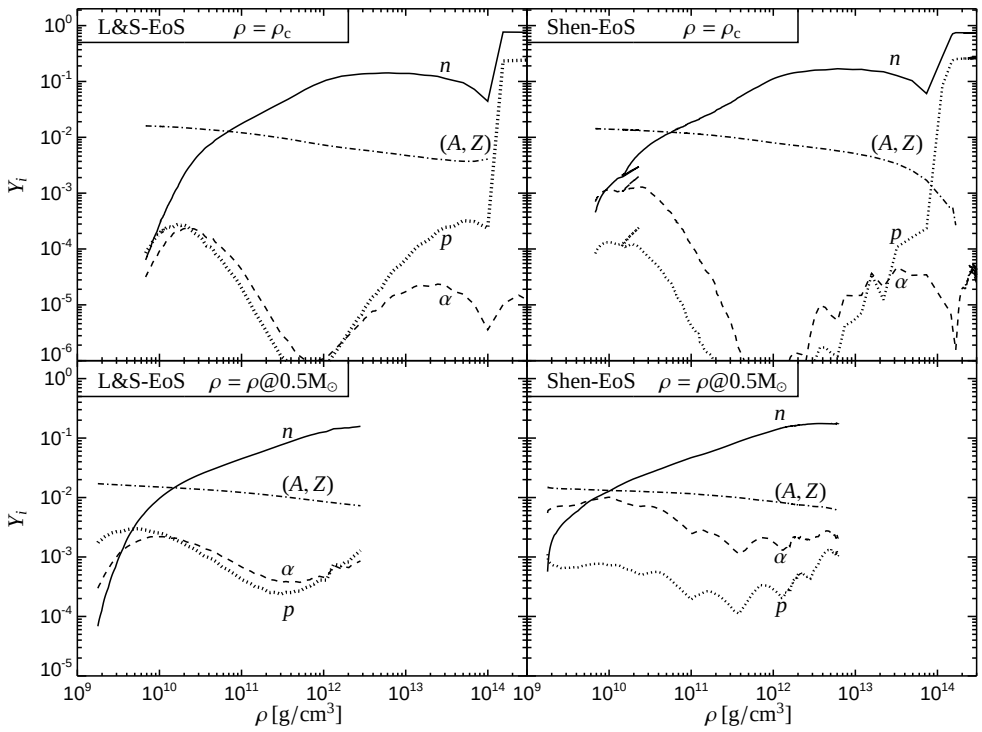

Figure A.2.: Composition as a function of density at the centre (top) and at an enclosed mass of 0.5 $M_\odot$ (bottom) for the evolution during core collapse with the EoSs of Lattimer & Swesty (1991; left) and Shen et al. (1998a,b; right). The plots show the evolution of the number fractions Y for free neutrons, protons, α-particles, and the representative heavy nucleus until shock formation. The results were obtained with ion-ion screening treated according to case "EoS_ion_Itoh" (see text).

The simulations presented here intend to study the dynamical consequences of these differences during supernova core collapse.

Up to now we have considered a stellar medium consisting of only one nuclear species and referred to formulae derived for a classical one-component plasma. However, in the collapsing core of a massive star a mixture of nuclei besides free neutrons and protons is present, usually approximated by α particles plus one representative, heavy nucleus. To deal with that we decided, in the simplest approach, to calculate the suppression factor $\langle S_{\rm ion}(\xi,\Gamma)\rangle$ for α particles and for the heavy nucleus independently, using the values for the average distance $a_{\rm ion}$ between ions of the same kind, derived from the number densities n_α or n_A, respectively. This assumes that different ionic components coexist without collectively affecting the screening of neutrino-nucleus interactions. Alpha particles thus change the ion screening for heavy nuclei only by the fact that their presence may reduce the number density of heavier nuclei.

Ionic mixtures

For a liquid mixture of different ions (Z_j, A_j) including free protons, Itoh et al. (2004) suggest a modified treatment, referring to earlier work by Itoh et al. (1979). Employing the so-called linear mixing rule, one can extend the calculations of neutrino-nucleus scattering cross sections, obtained for a one-component ion liquid, to the case of multi-component fluids.

The ion sphere radius for an ion j in the mix is now given by

$$a_j = a_{\rm e}\, Z_j^{1/3} \tag{A.6}$$

with $a_{\rm e}$ being the electron sphere radius,

$$a_{\rm e} = \left(\frac{3}{4\pi \sum_i Z_i n_i}\right)^{1/3} , \tag{A.7}$$

where the sum extends over free protons and all nuclei with number densities n_i. The dimensionless variable ξ_j then becomes

$$\xi_j = a_j \frac{\epsilon_\nu}{\hbar c} . \tag{A.8}$$

The ion-ion correlations of nuclear species j depend on the dimensionless parameter Γ_j defined as

$$\begin{aligned} \Gamma_j &= \frac{{Z_j}^{5/3} e^2}{a_{\rm e} k_{\rm B} T} = \frac{Z_j^2 e^2}{k_{\rm B} T}\left(\frac{4\pi}{3}\sum_i \frac{Z_i}{Z_j} n_i\right)^{1/3} \\ &= 0.2275\, \frac{Z_j^{5/3}}{T_{10}}\left(\rho_{12}\sum_i \frac{X_i Z_i}{A_i}\right)^{1/3} . \end{aligned} \tag{A.9}$$

The angle-averaged ion-ion correlation factor $\langle S_{\rm ion}(\xi_j,\Gamma_j)\rangle$ is now evaluated for α particles and heavy nuclei with the fitting formula provided by Itoh et al. (2004), using ξ_j and Γ_j as given in Eqs. (A.8) and (A.9), respectively.

Applying the naive procedure of Sect. A.1.1 for the conditions in a supernova core shows that usually $\xi \gg 1$ for α particles because α's are less abundant than heavy nuclei in the central part

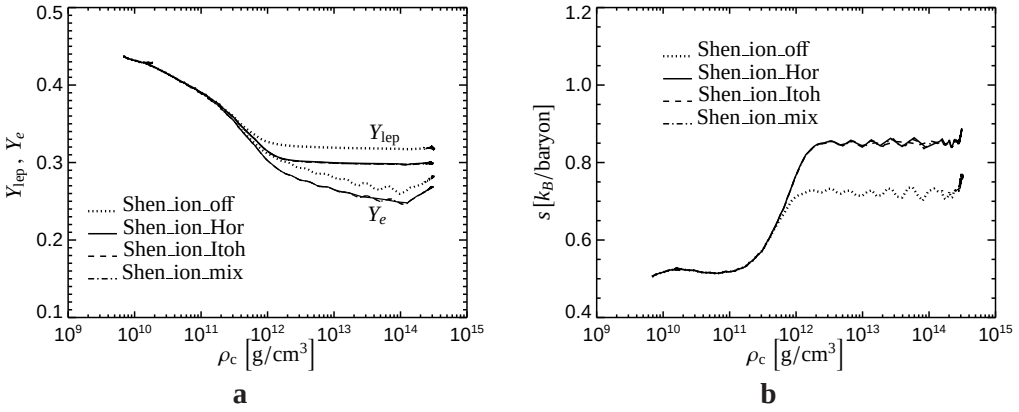

Figure A.3.: a: Central electron fraction Y_e and lepton fraction $Y_{\rm lep}$ as functions of central density for core collapse calculations with the EoS of Shen et al. (1998a,b). Model Shen_ion_off does not include the effects of ion-ion correlations, Model Shen_ion_Hor uses the description of ion screening according to Horowitz (1997), Model Shen_ion_Itoh employs Itoh et al.'s (2004) treatment for a one-component plasma, and Model Shen_ion_mix their treatment of ionic mixtures. **b**: Same as panel a but for the central (matter) entropy s.

of the core and during most phases of the collapse. Their Γ is then less than unity. Both factors diminish ion screening for α's to a negligible level. In contrast, following the description in this section, the presence of α's can affect also the ion screening of heavy nuclei by reducing the inter-ion separation (Eqn. A.6) and thus ξ_j (Eqn. A.8). Moreover, Γ_j for heavy nuclei according to Eqn. (A.9) might become larger than in Eqn. (A.2). Therefore the presence of α's has an indirect influence on neutrino scattering off heavy nuclei and thus on ion-ion correlations during stellar core collapse, despite the fact that the screening effects for α particles are still small because their Γ is usually below unity (following Horowitz (1997), Γ is then set to unity for evaluating the angle-averaged cross section suppression factor).

While our procedure for treating the effects of α particles in an ionic mixture with heavy nuclei and free nucleons adopts the recipe of Itoh et al. (2004), Sawyer (2005) recently discussed an alternative approach to the problem for multi-component fluids by applying the Debye-Hückel approximation. He pointed out that in multi-component plasmas the ion-ion correlation effects might be greatly *reduced*, leading to much larger neutrino opacities than for a one-component plasma, even if the constituent ions have only a small range of N/Z ratios. Electron density fluctuations for an ionic mixture enhance this tendency. Sawyer's calculations therefore yield a result which is *opposite to* our application of the linear mixing rule for calculating multi-component plasma parameters. They tend to bring one back closer to the case with ion-ion correlations being ignored, simulations of which will be presented below, too. Thus we provide a set of models with the intention to encompass and bracket the "extreme" possibilities discussed in the literature.

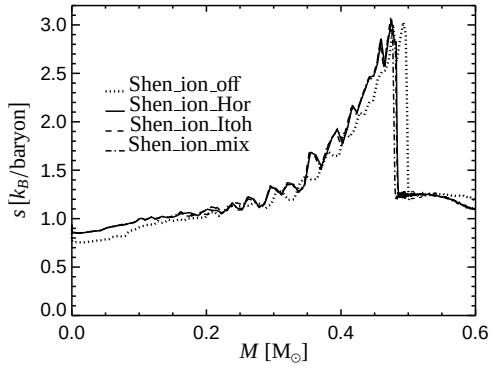

Figure A.4.: Gas entropy vs. enclosed mass at the moment of shock formation in the models of Fig. A.3. The shock formation is defined by the instant when the entropy in the core first reaches a value of $3\,k_{\rm B}$ per nucleon.

A.1.2. Numerical simulations

For our study we apply the same micro-physical input as described in Section 3.2. The core collapse simulations presented here were started from the 15 $M_\odot$ progenitor s15a28 from Heger et al. (2001).

For describing the thermodynamics and composition of the stellar plasma, the EoS of Lattimer & Swesty (1991) and the one of Shen et al. (1998a,b) are applied at high densities ($\rho > 6.7 \times 10^7\,{\rm g\,cm^{-3}}$ or $\rho > 2.7 \times 10^8\,{\rm g\,cm^{-3}}$, respectively). At lower densities the EoS contains a mixture of electrons, positrons, photons, nucleons and nuclei, with the nuclear composition being described by a simple approximation to a four-species NSE for temperatures above about 0.5 MeV. Below that temperature the composition is adopted from the progenitor star and modified if nuclear burning plays a role during collapse (for details, see Appendix B in Rampp & Janka 2002). The two EoSs show major differences in the abundances of α particles, which can be larger by up to a factor of ~ 10 in case of the Shen et al. (1998a,b) EoS. This is visible in Fig. A.2 where the number fractions of free neutrons, protons, α's and of the representative heavy nucleus (whose mass and charge numbers typically grow with density until nuclei disappear at the phase transition to nuclear matter) are displayed as functions of increasing density during collapse both at the stellar centre and at an enclosed mass of $0.5\,M_\odot$. Although their mass fraction is much lower, α particles in the Shen et al. (1998a,b) EoS can become equally or even more abundant (by a factor up to about two) than heavy nuclei in the outer layers of the collapsing core, in particular exterior to $M(r) \gtrsim 0.5$–$0.6\,M_\odot$.

For each of the employed EoSs four core collapse simulations were performed, all starting from the onset of gravitational instability and carried on until the moment of shock formation. Calculations with ion-ion correlation (and electron screening) effects in neutrino-nucleus scattering being switched off, i.e. for $\langle S_{\rm ion}\rangle \equiv 1$ (and $R_{\rm e} \equiv 1$ instead of Eqn. 19 of Horowitz 1997), are denoted with "EoS_ion_off", where EoS stands for "L&S" or "Shen". They are compared with simulations (models "EoS_ion_Hor") where the ion-ion correlation factor of Horowitz (1997; Eqs. A.3,A.4) is used, and with models in which ion-ion correlations are described ac-

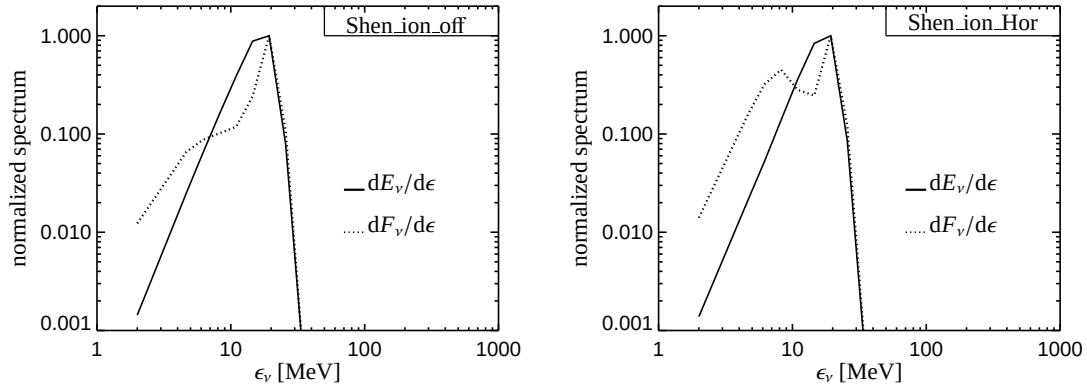

Figure A.5.: Spectra of neutrino energy density (solid line) and energy flux (dashed) for Model Shen_ion_off (left) and Model Shen_ion_Hor (right) when a density of 10^{12} g cm^{-3} is reached at an enclosed mass of 0.3 $M_\odot$.

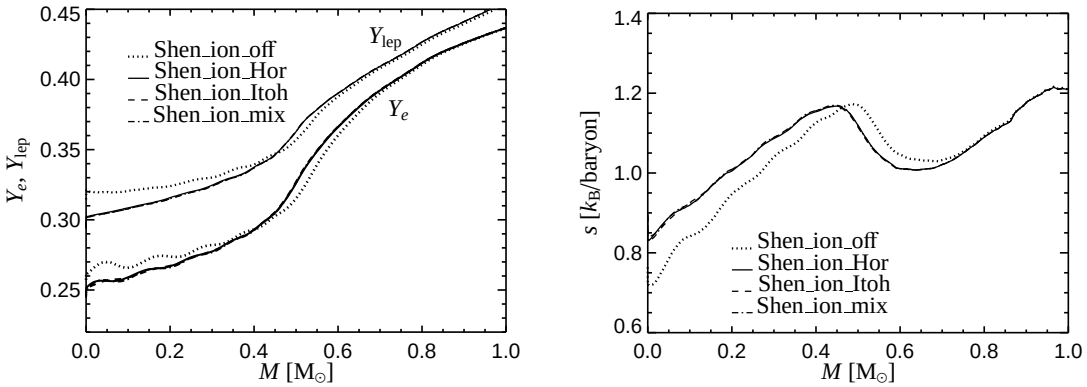

Figure A.6.: Profiles of electron fraction Y_e, lepton fraction $Y_{\rm lep}$ (left), and (gas) entropy s (right) versus enclosed mass for Models Shen_ion_off (dotted), Shen_ion_Hor (solid), Shen_ion_Itoh (dashed), and Shen_ion_mix (dash-dotted) at the time when the central density has reached a value of 10^{14} g cm^{-3}.

cording to Itoh et al. (2004) (models "EoS_ion_Itoh"). Finally, the sensitivity of stellar core collapse to the treatment of ion screening for ionic mixtures is investigated by simulations (models "EoS_ion_mix") in which the correction factors $\langle S_{\rm ion}(\xi_j, \Gamma_j)\rangle$ are calculated from Itoh et al.'s (2004) formulae with ξ_j and Γ_j as given in Sect. A.1.1.

A.1.3. Results

Figure A.3 shows electron fraction Y_e, lepton fraction $Y_{\rm lep}$ and (gas) entropy s, respectively, at the core centre during collapse simulations with the Shen et al. (1998a,b) EoS. For both EoSs employed in this work, the same relative changes are found when models without ion screening

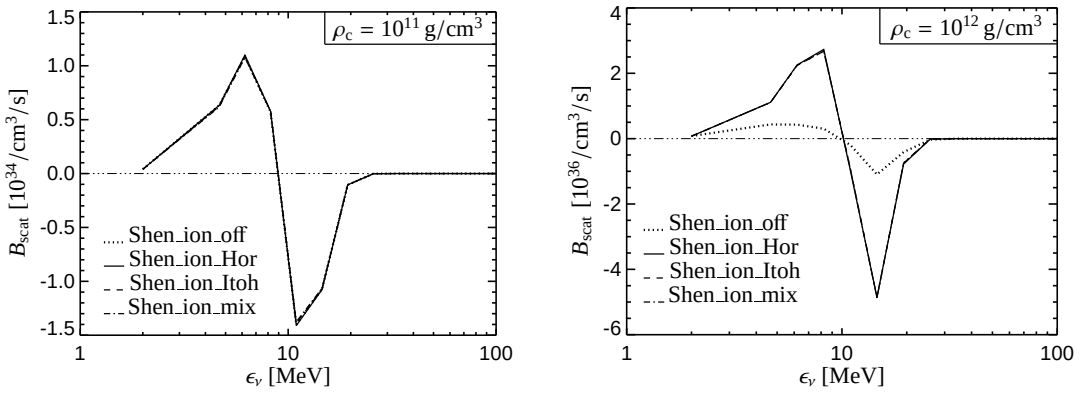

Figure A.7.: The energy source term for neutrino-electron scattering for densities of (a) 10^{11} g cm^{-3} and (b) 10^{12} g cm^{-3} at the stellar center in the collapse models with the Shen et al. (1998a,b) EoS. Negative values mean that neutrino energy is "absorbed" (net scattering out of the corresponding energy bin), positive values mean "emission" of neutrino energy (i.e., net scattering of neutrinos into the energy bin).

are compared with calculations with ion-ion correlations according to Horowitz (1997) (see Models Shen_ion_Hor and Shen_ion_off in Fig. A.3). We shall mostly concentrate here on the results obtained with the Shen et al. (1998a,b) EoS, because α particles are much more abundant there (see Fig. A.2) and many aspects of ion screening in simulations with the EoS of Lattimer & Swesty (1991) were already discussed by Bruenn & Mezzacappa (1997). Our results agree qualitatively with those of the latter paper. Quantitative differences compared to Bruenn & Mezzacappa (1997) are caused by the inclusion of improved electron capture rates on nuclei in our work, which significantly increase electron captures above a few 10^{10} g cm^{-3} so that lower values of $Y_{\rm lep}$ and s result after trapping (cf. Langanke et al. 2003, Martínez–Pinedo et al. 2005).

As explained in detail by Bruenn & Mezzacappa (1997), the screened cross section for neutrino-nucleus scattering reduces the transport optical depth of low-energy neutrinos (cf. Fig. 3 in Bruenn & Mezzacappa 1997) and allows them to escape from the core more easily. This is obvious from a flux enhancement of neutrinos at energies $\epsilon_\nu \lesssim 10$ MeV in Fig. A.5, where the situation is displayed at a density of $\rho = 10^{12}$ g cm^{-3}. Ion-ion correlations thus cause a decrease of Y_e and $Y_{\rm lep}$ that is stronger by about 0.02 until neutrino trapping sets in (Fig. A.3a). The homologously collapsing stellar core correspondingly shrinks and the shock forms at a somewhat smaller enclosed mass (Fig. A.4). The shock formation is defined by the moment when the postshock entropy first reaches a value of $3\,k_{\rm B}$ per nucleon. A part of the effect visible in Fig. A.4 might therefore be a consequence of the slightly higher core entropy after neutrino trapping in models with ion screening (see Figs. A.3b and A.6).

Neutrino-electron scattering is very efficient in downscattering neutrinos from the high energies, where they are mostly created by electron captures, to lower energy states. Therefore the phase space at low energies is quickly refilled. Figure A.7 shows the source term for

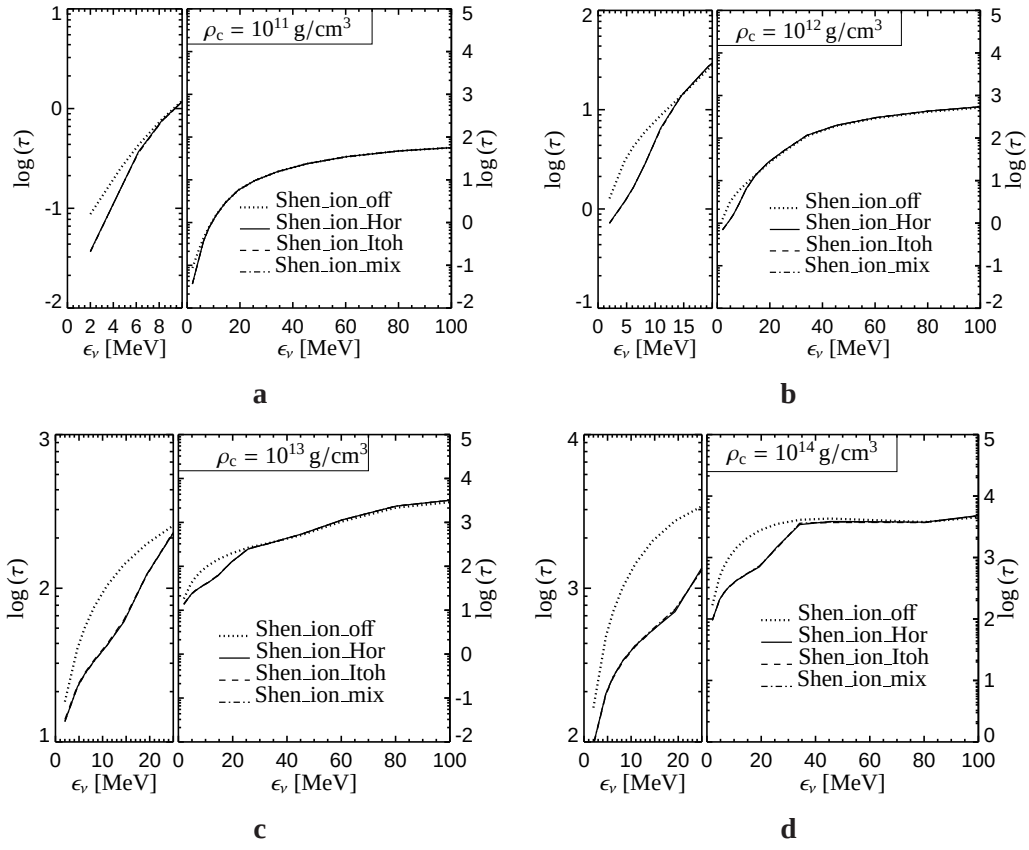

Figure A.8.: The optical depth for energy exchange between neutrinos and stellar plasma as a function of the neutrino energy at the centre of the iron core for densities of (a) 10^{11} g cm^{-3}, (b) 10^{12} g cm^{-3}, (c) 10^{13} g cm^{-3}, and (d) 10^{14} g cm^{-3}. The results are taken from collapse calculations with the Shen et al. (1998a,b) EoS. The left panels show enlargements of the low-energy window where ion-ion correlations have the largest effect.

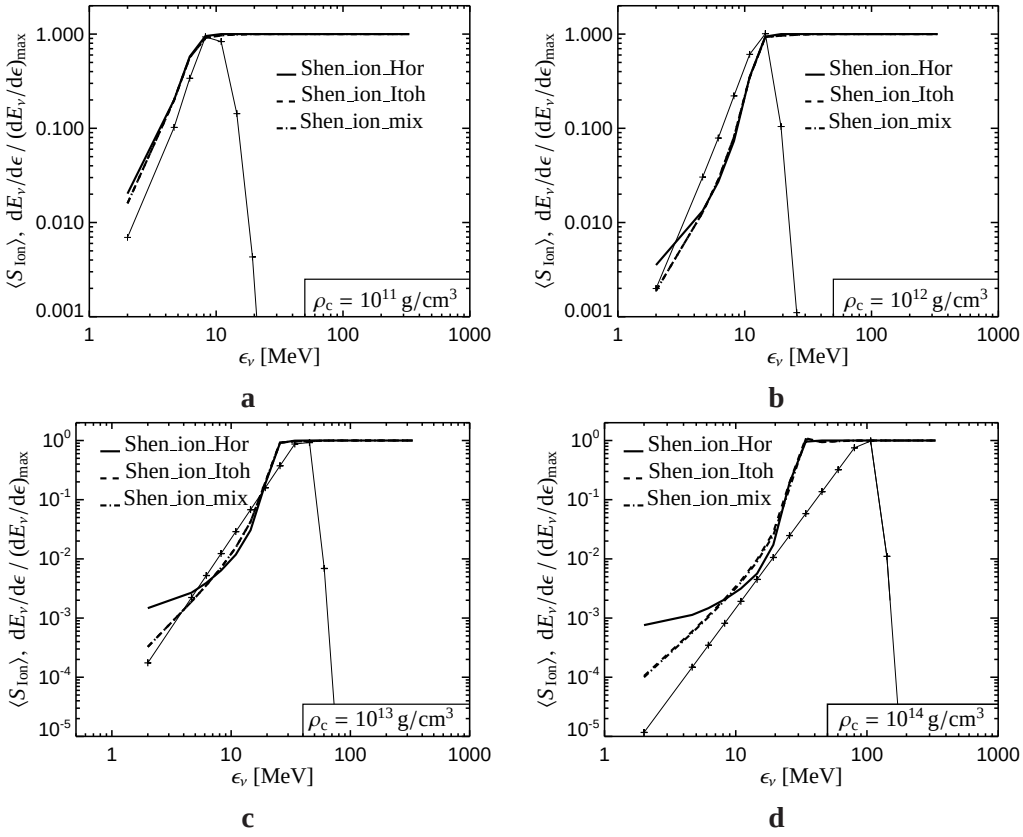

Figure A.9.: The cross section suppression factor $\langle S_{\rm ion}\rangle$ for neutrino scattering off heavy nuclei (bold lines) as function of neutrino energy at the center of the iron core for densities of (a) 10^{11} g cm^{-3}, (b) 10^{12} g cm^{-3}, (c) 10^{13} g cm^{-3}, and (d) 10^{14} g cm^{-3}. The results are taken from collapse simulations with the Shen et al. (1998a,b) EoS. Also plotted (thin solid lines with crosses) are the local spectra of the neutrino energy density (normalised to the spectral maximum), which are practically identical for all simulations.

energy redistribution by neutrino scatterings off electrons for two density values below trapping conditions. The downscattering of high-energy neutrinos explains why the local energy spectra, dE_ν/dϵ_ν with E_ν being the neutrino energy density, are essentially the same in Models Shen_ion_off and Shen_ion_Hor, despite of clear differences between the energy flux spectra of both runs (Fig. A.5).

On their way out escaping neutrinos transfer a part of their energy to electrons in collisions, thus heating the stellar medium (Bruenn 1986). Since ion screening of neutrino-nucleus scatterings reduces the transport opacity and therefore the effective optical depth for energy exchange with the stellar background mainly for low-energy neutrinos, but hardly changes the downscattering probability of high-energy neutrinos (Fig. A.8), the larger loss of lepton number leads to an increase of the central entropy by about $0.12\,k_{\rm B}$ per nucleon (Fig. A.3b). In Fig. A.8 the

optical depth τ at the centre is calculated as

$$\tau(\epsilon) = \int_0^\infty \mathrm{d}r \, (\lambda_{\mathrm{eff}}(\epsilon, r))^{-1} \, , \tag{A.10}$$

where $\lambda_{\mathrm{eff}}(\epsilon, r)$ is the effective mean path for energy exchange, i.e., the average displacement between two reactions with energy exchange between neutrinos and target particles (see Rybicki & Lightman 1979). It can be expressed as

$$\lambda_{\mathrm{eff}}(\epsilon, r) = \sqrt{\lambda_{\mathrm{t}}(\epsilon, r) \, \lambda_{\mathrm{e}}(\epsilon, r)} \, , \tag{A.11}$$

when λ_{e} is the mean free path for reactions with energy exchange, i.e. neutrino absorption and neutrino-electron scattering in the present context, and λ_{t} is the total mean free path for momentum transfer ("transport mean free path"), which includes all processes by which neutrinos interact with the stellar fluid.

Figure A.9 displays the ion screening factors $\langle S_{\mathrm{ion}} \rangle$ superimposed to the normalised neutrino energy spectra $\mathrm{d}E_\nu/\mathrm{d}\epsilon_\nu$ at the stellar centre for densities of $10^{11}\,\mathrm{g\,cm^{-3}}$, $10^{12}\,\mathrm{g\,cm^{-3}}$, $10^{13}\,\mathrm{g\,cm^{-3}}$, and $10^{14}\,\mathrm{g\,cm^{-3}}$. Figure A.9 once more demonstrates that the reduction of neutrino-nucleus scattering mostly affects neutrinos at energies below the spectral maximum for all plotted cases. In combination with Fig. A.8 it also shows that the trapping conditions for the bulk of the neutrino spectrum are not influenced strongly by ion screening. This was identified by Bruenn & Mezzacappa (1997) as the reason why ion-ion correlations have no dramatic effect on the core deleptonization.

From Fig. A.1 it is clear that differences between the treatments of ion-ion correlations by Horowitz (1997) and Itoh et al. (2004) are largest for $\xi \lesssim 0.5$. The improvements by Itoh et al. (2004) are therefore most important for the lowest neutrino energies in the energy window affected by ion screening. Since the phase space available at such low energies is small, one cannot expect large quantitative consequences for stellar core collapse. This is confirmed by Figs. A.3–A.4 and Fig. A.6. Itoh et al.'s (2004) description (in Model Shen_ion_Itoh) leads to values of Y_e, Y_{lep}, and s after trapping which are essentially indistinguishable from those obtained with Horowitz's (1997) formulae, consistent with the insignificant differences between Models Shen_ion_Hor and Shen_ion_Itoh seen in the other plots. Note that the crossing of the Y_e-, Y_{lep}- and s-profiles for simulations with and without ion screening at $0.45\,M_\odot$ (Fig. A.6) was also present in the results of Bruenn & Mezzacappa (1997). Finally testing the sensitivity of the core collapse evolution to the treatment of ion screening for the ionic mixture of free protons, α particles and a representative heavy nucleus, we also could not discover any differences of relevance.

A more detailed analysis reveals the reasons for this insensitivity, which are valid for both employed EoSs: Below the neutrino trapping regime (i.e., for $\rho \lesssim 10^{12}\,\mathrm{g\,cm^{-3}}$) even for low-energy neutrinos ($\epsilon_\nu \approx 5\,\mathrm{MeV}$) the parameter ξ is larger than or around unity (except for neutrinos interacting with α particles in an ionic mix when ξ_α is computed from Eqs. A.6–A.8). Moreover, $\Gamma \lesssim 50$ holds at the same time, implying that the ion-ion correlation factors $\langle S_{\mathrm{ion}}(\xi, \Gamma) \rangle_{\mathrm{Hor}}$ and $\langle S_{\mathrm{ion}}(\xi, \Gamma) \rangle_{\mathrm{Itoh}}$ for neutrino scattering off heavy nuclei are essentially the same (see Fig. A.1). Only at densities above the trapping density the value of ξ drops significantly below unity and Γ exceeds 50, causing visible (typically factors 2–3 for $\epsilon_\nu \lesssim 5\,\mathrm{MeV}$; Fig. A.9) differences in the

ion-ion suppression factors $\langle S_{\rm ion} \rangle$. At these densities, however, the exact value of the neutrino-nucleus scattering cross section has no noticeable influence on the evolution of the core properties and on the neutrino transport.

Alpha particles in the inner core do not become sufficiently abundant to cause mentionable differences. Their indirect effect on ion-ion correlations of heavy nuclei in an ion mixture by reducing a_j (and thus ξ_j) and increasing Γ_j (Sect. A.1.1) for the heavier nuclei is essentially negligible, because their contribution to the sum in Eqn. (A.7) is diminished by their number density being multiplied with a factor $Z_\alpha/Z_j \ll 1$. Moreover, α particles do not account for a significant contribution to the total neutral-current scattering opacity, because the opacity for coherent scattering of neutrinos by nuclei (Z, N, A) scales roughly with N^2/A and therefore is much smaller for α particles than for heavy nuclei. For this reason the direct influence of α particles and thus of the suppression of their coherent (elastic) scattering cross section for low neutrino energies is miniscule, despite the fact that ξ_α drops below unity already at densities $\rho \lesssim 10^{11}\,\mathrm{g\,cm^{-3}}$ in a mixture with heavy nuclei. (On the other hand, Γ_α turns out to be always less than unity and, following Horowitz (1997), is therefore set to $\Gamma_\alpha = 1$ for evaluating the angle-averaged ion screening correction factor.)

In this Section we presented results from simulations of stellar core collapse with the aim to investigate the consequences of ion-ion correlations in neutrino-nucleus scattering, comparing Itoh et al.'s (2004) improved description with an older one by Horowitz (1997). We employed the EoS of Shen et al. (1998a,b) in addition to Lattimer and Swesty's (1991) EoS and treated electron captures on heavy nuclei according to Langanke et al. (2003), making nuclei dominant over protons in producing neutrinos up to the density of the phase transition to nuclear matter.

Despite these differences in the input physics, our models essentially confirmed the previous calculations by Bruenn & Mezzacappa (1997) who followed Horowitz (1997) in their description of ion screening. Because ion screening is effective only in a low-energy window where the available phase space is rather small, the influence of ion-ion correlations during stellar core collapse and on the formation of the supernova shock is moderate (Bruenn & Mezzacappa 1997).

We found that the improvement by Itoh et al. (2004) does not lead to any noticeable differences because it affects only neutrinos of very low energies ($\lesssim 5\,\mathrm{MeV}$) before trapping densities ($\rho \approx 10^{12}\,\mathrm{g\,cm^{-3}}$) are reached. Differences at larger neutrino energies occur only at higher densities and thus do not affect the deleptonization and entropy evolution. Effects due to the ionic mixture of free protons, α particles, and a representative heavy nucleus — using the linear mixing rule as suggested by Itoh et al. (2004) — were found to be negligibly small, too, mainly because the abundance of α particles in the inner regions of the collapsing stellar core is too low to affect the ion screening of heavy nuclei indirectly (see Sect. A.1.1). Alpha particles do not contribute to the total opacity for elastic neutrino-nucleus scattering on a level where their ion screening (which becomes sizable only when the mixture effects of Sect. A.1.1 are accounted for) might be relevant.

Improving the description of ion-ion correlations for the complex mix of heavy nuclei with a large variety of components, alpha particles, and free nucleons in the supernova core, however, is desirable. Referring to multi-component calculations based on the Debye-Hückel approximation in the limit of small momentum transfer, Sawyer (2005) argues that a range of N/Z ratios in ionic mixtures can protect against the strong ion screening suppression of neutrino-nuclei scat-

tering predicted by the effective averages of one-component plasma parameters applied in the current literature and in this work. Moreover, the description of nearly free nucleons and nuclei in NSE is expected to hold only up to a density of about $10^{13}\,\mathrm{g\,cm^{-3}}$. Above this density and below the normal nuclear matter saturation density, a pasta phase may develop with nucleons clustered in subtle and complex shapes. Correlation effects for coherent neutrino scattering can then not be treated within the single heavy nucleus approximation (e.g., Horowitz et al. 2004a,b, Watanabe et al. 2004).

A.2. Effects of electron polarisation

In the previous Section A.1 we described the effects of ion-ion correlations during the stellar core collapse phase. In the following Section we will discuss the related effect of electron polarisation that also modifies the iso-energetic scattering cross section of neutrinos on nuclei.

Traditionally, the differential cross section for energy conserving scattering of neutrinos off nuclei is written as (see, e.g. Rampp & Janka 2002)

$$\frac{\mathrm{d}\sigma}{\mathrm{d}\Omega} = \frac{\sigma_0}{128\pi^2}\left(\frac{\epsilon_\nu}{m_\mathrm{e}c^2}\right)^2 A^2 n_\mathrm{A} W^2 \mathrm{e}^{-4b\epsilon^2/c^2(1-\omega)} S_\mathrm{ion}(\omega)(1+\omega) \tag{A.12}$$

where ω is a abbreviation for the cosine of the scattering angle θ, $\mathrm{e}^{-4b\epsilon^2/c^2(1-\omega)}$ represents the nuclear form factor, $S_\mathrm{ion}(\omega)$ is due to the ion–ion corelation (see Section A.1), and

$$W := \left[(C_\mathrm{A} - C_\mathrm{V}) + (2 - (C_\mathrm{A} - C_\mathrm{V})\frac{2Z - A}{A}\right], \text{ where} \tag{A.13}$$

$C_\mathrm{A}, C_\mathrm{V}$ are the coupling constants for axial and vector currents of the weak interaction.

Then the total cross section reads

$$\begin{aligned}\sigma^\mathrm{tot} &= \int \frac{\mathrm{d}\sigma}{\mathrm{d}\Omega}(1-\omega)\mathrm{d}\Omega = 2\pi \int_{-1}^{1} \mathrm{d}\omega \frac{\mathrm{d}\sigma}{\mathrm{d}\Omega}(1-\omega) = \\ &\frac{\sigma_0}{64\pi}\left(\frac{\epsilon_\nu}{m_\mathrm{e}c^2}\right)^2 A^2 n_\mathrm{A} W^2 \int_{-1}^{1} \mathrm{d}\omega (1+\omega)(1-\omega) S_\mathrm{ion}(\omega) = \\ &\frac{\sigma_0}{64\pi}\left(\frac{\epsilon_\nu}{m_\mathrm{e}c^2}\right)^2 A^2 n_\mathrm{A} W^2 \cdot \frac{4}{3}\left\langle S(\epsilon)\right\rangle_\mathrm{ion} \ ,\end{aligned} \tag{A.14}$$

where $\langle S(\epsilon)\rangle_\mathrm{ion}$ now indicates the angularly averaged ion–ion corelation factor (see Section A.1).

Expressing this in the first two Legendre coefficients, and by considering the low and high neutrino energy limits one finally obtains (see Bruenn & Mezzacappa 1997) for the transport

opacity due to scattering

$$\kappa^{(0)}(\epsilon) - \frac{1}{3}\kappa^{(1)}(\epsilon) = 2\pi\epsilon^2\left(\Phi_0(\epsilon) - \Phi_1(\epsilon)\right) = \frac{\sigma_0}{32\pi}\left(\frac{\epsilon_\nu}{m_\mathrm{e}c^2}\right)^2 A^2 n_\mathrm{A} W^2 2\frac{y - 1 + (1+y)\mathrm{e}^{-2y}}{y^3}\langle S_\mathrm{ion}\rangle\,, \tag{A.15}$$

where $\langle S_\mathrm{ion}\rangle$ takes account of the angularly averaged ion–ion correlations. The implementation of the transport opacity is straightforward. However, we make the assumption that the ion correlation correction factor $\langle S_\mathrm{ion}\rangle$ is proportional to both Φ_0 and Φ_1 and not only to the combination $\Phi_0 - \Phi_1$ (see Rampp 2000)

Seizing a suggestion of Leinson et al. (1988), Burrows et al. (2004) describes an additional C_los term to the cross section of Eqn. A.12 that includes the contributions of the electron polarisation in the iso–energetic scattering of neutrinos on nuclei at low neutrino energies (i.e. $\epsilon_\nu < 5$ MeV).

Taking this additional term into account, the differential cross section for isoenergetic scattering reads

$$\frac{\mathrm{d}\sigma}{\mathrm{d}\Omega} = \frac{\sigma_0}{64\pi}\left(\frac{\epsilon_\nu}{m_\mathrm{e}c^2}\right)^2 A^2 n_\mathrm{A}\left(W\mathrm{e}^{-2b\epsilon^2/c^2(1-\omega)} + C_\mathrm{los}(\omega)\right)^2 S_\mathrm{ion}(\omega)(1+\omega)\,, \tag{A.16}$$

where

$$C_\mathrm{los}(\omega) = \frac{Z}{A}\left(\frac{1 + 4\sin^2\Theta_\mathrm{W}}{1 + (kr_\mathrm{D})^2}\right) \tag{A.17}$$

and r_D is the Debye radius

$$r_\mathrm{D} = \sqrt{\frac{\pi\hbar^2 c}{4\alpha p_\mathrm{F} E_\mathrm{F}}}, \tag{A.18}$$

$k^2 = |p - p'|^2 = 2(\epsilon_\nu/c)^2(1-\omega)$, p_F and E_F are the electron Fermi momentum and energy, and α is the fine–structure constant.

Note, that $C_\mathrm{los}(\omega)$ is in principal angle dependent and thus the straightforward integration from Eqn. A.16 is not possible.

We thus simply assume, that the angle dependence of $C_\mathrm{los}(\omega)$ can be mimicked by introducing an average angle $\langle\omega\rangle$ into $C_\mathrm{los}(\omega)$.

Then by using $\left(W\mathrm{e}^{-2b\epsilon^2/c^2(1-\omega)} + C_\mathrm{los}(\omega)\right)^2 = W^2\mathrm{e}^{-4b\epsilon^2/c^2(1-\omega)} + 2W\mathrm{e}^{-2b\epsilon^2/c^2(1-\omega)}C_\mathrm{los} + C_\mathrm{los}^2$ in the integral from Eqn. A.16 we obtain:

$$\kappa^{(0)}(\epsilon) - \frac{1}{3}\kappa^{(1)}(\epsilon) = 2\pi\epsilon^2\left(\Phi_0(\epsilon) - \Phi_1(\epsilon)\right)$$
$$= \frac{\sigma_0}{32\pi}\left(\frac{\epsilon_\nu}{m_e c^2}\right)^2 A^2 n_A W^2 2\frac{y - 1 + (1+y)e^{-2y}}{y^3}\langle S_{ion}\rangle +$$
$$2\frac{\sigma_0}{32\pi}\left(\frac{\epsilon_\nu}{m_e c^2}\right)^2 A^2 n_A W 2\frac{y/2 - 1 + (1+y/2)e^{-y}}{(y/2)^3}\langle S_{ion}\rangle C_{los} +$$
$$\frac{\sigma_0}{32\pi}\left(\frac{\epsilon_\nu}{m_e c^2}\right)^2 A^2 n_A \langle S_{ion}\rangle C_{los}^2 \frac{4}{3} \qquad \text{(A.19)}$$

Note that the original implementation is retained as $lim_{\epsilon\to\infty} C_{los} = 0$.

Again, we assume that the ion correlation correction factor $\langle S_{ion}\rangle$ is proportional to both Φ_0 and Φ_1 and not only to the combination $\Phi_0 - \Phi_1$, see Rampp (2000).

As we have already stated $C_{los} = 0$ is negligible for neutrino energies ϵ above roughly 5 MeV. To guarantee numerically a smooth transition we have thus added an additional "Fermi–like " suppression factor F_{sup}

$$F_{sup} = \left(1 + \exp\left(\epsilon_\nu - a\right)/b\right)^{-1} \quad , \qquad \text{(A.20)}$$

where ϵ_ν is the neutrino energy, a and b are parameters that can be chosen such that the contributions of C_{los} is smoothly suppressed for higher neutrino energies.

Though the contribution of the additional term C_{los} is not likely to produce significant changes during a core collapse simulation we have simulated a few simulations from onset of gravitational instability to core bounce of a 15 $M_\odot$ progenitor star of Heger et al. (2001). We have calculated a series of core collapse simulations where we did not regard the polarisation term (C_{los}=0 for all neutrino energies, model “NoClos”), and where we considered the polarisation term. For the latter simulations we used the extreme cases of mean angles of ω=-1,0,1. Additionally, we simulated one collapse where the mean angle was randomly varied between –1 and 1 for each time step. Furthermore, we have varied the values a and b from Eqn. A.20 in order to suppress the polarisation term for different neutrino energies (see Table A.2) between 5 MeV and 20 MeV. The reason for the latter cases is that though the contribution of the polarisation term should vanish for neutrino energies below 10 MeV, our choice of the neutrino energy grid allows for only 2–3 energy bins in that neutrino energy range. Thus by suppressing the polarisation term in Eqn. A.16 at higher energies we can test if our results converge and whether the number of neutrino energy bins is important for the effects of the polarisation term.

A.2.1. Results

As one can see in Fig. A.10 considering the additional polarisation term has — as expected — only minor influences on the collapse phase. The difference in the deleptonisation of the core is roughly 3% and the entropy rises by roughly 2%. As one can also see this effect is even weaker in the models where the contribution of the polarisation term was suppressed above neutrino energies of 5 MeV (and with two energy bins below 5 MeV) and the effect saturates for a suppression of the polarisation term for neutrino energies above 10 MeV (and 4 energy bins below 10 MeV) and 20 MeV, respectively. This implies that indeed the effect of the polarisation term

Model	$\epsilon_{\rm sup}$ [MeV]	ω
NoClos	0	—
Clos–5–0	5	0
Clos–5–1	5	+1
Clos–5–m1	5	–1
Clos–5–ran	5	random
Clos–10–1	10	+1
Clos–10–m1	10	–1
Clos–10–ran	10	random
Clos–20–ran	20	random

Table A.1.: Overview over all models calculated with the polarisation term $C_{\rm los}$. $\epsilon_{\rm sup}$ denotes the cutoff value of the neutrino energy above which polarisation term $C_{\rm los}$ is suppressed.

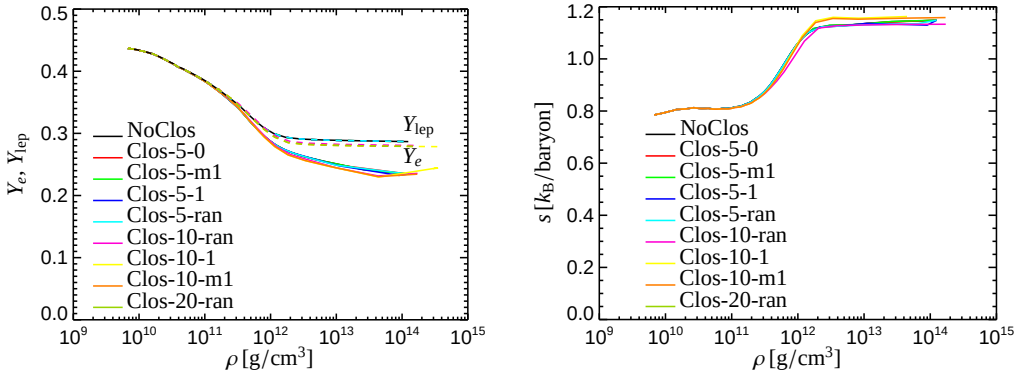

a **b**

Figure A.10.: **a**: The central electron fraction as function of central density for all models. **b**: The central entropy as function of central density for all models.

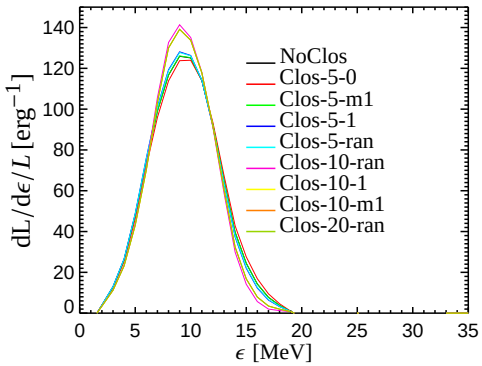

Figure A.11.: The spectrum of electron neutrinos measured at 400 km, for an observer who rests at infinity at a time when the central density reaches 10^{12} g/cm^3.

is limited to neutrino energies below 10 MeV. As one can conclude from Fig. A.10 (small) differences show up at a central density of 10^{12}g/cm^3, shortly before neutrino trapping sets in. The reason for this can be deduced from Fig. A.11, where the spectra of electron neutrinos are shown at the moment when a central density of 10^{12}g/cm^{3}is reached. Obviously, the polarisation term tends to reduce the high energy flux ($\epsilon_\nu > 13$ MeV) and increases the number of neutrinos with an energy of 10 MeV. Those leave by down scattering to lower energies the core, as explained in the previous Section A.1, and thereby increase the entropy. Freeing the phase–space for higher energetic neutrinos also allows for more electron capture, which together leads to the results in Fig. A.10. All in all, we conclude that the inclusion of the polarisation term in core collapse supernova simulations, has a small effect on the deleptonisation and the neutrino spectra. However, this effect is smaller than the effect of correlated neutrino scattering on the ion–ion lattice, which was discussed in the previous Section A.1, and therefore was not considered in previous calculations. However, it is still an open question if this effect influences the neutrino spectra at the time of shock breakout. If this is the cases, then it might be interesting to consider this effect in the prediction of the measurements of the burst signal in neutrino detectors. However, to answer this question it is necessary, to evaluate the models, which were presented here, to longer times in the postbounce phase, which will be done in the near future. However, the effect of the polarisation term during the collapse phase is also much smaller than the influence of different nuclear equations of state, see Section 3.2. Since the EoS effect in the shock breakout, though obvious in our simulations, is not measurable in current neutrino detectors, see Kachelrieß et al. (2005), it is unlikely that the inclusion of the polarisation term in postbounce calculations will lead to detectable differences in measurements of supernova neutrinos.

A.3. Electron capture during stellar core collapse

In this Section we will discuss the importance of electron captures (EC) on heavy nuclei during the collapse phase and the evolution after the shock formation. Electron captures play an important role during the supernova evolution: On the one hand electron captures reduce the electron degeneracy pressure, thereby supporting the onset of gravitational instability and thus influencing the collapse dynamics. On the other hand, EC produce the neutrinos that store the released gravitational binding energy and which are crucial for the neutrino driven supernova explosion. Thus, it is very important to use an accurate description for EC in core collapse supernova simulations that describes not only the capture process as accurate as possible but also the spectral information of the emitted neutrinos.

Electron capture can occur in two ways in the stellar core: On the one hand, electrons can be captured by free (i.e. unbound protons), and on the other hand electrons can be captured by protons which are bound in nuclei. Since in a stellar core heavy nuclei are some orders of magnitude more abundant than free protons, EC on heavy nuclei are despite the smaller rates more important than EC on free protons.

Traditionally, supernova modellers use the EC description of Bruenn (1985) (which goes back to Fuller et al. 1982) that gives analytic expression for the capture on free protons and heavy nuclei. However, the major shortcoming in this description of EC on heavy nuclei is that – according to the approximations used – it is suppressed in supernova calculations as soon as

the N=40 shell of the nuclei is reached, which roughly happens when the central density in the stellar core exceeds 10^{11} g/cm^3. This implies that throughout most of the collapse phase the EC in core collapse simulations, which make use of the description of Bruenn (1985), is un-physically dominated by captures on free protons.

Because of the complicated (shell)-structure of a nucleus, it is a hard task to calculate in detail the capture rate and Q-value of the reaction for a large set of heavy nuclei. Only recently, Langanke & Martínez-Pinedo (2000, 2001) started to calculate detailed EC-rates on heavy nuclei. Langanke and collaborators use the shell model Monte Carlo (SMMC) (see Koonin et al. 1997) supplemented with calculations based on the random phase approximation for the transition operators (see Langanke et al. 2003).

Only a few supernova modellers have sofar made use of these new EC-rates (see Langanke et al. 2003, Hix et al. 2003) (from here on LMSH-rates) but a detailed analysis that results from the change of the physical EC-rates has not yet been done.

It is well known that calculations with the standard description of EC on heavy nuclei of Bruenn (1985) (from here on FFN-rates) and different initial stellar progenitors converge to a "norm" collapse (see, e.g. Liebendörfer et al. 2002, Buras et al. 2006a). This leads to only small differences in the evolution of different progenitors up to shock breakout (see Fig. 2 in Liebendörfer et al. (2002) and Fig. 5 in Buras et al. (2006a), for a detailed progenitor comparison).

This astonishing feature is explained by the fact that in the standard description for EC the electrons are solely captured on free protons above densities of roughly 10^{11}g/cm^3 and the free proton abundance is tightly coupled to the value of the electron fraction. Thus the stronger the EC on unbound protons reduces the electron fraction the more the EC quenches itself, thereby establishing a feedback cycle that drives the electron fraction towards a "norm" trajectory (for an elaborate discussion the reader is referred to Liebendörfer et al. 2002) .

In the following Sections it will be investigated how the evolution of a core collapse supernova simulation is changed if the physical influence of EC on heavy nuclei is regarded during the whole collapse phase. It will also be addressed whether the convergence to "norm"trajectories and thus the similarity of the neutrino burst signal still holds when this newly description of electron captures is used. In Section A.3.1 we will first discuss an implementation of EC on heavy nuclei where the spectra of emitted neutrinos in described by a fit–formula, before we will discuss in Section A.3.2 a more accurate description of the spectral information of the emitted neutrinos.

A.3.1. A spectral fit for electron captures

Before the results of the simulations with the newly available electron capture of Langanke & Martínez-Pinedo (2000, 2001) will be discussed, a short description of the implementation of these electron capture rates into the V /M DB TH code is given.

The rate of change (modulo a factor $1/c$) of the neutrino distribution function due to absorption and emission processes is given (see Bruenn 1985)

$$B_{\mathrm{AE}}(\epsilon,\mu) = j(\epsilon)[1 - f(\epsilon,\mu)] - f(\epsilon,\mu)/\lambda(\epsilon) \ , \tag{A.21}$$

where j denotes the emissivity and λ is the mean free path for neutrino absorption and ϵ the neutrino energy. The factor $(1 - f)$ accounts for fermion phase space blocking effects of neutrinos. Using the Kirchhoff-Planck relation ("detailed balance"), and introducing the absorption opacity corrected for stimulated absorption,

$$\kappa_{\rm a}^{*} := \frac{1}{1 - f^{\rm eq}} \frac{1}{\lambda} = j + \frac{1}{\lambda} \,, \tag{A.22}$$

Eqn. A.21 can be rewritten as

$$B_{\rm AE}(\epsilon, \mu) = \kappa_{\rm a}^{*}(\epsilon)[\, f^{\rm eq}(\epsilon) - f(\epsilon, \mu)] \,. \tag{A.23}$$

Here $f^{\rm eq} := (1 + \exp\,[\beta(\epsilon - \mu_\nu^{\rm eq})])^{-1}$ is the equilibrium value of the distribution function, $\beta := k_{\rm B}T$, and $\mu_\nu^{\rm eq}$ is the equilibrium neutrino chemical potential.

Eqn. A.23 is the important equation for the implementation of the electron capture rates on heavy nuclei: Using the form for the neutrino spectrum, see Langanke et al. (2001),

$$n(\epsilon) = \epsilon^2(\epsilon - q)^2 \frac{N}{1 + \exp\,[\beta(\epsilon - q - \mu_e)]} \,, \tag{A.24}$$

with q being the "Q-value' of the reaction and a constant N that normalises the neutrino spectrum to unity, $\kappa_{\rm a}^{*}$ can be written as ($\hbar = c = 1$!):

$$\kappa_{\rm a}^{*} = (4\pi)^{-1} \frac{n_{\rm B}}{f^{\rm eq}(\epsilon)} \frac{\mathcal{R}^{\rm tot}}{1 + \exp\beta(\epsilon - q - \mu_e)} \mathcal{F}_e^{\,-1} \,, \tag{A.25}$$

with

$$\mathcal{F}_e := \int {\rm d}\epsilon \frac{\epsilon^3(\epsilon - q)^2}{1 + \exp\beta(\epsilon - q - \mu_e)} \tag{A.26}$$

and the baryon number density

$$n_{\rm B} = \rho / m_{\rm B} Y_{\rm H} = \rho / m_{\rm B} X_{\rm H} / A_{\rm H} \,, \tag{A.27}$$

where ρ is the matter density, $m_{\rm B}$ the baryon mass, and $A_{\rm H}$, $Z_{\rm H}$ the mass and charge number of the representative heavy nucleus. Note that thus N in Eqn. A.24 was written as

$$N = (4\pi)^{-1} n_{\rm B} \mathcal{R}^{\rm tot} \mathcal{F}_e^{\,-1} \,. \tag{A.28}$$

Here a few facts are worth to mention: first, Langanke & Martínez-Pinedo (2001) provide $\mathcal{R}^{\rm tot}$ and q in tabular form (see below). Second, in Eqn. A.25 a factor $n_{\rm B}$ appears that can be *either* calculated according to Eqn. A.27, with the representative heavy nucleus provided in tabular form by Langanke & Martínez-Pinedo (2001) *or* with the representative heavy nucleus of the used EoS. Thus, one can "rescale" the EC-rates on heavy nuclei to the particular EoS employed.

Langanke & Martínez-Pinedo (2001) provide the quantities $\mathcal{R}^{\rm tot}$, q, and $Y_{\rm H}$ tabulated as functions of the density ρ, temperature T, and electron fraction Y_e. Since the table is confined to a strip in parameter space typical for core collapse conditions, (see Fig. A.12), we employ the following procedure:

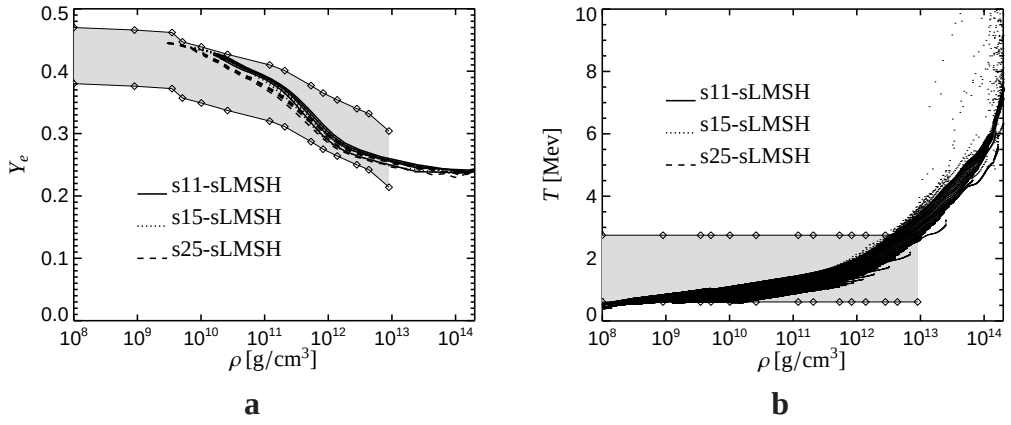

Figure A.12.: a: Trajectories of core collapse simulations in the electron fraction-density plane for different models. The grey shaded region indicates the rate table of Langanke et al. . **b**: The same as panel a, only in the density-temperature plane.

- with the fluid density, temperature, and electron fraction we interpolate the values of $\mathcal{R}^{\rm tot}$, q, and $Y_{\rm H}$ in the table.

- Calculate $\kappa_{\rm a}^*$ according to Eqn. A.25: if we "rescale" the rate with representative heavy nucleus of the EoS, $Y_{\rm H}$ is replaced with the EoS-values.

- If, by chance, the physical conditions of a fluid cell do not fit in the LMSH-table, the description for electron captures on heavy nuclei of Bruenn (1985) is used. For a smooth transition both rates are interpolated linearly.

Justification: As one can see in Fig. A.12 for a standard progenitors the LMSH-table is chosen such that trajectories of fluid cells lie well inside this table. Therefore only in minor parts of the simulations the description of Bruenn (1985) becomes effective as a source for EC on heavy nuclei.

Figure A.14 shows that the properties of the representative heavy nucleus as given by Langanke & Martínez-Pinedo (2001) and calculated by a sophisticated NSE-solver of Hix et al. (2003) is very similar to the one given by the L&S–EoS. However, Fig. A.14 also reveals, that different EoSs can predict different representative heavy nuclei. We have thus also performed calculations where in the rate evaluation of Eqn. A.25 the representative heavy nucleus of the EoS was used. With these calculations we have tested in how far the dynamics of the simulations is effected by the factor $n_{\rm B}$ in Eqn. A.25.

Thus, in this Section we investigate the importance of electron capture rates on heavy nuclei with different progenitor models and two equations of state: on the one hand we examine progenitor variations and the difference of the new LMSH-rates and the conventional description of FFN. On the other hand we investigate the importance of the properties of the representative heavy nucleus on the electron capture rates. To this end we therefore use two different EoS, namely the L&S-EoS and the Wolff–EoS.

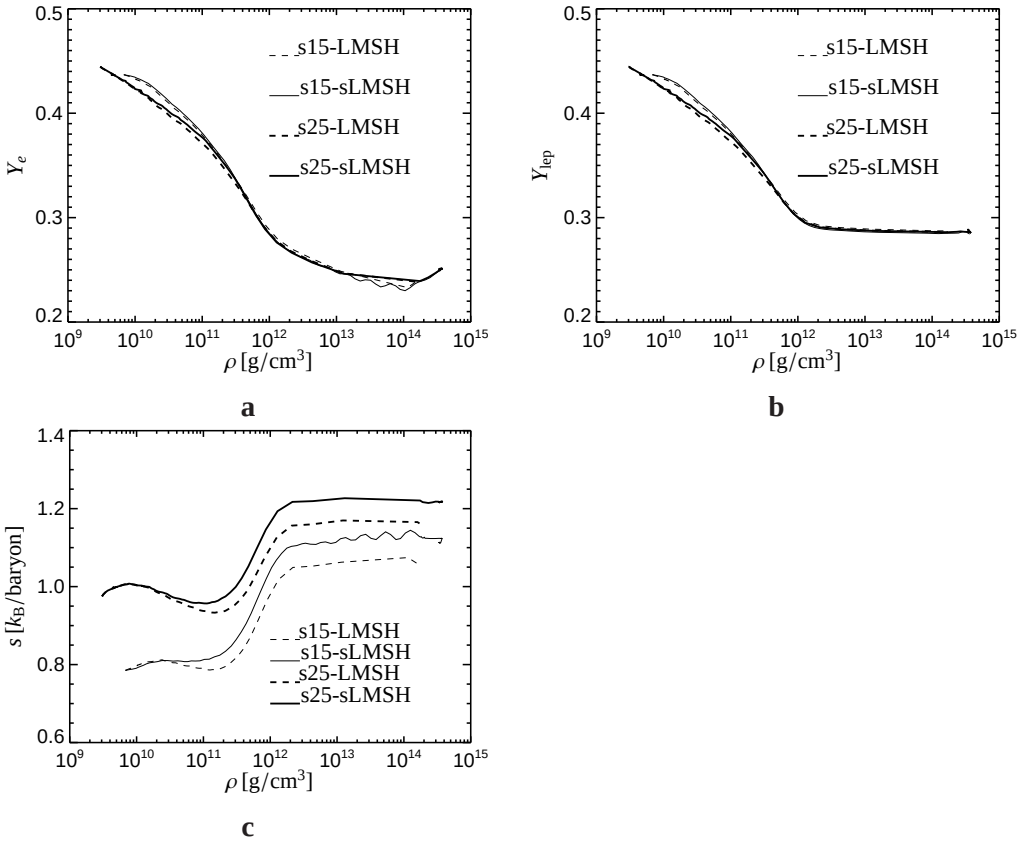

Figure A.13.: **a**: The central electron fraction Y_e as function of the central density for the models without screening effects (-lmsh) and with screening effects (-slmsh) for a $15M_\odot$ (thin lines) and $25M_\odot$ (thick lines) progenitor star. **b**: The lepton fraction Y_{lep} for the same models. **c**: The central entropy as function of the central density.

The simulations discussed in the following were calculated in spherical symmetry and the neutrino–matter interactions described in Chapter 2 were used. In order to take different stellar progenitors into account, simulations were performed with a $11.2\,M_\odot$ progenitor of Woosley et al. (2002) (see also Section 4.2), a $15\,M_\odot$ progenitor provided by Heger et al. (2001) (see also Section 3.2), a $20\,M_\odot$ progenitor (Woosley et al. 2002), and a $25\,M_\odot$ progenitor star (Heger et al. 2001) were used. Note that in the stellar evolution calculations of the progenitors of Heger et al. (2001) already the electron capture rates of Langanke et al. were used.

In Table A.2 we summarise the models presented in this study together with the used EoS and the used progenitor model .

We start the discussion of the importance of EC on heavy nuclei by mentioning that the new LMSH rates used in this Section include electron screening effects, whereas in previous studies of Langanke et al. (2003) and Hix et al. (2003) electron screening effects were not included. Electron screening tends to shield the nucleus and thus generically reduces the Q–value of an

Model	Progenitor	EC-rates	Nuclei	EoS
s11-FFN	s11.2	FFN	EoS	L&S
s11-LMSH	s11.2	LMSH	LMSH	L&S
s11-oLMSH	s11.2	LMSH	LMSH	L&S
s11-sLMSH	s11.2	sLMSH	LMSH	L&S
s11-osLMSH	s11.2	sLMSH	LMSH	L&S
s15-FFN	s15a28	FFN	EoS	L&S
s15-LMSH	s15a28	LMSH	LMSH	L&S
s15-oLMSH	s15a28	LMSH	LMSH	L&S
s15-sLMSH	s15a28	sLMSH	LMSH	L&S
s15-osLMSH	s15a28	sLMSH	LMSH	L&S
s15-LS(a)	s15a28	sLMSH	LMSH	L&S
s15-LS(b)	s15a28	sLMSH	EoS	L&S
s15-W(a)	s15a28	sLMSH	LMSH	Wolff
s15-W(b)	s15a28	sLMSH	EoS	Wolff
s20-FFN	s20	FFN	EoS	L&S
s20-LMSH	s20	LMSH	LMSH	L&S
s20-oLMSH	s20	LMSH	LMSH	L&S
s20-sLMSH	s20	sLMSH	LMSH	L&S
s20-osLMSH	s20	sLMSH	LMSH	L&S
s25-FFN	s25a28	FFN	EoS	L&S
s25-LMSH	s25a28	LMSH	LMSH	L&S
s25-oLMSH	s25a28	LMSH	LMSH	L&S
s25-sLMSH	s25a28	sLMSH	LMSH	L&S
s25-osLMSH	s25a28	sLMSH	LMSH	L&S

Table A.2.: Overview of all models presented in this paper. Together with the progenitor model we state the employed description of electron capture rates (FFN: Bruenn description, LMSH: LMSH-rates without screening corrections, and sLMSH: LMSH-rates including screening effects), the used EoS, and information how the representative heavy nucleus is determined (see the text for details). Note that in the models with suffixes -oLMSH and -osLMSH only electron captures on heavy nuclei were taken into account and electron capture on free nucleons was switched off.

electron capture reaction. To study the influence of this effect, we shall compare a set of simulations that include (models with suffix "sLMSH") or neglect (models with suffix "LMSH") these screening effects and were calculated with a $15\,M_\odot$ and $25\,M_\odot$ progenitor model. In Fig. A.13 we show the evolution of the central electron and lepton fractions, and the central entropy during stellar core collapse. Electron screening has obviously almost no influence on the development of the central electron and lepton fraction. Only for a short period of time minor differences are visible at early stages of the collapse. In calculations including screening effects, the central entropy is slightly higher (roughly 0.05 k_B/Baryon) compared with calculations that neglect

Model	Progenitor	EC-rates	Factor
s15a28-0.9	s15a28	sLMSH	0.9
s15a28-0.8	s15a28	sLMSH	0.8
s15a28-0.7	s15a28	sLMSH	0.7
s15-oLMSH-0.125	s15a28	LMSH	0.125
s15-oLMSH-0.25	s15a28	LMSH	0.25
s15-oLMSH-0.5	s15a28	LMSH	0.5

Table A.3.: Overview of the test models. Stated is the used progenitor, the applied electron capture rate, and the factor by which the EC-rate was scaled down with. Note that this scaling was only performed if $\rho \geq 10^{11}$ g/cm^3.

electron screening effects. Note that all results presented in the following were obtained by calculations including electron screening effects.

As already mentioned, the electron capture rates used in our simulations were calculated such that they have to be multiplied with the number fraction of the representative heavy nucleus of the NSE-composition. Up to now for this number fraction the results of the NSE-solver of Hix et al. (2003) were used, which gives very similar nuclei compared to the L&S–EoS, see Fig. A.14a. However, as was shown in Section 3.2, different EoSs in core collapse simulations do predict heavy nuclei that may differ significantly from each other. This can also be seen in Fig. A.14a. Then, of course, the question arises whether our findings with the LMSH-rates are influenced by the choice of the particular nuclear EoS which changes the representative heavy nucleus and thus the target for EC on nuclei. We have thus calculated a few collapse models with different nuclear EoS and used their predictions of the heavy nucleus to calculate the electron capture on heavy nuclei, i.e. in the rates we replace the number fractions of nuclei as given by Hix et al. (2003) with the number fraction of the used EoS, see Eqn. A.27. In particular we want to stress here that the number fraction $Y_{\rm H}$ contains the information of the mass number $A_{\rm H}$ of the representative heavy nucleus. In the Figs. A.15a-b we show the evolution of the central electron and lepton fraction, and the central entropy during collapse and the electron luminosities and rms-energies during the postbounce phase. As one can see it makes hardly a difference whether the number fraction is taken from the EoS or from the NSE-solver of Hix et al. (2003). Figure A.14b reveals the explanation for this: finding the number fraction of the representative heavy nucleus that is predicted by the LMSH-table or the particular EoS do not differ by more than 10% and as one can infer from Fig. A.14a the difference in the properties of the representative heavy nucleus only occur at densities above 10^{11} g/cm^3.

We have performed some test calculations where we have artifically reduced the EC-rate on heavy nuclei by 10%, 20%, and 30% if the density was larger than 10^{11} g/cm^3, (see Table A.3.1). These calculations showed nearly identical results when compared with calculations performed with the Wolff-EOS, see Fig. A.16.

Thus the particular choice of an EoS does not change our findings, as long as the variations of the number fraction of the predicted representative heavy nucleus are in the range of some ten percent. All calculations presented in the following will thus make use of the representative heavy nucleus as given by the NSE-solver of Hix et al. (2003).

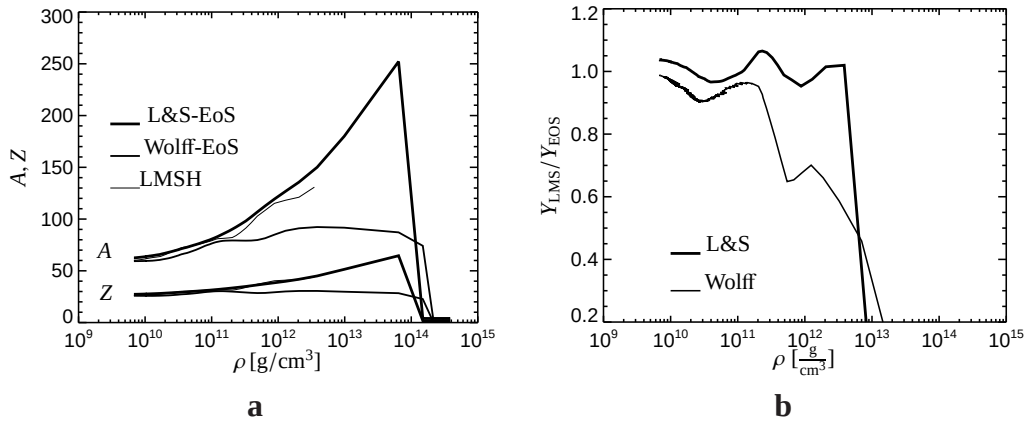

Figure A.14.: a: The mass number and charge number of the representative heavy nucleus that of the L&S-EoS and of the Wolff-EoS, compared to the average mass and charge number of the NSE nuclei considered for the LMSH rate calculations. Note that these values are obtained for the conditions along a typical collapse trajectory of matter at the core centre. **b:** The ratio of the number fractions of the representative heavy nucleus as given by the LMSH-table and the respective EoS as function of central density.

Next, we will discuss the results with regard to the variations of the stellar progenitor models (see Table. A.2). In Fig. A.17 we show exemplary for the $15M_{\odot}$ progenitor the evolution of the central electron and lepton fraction and of the central entropy, if the FFN–rates or the the sLMSH–rates are used in the calculations. If electron captures on nuclei are taken into account, and this process is not (artificially) suppressed at densities larger than 10^{11} g/cm^3 — as it is done in the FFN description — then the core delpetonises stronger. Furthermore, since the Q–values for EC on free protons and heavy nuclei are different, electron capture on heavy nuclei produces more neutrinos with lower energies than electron capture on free protons. Thus, in the FFN description, where EC on free protons is dominant for almost all the collapse phase, high energetic neutrinos are produced that leave the core by down–scattering to lower energies (cf. the discussion in Section A.1), thereby increasing the entropy. Since this process happens not so frequently in the models with EC on heavy nuclei, the entropy in these models stays generically lower. A more detailed impression of the differences in the models using the FFN or LMSH rates can be obtained from Fig. A.18, where the same quantities as in Fig. A.17 are shown, however, for more progenitor models.

Obviously, Figs. A.18a–b show the already mentioned convergence of the trajectories of the central electron and lepton fraction in models with the FFN description: Although, the initial values of the electron fraction and lepton fraction show a progenitor dependent spread, the final values show, as already explained, a much smaller deviation. Strikingly, the trajectories of models calculated with the sLMSH rates converge even better. Thus, is it possibly that a self–regulating mechanism, similar to the feedback cycle for electron captures of protons, does act during the collapse phase? If this is the case, than Fig. A.18c immediately reveals that the entropy can not be — unlike in the feedback mechanism with EC on free protons — integrated

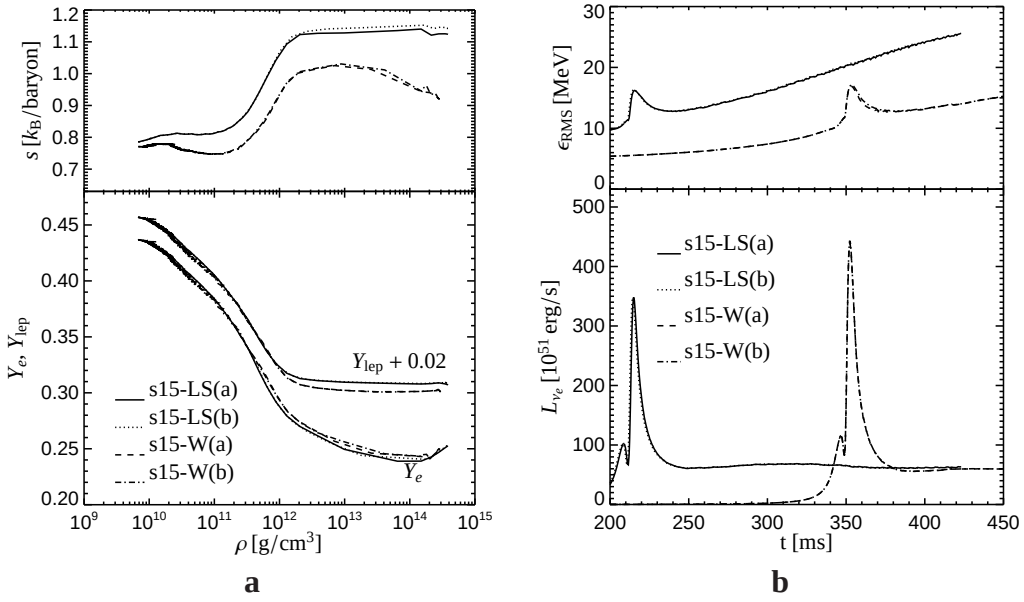

Figure A.15.: Comparison of collapse simulations for a 15 $M_\odot$ star with the EoSs of Lattimer & Swesty (L&S) and of Wolff (W) for the electron capture rates on nuclei calculated (a) with the nuclei abundance as given by the employed EoS and (b) with the abundance of heavy nuclei as provided by a NSE-solver. **a:** The entropy, and electron and lepton fraction Y_e , Y_{lep} as functions of central density. **b:** The rms energy and luminosity of electron neutrinos as function of time for an observer at rest located at 400 km. Note that the collapse of the stellar core takes more time with the Wolff-EoS and therefore the shock breakout happens at a later time than in the models with the L&S-EoS. Time is measured from the beginning of the simulations.

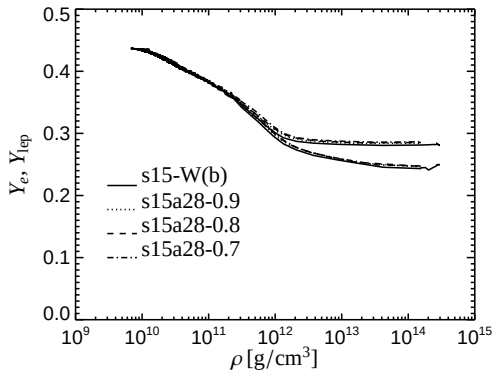

Figure A.16.: The electron and lepton fraction as functions of the central density for models s15a28-W(b), s15a28-0.9, s15a28-0.8, and s15a28-0.7. Note, that in the latter three models the EC-rate on heavy nuclei was artificially reduced by 10%, 20%, and 30%, respectively, if the density was larger than 10^{11} g/cm^3.

in this potential cycle, since the entropies do *not* converge. In order to test a hypothetical feedback mechanism working on the electron capture rates on heavy nuclei, we have calculated

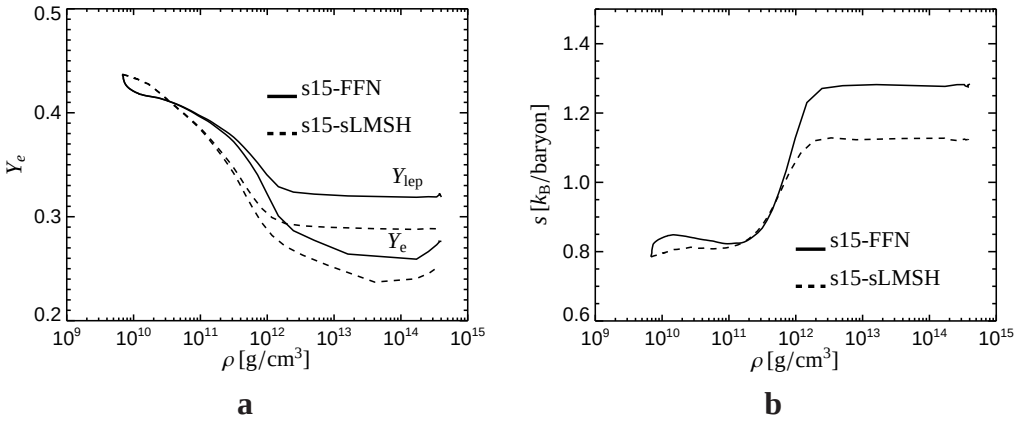

Figure A.17.: **a**: The central lepton and electron fraction for the models s15-FFN and s15-sLMSH. This model is taken as an example for all other models with different progenitor stars where similar differences between the FFN and LMSH-rates are found. **b**: The central entropy for the same model.

some — unphysical — test models, where only electron capture on heavy nuclei according to the description of Langanke et al. was considered and electron capture on free protons was completely switched off. In the following these models will be denoted "osLMSH"or "oLMSH" depending on whether screening effects were taken into account or not. From the convergence of the electron and lepton fraction of these models, see Figs. A.18a–b, one concludes that the convergence sets in before a central density of roughly $1 - 2 \times 10^{11}$ g/cm^3 is reached. Indeed Fig. A.19 shows that the total (i.e. EC on free protons and nuclei) neutrino production rates in models with LMSH rates are different below a density of $1 - 2 \times 10^{11}$ g/cm^3 and at larger densities the rates become very similar.

As Fig. A.19b shows the electron capture rates on heavy nuclei are very similar for all different models, which suggests that the similar deleptonisation (despite different initial values) is caused by some complex behaviour in our models. A possible way to establish a same deleptonisation of the core, with similar capture rates but different initial values of the electron fraction, is that the collapse timescale changes such that the same degree of deleptonisation is reached. We have thus analysed for all our models, whether a consistent connection between the collapse timescale and the electron capture rate exists. However, for several models a slower collapse does not imply less electron captures, which renders a timescale controlled regulation model impossible, see Table A.3.1. Electron captures on nuclei *alone* (i.e. when electron captures on free protons are switched off which is indicated by an "o" in the model name) do not produce a convergence of the final values of the electron fraction. This can be clearly seen in Table A.3.1 by a comparison of the models s15-oLMSH, s25-oLMSH to models s15-oSLMSH, and s25-oSLMSH. Furthermore, the models s15-oLMSH-0.5, s15-oLMSH-0.25, and s15-oLMSH-0.125 with artificially reduced rates compared to model s15-oLMSH do also not converge. This clearly demonstrates that electron captures on heavy nuclei do not produce a convergence of the collapse trajectories. Realistic calculations that include electron captures on free protons, on

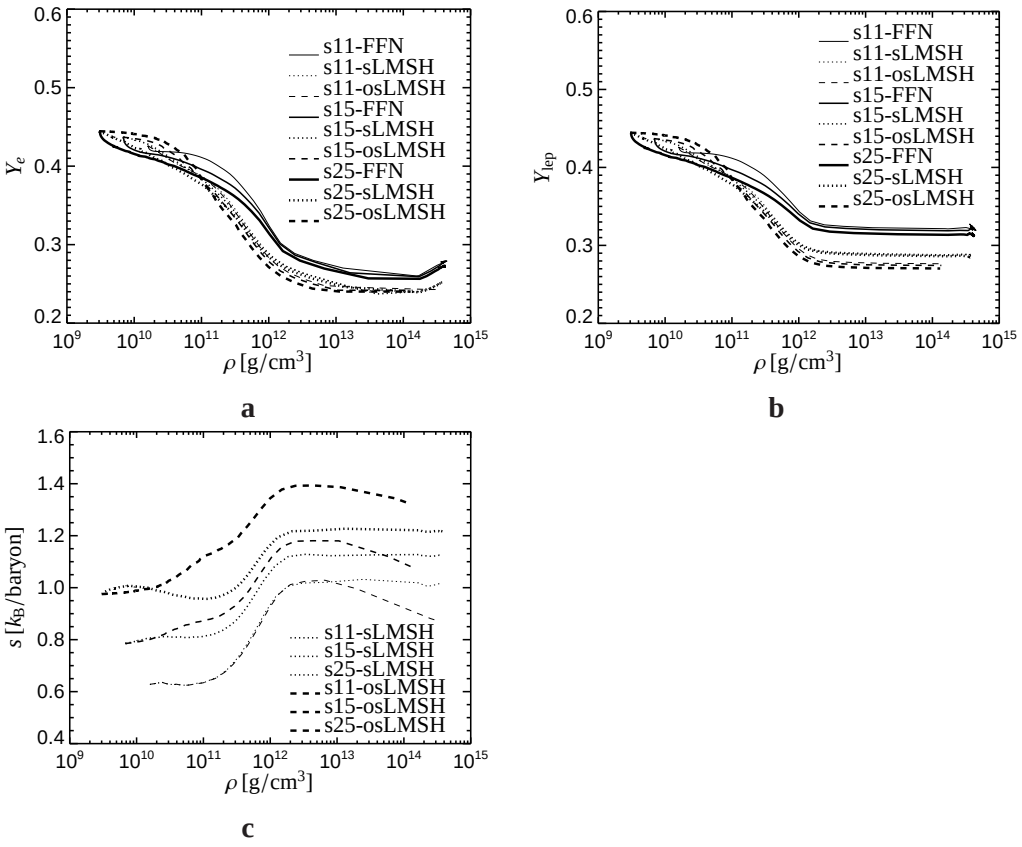

Figure A.18.: **a**: The central electron fraction for different progenitor models and different implementations of EC rates. In the models suffixed with "FFN" EC on free protons and on heavy nuclei was implemented according to Bruenn (1985). The model names "sLMSH" indicate that the conventional EC on free protons was used and for EC on heavy nuclei the (screened) description of Langanke & Martínez-Pinedo (2001) was used. The models "osLMSH" are test cases where only EC capture on heavy nuclei according to Langanke & Martínez-Pinedo (2001) was considered and EC on free protons was switched off. **b**: The central lepton fraction for these models. **c**: The central *matter* entropy for these models. Note that in models "osLMSH" at a density of 10^{13} g/cm^3 no neutrinos are produced anymore (due to the "border" of the LMSH-table) and neutrinos are only redistributed by scattering. This transfers matter entropy in neutrino entropy.

the other hand, tend to converge, since the feedback mechanism ((Bruenn & Mezzacappa 1997) for electron captures on free protons does work. However, if the difference in the values of the electron and lepton fraction is too large, either because of the initial values (like in case of the $25M_\odot$ progenitor model) or if during the early stages of the collapse the electron fraction differences first grow compared to the initial state (like in case of the FFN-models, see Fig. A.18) then also the feedback mechanism for electron captures of free protons is not able to achieve a

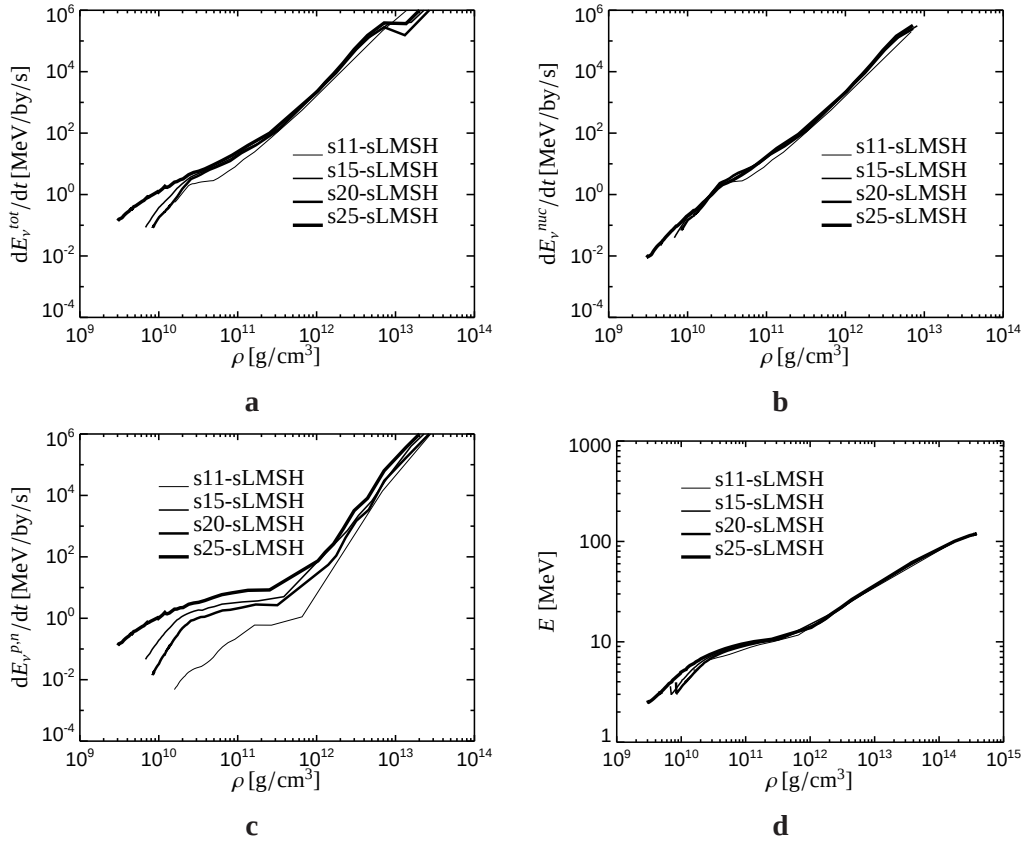

Figure A.19.: The rates of produced neutrinos for the central zone for the models with the description of EC on heavy nuclei according to Langanke et al. .**a:** The total rate (i.e. for EC on free protons and heavy nuclei. **b:** The contribution of EC on heavy nuclei to the rate from panel a. **c:** The free proton contribution. **d:** The mean energy of produced electron neutrinos that are produced by the rates of panel a.

full convergence.

Finally, the progenitor differences in supernova calculations with the new electron capture rates of Langanke et al. are shown in Figs. A.20, A.21 and A.22. The moment of shock formation (as defined by Bruenn & Mezzacappa 1997) is shown in Fig. A.20. A lower value of the lepton fraction $Y_{\rm lep}$ in the models with the sLMSH rates (see Fig. A.18b) implies also a smaller core and a shock formation at smaller radii (or smaller mass coordinates), which is consistent with Fig. A.20. Though, these changes are not dramatic they are comparable to the changes of in the shock formation point resulting from different nuclear EoS, see Section 3.2. Note, that in the models calculated with the electron capture rates of Langanke et al. the shocks form at the same mass coordinate due to the fact that the trajectories of the electron and lepton fraction converge during the collapse phase, see Fig. A.21. As explained, however, it seems likely that this convergence is poorly coincidence due to rather similar progenitor properties, where the

model	$\Delta\, t$ [ms]	$\overline{R}^{\rm net}$ [1/by/s]	$\overline{R}^{\rm emi}$ [1/by/s]	$\Delta\, Y_{\rm lep}$	$Y_e^{\rm initial}$	$Y_{\rm lep}^{\rm final}$
s15-oSLMSH	18.87	5.51	15.65	0.091	0.437	0.275
s15-oLMSH	17.11	5.38	24.58	0.079	0.437	0.283
s15-sLMSH	15.37	6.24	17.88	0.081	0.437	0.288
s15-LMSH	15.08	5.98	27.58	0.077	0.437	0.287
s25-oSLMSH	15.94	7.07	20.02	0.099	0.444	0.272
s25-oLMSH	14.13	6.36	29.71	0.077	0.444	0.281
s25-sLMSH	13.60	6.78	20.51	0.077	0.444	0.286
s25-LMSH	13.21	6.45	30.44	0.071	0.444	0.286
s15-oLMSH-0.125	19.89	5.84	8.80	0.095	0.437	0.301
s15-oLMSH-0.25	19.05	5.69	11.20	0.091	0.437	0.297
s15-oLMSH-0.5	17.77	5.57	16.31	0.084	0.437	0.287
s15-oLMSH	17.11	5.38	24.58	0.079	0.437	0.283
s11-osLMSH	22.76	4.56	12.59	0.091	0.426	0.278
s15-osLMSH	18.87	5.51	15.65	0.091	0.437	0.275
s20-osLMSH	19.64	5.28	14.78	0.091	0.435	0.277
s25-osLMSH	15.94	7.07	20.02	0.099	0.444	0.272
s11-sLMSH	19.63	5.02	14.04	0.084	0.426	0.289
s15-sLMSH	15.37	6.24	17.88	0.081	0.437	0.289
s20-sLMSH	16.18	6.03	16.98	0.081	0.435	0.289
s25-sLMSH	13.60	6.78	20.51	0.077	0.444	0.286
s11-FFN	19.65	4.60	6.60	0.068	0.426	0.321
s15-FFN	16.21	4.79	7.34	0.057	0.437	0.318
s20-FFN	17.38	4.63	6.87	0.059	0.435	0.320
s25-FFN	14.57	5.03	8.59	0.053	0.444	0.314

Table A.4.: Overview over all models. Tabulated is the time $\Delta\, t$ for the collapse between a central density of 10^{11} g/cm^3 to a central density of 10^{12} g/cm^3. $\overline{R}^{\rm net}$ is the time averaged net-rate (neutrino emission and absorption) for this density range, whereas $\overline{R}^{\rm emi}$ is the time-averaged neutrino emission rate.. Also given are the change of $Y_{\rm lep}$ in this density range, the value of Y_e at the beginning of the simulation, and the value of $Y_{\rm lep}$ after trapping.

initial values of the electron fraction are such that electron capture on free protons achieves a convergence. Figure A.22 depicts the evolution of the luminosity of electron neutrinos and of their rms energy. The variations in the neutrino luminosities and neutrino energies clearly become larger, and progenitor differences become more important at later times of the supernova evolution.

We conclude the discussion of this Section by summarising that though the production of neutrinos by electron captures during the whole core collapse supernova evolution is of large importance, the results of simulations which differ in the description of electron captures are only small. Even changing the physical picture by switching from collapse simulations that are dominated by electron capture on free protons to collapse simulations where electron cap-

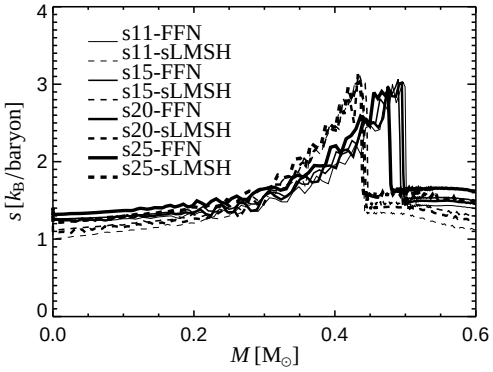

Figure A.20.: The moment of shock formation for all models calculated with the FFN or sLMSH description for electron captures.

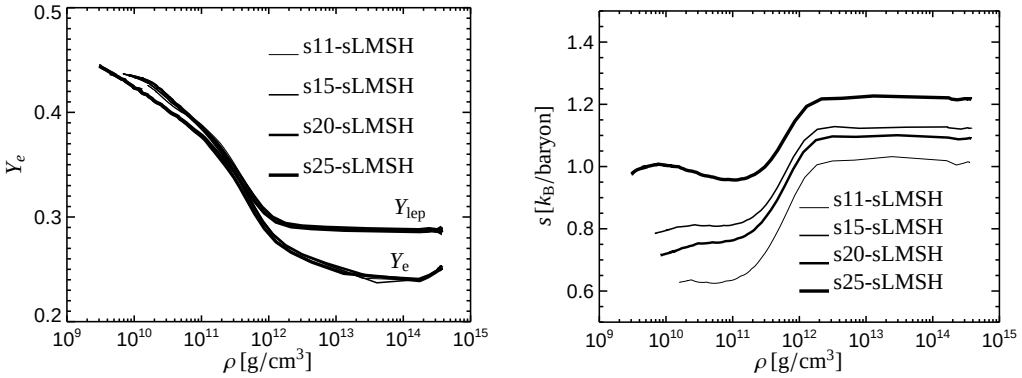

a **b**

Figure A.21.: **a**: The central electron fraction Y_e and lepton fraction $Y_{\rm lep}$ as function of central density for four different progenitors models. **b**: The central entropy as function of central density.

tures on heavy nuclei are dominant, changes the results of the simulations only little. Thus further changes of the electron capture rates on nuclei, such as the inclusion of screening effects or different nuclear compositions, have also only small effect on the result of the supernova evolution. Furthermore, we do not find any feedback mechanism involving only electron captures on heavy nuclei that acts in producing a convergence of the central electron fractions and lepton fractions. We rather find that the convergence we see is a result of the similar initial states of the different progenitor models and of the well known convergence mechanism (see, e.g. Bruenn & Mezzacappa 1997) for electron captures on free protons. Thus, it is extremely likely that with different progenitor models (where the initial electron fraction profiles deviate more strongly) the discussed convergence of the collapse trajectories and of the neutrino burst signals (Liebendörfer et al. 2002, Buras et al. 2006a) will disappear.

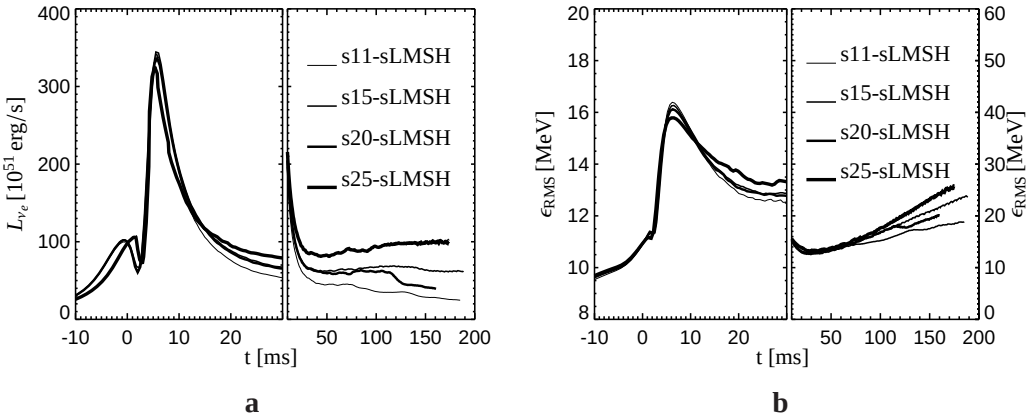

Figure A.22.: **a**: The luminosity of electron neutrinos as a function of time for all models that were calculated with sLMSH-rates. Note that time is normalised to the moment of shock formation. **b**: The rms-energy of electron neutrinos as a function of time.

A.3.2. Considering real spectra

In the previous Section we have discussed the importance of newly improved electron captures on heavy nuclei during stellar core collapse and the postbounce evolution. However, these rates still used a simple form of the spectrum of emitted neutrinos (remember Eqn. A.24). As Sampaio (2003) pointed out the spectral fit from Eqn. A.24 is noticeably narrower than the real data obtained from shell calculation of the nuclei, since the spectral fit does only consider the transition from a definite state in the parent nucleus to a definite state in the daughter nucleus. However, a real spectrum is a superposition of several spectra of different nuclei with different excitation energies. In order to take these effects into account Sampaio (2003) gives a new Gaussian parametrisation for the spectra, which reads:

$$n(\epsilon) = \int_0^\infty \epsilon^2 (\epsilon - q' + E_X)^2 \frac{e^{-\left(\frac{E_X - E_X^0}{\Delta}\right)^2}}{\Delta\sqrt{\pi}} \frac{N}{1 + e^{\frac{\epsilon - q' + E_X}{k_B T}}} \mathrm{d}E_X \ , \tag{A.29}$$

where q' is the new fitting parameter to the average neutrino energy, N is a normalisation constant and $E_X^0 = 2.5$ MeV. Note, that in this notation it is suppressed that the width of the distribution Δ is a function of temperature T and that good agreement with the NSE-average spectra is obtained with

$$\Delta = 2/3 + (50/9) k_B T \ . \tag{A.30}$$

Note also that for $\Delta \approx 0$ the parametrisation reduces to the fit of Eqn. A.24. In Fig. A.23 a comparison of the spectral fit of Eqn. A.24 (denoted from hereon "old spectral fit") and of Eqn. A.3.2 (denoted from hereon "new spectral fit) is shown.

Langanke and collaborators kindly provided us with a similar table of electron captures for core collapse supernovae as described in Section A.3.1, but additionally this new table also

Model	Progenitor	EC-rates	Nuclei	EoS
s11-SLMSH	s11.2	OLD	LMS	L&S
s11-SPEC	s11.2	NEW	LMS	L&S
s15-SLMSH	s15a28	OLD	LMS	L&S
s15-SPEC	s15a28	NEW	LMS	L&S
s15-SPEC-EoS	s15a28	NEW	L&S	L&S
s15-SPEC-EoS-W	s15a28	NEW	Wolff	Wolff
s20-SLMSH	s20	OLD	LMS	L&S
s20-SPEC	s20	NEW	LMS	L&S
s25-SLMSH	s25a28	OLD	LMS	L&S
s25-SPEC	s25a28	NEW	LMS	L&S
s25-SPEC-EoS	s25a28	NEW	L&S	L&S

Table A.5.: Overview of all models calculated for the following discussion. Together with the progenitor model (cf. Section A.3.1) we state whether the "old spectral fit" or the "new spectral fit" was used. Furthermore, the used EoS is stated, and information how the representative heavy nucleus (cf. the discussion in Section A.3.1) was evaluated.

contains the numerically integrated spectra $n(\epsilon)$ from Eqn. A.3.2. In principle this table is identical to the one already described in Section A.3.1, and therefore the numerical implementation is straight forward. This table allows us to treat electron capture on heavy nuclei in a very accurate form and allows us to consider realistic spectra of the emitted neutrinos.

In order to test the influence of this new spectral information we have again calculated a series of core collapse and postbounce evolution models with this new spectral treatment. In order to make a comparison as easy as possible, we have orientated our choice of models on the previous study of electron capture in core collapse supernova simulations which were discussed in the previous Section. This means that we have used the same physical description (except for the spectral treatment) as the models with the LMSH-rates discussed in Section A.3.1. The models which were calculated for this discussion are summarised in Table A.5. Again, as indicated in Table A.5, we either used the number fraction of the representative heavy nucleus as given by the LMS-table or as given by the used EoS. As already explained in Section A.3.1, this different treatment was done in order to test the influence of nuclear compositions differences on the electron captures. However, since using different number fractions of heavy nuclei does not lead to different results (cf. the discussion in Section A.3.1), we will in the following not discuss these models.

In Fig. A.24 we show for the collapse phase the trajectories of the central electron fraction and central lepton fraction for some models with the old and new spectral fit. As expected the spectral treatment has no influence of the deleptonisation of the core and the trajectories for one progenitor model practically lie on top of each other. Note that the small differences one nevertheless observes are not a result from the new spectral treatment: using the same new table of rates, however, with the old spectral treatment leads to the same small changes. However, comparing the new spectral treatment with the the old spectral fit on calculations which both use

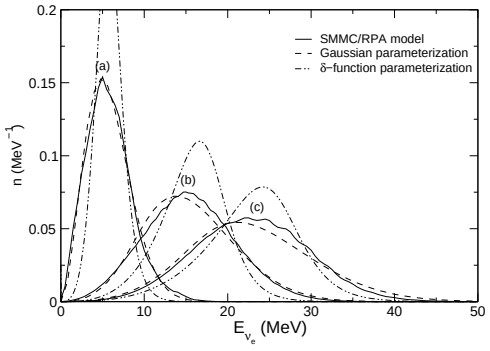

Figure A.23.: Solid lines: Spectra of emitted neutrinos produced by electron captures on heavy nuclei. These results were obtained from shell calculations by Langanke & Martínez-Pinedo (2000, 2001). The dashed lines represent representations of the spectra obtained from Eqn. A.3.2. The dashed–dotted lines represent the spectral fit used in the previous Section A.3.1. Note that this plot was kindly provided by Sampaio (2003) and corresponds to Fig. 6.9 in his thesis.

the new rates table, one discovers that these small differences dissappear. Thus, the differences we discuss here are related to the rates tables and esteem from slightly different grid points of both tables, which lead by slightly different interpolation during the calculation to these small changes. Trajectories of the central entropy for the models are shown in Fig. A.25. Here it is clearly visible that during the first phase of the collapse the new spectral treatment slightly increases the entropy stronger than the old spectral fit does. This leads than also to the slightly higher entropies of the models with the new spectral fit at the end of the stellar collapse.

This effect is caused by the slightly higher emission of neutrinos in the energy range above 15 MeV in the early phase of the collapse, see Fig. A.26, for models that are calculated with the new spectral treatment. These neutrinos are than down scattered to lower energies which causes a rise of the entropy in the models with the new spectral treatment. This effect is identical to the rising of entropy in some of the models discussed in Sections A.1 and A.3.1. At later times, around the time when trapping sets in, this effect disappears, see Fig. A.27. However, since shortly afterwards trapping conditions set in, the already reached entropy difference stay behind.

We finish this discussion by stating, that the details of the spectral treatment have only little influence on the results of our simulations of the collapse phase. However, it is still unclear to what extend the new spectral treatment of the electron captures on heavy nuclei may influence the neutrino emission at later stages after the shock formation, which will have to be addressed by future studies.

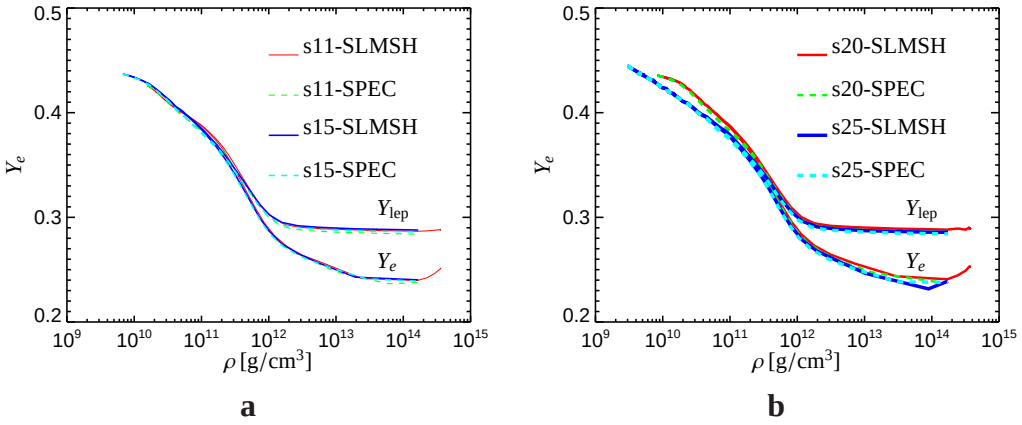

Figure A.24.: The electron fraction Y_e and the lepton fraction Y_{lep} as function of central density for models that were calculated with the old spectral fit and the new one. **a**: for the models calculated from a 11.2M$_\odot$ and 15M$_\odot$ progenitor star. **b**: for the models calculated from a 20M$_\odot$ and 25M$_\odot$ progenitor star.

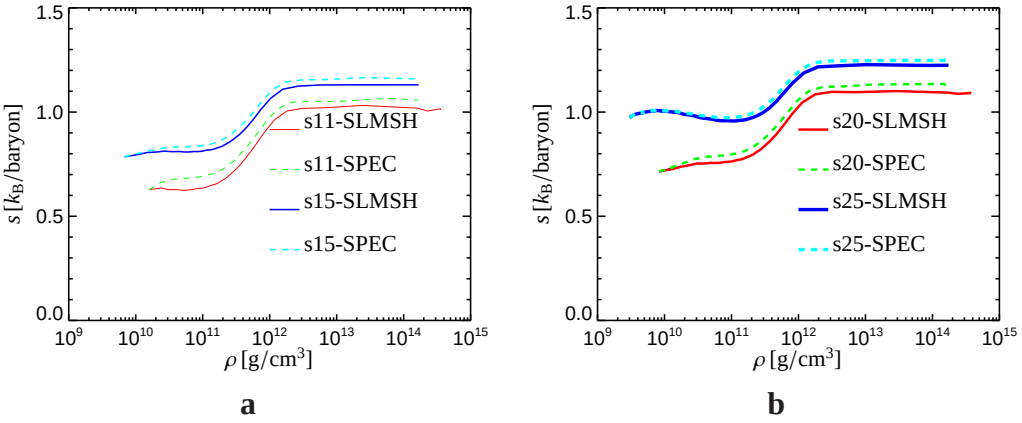

Figure A.25.: The entropy as function of central density for the same models as in Fig. A.24. **a**: for the models calculated from a 11.2M$_\odot$ and 15M$_\odot$ progenitor star. **b**: for the models calculated from a 20M$_\odot$ and 25M$_\odot$ progenitor star.

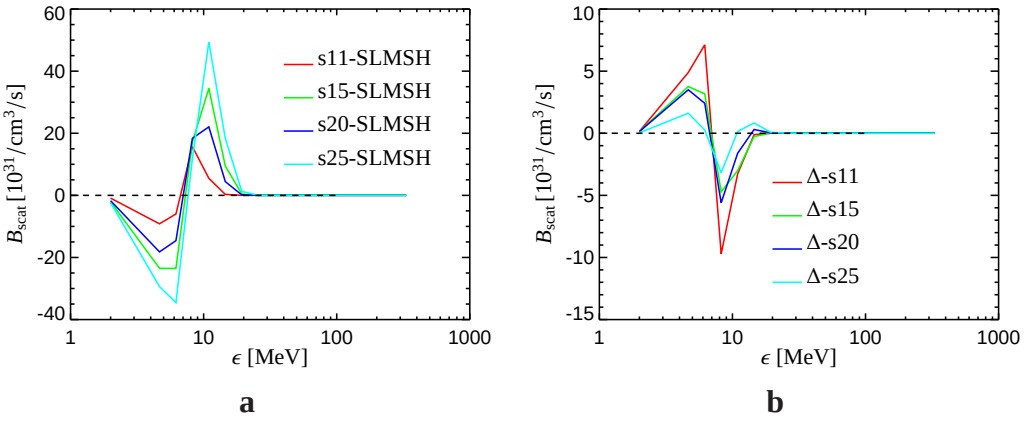

Figure A.26.: **a**: The energy source term for neutrino–electron scattering at the stellar centre in the collapse models using the old spectral fit. The plot shows the moment when the central density reaches a value of 3×10^{10} g/cm^3. Positive values indicate that neutrinos are "absorbed" (net scattering out of the corresponding energy bin), and negative values indicate that neutrinos are "emitted" (net scattering into the corresponding energy bin). **b**: The difference of the energy source term for different models. Calculated is for each progenitor the difference between the models "SLMSH" and "SPEC".

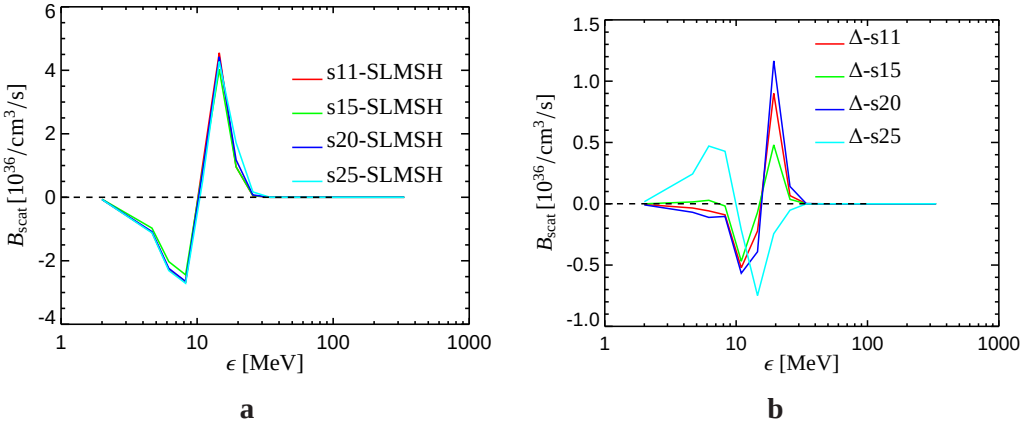

Figure A.27.: **a**: The energy source term for neutrino–electron scattering at the stellar centre in the collapse models using the old spectral fit. The plot shows, shortly before neutrino trapping sets in, the moment when the central density reaches a value of 10^{12} g/cm^3. Positive values indicate that neutrinos are "absorbed" (net scattering out of the corresponding energy bin), and negative values indicate that neutrinos are "emitted" (net scattering into the corresponding energy bin). **b**: The difference of the energy source term for different models. Calculated is for each progenitor the difference between the models "SLMSH" and "SPEC".

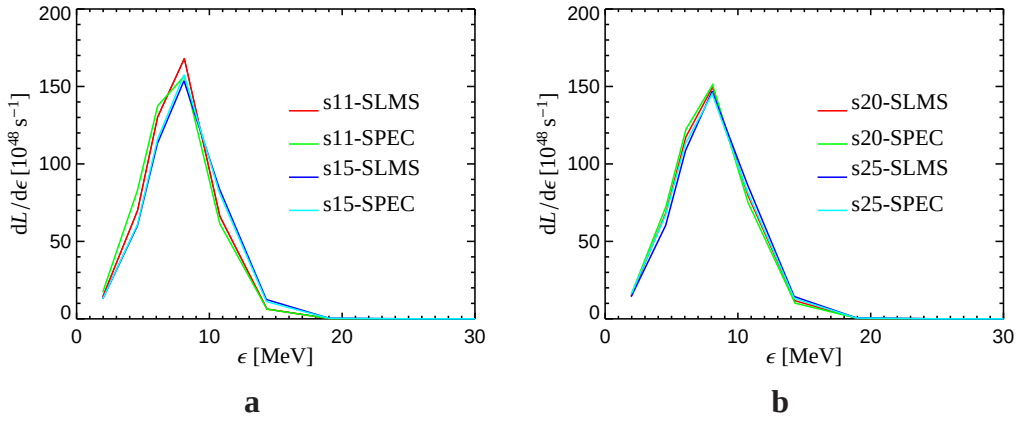

Figure A.28.: The neutrino spectra for the central zone at the moment when the density reaches a value of 10^{11} g/cm^3. **a:** For the models calculated from a 11.2M$_\odot$ and 15M$_\odot$ progenitor star. **b**: For the models calculated from a 20M$_\odot$ and 25M$_\odot$ progenitor star.

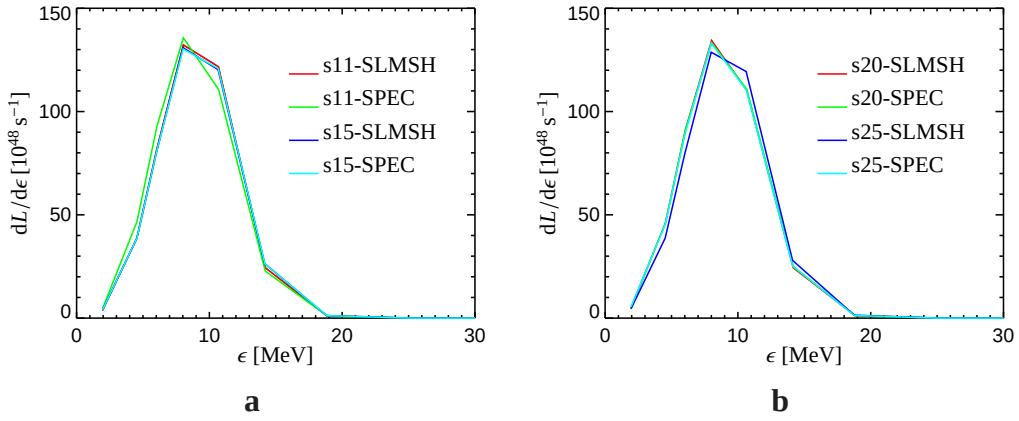

Figure A.29.: The neutrino spectra for the central zone shortly before neutrino trapping sets in when the density reaches a value of 10^{12} g/cm^3. **a:** For the models calculated from a 11.2M$_\odot$ and 15M$_\odot$ progenitor star. **b**: For the models calculated from a 20M$_\odot$ and 25M$_\odot$ progenitor star.

B

A general relativistic potential

This Section is a discussion[1] of the approximations that were included into the V /M DB TH code in order to include general relativistic effects. The necessity to include general relativity or appropriate approximations to general relativity in numerical codes that one uses to study core collapse supernovae can be easily summarised:

It is a well known fact that gravity plays an important role during all stages of a core collapse supernova. Gravity is the driving force that at the end of the life of massive stars overcomes the pressure forces and causes the collapse of the stellar core. Furthermore, the subsequent supernova explosion results from the fact that various processes tap the enormous amount of gravitational binding energy released during the formation of the proto-neutron star. General relativistic effects are important for this process and cannot be neglected in quantitative models because of the increasing compactness of the proto-neutron star.

Recently Liebendörfer et al. (2005) performed a comparison of the results obtained with the supernova simulation codes V and A -B T which both solve the Boltzmann transport equation for neutrinos. The V code (see Rampp & Janka 2002) is based on the Newtonian hydrodynamics code P (Fryxell et al. 1989) and utilises a generalised potential to approximate relativistic gravity. The A -B T code of the Oak Ridge-Basel group (Liebendörfer et al. 2001, 2002, 2004, 2005) is a fully relativistic (1D) hydrodynamics code. The comparison showed that both codes produce qualitatively very similar results except for some small (but growing) quantitative differences occurring in the late post-bounce evolution. Inspired by this comparison we explored improvements of the effective relativistic potential used by Rampp & Janka (2002) in order to achieve an even better agreement than that reported by Liebendörfer et al. (2005). To this end we tested different variants of approximations to relativistic gravity which we will discuss in this Section. The results of these calculations performed with different effective relativistic potentials are compared with those

[1] This work was done in collaboration with H. Dimmelmeier and was published in Marek et al. (2006).

obtained with the general relativistic A -B T code of the Oak Ridge-Basel group (cf. Liebendörfer et al. 2005). Since this thesis is focused on the investigation of core collapse supernovae with the V /M DB TH code, the numerical results of Dimmelmeier, the collaborator to this study, will not be discussed. However, the interested reader can find more details in Marek et al. (2006).

Note that throughout this Section, we use geometrised units with $c = G = 1$.

B.1. Effective relativistic potential

Approximating the effects of general relativistic gravity in a Newtonian hydrodynamics code may be attempted by using an effective relativistic gravitational potential $\Phi_{\rm eff}$ which mimics the deeper gravitational well of the relativistic case. In the following Subsections B.1.1 and B.1.2, several of these effective relativistic potentials will be discussed.

B.1.1. TOV potential for a self-gravitating fluid

For a self-gravitating fluid it is desirable that an effective relativistic potential reproduces the solution of hydrostatic equilibrium according to the Tolman–Oppenheimer–Volkoff (TOV) equation. With this requirement in mind and comparing the relativistic equation of motion (cf. van Riper 1978, Baron et al. 1989) with its Newtonian analogon, Rampp & Janka (2002) rearranged the relativistic terms into an effective relativistic potential (see Kippenhahn & Weigert 1990, for the hydrostatic, neutrino-less case).

Thus for spherically symmetric simulations using a Newtonian hydrodynamics code the idea is to replace the Newtonian gravitational potential

$$\Phi(r) = -4\pi \int_0^\infty \mathrm{d}r'\, r'^2 \frac{\rho}{|r - r'|} \tag{B.1}$$

by the TOV potential

$$\begin{aligned} \Phi_{\rm TOV}(r) \;\; = \;\; & -4\pi \int_r^\infty \frac{\mathrm{d}r'}{r'^2} \left(\frac{m_{\rm TOV}}{4\pi} + r'^3 (P + p_\nu) \right) \\ & \times \frac{1}{\Gamma^2} \left(\frac{\rho + e + P}{\rho} \right), \end{aligned} \tag{B.2}$$

to obtain the effective relativistic potential $\Phi_{\rm eff}$ as

$$S\,\Phi_{\rm eff} = \Phi_{\rm TOV}. \tag{B.3}$$

Here ρ is the rest-mass density, $e = \rho\epsilon$ is the internal energy density with ϵ being the specific internal energy, and P is the gas pressure. The TOV mass is given by

$$m_{\rm TOV}(r) = 4\pi \int_0^r \mathrm{d}r'\, r'^2 \left(\rho + e + E + \frac{vF}{\Gamma} \right), \tag{B.4}$$

where p_ν, E, and F are the neutrino pressure, the neutrino energy density, and the neutrino flux, respectively (Baron et al. 1989, Rampp & Janka 2002).

The fluid velocity v is identified with the local radial velocity calculated by the Newtonian code and the metric function Γ is given by

$$\Gamma = \sqrt{1 + v^2 - \frac{2m_{\rm TOV}}{r}}. \tag{B.5}$$

The velocity-dependent terms were added for a closer match with the general relativistic form of the equation of motion (van Riper 1978, Baron et al. 1989). In the treatment of neutrino transport general relativistic redshift and time dilation effects are included, but for reasons of consistency with the Newtonian hydrodynamics part of the code the distinction between coordinate and proper radius is ignored in the relativistic transport equations (for details, see Sect. 3.7.2 of Rampp & Janka 2002). The quality of this approach was ascertained by a comparison with fully relativistic calculations (Rampp & Janka 2002, Liebendörfer et al. 2005).

In order to calculate the effective relativistic potential for multi-dimensional flows we substitute the "spherical contribution" $\bar{\Phi}(r)$ to the multi-dimensional Newtonian gravitational potential

$$\Phi(r,\theta,\varphi) = -\int_V \mathrm{d}r'\,\mathrm{d}\theta'\,\mathrm{d}\varphi'\,r'^2\sin\theta'\,\frac{\rho}{|\boldsymbol{r}-\boldsymbol{r}'|} \tag{B.6}$$

by the TOV potential $\bar{\Phi}_{\rm TOV}$:

$$\Phi_{\rm eff} = \Phi - \bar{\Phi} + \bar{\Phi}_{\rm TOV}. \tag{B.7}$$

Here $\bar{\Phi}(r)$ and $\bar{\Phi}_{\rm TOV}$ are calculated according to Eqs. (B.1) and (B.2), respectively, however with the hydrodynamic quantities ρ, e, P, v and the neutrino quantities E, F, p_ν being replaced by their corresponding angularly averaged values. Note that v here refers to the radial component of the velocity, only.

B.1.2. Modifications of the TOV potential

In a recent comparison Liebendörfer et al. (2005) found that gravity as described by the TOV potential in Eqn. (B.3) overrates the relativistic effects, because in combination with Newtonian kinematics it tends to overestimate the infall velocities and to underestimate the flow inertia in the pre-shock region. Thus, supposedly via the nonlinear dependence of $\Phi_{\rm eff}$ on e and P the compactness of the proto-neutron star is overestimated, with this tendency increasing at later times after core bounce. Consequently, the neutrino luminosities and the mean energies of the emitted neutrinos are larger than in the corresponding relativistic simulation.

In order to reduce these discrepancies – without sacrificing the simplicity of Newtonian dynamics – we tested several modifications of the TOV potential, Eqs. (B.2), which all act to weaken it. In particular, we studied the following variations[2]

Case A: In the integrand of Eqn. (B.4) a factor Γ, Eqn. (B.5) is added. Since $\Gamma < 1$ this reduces the gravitational TOV mass used in the potential.

[2]Note, all of the cases listed here were tested in Marek et al. (2006) with the C C N T code of Dimmelmeier et al. (2002, 2005). Only, the most promising cases were also implemented in the numerically much more expensive V code.

Case B: In Eqn. (B.4) the internal gas energy density and the neutrino terms are set to zero, $e = E = F = 0$, which again decreases the gravitational TOV mass.

Case C: In Eqn. (B.2) the internal gas energy is set to zero, $e = 0$, which directly weakens the TOV potential.

Case D: In the equation for the TOV potential, Eqn. (B.2), $m_{\rm TOV}$ is replaced by $\frac{1}{2}(m_{\rm TOV} + m_{\rm g})$. Here a Newtonian gravitational mass is defined as $m_{\rm g} = m_{\rm r} - m_{\rm b}$ with the rest mass $m_{\rm r} = 4\pi \int_0^r {\rm d}r'\, r'^2 \rho$ and the mass equivalent of the binding energy $m_{\rm b} = 2\pi |\int_0^r {\rm d}r'\, r'^2 \rho\, \Phi|$. As $m_{\rm g} < m_{\rm TOV}$, the strength of the potential is reduced.

Case E: Both in the equation for the TOV potential, Eqn. (B.2), and the equation for the TOV mass, Eqn. (B.4), we set $e = 0$.

Case F: In the equation for the TOV potential, Eqn. (B.2), we set $\Gamma = 1$. As $\Gamma < 1$ otherwise, this weakens the potential.

Case G: In the expression for Γ, Eqn. (B.5), the velocity is set to zero, $v = 0$. Hence, Γ^{-2} increases in Eqn. (B.2). This modification is used to also test a potential which is even stronger than the unmodified TOV potential.

In addition to these cases with a modified version of the TOV potential, we use the following notations:

Case N: This denotes the purely Newtonian runs with "regular" Newtonian potential.

Case R: This is the "reference" case with the TOV potential as defined by Eqn. (B.2).

Case GR: This case refers to fully relativistic simulations with the A -B T neutrino radiation-hydrodynamics code of the Oak Ridge-Basel collaboration.

Note that setting the internal energy density e to zero in Case B is unambiguous when a simple EoS is used and the particle rest masses are conserved. In general, however, particles can be created and destroyed, or bound states can be formed (e.g., in pair annihilation processes or nuclear reactions, respectively). Then only the sum of the rest mass energy and internal energy per nucleon – both appear in Eqs. (B.2, B.4) only combined in form of the "relativistic energy" per unit of mass, $(\rho + e)/\rho$ – is well defined, but not the individual parts. Therefore there exists ambiguity with respect to which contribution to the energy is set to zero. In order to assess a possible sensitivity of the core collapse results to this ambiguity, we tried two different variants of Case B in our V simulations with microphysical EoS. On the one hand we used $\widetilde{e} = E = F = 0$ in Eqn. (B.4), with $\widetilde{e}$ being the internal energy density plus an energy normalisation given by the EoS of Lattimer & Swesty (1991), $\widetilde{e} = (\rho+e) - \rho\,(m_{\rm n} - \Delta)/m_{\rm u}$ (where $m_{\rm u} = 1.66\times10^{-24}$ g is the atomic mass unit, $m_{\rm n}$ the neutron rest mass, and $\Delta = 8.8$MeV). On the other hand we tested

$e^* = E = F = 0$ with e^* being $\widetilde{e}$ without this energy normalisation, i.e. $e^* = (\rho + e) - \rho\, m_\mathrm{n}/m_\mathrm{u}$. Nucleons are then assumed to contribute to the TOV mass, Eqn. (B.4), with the vacuum rest mass of the neutron, increasing the mass integral and reducing Γ, Eqn. (B.5), relative to the first case, thus making the effective relativistic potential a bit stronger again. In order to compensate for this we also set $p_\nu = 0$ in the TOV potential, Eqn. (B.2). Both variants are found to yield extremely similar results and we therefore will discuss only one of them (the first variant) as Case B for the V simulations.

Ideally, a Newtonian simulation with an effective relativistic potential not only yields a solution of the TOV structure equations for an equilibrium state (as does Case R), but in addition closely reproduces the results from a relativistic simulation (Case GR) during a dynamic evolution. Applying the modifications of the TOV potential listed above, we find that Cases A to D yield improved results as compared to Case R, while Cases E to G either weaken the potential too much or are very close to Case R.

B.1.3. Theoretical motivation

There are (at least) two basic requirements which appear desirable for an effective relativistic potential in a Newtonian simulation. Firstly, the far field limit of the fully relativistic treatment should be approximated reasonably well in order to follow the long-term accretion of the neutron star and the associated growth of its baryonic mass. Secondly, the hydrostatic structure of the neutron star should well fit the solution of the TOV equations.

A closer consideration of the first point suggests the modified effective relativistic potential of Case A as promising, and in fact it turns out to be the most preferable choice concerning consistency and quality of the results. The other cases listed in Sect. B.1.2 are mostly ad hoc modifications of the original effective relativistic potential of Eqs. (B.2)–(B.4) (Case R) with the aim to reduce its strength, which was found to overestimate the effects of gravity compared to fully relativistic simulations in previous work (Liebendörfer et al. 2005). These cases are also discussed here for reasons of comparison and completeness.

In Eqn. (B.4) the hydrodynamic quantities (like rest-mass density ρ plus extra terms) are integrated over volume. In the Newtonian treatment there is no distinction between coordinate volume and local proper volume. Performing the integral of Eqn. (B.4) therefore leads to a mass – used as the mass which produces the gravitational potential in Eqs. (B.2) and (B.3) – which is *larger* than the baryonic mass, $m_\mathrm{b} = 4\pi \int \mathrm{d}r'\, r'^2 \rho$. In particular, it is also larger than the gravitational mass in a consistent relativistic treatment, which is the volume integral of the total energy density and includes the negative gravitational potential energy of the compact object. The latter reduces the gravitational mass relative to the baryonic mass by the gravitational binding energy of the star (see, e.g., Shapiro & Teukolsky 1983, page 125 for a corresponding discussion). Therefore, the effective relativistic potential introduced by Rampp & Janka (2002) [our Case R, Eqs. (B.2–B.4)] cannot properly reproduce the far field limit of the relativistic case and thus overestimates the effects of gravity. This particularly applies to the infall velocities of the stellar gas ahead of the supernova shock, as shown in Liebendörfer et al. (2005).

Introducing an extra factor Γ in the integral of Eqn. (B.4) for the TOV mass is motivated by the following considerations (where for reasons of simplicity contributions from neutrinos, though important, are neglected and spherical symmetry is assumed): In the relativistic treatment the

total (gravitating) mass of the star is given as

$$m_{\rm g} = 4\pi \int_0^\infty {\rm d}r'\, r'^2(\rho + e), \tag{B.8}$$

where ${\rm d}V' = 4\pi {\rm d}r'\, r'^2$ is the coordinate volume element, whereas the baryonic mass is

$$m_{\rm b} = 4\pi \int_0^\infty {\rm d}r'\, r'^2 \Gamma^{-1} \rho, \tag{B.9}$$

with ${\rm d}\mathcal{V}' = 4\pi {\rm d}r' r'^2 \Gamma^{-1}$ being the local proper volume element. The factor $\Gamma^{-1} > 1$ in the integrand of $m_{\rm b}$ thus ensures that $m_{\rm b} > m_{\rm g}$. The integral for $m_{\rm g}$ can also be written as

$$m_{\rm g} = 4\pi \int_0^\infty {\rm d}r'\, r'^2 \frac{\Gamma}{\Gamma} (\rho + e) = \int_0^\infty {\rm d}\mathcal{V}'\, \Gamma\, (\rho + e). \tag{B.10}$$

Since in Newtonian hydrodynamics no distinction is made between coordinate and proper volumes, one may identify ${\rm d}\mathcal{V}' \equiv {\rm d}V'$, consistent with the rest of our Newtonian code. This leaves the additional factor Γ in the integrand of Eqn. (B.10), leading to a redefined TOV mass used for computing the effective relativistic potential in Case A,

$$\widetilde{m}_{\rm TOV}(r) = 4\pi \int_0^r {\rm d}r'\, r'^2 \Gamma \left(\rho + e + E + \frac{vF}{\Gamma}\right). \tag{B.11}$$

The fact that a factor Γ^{-1} in the volume integral establishes the relation between gravitating mass, Eqn. (B.8), and baryonic mass, Eqn. (B.9), in the relativistic case suggests that the factor $\Gamma < 1$ in Eqn. (B.11) might lead to a suitable reduction of the overestimated effective potential that results when the original TOV mass of Eqn. (B.4) is used in Eqs. (B.2) and (B.5). Indeed, a comparison of the integral of Eqn. (B.11) for large r with the rest-mass energy of a neutron star reduced by its binding energy at time t (computed from the emitted neutrino energy, $\int_0^t {\rm d}t'\, L_\nu(t')$ with L_ν being the neutrino luminosity) reveals very good agreement.

The arguments given above only provide a heuristic justification for the manipulation of the TOV potential proposed in Case A. A deeper theoretical understanding and more rigorous analytical analysis of its consequences and implications is certainly desirable, but beyond the scope of the present discussion in this thesis. We plan to return to this question in future work.

In order to compare the results — obtained with the V code — presented here with those of the calculations of Liebendörfer et al. (2005) we used the same set of neutrino interaction rates as picked for Model G15 in Liebendörfer et al. (2005), and exactly the same parameters for the numerical setup (e.g., the grids for hydrodynamics and neutrino transport). Information about this setup can be found in Liebendörfer et al. (2005). The initial model for our calculations is the $15 M_\odot$ progenitor model "s15s7b2" from Woosley & Weaver (1995).

Since — as already mentioned above — solving the neutrino transport problem is computationally quite expensive we performed calculations only for Cases A, B, and F (as defined in Sect. B.1.2) with the V code[3]. The quality of these results is then compared to the fully relativistic treatment of the A -B T code.

[3] All other cases are discussed in greater detail in Marek et al. (2006).

B.1.4. Hydrodynamics and implementation of the effective relativistic potential

The implementation of an effective relativistic gravitational potential or of an effective relativistic gravitational force as its derivative into existing Newtonian hydrodynamics codes is straightforward and does not differ from the use of the Newtonian potential or force.

The equations solved by the code used for our simulations are described in much detail in previous publications (see, e.g., Rampp & Janka 2002, Müller & Steinmetz 1995,and references therein). The implementation of the source terms of the gravitational potential as discussed in Müller & Steinmetz (1995) is also applied for the handling of the effective relativistic potentials investigated in this work. The only specific feature here is the mutual dependence of Γ and $m_{\rm TOV}$, which is either accounted for by a rapidly converging iteration or by taking Γ from the old time step in the update of $m_{\rm TOV}$, when the changes during the time steps are sufficiently small.

Since the actual form of the gravitational source term is unspecified in the conservation laws of fluid dynamics, the Newtonian potential can be replaced by the effective relativistic potentials investigated in the current work in a technically straightforward way. Solving an equation for the internal plus kinetic energy (as in our codes) requires a treatment of the gravity source term in this equation that is consistent with its implementation in the equation of momentum.

Of course, the effective potential must be investigated concerning its consequences for the conservation of momentum and energy. Since a potential constructed according to Eqs. (B.2, B.4) does not satisfy the Poisson equation, the momentum equation cannot be cast into a conservation form (cf. Shu 1992, Part I, Chapter 4). As a consequence, the total linear momentum is strictly conserved only when certain assumptions about the symmetry of the matter distribution are made, for example in the case of spherical symmetry or axially symmetric configurations with equatorial symmetry, or when only one octant is modelled in the three-dimensional case. In axisymmetric simulations the conservation of specific angular momentum is fulfilled as well, when using the effective relativistic potential. In general, however, a sufficient quality of momentum (and angular momentum) conservation has to be verified by inspecting the numerical results.

The long-range nature of gravity prohibits to have an equation in pure conservation form for the total energy, i.e., for the sum of internal, kinetic, and gravitational energy (Shu 1992, Part I, Chapter 4). In contrast to the Newtonian case, however, our effective relativistic potential does also not allow one to derive a conservation equation for the total energy integrated over all space. Monitoring global energy conservation in a simulation with effective relativistic potential therefore requires integration of the gravitational source terms over all cells in time. If the local effects of relativistic gravity are convincingly approximated – as measured by good agreement with static solutions of the TOV equation and with fully relativistic, dynamical simulations – there is confidence that the integrated action of the employed gravitational source term approximates well also the global conversion between total kinetic, internal, and gravitational energies found in a relativistic simulation.

The recipes for approximating general relativity should be applicable equally well in hydrodynamic codes different from our (Eulerian) PPM schemes, provided the effects of gravity are consistently treated in the momentum and energy equations. The proposed effective potentials

are intended to yield a good representation of the effects of relativistic gravity in particular in the context of stellar core collapse and neutron star formation. For our approximation to work well, the fluid flow should be sub relativistic. The numerical tests described in the following sections show that velocities up to about 20% of the speed of light are unproblematic.

B.2. Simulations in spherical symmetry with the VERTEX code

We simulated the collapse and the post-bounce evolution of the progenitor model s15s7b2 with the V code as detailed in Chapter 2. The calculations were performed using the TOV potential given in Eqn. (B.2) (Model V-R, which is identical with the V calculation of Model G15 in Liebendörfer et al. 2005), and we also tested the modifications A, B, and F of the TOV potential (Models V-A, V-B, and V-F, respectively). For comparison, we refer in the following discussion also to the calculation of Liebendörfer et al. (2005) with the fully relativistic A -B T code (Case GR, Model AB-GR).

Fig. B.1a shows the central density as a function of time for the collapse (left panel) and for the subsequent post-bounce phase (right panel). The "central" density is the density value at the centre of the innermost grid zone of the AB-GR simulation. Because of a different numerical resolution it was necessary to interpolate the V results to this radial position. During the collapse only minor differences between the relativistic calculation (bold solid line) and the calculations with the V code are visible. Note that the trajectories from the V code, with the modifications A, B, and F of the TOV potential as well as with the TOV potential (case R), lie on top of each other.

We can thus infer that the differences between the modifications A, B, and F of the TOV potential are unimportant during the collapse phase. Furthermore, we can conclude from the good agreement of the general relativistic calculation and the V calculations that the TOV potential works well during the collapse phase. However, after core bounce this potential overestimates the compactness of the forming neutron star and therefore the density trajectories of Model AB-GR and Model V-R diverge (see Fig. B.1)a. At 250 ms after the shock formation the central density in Model V-R is about 20% higher than the one in the relativistic calculation. At this time the modifications A and B of the TOV potential give a central density only about 2% higher than Model AB-GR, and the absolute difference stays practically constant during the entire post-bounce evolution. This implies that both modifications yield very good quantitative agreement with the general relativistic treatment. In contrast, in Model V-F the central density after bounce is lower than the relativistic result of Model AB-GR. This indicates a strong underestimation of the depth of the gravitational potential in Case F, where $\Gamma = 1$ in the integrand of Eqn. (B.2).

Since the central densities suggest that differences between a fully relativistic calculation and Newtonian simulations with effective relativistic potential become significant only after shock formation (see also Liebendörfer et al. 2005), we discuss the implications of our potential modifications in the following only during the post-bounce evolution.

Fig. B.1b shows the shock positions as functions of time. Both Case A (thin solid line) and Case B (dashed-dotted line) reveal the desirable trend of a closer match with the general relativistic calculation (thick solid line) than seen for Model V-R, which gives a shock radius that is

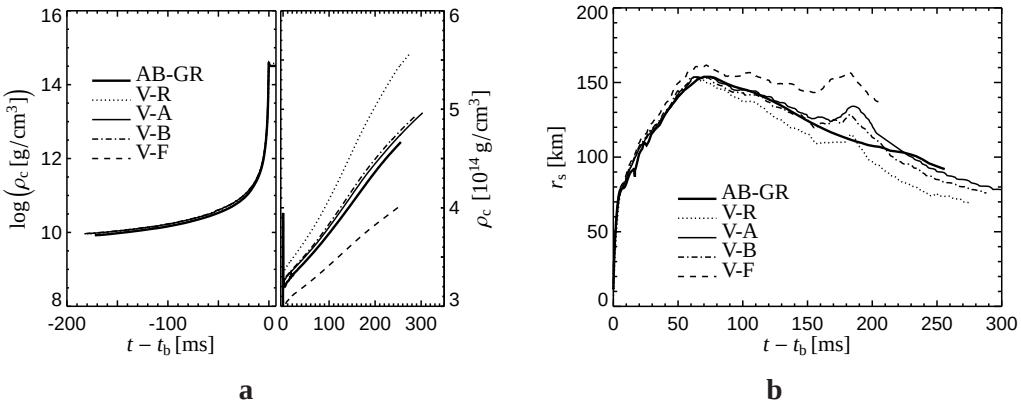

Figure B.1.: **a**: Time evolution of the central density ρ_c for Model AB-GR (bold solid line), V-A (solid line), V-B (dashed-dotted line), V-F (dashed line), and V-R (dotted line). The left panel shows the collapse phase (note that here all models with the V - code lie on top of each other), while the right panel shows the post-bounce evolution. Note the different axis scales in both panels. **b**: Time evolution of the shock position r_s for simulations with the V code using various modifications of the TOV potential compared to the general relativistic result from the A -B T code (Model AB-GR, thick solid line).

too small, and Model V-F, where the shock is too far out at all times. In particular, Model V-A reveals excellent agreement with Model AB-GR. The only major difference is visible between 170 ms and about 230 ms after shock formation when the shock transiently expands in the V - calculation. This behaviour is generic for the V results and independent of the choice of the gravitational potential. In the A -B T run the transient shock expansion is much less pronounced and also a bit delayed relative to the V feature (it is visible as a deceleration of the shock retraction between about 200 ms and 250 ms). This difference, however, is not caused by general relativistic effects but is a consequence of a different numerical tracking of the time evolution of interfaces between composition layers in the collapsing stellar core (for more details about the numerics and a discussion of the involved physics, see Liebendörfer et al. 2005). It is therefore irrelevant for our present comparison of approximations to general relativity. A good choice for the effective relativistic potential (like Case A) should just ensure that the corresponding shock trajectory converges again with the relativistic result (Case GR) after the transient period of shock expansion.

The time evolution of the central density or the shock position, however, is not the only relevant criterion for assessing the quality of approximations to general relativity. A good approximation does not only require good agreement for particular time-dependent quantities (like, e.g., the central density), but also requires that the radial structure of the models reproduces the relativistic case as well as possible at any time.

In the left panels of Fig. B.2 we show such profiles of the density and velocity (top panel) and of the entropy and electron fraction Y_e, i.e., the electron-to-baryon ratio (bottom panel), for Models AB-GR and V-A at a time of 250 ms after bounce, when the discrepancy between

relativistic and approximative treatment was found to be largest in Liebendörfer et al. (2005). Fig. B.2 can be directly compared with Fig. 12 in the latter reference. Obviously Model V-A fits the density profile of the general relativistic calculation (Model AB-GR) extremely well at all radii. Furthermore, both the velocity ahead of the shock front and behind it are in extremely good agreement between the two models (the differences at the shock jump have probably a numerical reason associated with the different handling of shock discontinuities in both codes). It is an important result that with this modification A of the TOV potential one is able to approximate the kinematics of the relativistic run with astonishingly good quality in a Newtonian calculation (at least in supernova simulations when the velocities do not become highly relativistic). In contrast, in V runs with the original TOV potential (Case R) the pre-shock velocities were found to be significantly too large (Liebendörfer et al. 2005), which is due to the overestimated strength of gravity in the far field limit as compared to the relativistic calculations (see the discussion in Sect. B.1.3).

Also the entropy and Y_e profiles (bottom left panel of Fig. B.2) reveal a similarly excellent agreement between Models V-A and AB-GR. The minor entropy differences ahead of the shock are associated with a slightly different description of the microphysics (nuclear burning and equation of state) in the infall region (for details we refer to Liebendörfer et al. 2005).

Not only the radial structure of the forming neutron star in all relevant quantities is well reproduced, but also the neutrino transport results of the relativistic calculation and of the approximative description of Case A are in nearly perfect agreement. Corresponding radial profiles of the luminosities and root mean square energies – both as defined in Sect. 4 of Liebendörfer et al. (2005) – for electron neutrinos, ν_e, electron antineutrinos, $\bar{\nu}_e$, and heavy-lepton neutrinos[4], ν_x, are displayed in the right panels of Fig. B.2. The results for Models V-A and AB-GR for all neutrino flavours share their characteristic features, and in particular agree in the radial positions where the different luminosities start to rise. While the ν_x luminosities are nearly indistinguishable below the shock, the jump at the shock is slightly higher for the V run and reflects the larger effects due to observer motion, e.g., Doppler blueshift and angular aberration, for an observer comoving with the rapidly infalling stellar fluid ahead of the shock. The offset between results of Models V-A and AB-GR decreases at larger radii where the infall velocities are lower. This discrepancy was not discovered by Liebendörfer et al. (2005), because there the agreement of the radial structure for both investigated models was generally found to be poorer than in the present work.

General relativistic effects are unlikely as an explanation, because they are very small around the shock (see Fig. 13 in Liebendörfer et al. 2005). A detailed analysis reveals that both codes produce internally consistent results, conserving to good precision the luminosity through the shock for an observer at rest and showing the expected and physically correct behaviour in the limit of large radii. Most of the observed difference (which has no mentionable significance for supernova modelling) could be traced back to the fact that V achieves only order (v/c) accuracy, whereas A -B T produces the full relativistic result including higher orders in (v/c). Corresponding effects become noticeable when $v/c \gtrsim 0.1$. The mean neutrino energies are hardly affected by this difference (Fig. B.2, bottom right panel). In case of the ν_e and

[4] Since the transport of muon and tau neutrinos and antineutrinos differs only in minor details we treat all heavy-lepton neutrinos identically in the V simulations.

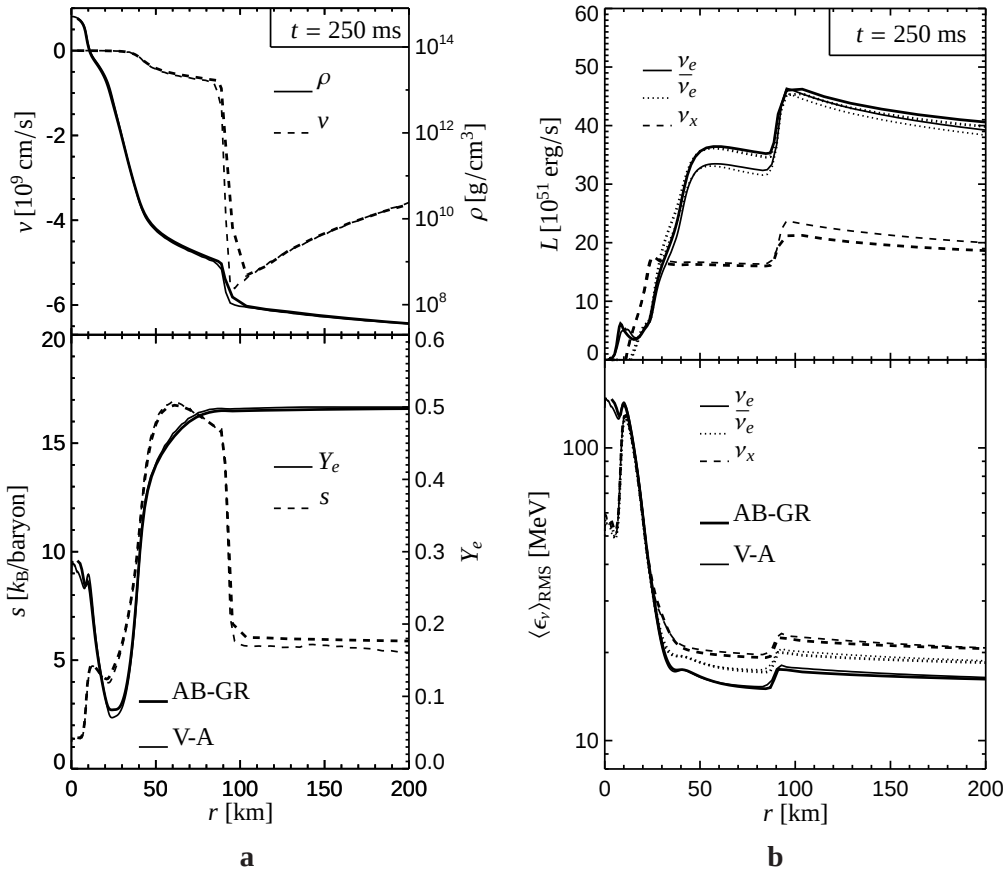

Figure B.2.: Left: Radial profiles of the velocity v (dashed lines) and density ρ (solid lines) for Model V-A (thin) and the relativistic Model AB-GR (bold) at a time of 250 ms after shock formation (top panel), as well as radial profiles of the entropy s (dashed lines) and of the electron fraction Y_e (solid lines) for the same models and the same time (bottom panel). As in Liebendörfer et al. (2005), r is the circumferential radius in case of the relativistic results. Note the different vertical axes on both sides of the two panels. Right: Radial profiles of the luminosities L of electron neutrinos (solid lines), electron anti-neutrinos (dotted lines), and heavy-lepton neutrinos (dashed lines) for Models V-A (thin) and AB-GR (bold) at a time of 250 ms after shock formation (top panel), as well as radial profiles of the root mean square energies $\langle\epsilon_\nu\rangle_{\rm RMS}$ for the number densities of ν_e, $\bar{\nu}_e$, and heavy-lepton neutrinos for Models V-A and AB-GR (bottom panel). The labelling is the same as in the panel above, and all neutrino quantities are given for a comoving observer.

$\bar{\nu}_e$ luminosities the V run yields roughly 10% lower values outside of the corresponding neutrino spheres (i.e., between about 50 km and 90 km), but values much closer to those from the A -B T calculation ahead of the shock. Since the neutrinospheric emission of ν_e and $\bar{\nu}_e$ is strongly affected by the mass accretion rate of the nascent neutron star and the corre-

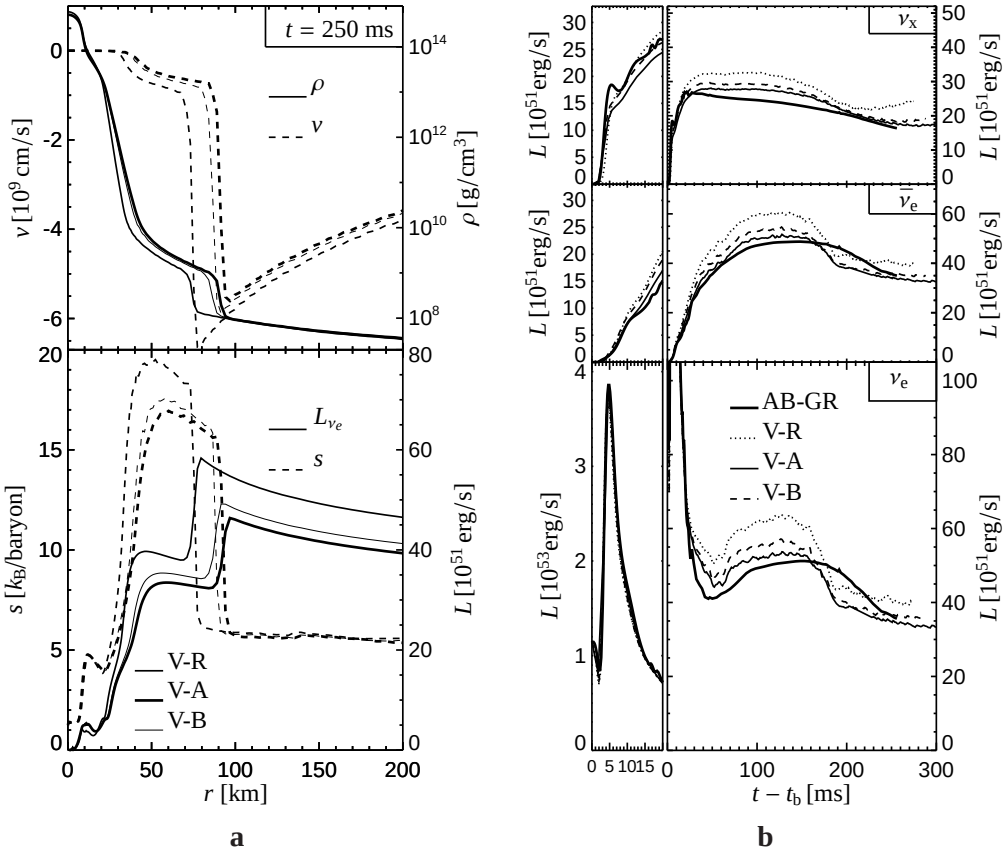

Figure B.3.: **a**: Luminosities as functions of post-bounce time for different cases computed with the V code and for Model AB-GR. The top panel shows the results for heavy-lepton neutrinos, the centre panel those for the electron antineutrinos, and the bottom panel the results for electron neutrinos. The panels on the left magnify the early post-bounce phase. All luminosities are given for an observer comoving with the stellar fluid at a radius of 500 km. Note the different scales of the vertical axes. **b**: Radial profiles of the velocity v (dashed lines) and density ρ (solid lines) for Models V-A (bold lines), V-B (thin), and V-R (medium) at a time of 250 ms after shock formation (top panel). Radial profiles of the entropy s (dashed lines) and of the electron neutrino luminosity L_{ν_e}(solid lines) for the same models and the same time (bottom panel). The luminosity is given for an observer comoving with the stellar fluid.

sponding accretion luminosity (which both seem to have the tendency of being slightly higher in Model AB-GR), we refrain from ascribing the different magnitude of the ν_e and $\overline{\nu_e}$ luminosities only to the treatment of relativistic effects. Although such a connection cannot be excluded, the luminosity differences might (partly) also be a consequence of the different accretion histories in Models AB-GR and V-A, which manifest themselves in the shock trajectories (Fig. B.1b) and are attributable to the different handling of the microphysics and computational grid in the infall

layer (see above and Liebendörfer et al. 2005). This interpretation seems to be supported by the time evolution of the neutrino luminosities plotted in Fig. B.3a. The accretion bump in the ν_e and $\bar{\nu}_e$ luminosities which follows after the prompt ν_e burst is stretched in time in case of Model AB-GR, indicating the delay of mass infall at higher rates relative to all V simulations. Note that the neutrino emission reacts with a time lag of some 10 ms (corresponding to the cooling timescale of the accretion layer on the neutron star) to variations of the mass accretion rate.

Moreover, Fig. B.3a shows that our variations of the effective relativistic potential in the V - models have little influence on the prompt burst of ν_e at shock breakout. But subsequently the overestimated compactness of the proto-neutron star in Model V-R, which causes the faster contraction of the stalled shock after maximal expansion (Fig. B.1b), also leads to higher neutrino luminosities during the accretion phase. Consistent with the shock trajectories, Model V-A yields the closest match with the general relativistic run of Model AB-GR also for the neutrino luminosities. It is very satisfactory that the results (shock radius r_s as well as the neutrino luminosities L) from both simulations reveal convergence at later times when the period of massive post-bounce accretion comes to an end.

In Fig. B.3b we present the radial structure at 250 ms after bounce for the V simulations with the modifications A and B of the TOV potential, compared to the results with the TOV potential (Case R) which was already discussed in Liebendörfer et al. (2005). Note that because of the excellent agreement seen in Fig. B.2, Model V-A (Case A) can also be considered as a representation of the fully relativistic run of Model AB-GR. Models V-A and V-B show results of similar quality. The little offset of the shock position (which is causally linked to the differences in all profiles) might suggest that Model V-B is slightly inferior to Model V-A in approximating relativity. This conclusion could also be drawn from the post-bounce luminosities in Fig. B.3a. However, caution seems to be advisable with such an interpretation, being aware of the uncertainties in the accretion phase and infall layer discussed above, and in view of the fact that the central densities (Fig. B.1a) and radial density profiles (Fig. B.3b) agree well. Moreover, the quality of the agreement at "very late" times cannot be judged, because no information is available for the behaviour of Model AB-GR after 250 ms post bounce, a time when the settling of the shock radius and luminosities to their post-accretion levels seems not yet over in this model (Figs. B.1b, B.3a). The TOV potential of Case R clearly produces too large infall velocities ahead of the shock (and therefore does not agree well with the kinematics of the relativistic calculation), overestimates the compactness of the forming neutron star, and thus produces too high neutrino luminosities during the simulated period of evolution (for a detailed discussion, see Liebendörfer et al. 2005). Cases A and B clearly perform better and must be considered as significant improvements for use in Newtonian simulations with an effective relativistic potential as approximations to fully relativistic calculations.

C

Test of momentum conservation

This Section is a discussion of some test calculations that were done in order to understand the results of Section 5.1, where it was found that though momentum conservation is good in calculations including general relativistic effects, a (small) momentum conservation violation is found in Newtonian calculations. This is somewhat unsatisfactory, since physically momentum conservation is only ensured in a Newtonian framework but not in the approximations we use to include general relativistic effects, see also the discussion in Appendix B. Thus from a physical point of view momentum conservation should be guaranteed in an Newtonian calculation. Numerically, however, it is quite difficult to ensure momentum conservation in both approaches, the reason being that P — the numerical scheme we use for solving the hydrodynamics equations — uses a operator–splitting method to include the source term of the (Newtonian or general relativistic) potential. Nevertheless, the fact that despite these complications momentum conservation is guaranteed in the less plausible — the general relativistic case — makes it desirable to achieve at least similar results in Newtonian calculations.

A representative overview of the momentum conservation that is achieved in general relativistic calculations is shown in Fig. C.1, where we show the z–component of the momentum and the corresponding movement of the core for model L&S–2D.

The same quantities evaluated for model L&S–2D–Newt are shown in Fig. C.2. Clearly, in contrast to model L&S–2D, model L&S–2D–Newt does not show an oscillation of the z–component of the momentum but rather shows a continously drift towards one hemisphere. However, it is also visible that this momentum conservation violation is much smaller than the amplitude observed in model L&S–2D, but nevertheless since it produces a force always in the same direction an at least equivalent displacement of the core is observed. Since numerically the only difference between the calculation of model L&S–2D and of model L&S–2D–Newt is that in the former a monopole term to the gravitational potential is included which accounts for general relativistic effects (see Section 2 and Appendix B), it seems plausible that the different evolution of both models is caused by the different calculation of the source term for gravita-

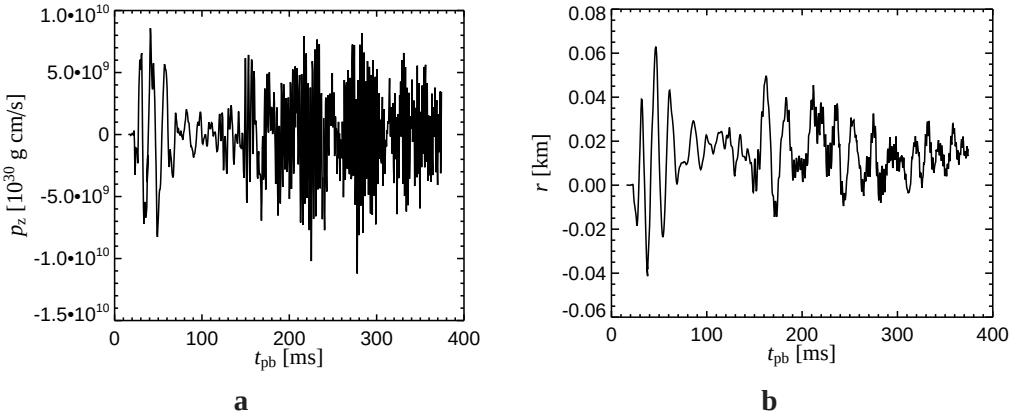

Figure C.1.: a: The z–component of the momentum as function of time for model L&S–2D. Note that though, the momentum is not zero, it oscillates such that on time average the momentum is conserved. **b**: The displacement r of the centre of mass evaluated from the momentum evolution in panel a. Note that the predicted movement is at all times much smaller than the width (300 m) of the inner most grid zone at centre.

tional forces. In order to test this hypothesis we have calculated several test models, see Table C.1, which were all mend to investigate the momentum conservation in Newtonian runs. Both the "full" Newtonian 2D gravitational potential (i.e. without the general relativistic monopole term) as a Newtonian spherically symmetric potential were used.

As the purely hydrodynamical models show, the momentum evolution in the Newtonian models is not caused by the calculation of the neutrino transport. Furthermore model Hydro–no–pert shows that a model stays exactly spherical symmetric — even in 2D — as long as no random perturbations are used and thus no momentum conservation violation is observed. This shows that the reason for the momentum conservation violation observed in our models is not caused by an error in the code which artificially breaks spherical symmetry. Furthermore, model L&S–2D and Hydro–1Dpot behave similar in the sense that a strong oscillation of the z–component of the total momentum is observed and thus an oscillatory movement of the core is seen. Since in both models the monopole term dominates (either because it is the strongest contribution as ii is the case in the GR–approximation of model L&S–2D, or because all other contributions were switched of as it was done in model Hydro–1Dpot) the behaviour in the models with the two–dimensional Newtonian potential have to be caused by the non–spherical part of the gravitational potential. It is also interesting that the evolution of the momentum is not influenced by the numerical treatment of the innermost core: independent of a spherical symmetric (1D) core a 2D core the momentum evolution is very similar, compare models Hydro and Hydro–2Dcore. Thus, the question remains what causes the momentum evolution in Newtonian (hydro) models?

As one can deduce from Figs. C.2a,b model Hydro for example shows the build up of a net momentum at a time of around 10ms after the shock formation. At this time, however, the density as well as the radial velocity are still perfectly spherically symmetric, see Fig. C.3a–c. The z–component of the velocity field, however, shows suddenly at this time a breaking of

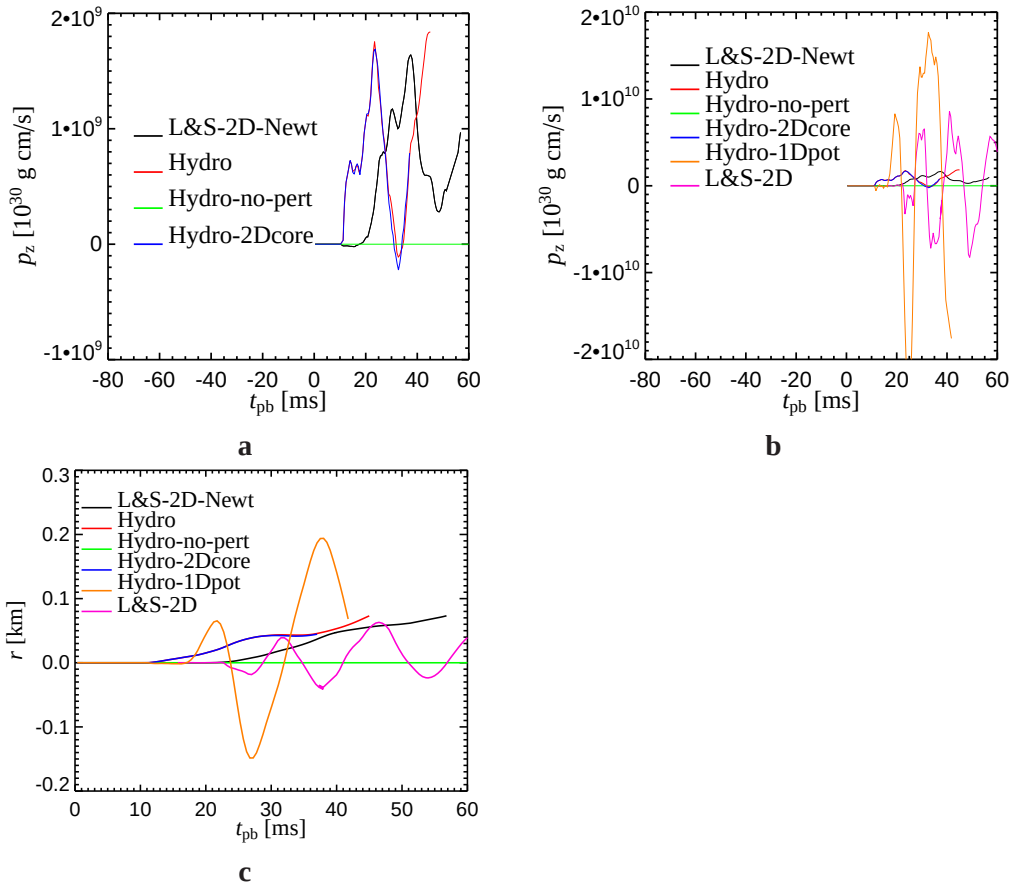

Figure C.2.: a,b: The z–component of the momentum as function of time for model L&S–2D (purple), L&S–2D–Newt (black) and the test calculations. Note the different axis scales in both plots. **c**: The displacement *r* of the core evaluated from the momentum evolution in panel a. Note that the predicted movement is at all times much smaller than the width (300 m) of the inner most grid zone at centre.

Model	Potential	2D–Expansion	Neutrino Transport	1D core in centre
L&S–2D	GR	Yes	Yes	Yes
L&S–2D–Newt	NEWT	Yes	Yes	Yes
Hydro	NEWT	Yes	No	Yes
Hydro–2Dcore	NEWT	Yes	No	No
Hydro–1Dpot	NEWT	No	No	No
Hydro–no–pert	NEWT	Yes	No	Yes

Table C.1.: Overview over all models used in this Section. Stated are the model names, the used gravitational potential (i.e. purley 2D Newtonian or 2D Newtonian with monopole GR corrections), whether Neutrino transport is taken into account, and if the innermost 6 zones (i.e. 1.6 km) are calculated in spherical symmetry. Note that model Hydro–1Dpot was calculated with only the Newtonian monopole potential, i.e. the 2D potential was switched of. Note that model Hydro–no–pert was calculated without applying the usual random perturbations in density (i.e. no breaking of radial symmetry was induced.

symmetry which leads to the momentum conservation violation. This can be seen in Fig. C.3c, where we plot the difference of this velocity for corresponding rays:

$$|u_z(0^\circ + \theta)| - |u_z(180^\circ - \theta)|\,, \forall \text{angular rays}\,\theta \tag{C.1}$$

Since the radial velocity (which contributes to the z–component of the velocity field) is still spherically symmetric at this time, this finding implies that the lateral velocity u_θ has to develop differently on different angular rays. Indeed, the momentum conservation violation first appears at a radius of around 20 km, see Fig. C.3c, where the convection in the dense core appears. Thus, obviously the appearance of convection causes the build up of a net momentum along the polar axis and not the asymmetric clumping of the density field due to gravitational forces[1]. Thus, in the Newtonian calculations with non–spherical gravitational potential the momentum conservation violation appears as soon as convection sets in and non–spherically symmetric fluid flows appear. The implementation of the gravitational potential in the M DB TH–code does thus obviously not completely conserve the total momentum. However, the momentum conservation violation we observe is very small and seems to saturate which means that the centre of the core does not leave (or only at very late evolution times) the first grid zone. The fact that in models with a dominant monopole term the momentum conservation is much better is due to the fact that the spherical part of the gravitational potential acts as a restoring force that acts against the direction of the momentum conservation violation.

[1] However, the matter flow in the region of proto–neutron star convection is of course influenced by the gravitational field.

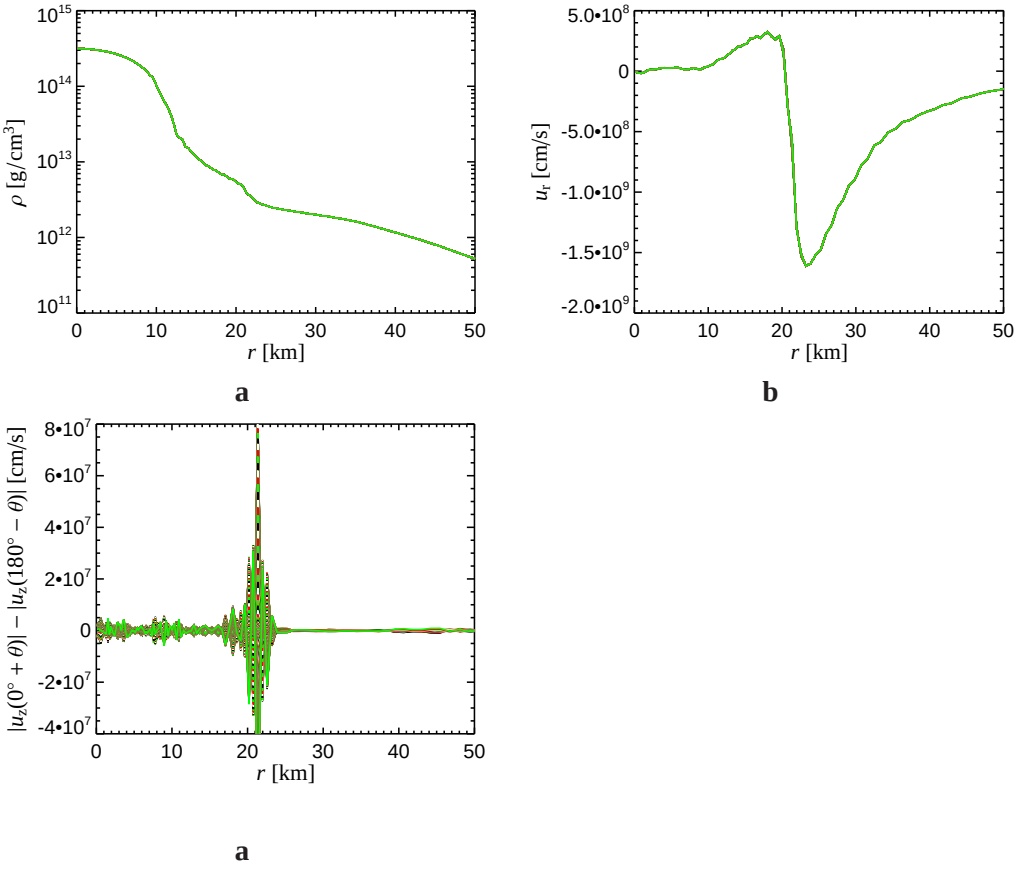

Figure C.3.: **a**: The density as function of radius of model Hydro at a time of 12 ms after the shock formation. This time was chosen since the momentum conservation violation already appears at this time. Note that profiles for all angular rays are plotted, which, however, due to a still spherically symmetric density structure lie on top of each other. **b**: The radial velocity profiles at the same time as the density profiles from panel a. Note that also here all angular bins as shown, which lie on top of each other. **c**: The difference of the z–component of the velocity field for angular rays being symmetric to the equator, see Eqn. C.1. Note that in the region where proto–neutron star convection develops, the contributions of the different angular rays do not exactly cancel each other which leads to the build up of the observed net momentum.

D

The growth of modes in the standing accretion shock instability

As we have already discussed in Section 5.1, for reasons of computer time, model Wolff–2D was initially calculated in a computational domain which covered the area between the north pole and the equator. Then, at a time of 130 ms after the shock formation, a mapping to a 180° degree grid was done and the calculation was continued on this new grid. As we have already mentioned, we have indications that a calculation of a model which covers the area between a pole and the equator, does not suppress essential physics and explosion can be obtained, see the discussion in Section 4.2. The reason for this is that in the particular model discussed in Section 4.2 the lowest possible mode in the pole–equator setup, the $l = 2$–mode, grows comparable, as the $l = 1$–mode in the corresponding 180°–model. Also the comparison of two rotating models one calculated from pole to pole and the other one calculated from pole to equator, see Section 6.1, reveals only minor differences, which is another hint that a calculation on a grid domain from pole to equator does not produce wrong results. However, things are different when one switches from a 90° to a 180° model during a simulation, since one then changes the wave–number of the lowest mode which can be excited. Thus the question has to be answered if by doing this kind of change during a simulation, one artifically influences the evolution of model Wolff–2D. Of course, this answer can only be obtained by simulating the model once again in 180° from a earlier time on[1]. Thus we have redone a calculation of this particular model, where the mapping to a full 2D computational domain was done at a time of 70 ms (i.e. 60 ms earlier than in model Wolff–2D) and we followed this model, denoted Wolff–2D–ear, as long as possible. In the following we will compare both models and check whether the supernova evolution is different in both runs.

[1] Here, this can either mean that the simulation is started from the beginning in 180° or that the mapping to 180° is done at a earlier time.

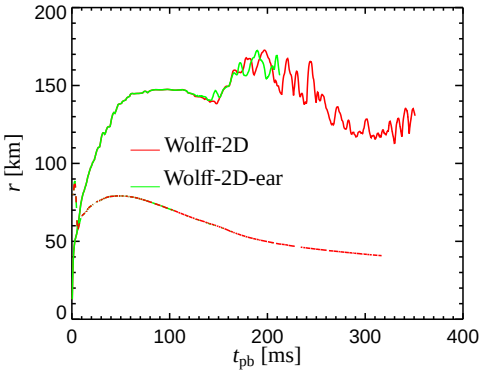

Figure D.1.: The laterally averaged shock positions (upper solid lines) and the electron neutrino spheres (lower solid lines) as function of time for both models. Note that the position of the electron neutrinospheres is equal in both models, since the electron neutrinosphere is not subject to low mode deformations for the evolution times regarded here.

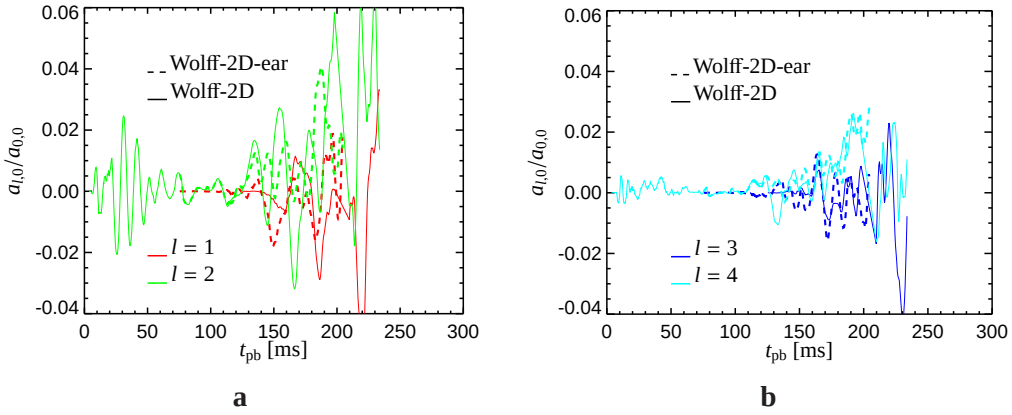

Figure D.2.: The expansion of the shock surface into spherical harmonics, see Section 4.2. Shown are the normalised amplitudes $a_{l,0}/a_{0,0}$ of the contribution of the wave–number l for model Wolff–2D (thin solid) and model Wolff–2D–ear (thick dashed). **a**: The lowest possible non spherical modes $l = 1, 2$. **b**: The next higher modes $l = 2, 3$.

We again begin our discussion by showing in Fig. D.1 the laterally averaged shock positions and the laterally averaged positions of the electron neutrinospheres of models Wolff–2D and Wolff–2D–ear.

Though the switch to a full 2D–model was applied at 70 ms and 130 ms after the shock formation in the models Wolff–2D–ear and Wolff–2D, respectively, we do not find a different angularly averaged shock position. At the time when the Si–O–interface reaches the shock front and triggers a shock expansion (at roughly 150 ms after the shock formation), however, both models show a slightly different evolution of the averaged shock position. Nevertheless for all the time we were able to recompute model Wolff–2D–ear we do not find a significantly changed (laterally averaged) position of the standing accretion shock front.

Also the projection of the shock deformation into the space of spherical harmonics shows that the contribution of the different modes to the shock position changes initially very slow,

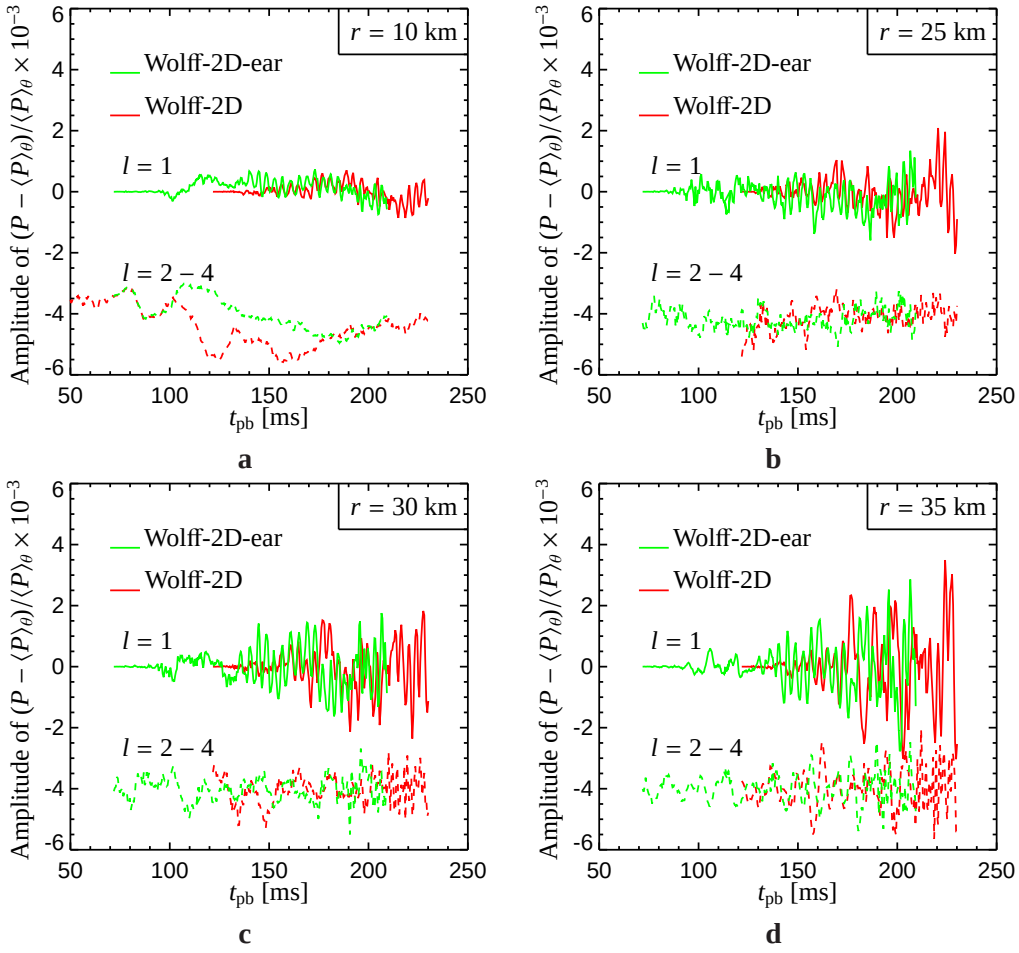

Figure D.3.: The expansion of the pressure fluctuations into spherical harmonics, cf. Eqn. 5.1.1, as function of time. Shown are the lowest possible non–spherical modes, namely $l = 1$ and $l = 2$. Note that the position of the amplitudes of the $l = 2$–modes were shifted. **a**: the fluctuations at a radius of 10 km. **b**: the fluctuations at a radius of 25 km. **c**: the fluctuations at a radius of 30 km. **d**: the fluctuations at a radius of 35 km.

see Fig. D.2: Roughly for the first 50 ms, where both models were calculated on different 2D–domains the coefficients of the spherical harmonics are essentially equal. Only at a time of a 130 ms after the shock formation when finally both models were calculated as a 180°–setup the amplitudes start to change. As one would expect in model Wolff–2D–ear, where the $l = 1$ mode can grow earlier than in model Wolff–2D, the amplitude of the $l = 2$ mode shrinks and the $l = 1$ mode grows faster. However, for the time we were able to compute both models, the amplitudes of the $l = 1$ modes of the shock instabilities have roughly equal values (though the time evolution is different), which indicates that the growth of the $l = 1$ mode was not artificially suppressed in model Wolff–2D. Also the growth of g–mode neutron star oscillations, see the discussion in Section 5.1, is very similar in both models. As Fig. D.3 shows, though the time evolution of the g–modes is different in both models, the amplitudes are very similar. Thus we conclude that our numerical treatment in model Wolff–2D did not artificially suppress the growth of an $l = 1$ g–mode oscillation in the dense core. However, it must be noted here that this result for both the mode growth of the shock instability and the neutron star g–modes might not hold for two possible cases:

- Firstly, it can not be excluded that a later times the shock deformation modes may develop totally different strength. This can only be checked when both models Wolff–2D and Wolff–2D–ear are calculated to longer times.
- Secondly, it is also possible that if we had calculated a model on a 180°–grid from the moment of shock formation on, that the modes would have developed in a different manner. Testing this would require a time consuming simulation.

Thus our conclusion that the shock evolution and the neutron star g–mode excitation of model Wolff–2D was not seriously influenced by our numerical treatment may be proven wrong by doing the above mentioned test calculations.

E

A radial, energy-space, and angular resolution test with the Wolff-EoS

In general, the common sense of numerical treatments requires that the code one uses is tested against resolution artefacts. Such a test requires *several* runs where the resolution increases by a factor (typically chosen to be 2). One says the simulations are converged when the results[1] are independent of the resolution. This typically implies that the resolution has to be better than a certain value and the resolution test has no other importance than to proof its existence and to determine this value.

Since the V / M DB TH code uses several different grids (radial direction, energy space, and in 2D additional an angular direction) several resolution studies had to be performed. In spherically symmetric models we performed resolution test concerning the radial grid, and in another study we tested the dependence of our results on the energy–grid. The result of these studies will be presented in the following subsection.

E.1. Resolution studies in spherically symmetric models

E.1.1. Energy grid

In the calculations the spectrum of neutrino energies is normally resolved by 17 geometrically spaced energy bins between 0 MeV and 380 MeV. In order to test for resolution effects we have also calculated models where the number of bins was reduced or increased by roughly a factor of two. These models use, in the same energy range, 9 and 33 geometrically spaced energy bins, respectively. Additionally, also a model was calculated where 13 energy bins were used.

[1] Here the term results implies physical quantities that should be independent of the grid resolution. Especially, physical behaviour that is scale dependent (e.g the energy cascade in turbulent flows) is *not* included in this sense.

All models are based on model Wolff(io)slms which was discussed in Section 3.2 and exactly the same microphysical setup was chosen.

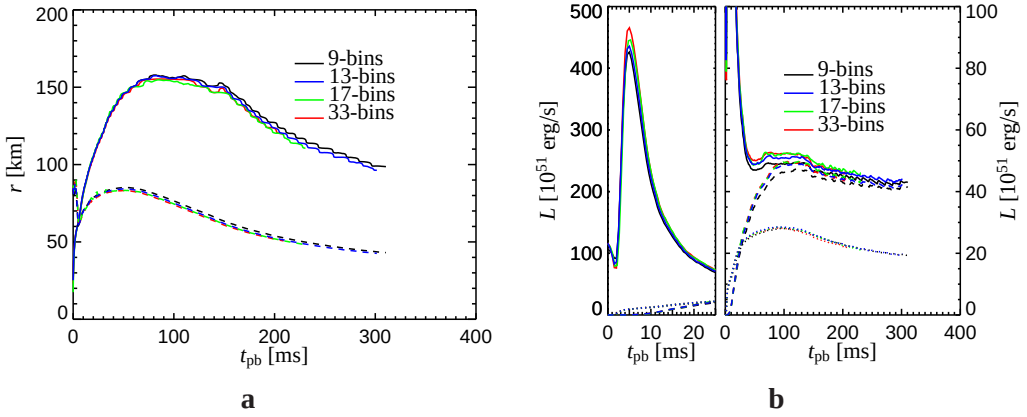

Figure E.1.: **a**: The shock position (solid) and the the position of the electron neutrinosphere (dashed) for the models that used 9, 12, 17, and 33 energy bins. **b**: The neutrino luminosities evaluated at 400 km. The values were transformed such as if the observer is resting at infinity. The solid line represents the luminosities of electron neutrinos, the dashed lines correspond to anti electron neutrinos, and the heavy (anti) lepton neutrinos are represented by the dotted lines.

In Fig. E.1a we show the shock trajectories as function of time for the three models and in Fig. E.1b we show the evolution of the neutrino luminosities as measured by an static observer resting at infinity. Whereas model 9–bins shows a larger electron neutrinosphere radius and a larger shock position, the models with 17 and 33 energy bins show almost identical behaviour. Model 12–bins lies in between these two groups. The luminosities of all neutrino flavours are also identical for the models with 17 and 33 energy bins except for the peak luminosity during shock breakout, where we find roughly 5% difference. However, the rise and fall time, as well as the later evolution are almost identical for these models. We find that model 9–bins generically underestimates the luminosity of all neutrino flavours, and again, model 12–bins predicts luminosities which lie between the ones of model 9–bins and 12–bins.

This implies that 17 energy bins seem to be enough to follow the supernova dynamics correctly. Clearly the step from 17 to 33 energy bins results in only a fraction of the changes that are observed when one uses 17 instead of 9 energy bins. Since the results for 17 and 33 energy bins are almost identical that implies that the numerics converge at these choices of the energy grid as far as the supernova dynamics are concerned.

However, it remains to be answered how well the different energy grid does sample the spectra of neutrino energies. This is shown in Figs. E.2a–f where we show the spectra of all neutrino flavours at a time of 50 ms after the shock formation as it would be measured by an observer resting at infinity.

Again, we find that 9 and 12 energy bins are too less in order to resolve the neutrino spectra. More importantly, the spectra of the models with 17 and 33 energy bins are again very similar. Except for the spectral maximum, in the low energy range ($\epsilon \leq 30$ MeV) the fits are very

similar. For larger neutrino energies the spectra begin to deviate stronger from each other. However, again, the differences between the runs with 17 and 33 energy bins are smaller than the differences between the ones with 9 and 17 energy bins. We can thus not say that our 17 energy bin run is converged in this high energy tail, since we have only a hint that increasing the number of energy bins will actually lead to a convergence in the high energy tail. However, runs with even larger number of energy bins were computationally not feasible in this study. In the high energy tail our run with 17 energy bins is thus not fully converged, but the resolution is good enough to overcome most of the resolution effects. Surely, in this sense a better resolved energy space would be preferable, but for two reasons we refrain from this approach: on the one hand the flux at these high energies is very low compared to the low energy flux[2]. Thus smaller errors do rarely contribute significantly to the total flux. Furthermore, our standard energy grid seems to slightly overestimate the neutrino flux in this energy range, which implies that we loose slightly more energy in neutrinos than the better resolved simulation suggests. This implies that we probably make an explosion harder to achieve (more energy is extracted from the post shock region) and we do not artificially enhance the explosion mechanism. More importantly, on the other hand, one can simply not allow for a higher resolution in energy space. The computational costs scale like ${N_\epsilon}^3$, which implies that a multi–dimensional simulation will scale up from a run–time of several months to over a year if the energy resolution is doubled. This would render supernova simulations impossible!

However, as Figs. E.1 through E.2 demonstrate, our "standard" energy grid with 17 energy bins is converged as far as the supernova dynamics is converged. Nevertheless, the details of the high energy tail of the neutrino spectra is still influenced by resolution effects. Thus with improved computers and numerical capabilities a better resolved energy space should be used in the future.

E.1.2. Radial grid

In a simulation of the postbounce phase a Eulerian grid is used, which is chosen such that at least 10 Zones per decade of density are available. Since the density gradient at the border of the proto–neutron star becomes steeper with ongoing time, this implies that from time to time a numerical refinement is applied that ensures a well resolved nascent neutron star. Typically, 400 Zones are used at the beginning of the postbounce phase and after 300 ms the radial grid consists of 500 to 600 radial zones depending on the progenitor model and the used EoS. Another constraint on the radial grid is that in a multi–dimensional simulation the numerical zones should be roughly quadratic in order to ensure that the PPM hydro-scheme works properly. Thus an increased angular resolution requires also an increased radial resolution (see below).

We performed some runs in order to test the dependence of our results on the radial grid. These runs were performed with the Wolff-EoS, the same micro-physics as described in Section 3.2, and an initial number of 400, 600, and 780 zones, respectively. The radial resolution $\mathrm{d}r/r$ is shown in Fig. E.3 for these three models. Note, that even in spherical symmetric calculations the simulations would be too expensive if the best resolution is used throughout the whole computational domain. For this reason, inside of the proto neutron star a transition to the

[2]This is at least true, as long as one regards the early supernova evolution for times smaller than roughly 1s.

well resolved resolution takes place. This is justified, since inside of the dense core no strong gradient in density develops and thus a lower resolution is sufficient. Also note that model "600–zones" is identical to model Wolff–1D , which was introduced in Section 5.1. As one can see in Fig. E.3 the grids were chosen such that in the relevant region between ≈20 km and ≈700 km the resolution increases substantially for the different grids.

The results of this resolution study are shown in Fig. E.4, where the positions of the shock fronts, of the neutrinospheres, and the neutrino luminosities as function of time are shown. Clearly, model "400–zones", which has the lowest resolution, shows a different shock trajectory and neutrino luminosities than the finer resolved models. Interestingly, the different shock trajectory establishes in the first 50 ms after the shock launch and the positions of the neutrinospheres are almost identical in all three models. From this one can conclude several things: Firstly, the proton neutron star is sufficiently resolved in all models since the position of the neutrinospheres is grid independent. Secondly, the shocks behave differently when they pass through the region between roughly 50 km and 130 km, a region where the resolution is different in all three models. At later times, the shock trajectories are roughly parallel. Thus, in the shock expansion phase the resolution should probably be better than the $dr/r \approx 3\%$ in model "400–zones". However, it must be noted here that the observed difference in the shock trajectory of roughly 10 km at a shock radius of 150 km and a dr/r of 3% corresponds to 2 or 3 grid zones which is even smaller than the value of the typical "shock–width" of the PPM–scheme which is normally 4 to 5 zones. Thus it is impossible to discriminate whether the larger shock trajectory is due to a "shock detection uncertainty" or due to a low grid resolution[3]. Furthermore, it is extremely reassuring that the evolution of the shock trajectories is nearly parallel. This implies that all simulations "capture" the same physics, which is a strong hint that our lowest resolved model is not severely contaminated by the radial resolution. However, to be on the save side, a radial grid resolution of model "600–zones" is clearly preferable to the grid of model "400–zones", whereas a further improvement of the radial resolution is not justified due to the increase of computational costs.

E.2. A "minimal" 2D–resolution study

Most of the 2D–simulations discussed in this volume were performed with 192 angular bins on a 180° (angular resolution of 0.94°) setup and with initially[4] 600 radial zones. This setup is now compared with previous simulations that used not more than 128 angular bins (which corresponds to an angular resolution of 1.41°) and initially 400 radial zones (see, e.g. Buras et al. 2006a). In this Section an attempt is made to investigate possible resolution differences in the angular grid, by comparing two simulations with different angular resolution. However, because of computational costs it was not possible to compute the same model with even better angular resolution than 0.94° and thus a "minimal" resolution test was done: additionally to the

[3] Note that here the case is different compared to the test runs with the energy grid. In the later, the small differences in the shock trajectories are clearly caused by the changed energy grid. The reason why the shock detection can not be responsible is that detecting the shock only dependence on the radial grid which was *not* changed in the energy grid test runs.

[4] As explained, during the simulation at several times a rezoning procedure was applied.

fine resolved simulation, with an angular resolution of 0.94° the otherwise identically problem was calculated with an angular resolution of 1.41°. As mentioned before, this also implies that the radial resolution had to be changed by a factor 2/3 (i.e. from 600 to 400 zones), because the PPM hydro–scheme used in the M DB TH–code, requires roughly quadratic grid zones (i.e. the axis ratio of the lengths in radial and angular direction must be near unity). In order to save computer time both models were only calculated from north pole to equator, which does not suppress any essential physics as we explained in Section 4.2 and Section 6.1.

These two simulations allow us to judge whether or not the resolution has influence on our numerical results. However, without more models, we are not able to judge whether our results are already numerically converged.

Firstly, a comparison of the laterally averaged shock positions and luminosities between both 2D–models, see Fig. E.6, reveals that the relative behaviour of these models is the same as the relative behaviour of the corresponding 1D–models. Thus most of the differences we find in the multi–dimensional models must be contributed to the different radial grids (see Subsection E.1.2). For example, the roughly 10 km larger shock radius in model Wolff–1.41° than in the better angularly resolved model, is also found in the corresponding 1D–model “Wolff-400” (see also Subsection E.1.2). However, Fig. E.6 also reveals a difference between model Wolff–1.41° and model Wolff–0.91°: in the early phase for $t < 20$ ms, model Wolff–1.41° shows a slightly stronger shock expansion, which is a reaction on more extended electron neutrinosphere radius. This feature can also be seen in Fig. E.7, which depicts the convection inside the proto neutron star for both 2D–models. The convective regions are very similar in both models, however, deep inside the core (between a mass coordinate of $0.4M_{\odot}$ and $0.5M_{\odot}$) model Wolff–1.41° shows more convection in the first 30 ms after the shock formation. Since this convective region is located deep in the nascent neutron star it is neither able to boost the neutrino luminosities nor does it lead to an expansion of the core. Figure E.8 gives a more detailed impression of the growth of convective instabilities, where the lateral velocities and the entropies are shown. At least for the first 50 ms after the shock formation the patterns as well as the value of lateral velocities are roughly comparable, but of course the details of the flows are different. The reasons for this can be shortly summarised:

- After the shock formation when the mapping of a spherically symmetric calculation onto a 2D–grid is done, a random perturbation of density from zone to zone is applied (see Section 4.1). Though we have used the same perturbation amplitude in both models, a zone to zone perturbation with different radial grids implies that we cannot control the wavelength of the perturbation. Thus the initial perturbation was not exactly the same in both models. One would expect that a better resolved model shows convection (at least for the beginning of the instability) on smaller scales and resolves finer structures, which is indeed the case in Fig. E.8.

- Convective flows are a non–linear, chaotic process. Thus one cannot expect to get the exactly same convective pattern[5] for different simulations, especially if the seed perturbations are not identical.

[5]Though the flow pattern is not exactly (i.e. the velocity field) the same, probably it is the same in the sense that e.g. the number of down flows and up flows are the same.

However, the fact that convective regions develop very similar for the whole simulated time, remember Fig. E.7, despite the "chaotic" character of convective flows, and despite slightly different convective flow patterns, is a strong hint that our low resolved model Wolff–1.41° does not suffer from resolution artefacts. It must be stressed here that this is statement can only be made for a time up to 100 ms after the shock formation, since we were not able to compute our low resolved model to a larger postbounce time. Moreover, this statement relies on the assumption that both models do *not* suffer from the same resolution artefacts, which might dissappear if a larger angular resolution would be used. As explained before, due to a for lack of computer time we were not able to calculate such a well resolved model[6].

An expansion of the shock surface into spherical harmonics gives surprisingly well agreement between both models with different resolution, see Fig. E.5. Both models show comparable amplitudes of the oscillation and more surprisingly even the frequency is the same for the first 50 ms of the simulations and only at later times the oscillations clearly loose their correlation. Since we have no theory to tell us the "exact" oscillation pattern, we can only conclude that the time evolution of shock deformations are resolution dependent. This, however, is expected since the angular dependence of the shock is triggered by the perturbations we impose on the velocity field when we start our 2D simulation. As already explained, these perturbations, however, change when we use different angular and radial resolutions.

We thus conclude from both models with different angular resolution that we do do not see any indication for resolution artefacts on the angular grid. The laterally averaged shock positions and neutrino luminosities behave very similar to the corresponding 1D–models, and the differences can be traced back to different radial grids, see Sect. E.1.2. Multi–dimensional effects like the growth of convection or the angular shock deformation, which depend on the (resolution dependent) imposed perturbations, develop surprisingly quite similar. However, since the quantities are somewhat chaotic to the initial conditions, it is not expected that a convergence with different grid resolutions can be obtained. However, the dependence of the results on the *radial* grid resolution, implies that the next generation of multi–dimensional supernova simulations should apply a higher angular resolution together with a higher radial resolution in order to maintain the constraint that numerical grid cells should be roughly quadratic.

[6] It should be noted here that simulations of Scheck (2006) indicate that no better angular resolution than 1° may be necessary. However these results are obtained with a different code and may thus not be applicable to our numerical scheme.

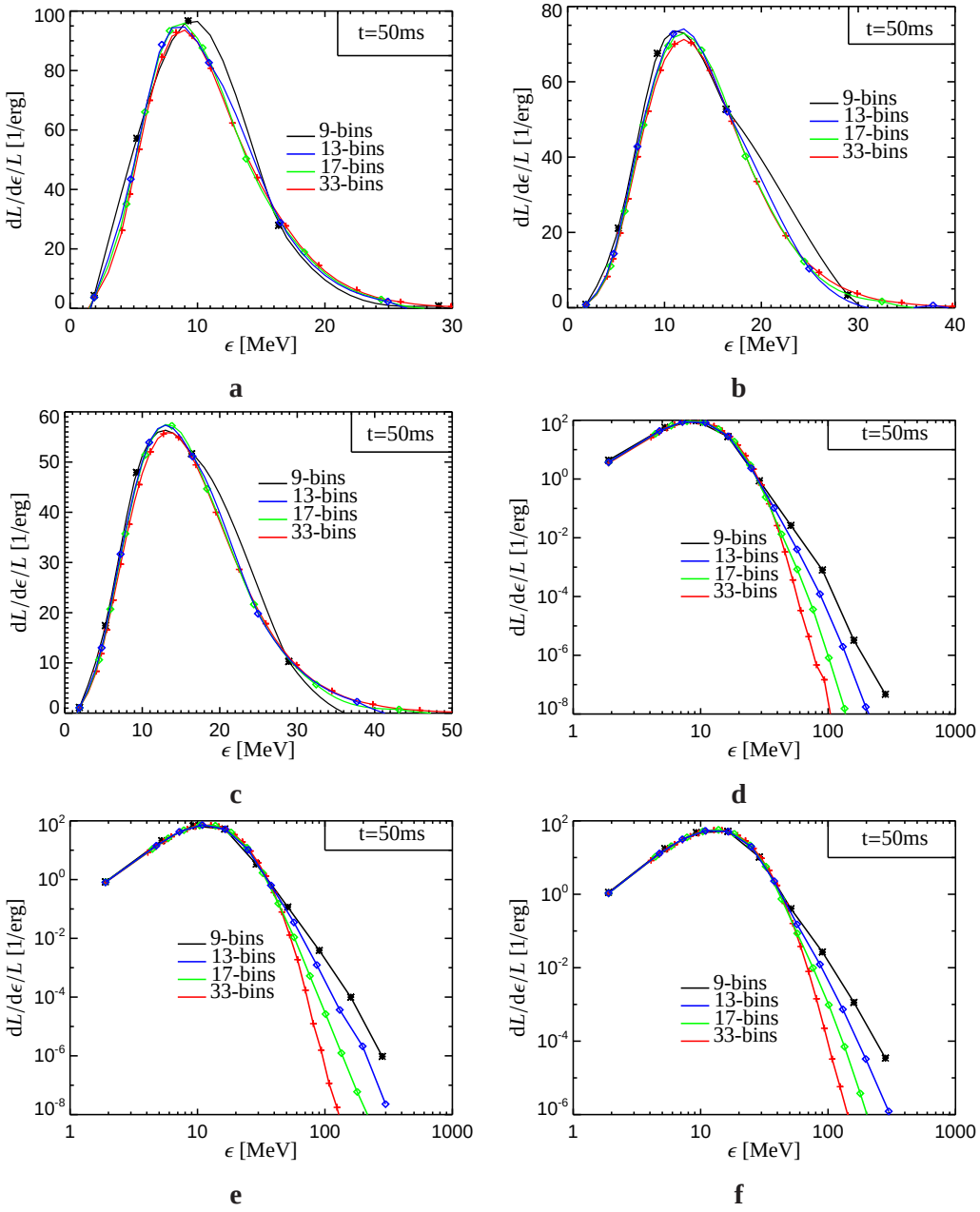

Figure E.2.: The neutrino spectra for the different models at a time of 50 ms after the shock formation as the would be measured by an observer at rest at infinity. The evaluation was done at 400 km from the centre of the star. Shown are the electron neutrinos (**a**), the anti–electron neutrinos (**b**), and all other neutrino flavours (**c**). Symbols represent the grid points, where as the spectral shape was obtained by a spline fit though these data points. Panels **d**–**f** show the same values, however, a double logarithmic scale was chosen.

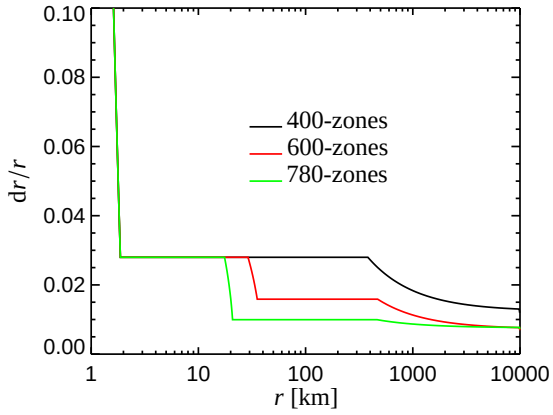

Figure E.3.: The radial resolution $\mathrm{d}r/r$ as function of radius for all models. Note that the important region which has to be resolved well enough lies between roughly 20 km and a few hundred km.

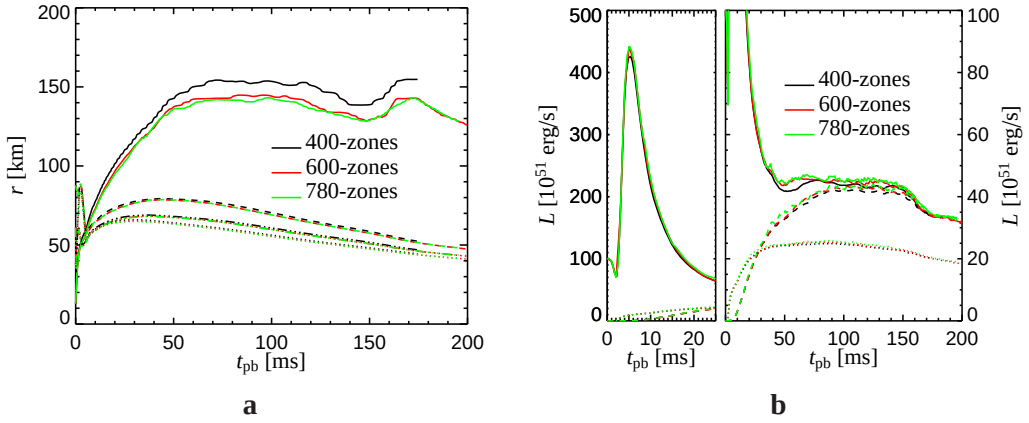

Figure E.4.: **a**: The trajectories of the shock fronts (solid) and the different neutrinospheres (dashed electron neutrinos, dashed–dotted anti electron neutrinos, and dotted muon and tauon neutrinos) for all models. **b**: The neutrino luminosities for all models measured at 400 km for an static observer resting at infinity. The solid lines represent electron neutrinos, the dashed lines show the values for anti electron neutrinos, and the dotted lines represent the heavy (anti) lepton neutrinos.

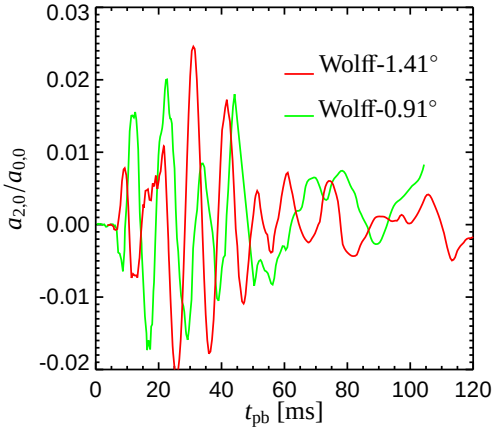

Figure E.5.: The coefficient corresponding to the $l = 2$–mode obtained by expanding the shock surface into spherical harmonics. Since both models were calculated on a grid from north–pole to the equator this mode corresponds to the lowest possible non–spherical mode.

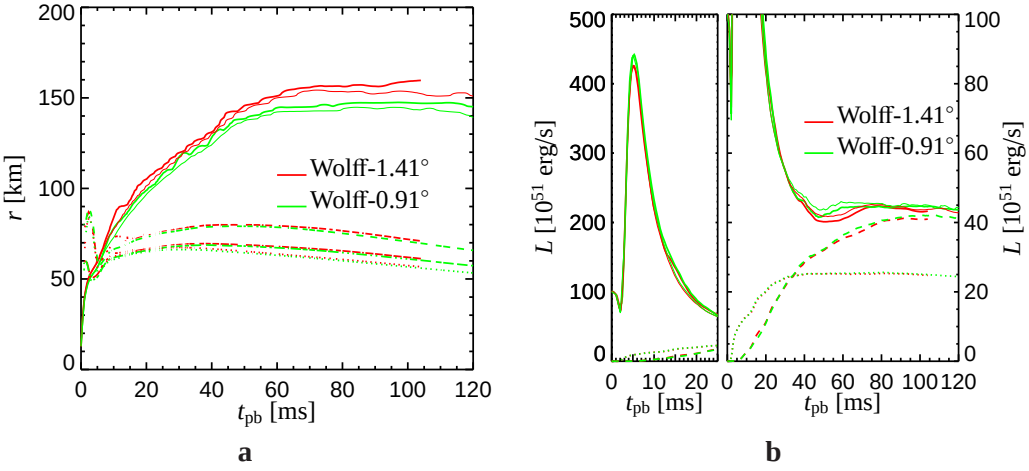

Figure E.6.: **a**: The angularly averaged positions of the shock front (solid) and the neutrinospheres (dashed electron neutrinos, dashed–dotted anti electron neutrinos, dotted heavy (anti) lepton neutrinos) for the low resolved model Wolff–1.41° and the better resolved model Wolff–0.91°. **b**: The neutrino luminosities measured at 400 km for a static observer resting at infinity. The solid lines represent the electron neutrinos, the dashed lines represent anti electron neutrinos, and the heavy (anti) lepton neutrinos are represented by the dotted lines.

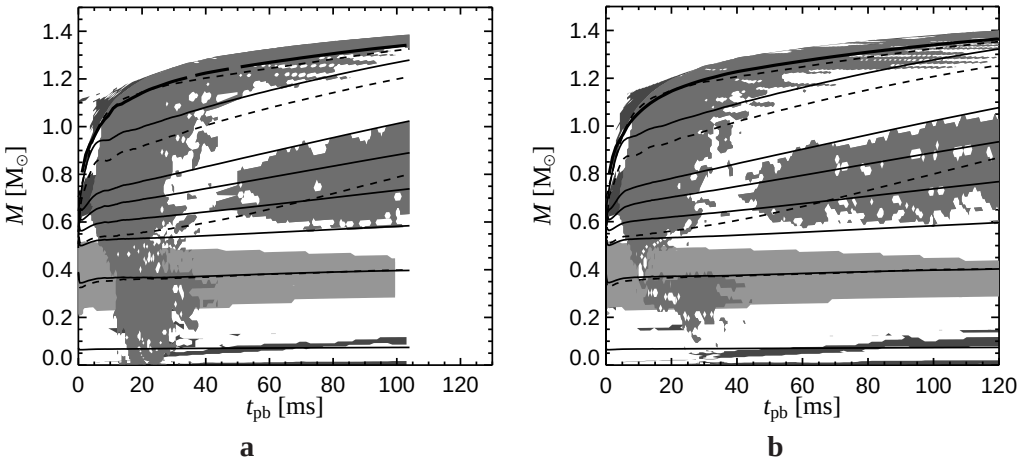

Figure E.7.: Regions of convective motions inside the nascent neutron star as function of time for **a**: model Wolff–1.41°. **b**: model Wolff–0.91°. Also shown are density contours (dashed) of $10^{14}, 10^{13}, 10^{12}, 10^{11}$ g/cm^3 (from bottom to top) and radii (thin solid) of 5, 10, 15, 20, 25, 30, 50 km (from bottom to top). The thick solid line represents the position of the electron neutrinosphere. The almost black shaded region indicates regions where the evaluation of the Ledoux criterion with the laterally averaged 2D–data indicates instability. The dark grey region indicates where the condition $v_\theta > 7 \times 10^7$ cm/s is fulfilled in a 2D–simulation. Finally, the light grey region indicates where heavy nuclei ($\langle A \rangle \geq 57 \wedge X_\mathrm{H} \geq 0.1$) are present (compare also to Fig. 3.8). Note that the evaluation of the Ledoux criterion with laterally averaged data predicts convective instability where indeed convective flows are found (compare e.g. to Fig. 3.17), except for the band for $M < 0.2\,\mathrm{M}_\odot$.

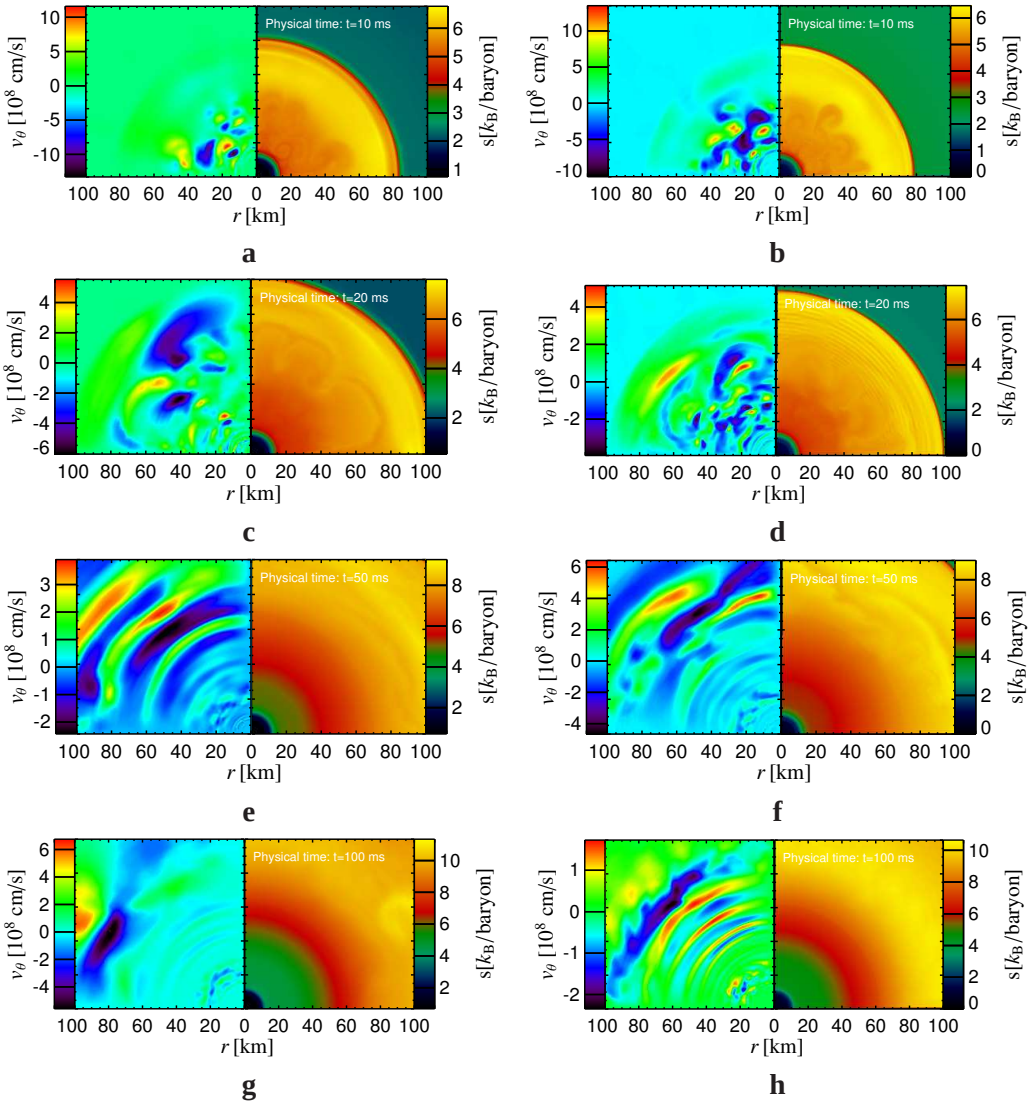

Figure E.8.: Snapshots of the lateral velocity (left) and entropy (right) for model Wolff–1.41° (first column) and model Wolff–0.91° (second column) at different times. Panels **a** and **b** depict the situation at 10 ms after the shock formation, panels **c** and **d** at 20 ms, panels **e** and **f** at 50 ms, and panels **g** and **h** at 100 ms after the shock formation.

Bibliography

Arcones, A., Janka, H. ., & Scheck, L. 2006, ArXiv Astrophysics e-prints

Arnett, W. D., Bahcall, J. N., Kirshner, R. P., & Woosley, S. E. 1989, ARA&A, 27, 629

Baron, E., Bethe, H. A., Brown, G. E., Cooperstein, J., & Kahana, S. 1987a, Physical Review Letters, 59, 736

Baron, E., Cooperstein, J., & Kahana, S. 1985, Physical Review Letters, 55, 126

—. 1987b, ApJ, 320, 300

Baron, E., Myra, E. S., Cooperstein, J., & van den Horn, L. J. 1989, ApJ, 339, 978

Bethe, H. A. 1990, Reviews of Modern Physics, 62, 801

Blondin, J. M. & Mezzacappa, A. 2006, ApJ, 642, 401

Blondin, J. M., Mezzacappa, A., & DeMarino, C. 2003, ApJ, 584, 971

Bruenn, S. W. 1985, ApJS, 58, 771

—. 1986, ApJL, 311, L69

—. 1989a, ApJ, 340, 955

—. 1989b, ApJ, 341, 385

Bruenn, S. W. 2005, in Open Issues in Core Collapse Supernova Theory, Ed. Mezzacappa, A. and Fuller, G. M., 99–+

Bruenn, S. W. & Mezzacappa, A. 1997, Phys. Rev. D, 56, 7529

Buras, R., Janka, H.−Th., Keil, M. T., Raffelt, G. G., & Rampp, M. 2003, ApJ, 587, 320

Buras, R., Janka, H.−Th., Rampp, M., & Kifonidis, K. 2006a, A&A, 457, 281

Buras, R., Rampp, M., Janka, H.−Th., & Kifonidis, K. 2006b, A&A, 447, 1049

Burrows, A. & Hayes, J. 1995, in Seventeeth Texas Symposium on Relativistic Astrophysics and Cosmology, Ed. Böhringer, H. and Morfill, G. E. and Trümper, J. E., 375–+

Burrows, A., Hayes, J., & Fryxell, B. A. 1995, ApJ, 450, 830

Burrows, A., Livne, E., Dessart, L., Ott, C. D., & Murphy, J. 2006a, ApJ, 640, 878

—. 2006b, New Astronomy Review, 50, 487

—. 2006c, ArXiv Astrophysics e–prints

Burrows, A., Reddy, S., & Thompson, T. A. 2004, ArXiv Astrophysics e–prints

Burrows, A. & Sawyer, R. F. 1998, Phys. Rev. C, 58, 554

—. 1999, Phys. Rev. C, 59, 510

Burrows, A., Young, T., Pinto, P., Eastman, R., & Thompson, T. A. 2000, ApJ, 539, 865

Carter, G. W. & Prakash, M. 2002, Physics Letters B, 525, 249

Cernohorsky, J. & Bludman, S. A. 1994, ApJ, 433, 250

Cernohorsky, J., van den Horn, L. J., & Cooperstein, J. 1989, J. Quant. Spectrosc. Radiat. Transfer, 43, 603

Colella, P. & Woodward, P. 1984, J. Comp. Phys., 54, 174

Colgate, S. A. & White, R. H. 1966, ApJ, 143, 626

Cooperstein, J. & Baron, E. A. 1990, in Supernova, Ed. A. Petschek (Springer), 213

Cowling, T. G. 1941, MNRAS, 101, 367

Dessart, L., Burrows, A., Livne, E., & Ott, C. D. 2006, ApJ, 645, 534

Dimmelmeier, H., Font, J. A., & Müller, E. 2002, A&A, 388, 917

Dimmelmeier, H., Novak, J., Font, J. A., Ibáñez, J. M., & Müller, E. 2005, Phys. Rev. D, 71, 064023

Epstein, R. I. 1979, MNRAS, 188, 305

Finn, L. S. 1986, MNRAS, 222, 393

—. 1987, MNRAS, 227, 265

Foglizzo, T. 2001, A&A, 368, 311

—. 2002, A&A, 392, 353

Foglizzo, T., Scheck, L., & Janka, H.−Th. 2005, in SF2A–2005: Semaine de l'Astrophysique Francaise, Ed. Casoli, F. and Contini, T. and Hameury, J. M. and Pagani, L., 483–+

Foglizzo, T. & Tagger, M. 2000, A&A, 363, 174

Fryer, C. L. 1999, ApJ, 522, 413

Fryer, C. L., Benz, W., & Herant, M. 1996, ApJ, 460, 801

Fryer, C. L. & Heger, A. 2000, ApJ, 541, 1033

Fryer, C. L. & Warren, M. S. 2002, ApJL, 574, L65

—. 2004, ApJ, 601, 391

Fryer, C. L. & Young, P. A. 2006, ArXiv Astrophysics e-prints

Fryxell, B., Müller, E., & Arnett, W. 1989, Hydrodynamics and Nuclear Burning, preprint MPA–449, Max Planck Institut für Astrophysik, Garching

Fryxell, B., Olson, K., Ricker, P., Timmes, F. X., Zingale, M., Lamb, D. Q., MacNeice, P., Rosner, R., Truran, J. W., & Tufo, H. 2000, ApJS, 131, 273

Fuller, G. M., Fowler, W. A., & Newman, M. J. 1982, ApJS, 48, 279

Guillot, T., Burrows, A., Hubbard, W. B., Lunine, J. I., & Saumon, D. 1995, in Bulletin of the American Astronomical Society, 1379–+

Hannestad, S. & Raffelt, G. 1998, ApJ, 507, 339

Heger, A., Woosley, S. E., Martínez–Pinedo, G., & Langanke, K. 2001, ApJ, 560, 307

Heger, A., Woosley, S. E., & Spruit, H. C. 2005, ApJ, 626, 350

Herant, M., Benz, W., & Colgate, S. 1992, ApJ, 395, 642

Herant, M., Benz, W., Hix, W. R., Fryer, C. L., & Colgate, S. A. 1994, ApJ, 435, 339

Hillebrandt, W., Höflich, P., Janka, H.−Th., & Mönchmeyer, R. 1989, in Big Bang, Active Galactic Nuclei and Supernovae, Ed. Hayakawa, S. and Sato, K., 441

Hillebrandt, W. & Wolff, R. G. 1985, in Nucleosynthesis : Challenges and New Developments, Ed. Arnett, W. D. and Truran, J. W., 131

Hillebrandt, W., Wolff, R. G., & Nomoto, K. 1984, A&A, 133, 175

Hix, W. R., Messer, O. E., Mezzacappa, A., Liebendörfer, M., Sampaio, J., Langanke, K., Dean, D. J., & Martínez–Pinedo, G. 2003, Physical Review Letters, 91, 201102

Horowitz, C. J. 1997, Phys. Rev. D, 55, 4577

—. 2002, Phys. Rev. D, 65, 043001

Horowitz, C. J., Pérez–García, M. A., Carriere, J., Berry, D. K., & Piekarewicz, J. 2004a, Phys. Rev. C, 70, 065806

Horowitz, C. J., Pérez–García, M. A., & Piekarewicz, J. 2004b, Phys. Rev. C, 69, 045804

Itoh, N. 1975, Progress of Theoretical Physics, 54, 1580

Itoh, N., Asahara, R., Tomizawa, N., Wanajo, S., & Nozawa, S. 2004, ApJ, 611, 1041

Itoh, N., Mitake, S., Iyetomi, H., & Ichimaru, S. 1983, ApJ, 273, 774

Itoh, N., Totsuji, H., Ichimaru, S., & Dewitt, H. E. 1979, ApJ, 234, 1079

Janka, H.−Th. 2001, A&A, 368, 527

Janka, H.−Th., Buras, R., Kifonidis, K., Rampp, M., & Plewa, T. 2002, in Review for "Core Collapse of Massive Stars", Ed. C.L. Fryer, Kluwer, Dordrecht, preprint astro–ph/0212314

Janka, H.−Th., Kifonidis, K., & Rampp, M. 2001, in Lecture Notes in Physics, Vol. 578, Proc. Workshop on Physics of Neutron Star Interiors, Ed. Blaschke, D. and Glendenning, N.K. and Sedrakian, A.D. (Springer), 333–363, preprint astro–ph/0103015

Janka, H.−Th. & Mueller, E. 1994, A&A, 290, 496

—. 1996, A&A, 306, 167

Kachelrieß, M., Tomàs, R., Buras, R., Janka, H.−Th., Marek, A., & Rampp, M. 2005, Phys. Rev. D, 71, 063003

Keil, W. 1997, PhD thesis, Technische Universität München

Keil, W., Janka, H.−Th., & Mueller, E. 1996, ApJL, 473, L111+

Kifonidis, K., Plewa, T., Janka, H.−Th., & Müller, E. 2003, A&A, 408, 621

Kifonidis, K., Plewa, T., Scheck, L., Janka, H.−Th., & Müller, E. 2006, A&A, 453, 661

Kippenhahn, R. & Weigert, A. 1990, Stellar structure and evolution (Springer)

Kitaura, F. S., Janka, H.−Th., & Hillebrandt, W. 2006, A&A, 450, 345

Köhler, H. S. 1975, Nucl. Phys. A, 258, 301

Koonin, S. E., Dean, D. J., & Langanke, K. 1997, Physics Reports, 278, 1

Kotake, K., Sawai, H., Yamada, S., & Sato, K. 2004, ApJ, 608, 391

Langanke, K., Martínez–Pinedo, G., Sampaio, J. M., Dean, D. J., Hix, W. R., Messer, O. E., Mezzacappa, A., Liebendörfer, M., Janka, H.−Th., & Rampp, M. 2003, Physical Review Letters, 90, 241102

Langanke, K. & Martínez-Pinedo, G. 2000, Nuclear Physics A, 673, 481

—. 2001, Atomic Data and Nuclear Data Tables, 79, 1

Langanke, K., Martínez-Pinedo, G., & Sampaio, J. M. 2001, Physical Review C, 64, 055801

Lattimer, J., Pethick, C., Ravenhall, D., & Lamb, D. 1985, Nucl. Phys. A, 432, 646

Lattimer, J. & Swesty, F. 1991, Nucl. Phys. A, 535, 331

Lattimer, J. M. 2005, in Bulletin of the American Astronomical Society, 1220–+

Lattimer, J. M. 2006, in American Institute of Physics Conference Series, 155–162

Lattimer, J. M. & Prakash, M. 2004, Science, 304, 536

—. 2006, astro–ph/061244

Leinson, L., Oraevsky, V., & Semikoz, V. 1988, Phys. Lett. B, 209

Liebendörfer, M., Messer, O. E. B., Mezzacappa, A., Bruenn, S. W., Cardall, C. Y., & Thielemann, F.−K. 2004, ApJS, 150, 263

Liebendörfer, M., Messer, O. E. B., Mezzacappa, A., Hix, W. R., Thielemann, F.−K., & Langanke, K. 2002, in Proceedings of the 11th Workshop on Nuclear Astrophysics, Ed. Müller, E. and Hillebrandt, W., 126–131, preprint astro-ph/0203260

Liebendörfer, M., Mezzacappa, A., & Thielemann, F.−K. 2001, Phys. Rev. D, 63, 104003

Liebendörfer, M., Rampp, M., Janka, H.−Th., & Mezzacappa, A. 2005, ApJ, 620, 840

Liebendörfer, M., Rosswog, S., & Thielemann, F.−K. 2002, ApJS, 141, 229

MacFadyen, A. & Woosley, S. E. 1998, in Bulletin of the American Astronomical Society, 874–+

Marek, A. 2003, Diploma thesis, Technische Universität München

Marek, A., Dimmelmeier, H., Janka, H.−Th., Müller, E., & Buras, R. 2006, A&A, 445, 273

Martínez–Pinedo, G., Langanke, K., Sampaio, J. M., Dean, D. J., Hix, W. R., Messer, O. E. B., Mezzacappa, A., Liebendörfer, M., Janka, H.−Th., & Rampp, M. 2005, in Cosmic Explosions, IAU Colloquium 192 (Springer, Berlin), 321

Mayle, R. W., Tavani, M., & Wilson, J. R. 1993, ApJ, 418, 398

McCray, R. 1993, ARA&A, 31, 175

Mezzacappa, A. & Bruenn, S. W. 1993a, ApJ, 405, 669

—. 1993b, ApJ, 410, 740

Mezzacappa, A., Calder, A. C., Bruenn, S. W., Blondin, J. M., Guidry, M. W., Strayer, M. R., & Umar, A. S. 1998a, ApJ, 495, 911

—. 1998b, ApJ, 493, 848

Mezzacappa, A., Liebendörfer, M., Messer, O. E., Hix, W. R., Thielemann, F.−K., & Bruenn, S. W. 2001, Physical Review Letters, 86, 1935

Mihalas, D. & Mihalas, B. 1984, Foundations of Radiation Hydrodynamics (Oxford University Press)

Müller, E. 1998, Simulation of Astrophysical Fluid Flow, Lecture Notes: Saas Fee Advanced Course 27 (Berlin: Springer)

Müller, E. & Steinmetz, M. 1995, Computer Phys. Commun., 89, 45

Myra, E. S. & Bludman, S. A. 1989, ApJ, 340, 384

Nomoto, K. 1984, ApJ, 277, 791

—. 1987, ApJ, 322, 206

Nomoto, K., Shigeyama, T., Kumagai, S., Yamaoka, H., & Suzuki, T. 1994, in Supernovae, Ed. Bludman, S. A. and Mochkovitch, R. and Zinn–Justin, J., 489–+

Ott, C. D., Burrows, A., Livne, E., & Walder, R. 2004, ApJ, 600, 834

Pons, J. A., Miralles, J. A., & Ibanez, J. M. A. 1998, A&AS, 129, 343

Rampp, M. 2000, PhD thesis, Technische Universität München

Rampp, M. & Janka, H.−Th. 2002, A&A, 396, 361

Reddy, S., Prakash, M., Lattimer, J. M., & Pons, J. A. 1999, Phys. Rev. C, 59, 2888

Rybicki, G. B. & Lightman, A. P. 1979, Radiative Processes in Astrophysics (John Wiley and Sons, New York)

Sampaio, J. M. 2003, PhD thesis, Aarhus Universitet

Sawyer, R. F. 2005, Physics Letters B, 630, 1

Scheck, L. 2006, PhD thesis, Technische Universität München

Scheck, L., Kifonidis, K., Janka, H.−Th., & Müller, E. 2006, A&A, 457, 963

Shapiro, S. L. & Teukolsky, S. A. 1983, Black holes, white dwarfs, and neutron stars: The physics of compact objects (New York, NY, U.S.A.: Wiley)

Shen, H., Toki, H., Oyamatsu, K., & Sumiyoshi, K. 1998a, Nucl. Phys. A, 637, 435

—. 1998b, Progress of Theoretical Physics, 100, 1013

Shu, F. H. 1992, The Physics of Astrophysics, Vol. II, Gas Dynamics (Mill Valley, CA, U.S.A.: University Science Books)

Straumann, N. 1989, Physics of type II supernova explosions (Particle Physics and Astrophysics – Current viewpoints), 79–170

Sumiyoshi, K., Suzuki, H., Otsuki, K., Terasawa, M., & Yamada, S. 2000, Publications of the Astronomical Society of Japan, 52, 601

Sumiyoshi, K., Suzuki, H., & Toki, H. 1995, A&A, 303, 475

Sumiyoshi, K., Yamada, S., Suzuki, H., Shen, H., Chiba, S., & Toki, H. 2005, ApJ, 629, 922

Swesty, F. D., Lattimer, J. M., & Myra, E. S. 1994, ApJ, 425, 195

Swesty, F. D. & Myra, E. S. 2005, Journal of Physics Conference Series, 16, 380

Tartamella, C. M., Swesty, F. D., & Lattimer, J. M. 2005, in Bulletin of the American Astronomical Society, 1182–+

Terasawa, M., Sumiyoshi, K., Kajino, T., Mathews, G. J., & Tanihata, I. 2001, ApJ, 562, 470

Thompson, T. A., Burrows, A., & Pinto, P. A. 2003, ApJ, 592, 434

Thompson, T. A., Quataert, E., & Burrows, A. 2004, ArXiv Astrophysics e–prints

Totani, T., Sato, K., Dalhed, H. E., & Wilson, J. R. 1998, ApJ, 496, 216

van Riper, K. A. 1978, ApJ, 221, 304

Watanabe, G., Sato, K., Yasuoka, K., & Ebisuzaki, T. 2004, Phys. Rev. C, 69, 055805

Wilson, J. R. 1982, in Proc. Univ. Illinois, Meeting on Numerical Astrophysiscs

Wilson, J. R. & Mayle, R. 1988, Physics Reports, 163, 63

Wooden, D. H. 1997, in American Institute of Physics Conference Series, Ed. Bernatowicz, T. J. and Zinner, E., 317–+

Woosley, S. E., Heger, A., & Weaver, T. A. 2002, Reviews of Modern Physics, 74, 1015

Woosley, S. E. & Weaver, T. A. 1995, NASA STI/Recon Technical Report N, 96, 22970

Yahil, A. 1983, ApJ, 265, 1047

Yamasaki, T. & Yamada, S. 2005, ApJ, 623, 1000

Young, P., Meakin, C., Arnett, D., & Fryer, C. 2005, astro–ph/0507104

Danksagung

Jetzt, nachdem ich beim Schreiben dieser Seiten angekommen bin, wird mir letztendlich klar, dass ein Lebensabschnitt vorüber ist, und es Zeit wird, über die letzten drei Jahre ein Resümee zu ziehen. Wie das im Leben so üblich ist, bestanden diese drei Jahre aus Höhen aber auch Tiefen; in meinem Fall haben aber die positiven Aspekte eindeutig überwogen. Das dem so ist, verdanke ich vielen lieben Menschen und Kollegen, bei denen ich mich nun hier bedanken möchte.

Aus meinem Arbeitsumfeld möchte ich mich an erster Stelle bei meinem Betreuer Hans–Thomas Janka bedanken. Zum einen dafür, dass ich die Gelegenheit hatte auf diesem interessanten Gebiet der Astrophysik zu promovieren, zum anderen aber auch für die Zusammenarbeit und für die Bereitschaft ständig über Probleme zu diskutieren und mir gute Anregungen zu geben. Robert Buras danke ich für die Zeit, die er sich oft genommen hat um Probleme mit dem Code zu diskutieren und für seine Bereitstellung vieler kleiner, aber sehr nützlicher Werkzeuge. Allen anderen Gruppenmitgliedern, Almudena, Harald, Nicolay, Martin, Roland, Bernhard, Leonhard und Konstantinos danke ich für die gute und enge Zusammenarbeit. Vor allem Konstaninos bin ich sehr dankbar dafür, dass er den Code auf den Rechner des HLRS portiert hat und auch den ersten Rechenzeitantrag geschrieben hat. Ohne diese Hilfe wäre ich sehr viel später in das spannende Arbeitsfeld des “Supercomputing” gestartet.

Supercomputinganwendung benötigen natürlich Supercomputer. Ich hatte das grosse Glück, auf den Einrichtungen des John von Neumann–Institus für Computing in Juelich, des Rechenzentrums der Max–Planck–Gesellschaft in Garching, des Höchstleistungsrechenzentrums in Stuttgart, und der Distributed European Infrastructure for Supercomputing Applications rechnen zu können. Ohne diese Einrichtungen wäre meine Doktorarbeit gar nicht möglich gewesen.

Aproppos Rechenzeit: den Direktoren des Institus, Wolffgang Hillebrandt, Rashid Sunayev und Simon White bin ich sehr verbunden, dass sie sich dafür eingesetzt haben, dass ich meinen persönlichen Rechner bekam. Ich hoffe meine Arbeit rechtfertigt diese Investition...

Auch bin ich den tapferen Administratoren am Institut, aber auch an den Rechenzentren in Garching, Stuttgart und in Jülich dankbar für ihre prompte Unterstützung bei (von mir verursachten?) Problemen. Insbesondere Bernt Christandl, Frau Weidl und Herr Guggenberger sollen in diesem Zusammenhang erwähnt werden.

Natürlich danke ich allen am MPA für die gute Arbeitsatmosphäre, ganz besonders aber Rüdiger, Anja, Emma und Dimitri. Ohne die Gespräche mit Euch wäre meine Promotionszeit sicherlich langweiliger gewesen! Emma, Dir muss ich noch besonders für das mühevolle Korrekturlesen danken. Alle Fehler, die sich dennoch in der Arbeit befinden, sind natürlich mir anzulasten...

Auf keinen Fall darf ich hier Bjoern und Karin vergessen, die mir sogar aus der Ferne immer helfen wollten und aufmunternde Worte parat hatten. Manchmal sieht man den Wald vor lauter Bäumen einfach nicht mehr...

Zuletzt gilt natürlich der Danke meiner Mutter und meinen Schwestern: Danke, dass Ihr immer für mich da gewesen seit und Ihr mir helfen wolltet.

Garching, den 29.01.2007